THE UNIVERSITY OF TEXAS AT AUSTIN
CENTER FOR TRANSPORTATION RESEARCH

TECHNICAL REPORT 0-7011-1
TxDOT PROJECT NUMBER 0-7011

Design and Behavior of Seamless Bridge-Pavement Systems

Xiaoyi Chen, Ph.D.
Jay Malviya
Behdad Mofarraj Kouchaki, Ph.D.
Xiaomeng Ge, Ph.D.
Todd Helwig, Ph.D.
Juan Murcia-Delso, Ph.D.
Jorge G. Zornberg, Ph.D.

September 2023

http://library.ctr.utexas.edu/ctr-publications/0-7011-1.pdf

Technical Report Documentation Page

1. Report No. FHWA/TX-23/0-7011-1	2. Government Accession No.	3. Recipient's Catalog No.
4. Title and Subtitle Design and Behavior of Seamless Bridge-Pavement Systems.		5. Report Date Submitted: August 2023; September 2023. 6. Performing Organization Code
7. Author(s) Xiaoyi Chen, Ph.D. http://orcid.org/0000-0002-4939-224X. Jay Malviya. Behdad Mofarraj Kouchaki, Ph.D. Xiaomeng Ge, Ph.D. Todd Helwig, Ph.D. Juan Murcia-Delso, Ph.D. http://orcid.org/0000-0001-6424-7262. Jorge G. Zornberg, Ph.D. http://orcid.org/0000-0002-6307-1047.		8. Performing Organization Report No. 0-7011-1
9. Performing Organization Name and Address Center for Transportation Research The University of Texas at Austin 3925 W. Braker Lane, 4th Floor Austin, TX 78759		10. Work Unit No. (TRAIS) 11. Contract or Grant No. 0-7011
12. Sponsoring Agency Name and Address Texas Department of Transportation Research and Technology Implementation Division 125 E. 11th Street Austin, TX 78701		13. Type of Report and Period Covered Technical Report August 2019 – August 2023 14. Sponsoring Agency Code
15. Supplementary Notes Project performed in cooperation with the Texas Department of Transportation and the Federal Highway Administration.		

16. Abstract

The seamless bridge concept eliminates expansion joints on the bridge deck and joints between the bridge and approach, which can significantly reduce the maintenance costs and improve the long-term durability of the primary load-carrying components. Past applications of seamless bridges have utilized Continuously Reinforced Concrete Pavement (CRCP) in which a transition zone is employed between the bridge deck and CRCP to accommodate deformations caused by the longitudinal expansion and contraction of the bridge. A critical aspect of the system response is the longitudinal load transfer mechanism in the transition zone, which is governed by the concrete slab-base interaction. This project aims to advance the development and implementation of seamless systems in the U.S. based on a comprehensive investigation including experimental testing and numerical modeling. The experimental study focused on the characterization of the concrete slab-base interaction through unit-cell direct shear tests and cyclic large-scale push-off tests. The load (shear) versus displacement behavior at the concrete slab-base interface was evaluated for different interface materials (geotextiles, polyethylene sheets, felt paper) intended to break the bond and control the level of interface restraint. The effects of cyclic movements were investigated. The numerical study involved the development of a structural model of the entire seamless system under longitudinal effects, and a more detailed continuum finite element model of the transition zone under combined longitudinal and out-of-plane (vertical) effects. The numerical models were used to study the influence of the friction coefficient at the concrete slab-base interface, reinforcement ratio and slab thickness of the transition zone on the axial response of the system. Potential design issues related to the seamless bridge connection were investigated through numerical parametric studies for various bridge prototype structures in Texas with different configurations. Based on the experimental results and numerical studies, general design recommendations were developed, including the selection of promising bond breakers (i.e., felt paper and double-sided textured linear low-density polyethylene sheet) in the transition zone, design verification criteria and design details. Simplified analytical models were developed to determine the stresses and deformations induced in the system considering axial and out-of-plane effects. A design example of an actual bridge in Texas modified to include a seamless connection with CRCP was presented using the proposed design procedure.

17. Key Words	18. Distribution Statement
Seamless bridge-pavement system, transition zone, approach slab, bond breaker, felt paper, textured linear low-density polyethylene sheet, push-off test, numerical modeling, bridge design, concrete cracking.	No restrictions. This document is available to the public through the National Technical Information Service, Alexandria, Virginia 22312; www.ntis.gov.

19. Security Classif. (of report)	20. Security Classif. (of this page)	21. No. of pages	22. Price
Unclassified	Unclassified	TBD [Total count excl. cover]	

Form DOT F 1700.7 (8-72) Reproduction of completed page authorized

THE UNIVERSITY OF TEXAS AT AUSTIN
CENTER FOR TRANSPORTATION RESEARCH

Design and Behavior of Seamless Bridge-Pavement Systems

Xiaoyi Chen, Ph.D.
Jay Malviya
Behdad Mofarraj Kouchaki, Ph.D.
Xiaomeng Ge, Ph.D.
Todd Helwig, Ph.D.
Juan Murcia-Delso, Ph.D.
Jorge G. Zornberg, Ph.D.

CTR Technical Report:	0-7011-1
Report Date:	Submitted: August 2023
Project:	0-7011
Project Title:	Evaluation of Seamless Bridges
Sponsoring Agency:	Texas Department of Transportation
Performing Agency:	Center for Transportation Research at The University of Texas at Austin

Project performed in cooperation with the Texas Department of Transportation and the Federal Highway Administration.

Center for Transportation Research
The University of Texas at Austin
3925 W. Braker Lane, 4th floor
Austin, TX 78759

http://ctr.utexas.edu/

Disclaimers

Author's Disclaimer: The contents of this report reflect the views of the authors, who are responsible for the facts and the accuracy of the data presented herein. The contents do not necessarily reflect the official view or policies of the Federal Highway Administration or the Texas Department of Transportation (TxDOT). This report does not constitute a standard, specification, or regulation.

Patent Disclaimer: There was no invention or discovery conceived or first actually reduced to practice in the course of or under this contract, including any art, method, process, machine manufacture, design or composition of matter, or any new useful improvement thereof, or any variety of plant, which is or may be patentable under the patent laws of the United States of America or any foreign country.

Engineering Disclaimer

NOT INTENDED FOR CONSTRUCTION, BIDDING, OR PERMIT PURPOSES.

Project Engineer: Todd Helwig
Professional Engineer License State and Number: Texas No. 94280
P.E. Designation: Research Supervisor

Acknowledgments

The authors express appreciation to the Texas Department of Transportation (TxDOT) for providing funding and resources that made this research possible. The authors would like to extend their special thanks to Project Manager Joanne Steele, members of the Project Monitoring Committee, Andy Naranjo, Lianxiang Du, Edward Galbavy, Niyi Arowojolu, Pan Gil Choi, and Michael Hyzak.

The authors would like to express their gratitude to HDR and Clinton Best for their assistance in obtaining CSB mixtures and technical guidance on CSB construction, and to Martin Marietta Materials, Titan Environmental USA, and Solmax for providing the cement, spike HDPE, and textured LLDPE sheet samples, respectively. The Phase I and Phase II experimental programs were conducted in the Geotechnical Engineering Laboratory and Ferguson Structural Engineering Laboratory at the University of Texas at Austin, respectively. The authors would also like to express their gratitude to the laboratory staff for their technical support.

Table of Contents

Evaluation of Seamless Bridges

1. Introduction

1.1 Background

Conventional bridge systems make use of expansion joints to accommodate movements caused primarily by thermal changes. Expansion joints are commonly located at the end of the bridge over the abutment or between adjacent spans over the intermediate piers for multi-span bridges with precast concrete girders, as shown in Figure 1.1. Figure 1.2 shows an example where expansion joints are located between the bridge deck, approach slab and pavement.

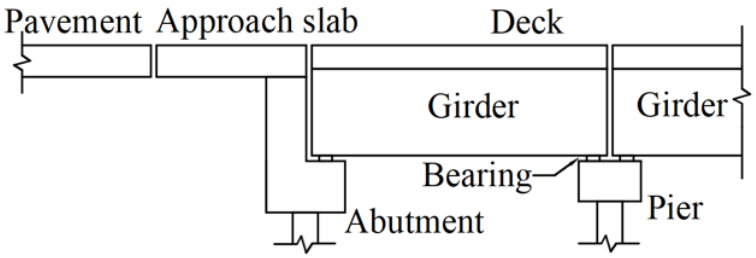

Figure 1.1: A scheme of conventional jointed bridge-pavement systems.

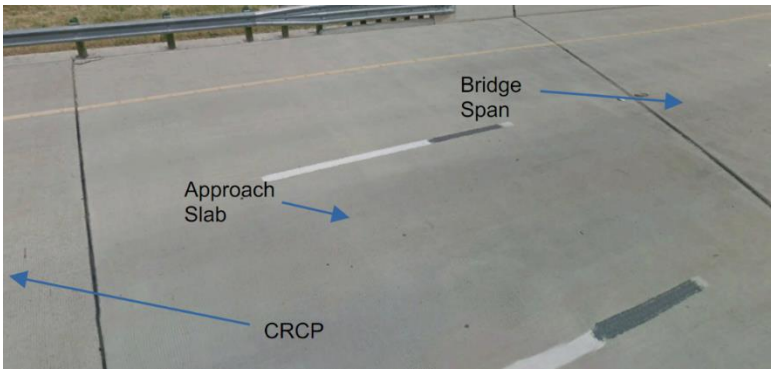

Figure 1.2: Expansion joints between bridge, approach slab and pavement (Beer, 2021).

Expansion joints in bridges are a significant source of deterioration in various bridge components. While the joints are primarily intended to allow movements caused by thermal changes, they also provide a direct conduit for water, debris, chemicals, and other corrosion-inducing contaminants to flow from the bridge/pavement surface, which tend to accelerate the deterioration of the girders, bearings, and substructure elements. Accumulation of debris also frequently leads to locking of the joints that can result in further deterioration of the deck or girders. Development of jointless bridges is one of corrosion avoidance strategies to improve structural performance and durability (Hyzak, 2021).

Figure 1.3: Leaking issues associated with expansion joints (Hyzak, 2021).

In addition, bumps at the end of the bridge are historically a common problem. The cause for the bumps can come from a myriad of sources including differential settlement, poor compaction of the embankment backfills, drainage and erosion, and traffic loading (Beer, 2021). The conventional connection deals with the differential embankment settlements at the abutment with an expansion joint which allows for the rotation at the end of the bridge deck. The "bump" commonly occurs at the joint due to the differential settlement of the embankment relative to the abutment, which affects ride quality in the bridge. Lastly, expansion joints require periodic inspections, and maintenance actions such as replacement of the joint seals, which lead to significant costs. These problems have spurred a number of studies focusing on the development of jointless bridges to decrease costs by simplifying periodic inspections as well as reducing the substantial maintenance demands that arise throughout the service life of the structure (Wolde-Tinsae et al., 1988; Thippeswamy et al., 2002).

Because joints can lead to so many problems, it has been said, that, "The only good joint is no joint (Henry Derthick – bridge engineer)" (Zhan et al., 2021). The development of jointless bridges is an emerging trend to address the issues stated above. Different types of jointless bridge technologies have been implemented to decrease the number of expansion joints, such as jointless deck bridges with the use of link slabs (see Figure 1.4), integral and semi-integral abutment bridges (see Figure 1.5). While these concepts reduce the number of expansion joints or move them to less critical locations, expansion joints are still required in the bridge-pavement system, which can still result in troublesome and expensive problems.

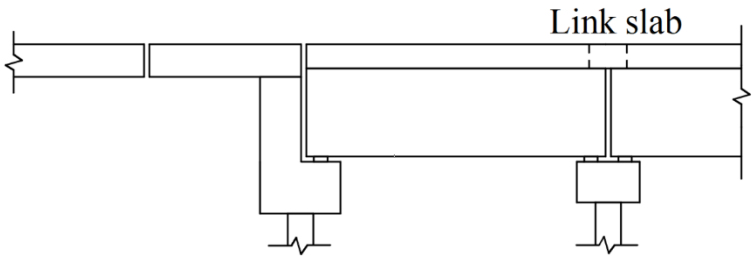

Figure 1.4: A scheme of jointless deck bridges.

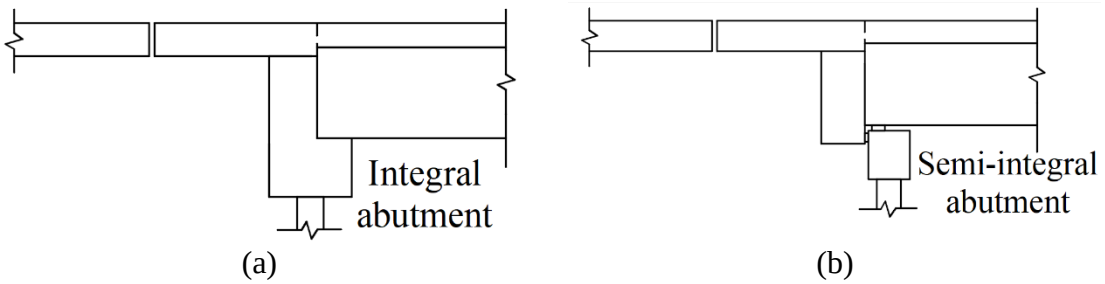

Figure 1.5: A scheme of integral and semi-integral bridges: (a) Integral bridge; (b) Semi-integral bridge.

The seamless bridge concept originally proposed in Bridge et al. (2005) and implemented in the Westlink M7 highway in Australia (Griffiths et al. 2005) eliminates the expansion joints on the bridge deck and joints between the bridge and approach slab to make the bridge-pavement system fully jointless. This technique has been used in over 50 bridge locations in Australia (Hyzak 2018). The seamless system features a transition zone that is seamlessly connected with continuously reinforced concrete pavement (CRCP), which is an excellent long-life performance solution for highly trafficked and heavily loaded roadways (Roesler et al., 2016). A scheme of the seamless bridge-CRCP system is presented in Figure 1.6. The complete elimination of expansion joints can significantly reduce the maintenance costs associated with expansion devices, improve the long-term durability of the primary load-carrying components, and improve vehicular performance through smoother ride quality (via reductions in concentrated "bumps") at the ends of the bridge (Griffiths et al. 2013).

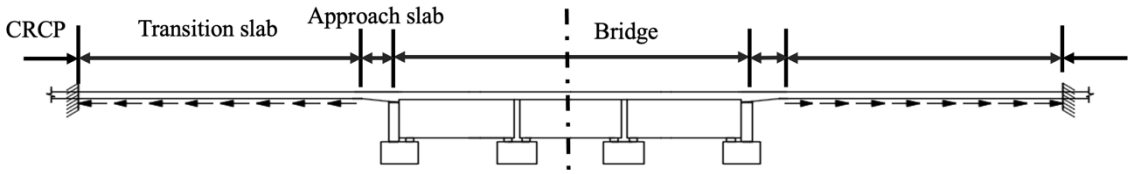

Figure 1.6: A scheme of seamless bridge-pavement systems.

1.2 Research Significance

In a seamless bridge-CRCP system, a continuously connected transition zone between the bridge deck and CRCP is employed to accommodate time-dependent deformations and stresses induced by shrinkage, creep, thermal strain, embankment settlement and traffic loads. Limited experimental and analytical research has been conducted on the performance and design of seamless bridge-CRCP systems. There are currently a number of knowledge gaps that hinder the development and implementation of the seamless bridge technology in the U.S. Some of these knowledge gaps consist of the following items:

- A critical aspect of the seamless system response is the longitudinal load transfer mechanism in the transition zone, which is governed by the restraint at the concrete pavement-base interface. While previous work on the slab-base characterization is insightful, experimental evaluation of commonly used bases and interface materials for the application of the transition zone in a seamless system remains incomplete. For example, the expected movement in the concrete pavement of a seamless bridge system must accommodate the induced deformations from the bridge expansion/contraction in addition to the expansion/contraction of the pavement itself. However, previous experimental

studies on the slab-base interaction have seldom considered such large displacements. Moreover, most of the experimental results reported in the literature were conducted with a single level of normal load representing the weight of a typical pavement thickness. However, in seamless bridge applications, the thickness of the transition and approach slabs are often different and likely to vary for different bridge geometries. While the interaction force when bond breakers are present is expected to increase linearly with the normal force, and characterized by a friction coefficient, experimental tests are needed for increasing normal forces to confirm the suitability of adopting a constant coefficient of friction. The characterization of concrete slab-base interaction must account for possible variations of the effective frictional resistance as a result of expansion-contraction cycles. Finally, experimental data are needed to explore the potential use of alternative types of interface materials, such as spike/textured polyethylene sheets and felt paper, as bond breakers in the transition zone of a seamless bridge-pavement system.

- The response of the transition zone in a seamless bridge-CRCP system needs to be further investigated to optimize their critical design parameters, namely their minimum required length and reinforcement. To date, the analysis of the response in a seamless bridge-CRCP system has basically assumed a linear elastic behavior of the pavement and bridge with an effective section stiffness after cracking. To better understand the response of transition pavements and to optimize their design, improvements in the sophistication of computational methods must be developed to capture the cracking response of CRCP and the interaction with the base material in both the longitudinal and vertical directions.
- The influence of the seamless bridge connections on the response and design of bridge structures needs to be further investigated. Previous studies have mainly focused on the performance of the transition zone, however the interaction between the bridge deck and CRCP also impacts the distribution of forces throughout the bridge components, particularly the bridge superstructure.

In this research report, experimental and numerical studies are presented to shed light to the existing research gaps on the concrete-base interface response, the performance and design of transition slab and bridge superstructure in seamless bridge systems. An experimental investigation was conducted to study the concrete slab-base interaction and effectiveness of different interface materials to act as bond breakers in the transition zone. Numerical models of the in-plane (longitudinal) and out-of-plane (vertical) responses of the seamless bridge-CRCP system were also proposed and employed to evaluate the system performance and inform design decisions. While primarily intended for CRCP, the results of this research are also useful in applications of the seamless concept for other roadway pavements (e.g., flexible and jointed concrete pavements) in which CRCP is only used in the transition slab to dissipate bridge movements and eliminate the need for bridge expansion joints.

1.3 Research Goals and Scope

This research is intended to obtain and develop much needed experimental data and analytical tools to study the performance of seamless bridge-CRCP systems and to identify design issues for the U.S. practice through a comprehensive research program including experimental testing and numerical modeling. It is aimed to achieve the following technical objectives:

- Characterize experimentally the concrete slab-base interactions and provide guidance on the selection of the bond breakers for the transition zone.
- Develop computationally-efficient numerical models to study the axial response of the seamless bridge-CRCP system, and use these models to identify design issues for standard bridge structures associated with seamless connections.
- Develop nonlinear finite element models capable of representing the cracking response of CRCP and CRCP-base interaction to study the behavior of the transition zone under the combined longitudinal and vertical effects.
- Develop guidelines for the determination of the optimal length and reinforcing steel of transition slab, and identify design issues for standard bridge structures associated with seamless connections.
- Provide design recommendations for CRCP and standard prestressed bridges to ensure compatibility with seamless bridge transitions.

1.4 Workflow and Organization

The project tasks and workflow are presented in Figure 1.7.

Following this introductory chapter, Chapter 2 presents a literature review of relevant topics conducted in Task 2, including different types of jointless bridge technologies, a summary of the design, construction and performance of the seamless bridge-CRCP system in Australia, and previous experimental studies on the concrete slab-base interaction and bond breakers.

Chapter 3 and Chapter 4 describe the Phase I (unit-cell direct shear tests) and Phase II (large-scale push-off tests) of the experimental program conducted in Task 3, including the test setup, instrumentation, test procedure, test specimens, experimental results, and discussions.

In Chapter 5, a numerical model of the axial (longitudinal) response of the seamless bridge-pavement system is presented to study thermal and shrinkage effects. The nonlinear modeling strategy and material laws employed are described. Analyses of prototype seamless bridge-pavement systems in Australia and in Texas are presented to understand the system longitudinal behavior. Numerical parametric studies are presented to identify critical parameters that affect the response.

Chapter 6 presents nonlinear continuum finite element models to study the out-of-plane response of the approach slab when subjected to settlement and traffic actions, in addition to the longitudinal actions. The modeling strategy is described. The overall response of the approach slab under the combined longitudinal and vertical effects are presented and discussed. Numerical parametric studies are also presented.

Chapter 7 presents a draft instrumentation plan for the measurements of interest for future potential field monitoring of a seamless bridge-pavement system.

Chapter 8 presents general design recommendations. The development of a simplified analytical method for the axial response of the seamless system, and a simplified analytical method for the combined out-of-plane and axial response of the transition slab, is described. A design example of an actual bridge with CRCP is also provided.

Finally, Chapter 9 presents a summary of key findings and conclusions resulting from the experimental and analytical studies along with recommendations for future research.

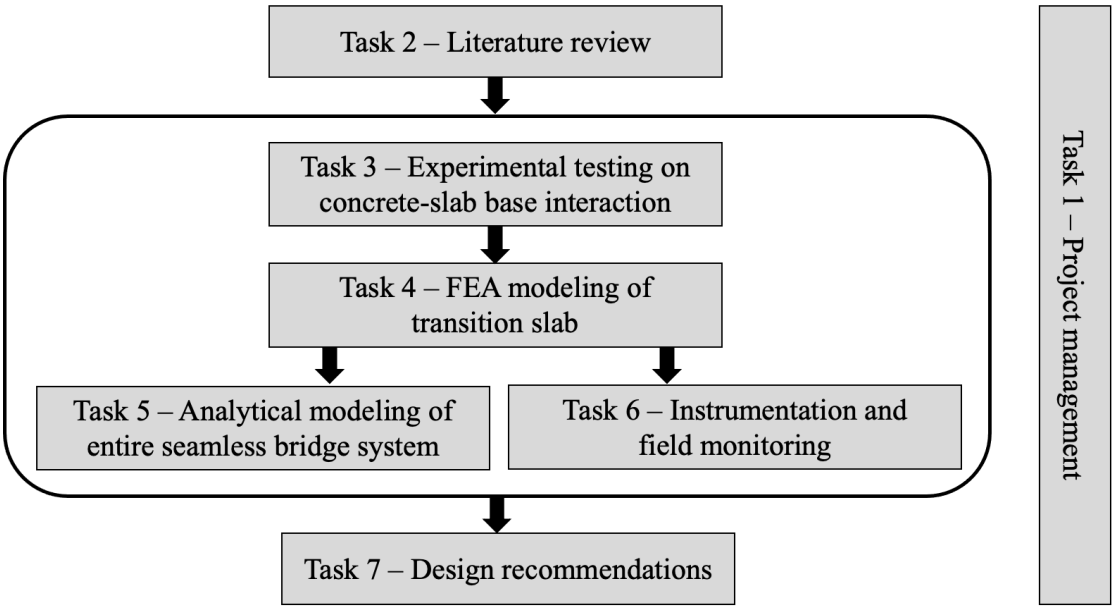

Figure 1.7: Project tasks and workflow.

2. Literature Review (Task 2)

2.1 Overview

This chapter presents a literature review to examine the current state-of-art research and application practice related to seamless bridge systems. First, the jointless bridge concepts and technologies proposed in previous research studies and/or implemented in bridge projects are presented. Second, the main characteristics of the seamless CRCP-bridge systems completed in Australia, including aspects related to design, analysis, construction, field monitoring and inspection are discussed. Lastly, previous experimental studies on the concrete slab-base interaction with a variety of different bond breakers, which is a key aspect of the seamless bridge technology, are summarized.

2.2 Jointless Bridges

More recently, three types of jointless bridge technologies have been implemented: jointless deck bridges, integral/semi-integral bridges, and seamless bridges.

2.2.1 Jointless Deck Bridges

Jointless deck bridges can be used for continuous girders or multiple simple-span girders. Bridges with multiple simple-span precast concrete girders and jointless deck systems have been implemented by replacing deck expansion joints between adjacent simply-supported spans with link slabs, as shown in Figure 2.1. Although it can be expected to develop fine cracks within the link slab region, jointless deck bridges minimize the water leakage and significantly reduce the costs related to construction and maintenance of expansion joints.

Caner and Zia (1998) experimentally investigated the behavior of link slabs connecting two adjacent simple-span girders, for both steel girders and precast reinforced concrete girders. At the link slab region, the deck was debonded from girders for a distance of 5% length of each span to reduce the stiffness of the link slab and thus stress level without affecting the global behavior of the structure. Based on the experimental and analytical studies, a simplified design approach was proposed for the link slab bridges. Each span of bridge was designed independently as simply supported without considering the effects of link slab because the stiffness of the link slab is negligible compared the stiffness of girders. The link slab is designed with the traffic wheel loads and the imposed end rotations from two adjacent simply supported spans. This concept and design method have been followed for some link slab bridges and generally showed satisfactory performance (Wing & Kowalsky, 2005; Au et al., 2013). Thorkildsen (2020) provided a comprehensive overview of design approaches for the use of link slabs adopted by U.S. State DOTs.

The use of high ductility materials for the link slab, such as ultra-high performance concrete (UHPC) with reinforcement steel, engineered cementitious composites (ECC), significantly increases the deflection capacity and enables the improved deck crack control in the link slab (Lepech & Li, 2009; Zheng et al., 2018).

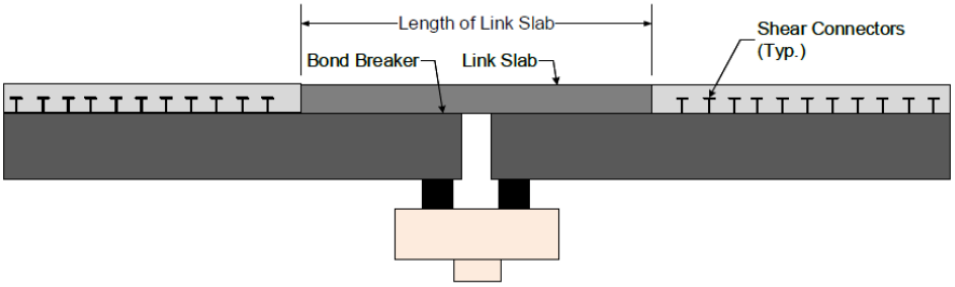

(a)

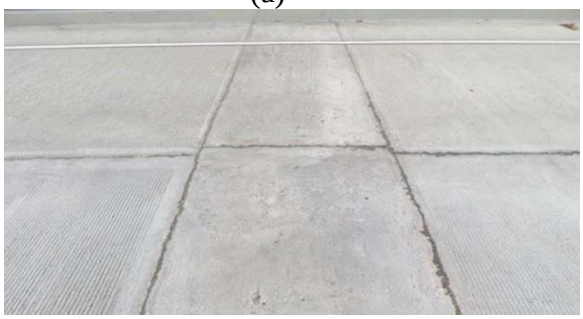

(b)

Figure 2.1: Link slabs (Thorkildsen, 2020): (a) A scheme of bridges with link slabs; (b) An example of link slab by VDOT.

In Texas, most simple-span bridges have been constructed with continuous decks at interior bents. These systems are generally referred to as "poor-boy continuous slabs", which are similar to the concept of the link slab. Throughout this technical memorandum, the term "link-slab" is used to reference the deck details for "poor-boy continuous construction" that is widely used in Texas. The construction details are shown in Figure 2.2. Crack formers are typically placed in this region to control the crack. One type of crack former that is shown in the figure is the use of a board labeled "23" in the detail. Another crack former consists of a plastic T-shaped "zip strip" that is inserted from the top of the slab that creates a reduced section near the top of the slab.

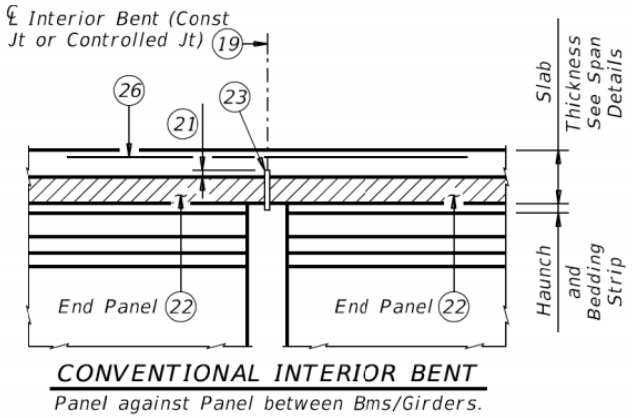

Figure 2.2: Link-slab detail for TxDOT poor-boy continuous deck.

2.2.2 Integral/Semi-Integral Bridges

In addition to the use of link slabs over interior bridge supports, significant efforts have also been directed at eliminating expansion joints near the ends of bridges. Integral and semi-integral bridge abutments have been constructed in the U.S. (including Texas) as well as other parts of the world. The use of integral abutments and semi-integral abutments can improve the durability of bridges and reduce maintenance needs.

Figure 2.3(a) directly compares the integral bridge and conventional bridge. For bridges with integral abutments, expansion joints between the bridge deck and approach slab are replaced by a continuous connection. Bridges with integral abutments also eliminate the end bearings, and as a result the bridge superstructure becomes rigidly connected with the abutments and approach slab. Flexible pilings are required in these systems to allow the superstructure and substructure to move together against backfill to accommodate expansion and contraction from thermal changes. Semi-integral bridges still require end bearings since in this case only the abutment backwall is directly connected with the bridge superstructure and approach slab (White, 2007). This whole part, which is isolated from the abutment and substructure by bearings, moves together into and away from the backfill. Figure 2.3(b) shows different types of semi-integral bridges.

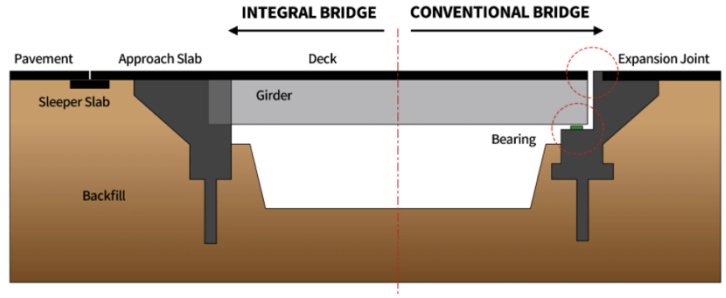

(a)

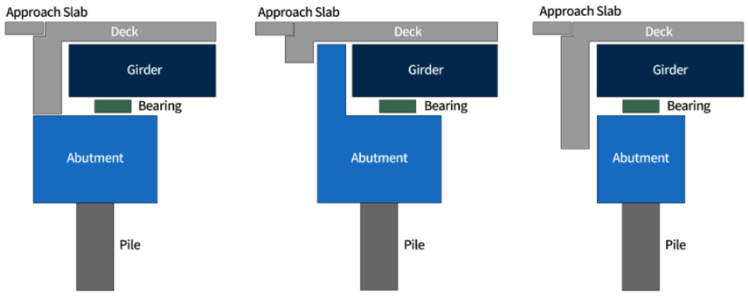

(b)

Figure 2.3: Integral and semi-integral abutment bridges (midas Bridge): (a) Integral bridge and conventional bridge; (b) Different types of semi-integral bridges.

Bridges with integral or semi-integral abutments have been reported as easier and more economical to maintain throughout the service life as compared to conventional bridges (Wolde-Tinsae et al., 1988; NYSDOT, 2005; Burke Jr, 2009; Civjan et al., 2007; Civjan et al., 2013). However, expansion joints are needed at the end of the approach slab, which therefore often require routine maintenance. Furthermore, integral or semi-integral abutments involve complicated soil-structure

interaction mechanisms to accommodate thermal movements, which may result in higher demand for abutments and cause long-term problems (Lock, 2002).

2.2.3 Seamless Bridges

Figure 2.4 shows two seamless bridge-pavement systems reported in previous investigations and/or construction projects. One system features a transition pavement zone that is seamlessly connected with CRCP, as shown in Figure 2.4(a), which was originally implemented in Australia (Griffiths et al., 2005).

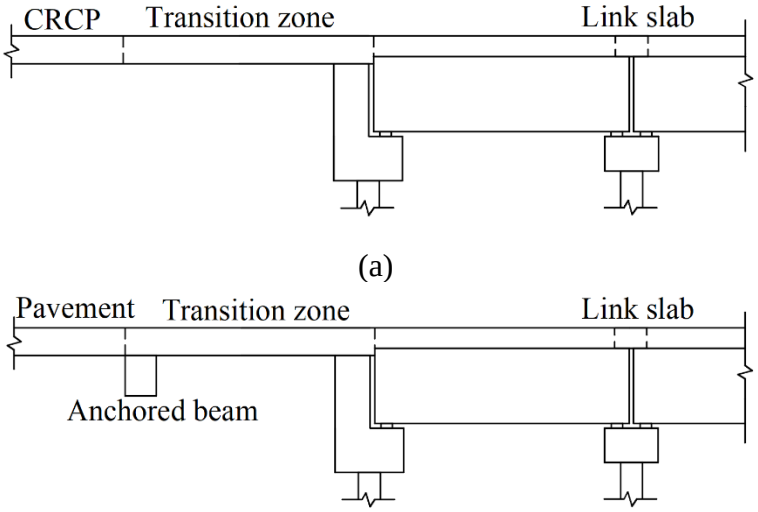

Figure 2.4: Two types of seamless bridge-pavement systems: (a) Seamless bridge-CRCP system; (b) Seamless bridge-pavement system with an anchor.

Ala (2011) proposed a modification of the Australia seamless bridge concept for flexible and jointed plain concrete pavements. In the proposed system, the transition slab is connected via "small piles" to a "secondary slab" embedded in the base soil (Ala & Azizinamini, 2016a, 2016b), as shown in Figure 2.5. Without using conventional CRCP at the end of the transition slab, the secondary slab functions to restrain the movement and transfer axial loads. This mechanism ensures that the displacement at the end of the transition pavement is small enough to eliminate the need for expansion joints. Though expansion joints are not needed, joints with dowel bars are recommended. Ala (2011) investigated numerically the response of their seamless bridge concept and studied experimentally the performance of the secondary slab-pavement connection (Ala & Azizinamini, 2016b).

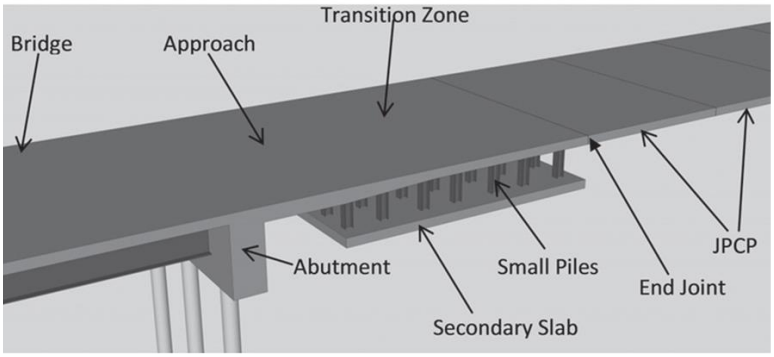

Figure 2.5: Seamless bridge concept proposed by Ala and and Azizinamini (2016a).

Another type of seamless bridge-pavement system reported in previous investigations (Jin et al., 2005; Zhan et al., 2014) involves an anchored beam at the end of the transition zone, as shown in Figure 2.4(b). Significant axial forces can be generated in the transition zone and potentially lead to severe cracking behavior if improperly detailed. Because of past successful applications of highly ductile materials for the link slab, materials such as engineered cementitious composites (ECC) have been considered for the transition pavement due to significantly higher tensile strain capabilities and tight crack patterns compared to reinforced concrete materials to improve serviceability and reliability (Zhan et al., 2021). The seamless connection can be considered analogous to a bridge-pavement "link slab". However, this structural form requires an anchored beam and large axial forces may develop in the anchored beam end. This is because the bridge-pavement link slabs are typically relatively short (16 to 33 ft. long) due to the high costs of ECC materials, thus the axial forces transferred through the slab-base interaction within the transition zone are relatively small.

2.3 Design, Construction and Performance of Seamless Bridges in Australia

Seamless connections between CRCP and bridge decks were first implemented in the Westlink M7 Motorway (WM7) in Sydney, Australia in 2004. The 25-mile-long roadway consists of two lanes of 35-ft.-wide CRCP with an asphaltic concrete wearing course intended to reduce noise. In total, 46 bridges with bridge lengths up to 400 ft. were constructed with seamless pavements. This section describes the anticipated behavior of the seamless bridge-CRCP system. In addition, relevant design, construction and in-service performance aspects of the seamless bridges completed in Australia are summarized.

2.3.1 Analysis and Design

In-Plane (Longitudinal) Behavior

In a seamless bridge-CRCP system, a continuous transition zone between the bridge deck and pavement accommodates time-dependent deformations. The transition zone typically comprises an approach slab and a transition slab. A bond breaker is placed between the base and approach/transition pavements such that the pavement is able to slide on the base to accommodate the bridge movements. These deformations include the longitudinal expansion and contraction of the bridge due to thermal changes, shrinkage, creep, as well as deformations of the pavement due to thermal and shrinkage effects. Due to the restraint provided by the jointless system, the transition

zone is subjected to compressive forces during bridge expansion and tensile forces during bridge contraction.

Figure 2.6(a) and (b) show an example to qualitatively illustrate the longitudinal movement and axial force expected in the transition slab (showing a bridge undergoing contraction in this example). The origin at the x-axis represents the bridge abutment position. The figures show that the maximum movement and axial force occur near the bridge abutment and gradually decrease until the movement is zero and the axial force reaches a constant value after a certain length. This anticipated behavior implies that the longitudinal effects due to the seamless connection have been completely dissipated within this range. It also indicates that beyond a certain distance from the bridge, the pavement is no longer affected by interactions with the bridge.

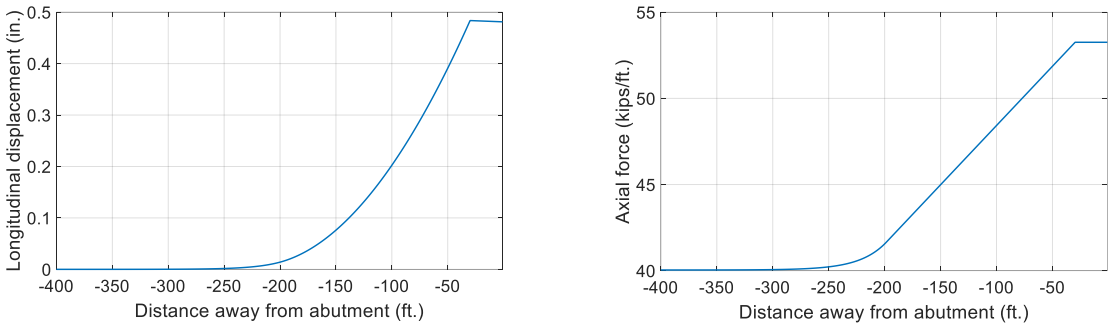

(a) (b)

Figure 2.6: Example of axial behavior of a transition slab in the case of bridge contraction: (a) Longitudinal movement; (b) Axial force.

A critical aspect of the response of seamless bridge-pavement systems and the magnitude of tensile/compressive forces in the transition zone is the interaction between the pavement and base layer and, more specifically, the coefficient of friction between the base and pavement during sliding leading to frictional forces. The primary mechanism by which bridge deformations are accommodated during bridge contraction corresponds to distributed cracking within the reinforced concrete transition pavement. Generally, a larger frictional restraint results in a shorter transition length, whereas higher localized tensile stresses/forces are likely to occur in the system. The friction coefficient provided by the bond breaker should be low enough to prevent large tensile stress demands and severe cracking in the concrete slab, but not excessively low to avoid an overly-long transition zone. The Australian applications with seamless bridges used bond breakers consisting of two coats of wax that were applied between the concrete pavement and (lean mix) concrete base layers under both regular CRCP and transition zone, which showed satisfactory performance as predicted from a serviceability perspective.

Griffiths et al. (2005) presented a numerical model of a seamless CRCP-bridge system with longitudinal effects. Table 2.1 summaries the primary assumptions used in the axial analyses and design. Griffiths and Bowmaker (2012) indicated that the performance under serviceability conditions governed the axial design of the seamless system. The pavement crack widths were controlled to ensure that the design tensile stresses in the reinforcement remained within the requirements of Australian Bridge Design Code AS 5100 (2004).

Table 2.1: Assumptions of analysis and design for seamless bridges in Australia.

Parameter	Assumption
Axial section stiffness	• Pavement in tension: ○ Effective section stiffness after cracking with the assumption of linear distribution of bond stress in slip regions • Pavement in compression: Gross composite section properties • Bridge (pre-stressed) section: Gross composite section properties
Concrete slab-base interaction	• μ (coefficient of friction between CRCP and base): 0.5-1.5
Environmental loading	• Pavement: 100 $\mu\varepsilon$ (micro strain) (expansion); 300 $\mu\varepsilon$ (contraction) • Bridge: 200 $\mu\varepsilon$ (expansion); 650 $\mu\varepsilon$ (contraction)
Embankment settlement	• 1.6 in. (twice the predicted long-term settlement)
Traffic loads on approach slab	• Live load: SM1600 bridge loading (AS 510, 2004)

Out-of-Plane (Vertical) Behavior

The purpose of the approach slab is to provide a gradual transition between the roadway pavement and bridge. The embankment underneath the approach slab is prone to settlement due to a variety of sources such as difficulties associated with the compaction of backfill after the construction of the bridge abutment. When implementing the seamless connection between the bridge deck and approach slab, the approach slab may separate from the supporting base layer due to the loss of support under the differential embankment settlement. The flexural effects of the approach slab should be accounted for due to vehicle loads. Griffiths et al. (2005, 2012) conducted an analysis considering flexural deformations in the vertical direction on the approach pavement based on the analytical model shown in Figure 2.7. The pavement was modeled using a linear elastic beam, and an elastic foundation model with a range of subgrade stiffness values.

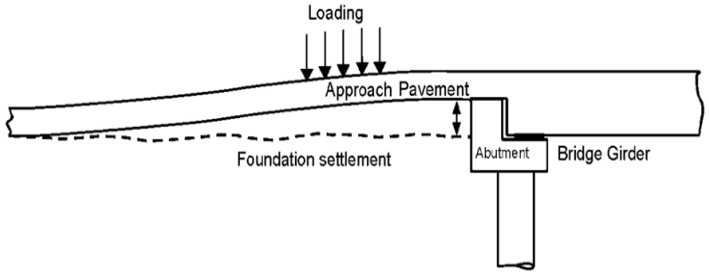

Figure 2.7: A scheme of approach slab under vertical loading (Griffiths et al., 2005).

Figure 2.8(a) and (b) show an example to qualitatively demonstrate the deflection and bending moment of the approach slab. The region near the abutment is subjected to the maximum bending moment.

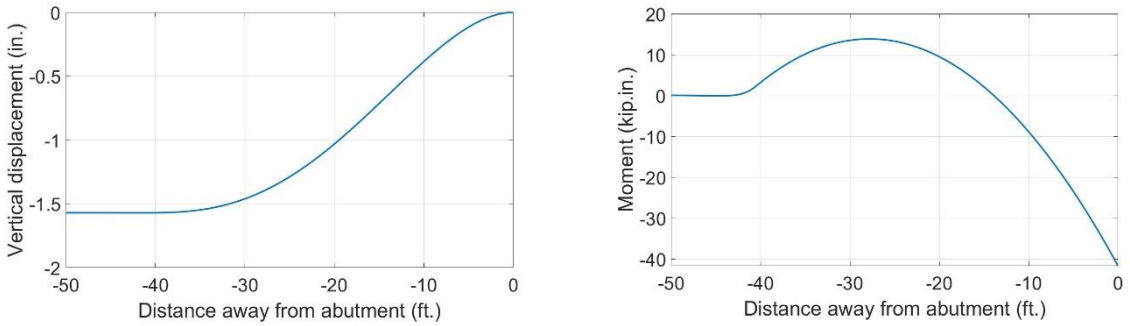

(a) (b)

Figure 2.8: Example of out-of-plane behavior of an approach slab: (a) Vertical displacement; (b) Bending moment.

2.3.2 Construction

In Australia, the seamless connection between the CRCP and bridge was made with a closure pour of a small gap located 60 ft. from the abutment. Prior to the closure pour, the movement at both pavement and bridge ends were unrestrained. Once poured, the pavement and bridge deck were locked together as the concrete strength was developing (see Figure 2.9(a)). Expansion and contraction of the bridge and pavement due to thermal changes generate compressive forces in the case of temperature increase and tensile forces in the case of temperature decrease. The early strength of concrete may be insufficient to resist those forces. Therefore, it was important to restrain the movement at both ends during a closure pour. Different strategies were implemented to provide restraint.

A closure-pour sequence, which relied on the closure-gap reinforcement to resist both compressive and tensile forces, was developed in the WM7 project to manage these possible variations, as shown in Figure 2.9(b). This was achieved by using a relatively narrow closure gap of 3 ft. and large diameter rebars. Two bundled reinforcing bars with a diameter of 1.26 in. from one end were lapped and welded with one 1.26 in. diameter reinforcing bar from the other end prior to a closure pour (see Figure 2.9(c)). This method generally performed well. Griffiths (2018) also recommended an alternative closure-pour strategy for future practice, which consisted of using a temporary strong back across the gap with two pavement ends anchored, as shown in Figure 2.9(d).

(a) (b)

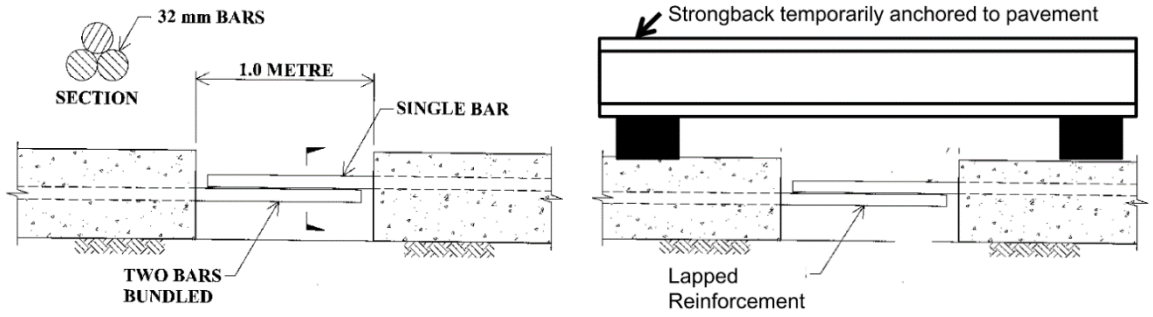

(c) (d)

Figure 2.9: Construction of closure pour for WM7 in Australia (Griffiths, 2018): (a) A scheme of closure pour; (b) Reinforcement at closure gap; (c) Reinforcemetn configuration; (d) Alternative strategy: Strongback and anchor.

2.3.3 Monitoring and Performance

The seamless bridges in Australia were monitored for six months to ensure that the system performance was satisfactory and consistent with the design goals. The monitoring revealed a good correlation between the field performance and the numerical predictions. In addition, the crack patterns and widths observed in the transition zone were similar to those found in conventional CRCP.

Pavement condition assessments have been conducted annually in WM7 to assess the serviceability performance and maintenance needs. Such assessments include visual inspections, roughness, rutting and texture surveys, and skid resistance assessments. Assessment results were reported by Griffiths et al. (2012, 2013, 2018). Nine years after the construction of the bridges, the bridge structures in WM7 performed as predicted from a serviceability perspective, with the pavements showing no signs of distress despite the increased longitudinal loads resulting from the seamless connection.

2.4 Concrete Slab-Base Interaction and Bond Breakers

The response and design of the transition slabs in seamless systems are greatly affected by the concrete slab-base interaction and the friction coefficients may vary significantly depending on the type of bases and interface conditions. Based on the findings of the Australian experience of seamless bridge systems and preliminary structural analyses conducted in the present study, a target range of friction coefficient is identified as approximately from 0.4 to 0.8, which is further discussed in Chapter 5. A major aspect for the successful implementation of seamless bridges is the need for a proper characterization of the concrete slab-base interaction for interface conditions commonly used in the U.S.

This section presents the characteristics of concrete pavement support layers and demonstrates the significance of concrete slab-base interaction for the performance of concrete pavements. In addition, classical friction models are introduced to describe the characteristics of the concrete slab-base interaction. Previous studies on the characterization of the concrete-base interaction are also summarized, from which the bond breakers typically being used are identified, together with recommended design values for the coefficient of friction for different interface conditions. Lastly,

existing data on interface materials (bond breakers) are summarized and discussed along with current knowledge gaps.

2.4.1 Concrete Pavement Support Layers

CRCP is an excellent long-life performance solution for highly-trafficked and heavily-loaded roadways (Roesler et al., 2016). CRCP is designed with continuously longitudinal reinforcement to restrain the concrete volume changes due to thermal changes. Aside from construction joints, CRCP does not contain transverse joints, as shown in Figure 2.10. The longitudinal reinforcement is designed and arranged in CRCP to develop a desirable transverse crack pattern, which is comprised of closely spaced cracks with small crack widths. This helps maintain an effective load transfer between adjacent CRCP panels by preserving the aggregate interlock (Roesler et al., 2016; TxDOT, 2019). The CRCP has been proven to be a solution for long-life performance with many benefits, such as ensuring smooth rides, allowing more options for rehabilitation, and reducing the maintenance requirements (Roesler et al., 2016; Won, 2021). Figure 2.11 depicts a section of CRCP in SH 347 in Beaumont District, Texas completed in 1963, showing excellent performance after more than 50 years with closely-spaced well-controlled transverse cracks.

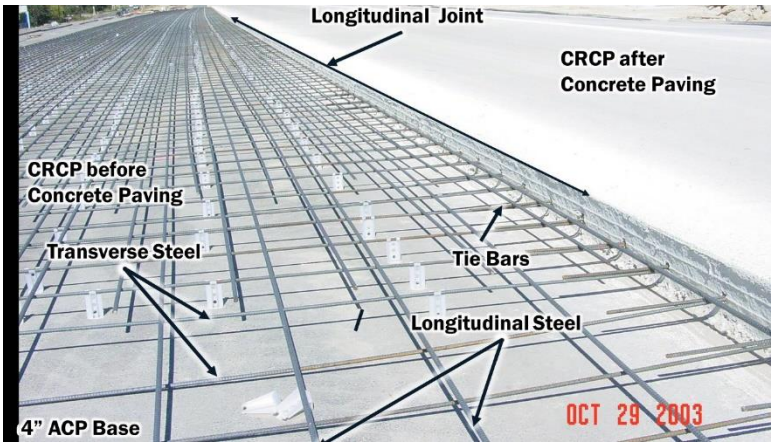

Figure 2.10: Construction details of CRCP in Texas (TxDOT, 2019).


Figure 2.11: CRCP with well-controlled transverse cracks in US 347 (Won, 2021).

Concrete pavements are typically supported by several layers of materials, including a base layer, subbase layer, and subgrade (Hein et al., 2017), as shown in Figure 2.12. Generally, bases can be categorized as untreated loose bases and treated (stabilized) bases. Untreated bases mainly refer to granular bases that are made of dense-graded aggregates, such as crushed stone, sand and gravel.

However, pumping, a phenomenon of the ejection of water and support material through cracks, pavement-shoulder edge joints, and longitudinal or transverse joints (Roesler et al., 2016), can commonly occur to loose base materials, which leads to loss of support of pavement and eventually cause distresses in the pavement. Stabilized bases reduce the risk of loss of support and base erosion, and provide higher stiffness by adding cement, asphalt or lime into bases, which are commonly used in high-traffic conditions.

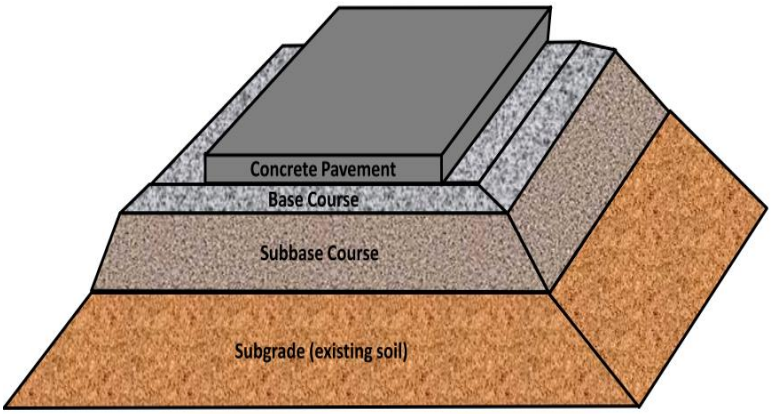

Figure 2.12: Concrete pavement support layers (Hein et al., 2017).

Frictional resistance is one of three primary aspects to be considered for base layers under concrete pavements according to the current AASHTO Pavement ME Design Procedure (VDOT, 2017). Daily and seasonal temperature and moisture variations, as well as concrete shrinkage and creep, can cause longitudinal expansion and contraction in pavements. Such movements are restrained by the frictional forces developed between the concrete pavement and base layers. As a result, the concrete in these pavements is subjected to tension when the pavement contracts and compression when the pavement expands. Friction characteristics at the concrete pavement-base interface influence the width and spacing of transverse cracks developed in CRCP. Insufficient friction can result in a relatively large crack spacing and excessive crack widths, which can lead to the deterioration of the pavement. In contrast, excessive frictional restraint at the slab-base interface can increase the concrete tensile stresses due to temperature decreases or traffic loading which can lead to poor cracking characteristics.

Since CRCP is usually used with roadways that have relatively high-traffic volumes, a stabilized base layer such as non-erodible cement stabilized base (CSB), lean concrete base (LCB) and asphalt treated base (ATB) is typically used underneath CRCP, to minimize pavement distress related to pumping or erosion. In practice, some actions are taken to decrease the strong bond between the stabilized bases and CRCP. For example, LCBs are un-textured at the surface to decrease the bond with concrete. A thin asphalt layer at the interface between CSB/LCB and CRCP is also commonly used. In addition, the asphalt layer provides erosion-resistance and moisture-resistance to prevent water infiltration into support layers through CRCP cracks and construction joints, thus decreasing the potential loss of support.

2.4.2 Theory: Concrete Slab-Base Interaction

Following a classical Coulomb-friction model (Figure 2.13 (a)), the frictional characteristics of interfaces can be described using the coefficient of friction μ, which is defined as:

$$\mu = \frac{F_{f0}}{N} = \frac{\tau_{f0}}{\sigma}, \quad \text{Eq. 2.1}$$

where F_{f0} and N are the friction force and normal force along the interface, respectively; τ_{f0} ($\tau_{f0} = \frac{F_{f0}}{A}$) and σ ($\sigma = \frac{N}{A}$) are the frictional shear strength and normal stress at the interface, respectively; and A is the area of the contact surface.

The concrete slab-base interaction may involve mechanism associated to pure friction, interlocking and adhesion (Rasmussen & Rozycki, 2001), as shown in Figure 2.14. Friction mainly depends on the roughness of the contact surface, which follows the classical friction law. Interlock refers to the "weaving" action of the coarse texture of the concrete slab and base layer. Adhesion is usually caused by the chemical bonding actions between concrete and base materials. Considering the multiple interaction components, it is more appropriate to represent the interface shear strength using a Mohr-Coulomb failure criterion (Figure 2.13(b)), which states that the interface failure can be represented by a linear envelope of normal and shear stresses. Accordingly, the shear strength of an interface can be represented by the following expression:

$$\tau_f = a + \mu\sigma = a + \sigma tan\delta, \quad \text{Eq. 2.2}$$

where τ_f is the shear strength at the interface; a denotes the adhesion and/or interlock of material (or interface); and δ is the internal friction angle. The parameters μ and a are defined as the slope and intercept of the linear regression line, respectively.

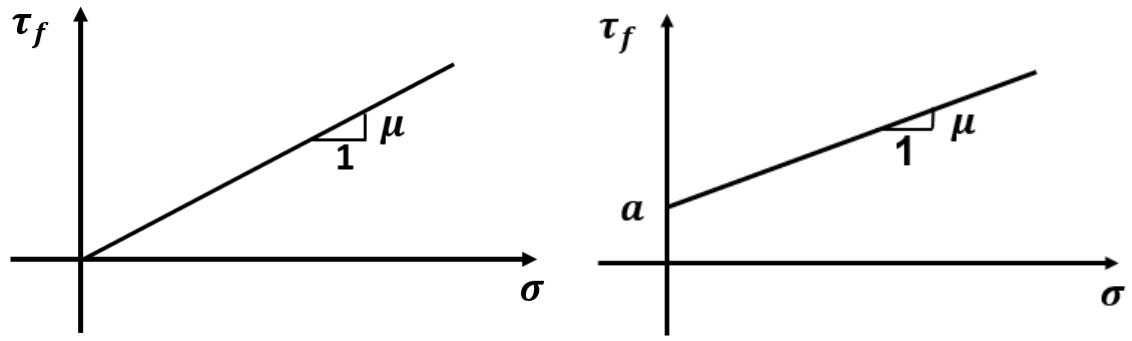

(a) (b)

Figure 2.13: Friction models: (a) Coulomb-friction; (b) Mohr-Coulomb failure criterion.

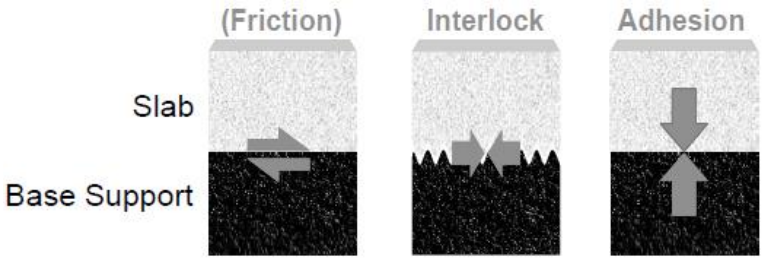

Figure 2.14: Components of concrete slab-base interaction.

Another parameter, the apparent coefficient of friction μ_{app} (as shown in Figure 2.15) is also defined:

$$\mu_{app} = \frac{F}{N} = \frac{\tau_f}{\sigma}, \quad \text{Eq. 2.3}$$

where F is the total shear force at the interface ($F = \tau_f A$). The coefficient of friction μ is determined by the nature of the materials and surface roughness and thus is independent of normal stresses, whereas μ_{app} reflects the interface shear strength resulting from all possible components and decreases as the normal stress increases if adhesion or interlock exists at the interface.

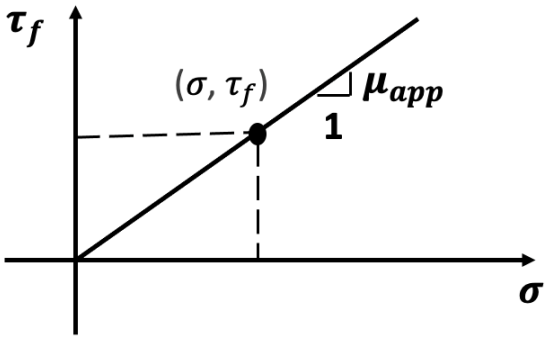

Figure 2.15: Apparent coefficient of friction.

2.4.3 Previous Studies on Concrete Slab-Base Interaction and Bond Breakers

Previous studies have been conducted related to the characterization of the concrete slab-base interaction and the corresponding effects on the performance of concrete pavements. Push-off tests have been used to determine concrete slab-base interactions (Rasmussen & Rozycki, 2001), as show in Figure 2.16. Prior to the 1970s, experimental studies mainly focused on loose untreated bases (Goldbeck, 1924; Friberg, 1934; Stott, 1961; Timms, 1963). Since the 1980s, experimental studies focused more on stabilized bases such as lime-treated bases, CSB, LCB and ATB, which can improve the long-term performance of CRCP by minimizing the pavement distress related to pumping and erosion that are common for untreated bases. Research projects (Wesevich et al., 1987; Wimsatt et al., 1987) investigated the coefficient of friction for a variety of base materials by conducting field push-off tests and evaluated the effects of concrete slab thickness and base texture on the interface restraint. These previous studies have reported that stabilized base materials provide much higher restraints as compared to untreated base materials. Lee (2000) provides a good summary of past investigations on the characterization of the concrete slab-base interaction.

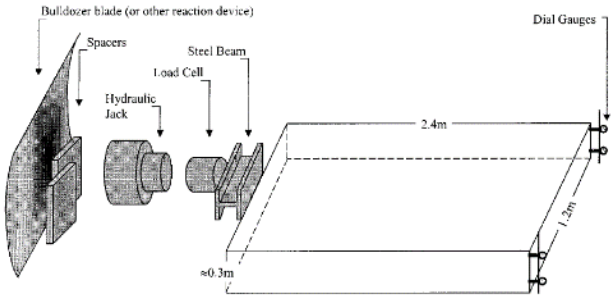

Figure 2.16: Push-off test setup on concrete slab-base interaction (Rasmussen and Rozycki, 2001).

For the design of concrete pavements, AASHTO Pavement ME proposes the recommended range of friction coefficients for the interaction between CRCP and different types of base layers (Roesler

et al. 2016), as listed in Table 2.2. For stabilized bases, for which a strong adhesion to the concrete is expected, these values represent the apparent friction coefficients.

Table 2.2: Recommended friction coefficients by AASHTO Pavement ME (Roesler et al. 2016).

Type of material beneath the slab	Friction coefficient (low-mean-high value)
Fine grained soil	0.5 - 1.1 - 2.0
Sand	0.5 - 0.8 - 1.0
Aggregate	0.5 - 2.5 - 4.0
Lime stabilized clay	3.0 - 4.1 - 5.3
Asphalt treated base	2.5 - 7.5 - 15
Cement treated base	3.5 - 8.9 - 13
Soil-cement	6.0 - 7.9 - 23
Lean concrete base	1.0 - 8.5 - 20

Practical applications have shown excessive cracking and premature failure in CRCP if directly placed on stabilized bases (TxDOT, 2019). To avoid excessive restraint, bond breakers have typically been used at the interface of the CRCP and stabilized base. Chia et al. (1986) evaluated the effectiveness of several friction-reducing materials through field push-off tests, including single and double layers of polyethylene (PE) sheets, and an oil-based bond breaker. Rasmussen and Rozycki (2001) conducted several push-off tests to examine the interface between concrete slab and hot mix asphalt (HMA) base with different interface materials, such as curing compound, PE sheet, slurry seal, or sand. Chan Suh et al. (2002) conducted cyclic push-off tests in the laboratory to evaluate the interaction between the concrete slab and lean concrete base with a single layer of PE sheet and a 1.57-in.-thick asphalt bond breaker. The effects of the cyclic movements, slab thickness, and movement rate were evaluated. Similar tests were conducted by Li et al. (2013) to investigate the friction reduction effects of geotextile, emulsified asphalt, and asphalt bond breakers (0.78-in.-, and 2.36-in.-thick), and by Jeong et al. (2014) on lean concrete bases/asphalt bases with and without PE sheet. Maitra et al (2009) investigated the effects of a 5-mil-thick impermeable plastic sheet as a bond breaker on top of the dry lean concrete bases by conducting cyclic push-off tests. For the seamless bridge project in Australia, field push-off tests were conducted to investigate different interface conditions (with two wax coats, bitumen seal, plastic sheets, and without debonding material) (Griffiths et al., 2005). The corresponding peak and steady coefficients of frication are listed in Table 2.3. Zollinger et al. (2014) experimentally compared the restraints provided by a 1-in.-thick asphalt layer and nonwoven geotextile to the concrete slab due to concrete shrinkage effects.

Table 2.3: Results of friction tests reported by Griffiths et al. (2005).

Debonding material	Coefficient of friction	
	μ_{peak}	μ_{steady}
Plastic	0.5	0.4
Two coats wax	0.8	0.6
Bitumen seal	1.4	0.9
None	1.5	0.8

2.4.4 Summary and Discussion

Table 2.4 summarizes the frictional characteristics of the concrete-base interface with different types of bond breakers reported from previous studies. The apparent coefficients of friction reported in Table 2.4 were obtained using Eq. 2.3. Mohr-Coulomb parameters (μ and a) can be defined only when the actual test data with two or more normal stress levels are reported. As shown in Table 2.4, experimental results in most of the previous studies were obtained at a single level of normal stress, providing data that only allows determination of the apparent coefficient of friction. This parameter only represents the interaction for a given slab thickness and cannot be directly extrapolated to other thicknesses.

In the study conducted by Chan et al. (2002), the interface with a single PE sheet presented apparent coefficients of friction μ_{app} that were very close to the actual friction coefficient μ because there was practically no adhesion (a is only 0.02 psi). However, when using a 1.57-in.-thick asphalt layer at the interface, apparent coefficient of friction μ_{app} decreased with the increase of normal stress due to the existence of strong adhesion component ($a = 0.26$ psi). Hence, a good characterization of the shear resistance of interfaces requires considering varying normal stress levels, even when bond breakers are used.

Among the different materials previously investigated, PE sheets (single or double layer) were generally shown to be effective bond breakers, with μ_{app} values ranging between 0.5 and 0.9. As a reference, μ_{app} values used for the design of CRCP without bond breakers range from 3.5 to 13 (Roesler et al., 2016).

While previous work on the concrete slab-base characterization is insightful, experimental evaluation of commonly used bases and interface materials remains, at best, incomplete. Another aspect requiring evaluation is the quantification of the expected movement in the concrete pavement of a seamless bridge system that must accommodate the induced deformations from bridge expansion/contraction in addition to the expansion/contraction of the pavement itself. A preliminary finite element analysis of the axial behavior of a seamless CRCP bridge system estimated pavement thermal displacements up to 0.5 in. for a typical 300-ft.-long bridge considering a maximum temperature decrease of 55°F (TxDOT, 2014; AASHTO, 2020; Ha et al., 2012). However, previous experimental studies on the concrete slab-base interaction have seldom considered such large displacements. Moreover, most of the experimental results reported in the literature were conducted with a single level of normal load representing the weight of a typical pavement thickness. However, in seamless bridge applications, the thickness of the transition and approach slabs are often different and are likely to vary for different bridge geometries. While the interaction force when bond breakers are present is expected to increase linearly with the normal force, and characterized by a friction coefficient, experimental tests are needed for increasing normal forces to confirm the suitability of adopting a constant coefficient of friction. Finally, experimental data are needed to explore the potential use of alternative types of interface materials as bond breakers in the transition zone of a seamless bridge system.

Table 2.4: Frictional characteristics for concrete slab-base interaction with bond breakers from previous studies.

Base type	Interface material	Test data			Mohr-Coulomb parameters		Reference
		$\sigma=N/A$ (psi)	$\tau=F/A$ (psi)	μ_{app}	μ	a (psi)	
Sand	Polyethylene	0.47	0.26	0.55	Insufficient information		Stott (1961)
Medium-textured| CSB	1/16 in. sand skin + polyethylene	0.50	0.36	0.72	0.69	0.02	Wimsatt et al. (1987)
		1.01	0.68	0.68			
		1.01	0.73	0.72			
	Double polyethylene	0.50	0.36	0.72	Insufficient information		
	1/16 in. sand skin	0.50	0.63	1.26			
Sand-mix asphalt base	Single polyethylene	0.50	0.44	0.88	Insufficient information		Chia et al. (1986)
	Double polyethylene	0.50	0.24	0.47			
	Spray compound with oil	0.50	1.61	3.20			
Lean concrete	Single polyethylene	0.66	0.38	0.58	0.57	0.02	Chan Suh et al. (2002)
		1.32	0.78	0.59			
		1.98	1.13	0.57			
	Asphalt bond breaker (1.57-in.-thick)	0.66	0.67	1.02	0.6	0.26	
		1.32	1.00	0.76			
		1.98	1.47	0.74			
Cement stabilized crush stone	Single polyethylene	0.86	0.54	0.63	Insufficient information		Li et al. (2013)
	Geotextile	0.86	2.13	2.48			
	Emulsified asphalt	0.86	6.55	7.62			
	Asphalt bond breaker (0.75-in.-thick)	0.86	1.60	1.86			

3. Phase I: Unit-Cell Direct Shear Test (Task 3.1)

3.1 Overview

The experimental program includes two phases of laboratory testing involving different scales and types of loading. The Phase I tests were conducted at a smaller scale than the full-scale tests conducted in Phase II. The results from the Phase I tests are presented in the current chapter while the Phase II test results are presented in Chapter 4. In Phase I, unit-cell direct shear tests were conducted to quantify the shear strength properties of relevant interfaces when subjected to monotonically increasing displacements. The Phase I studies allowed identification of the candidate interface materials to act as effective bond breakers and to be subsequently considered in the Phase II studies. In Phase II, large-scale push-off tests were conducted on a selected number of interfaces to verify the shear response considering a more representative scale and to quantify the effects of cyclic loading. Both testing phases provided load (shear) versus displacement relations for different normal stress levels and maximum relative interface displacement magnitude up to 1 in. The experimentally obtained data were used to characterize the shear strength of the interfaces using a Mohr-Coulomb failure criterion. The results and findings of the experimental studies are discussed in relation to the potential use of bond breakers in the transition zone of a seamless bridge-CRCP system.

This chapter outlines the results from Phase I, including the load (shear)-displacement relations, interface shear strengths and coefficients of friction for different interface conditions. The effects of interface materials on breaking the bond are discussed, and the bond breakers to be further examined in phase II are identified.

3.2 Experimental Program

The base materials investigated were primarily a cement stabilized base (CSB) and a hot mix asphalt (HMA) base, which are durable, stabilized and non-erodible bases typically constructed under CRCP. Granular base materials, such as AASHTO Gravel No.8 and TxDOT Grade 3 Aggregate (TxDOT Item 247, 2014), were also considered. AASHTO Gravel No.8 is a moisture-insensitive material and therefore helpful for density control, which is a desired feature for the baseline test. Grade 3 Aggregate was selected because it can be used as backfill materials underneath the concrete approach slab, which is a part of the transition zone in a seamless bridge-pavement system.

The following interface materials were considered in the Phase I testing program:

- Polyethylene (PE) sheets (ASTM E1745, 2017). PE sheets are geosynthetics, which are widely used for containment purposes and can also be used as bond breakers. For example, in South Korea, PE sheets have been widely used as bond breakers between a lean concrete base and concrete pavement (Jeong et al. 2014). These sheets present a wide range of densities and surface structures (e.g., smooth, spiked, and textured). Specifically, 6-mil-thick PE sheets with smooth surfaces were selected.
- Woven or non-woven geotextiles. These geosynthetics are commonly used for separation, filtration or reinforcement purposes. In Germany, non-woven geotextiles have been adopted successfully as bond breakers between a cementitious base and a newly-paved concrete for years (Cackler et al., 2018).

- Thin HMA layer (usually 1-in.-thick). A thin HMA layer has been commonly used in many applications for stress-relieving purposes between CSB and concrete pavements (TxDOT, 2019). An HMA layer can be utilized in addition to another bond breaker at the interface in the transition zone.

3.2.1 Test Setup and Instrumentation

A unit-cell direct shear test setup previously used to characterize the shear strength of aggregate materials (Mohamed, 2017) was employed in this study to characterize the concrete slab-base interaction with different interface conditions, as shown in Figure 3.1. The test setup, depicted in Figure 3.2(a), included a specimen container (box), with inner plane dimensions of 20 in. × 20 in., divided into two halves that can accommodate relatively shearing deformations which facilitated testing of the concrete-base interface under shear. This self-reacting system involved a horizontal reaction frame that applied shear forces at the interface via an electromechanical actuator and a vertical reaction frame that applied normal forces on top of the concrete via a pneumatic actuator, as shown in Figure 3.2(a). During testing, the base in the lower portion of the direct shear box was pulled/pushed in relation to the concrete block contained in the upper portion of the box, which reacted laterally against the test frame. Figure 3.2(b) shows a photo of the test setup.

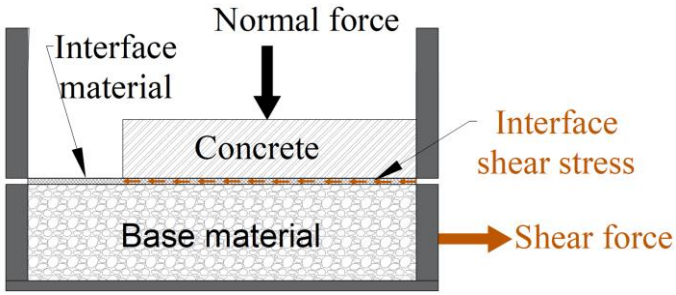

Figure 3.1: Phase I unit-cell direct shear test setup: specimen box.

The instrumentation is also shown in Figure 3.2. The actuator force and displacement were recorded using a Campbell Scientific 3000 (CR3000) data logger at a frequency of 5 Hz. A linear variable differential transformer (LVDT) with a range of 3 in. was attached to the side of the traveling cart to measure the horizontal displacement of the base specimen relative to the concrete block. A pancake load cell with a capacity of 5 kips was used to measure the normal force applied on top of the concrete block. Since the magnitude of the interface shear force was expected to vary significantly depending on the interface conditions, two sets of horizontal load cells with different capacities were employed for different test series to make sure that the force resolution was appropriate. One set included an S-shaped load cell with a capacity of 10 kips installed between the electromechanical actuator and traveling cart to measure the horizontal force component introduced by the actuator. The load cell reading also included the frictional forces generated between the rail guides and traveling cart, as the setup was not completely frictionless; however, the error introduced by this component was negligible in cases that adhesion generated relatively large interface shear forces. Consequently, the S-shaped load cell was used for the test series when a large shear force was expected with a strong bond at the interface. Two button load cells with a capacity of 2 kips were placed against the top half of the shear box, the readings from which eliminated the friction introduced from rail and provided direct measurement of the interaction at

the interface. These smaller capacity load cells were added to improve the accuracy of the test series in which a small shear force was expected with the use of a bond breaker.

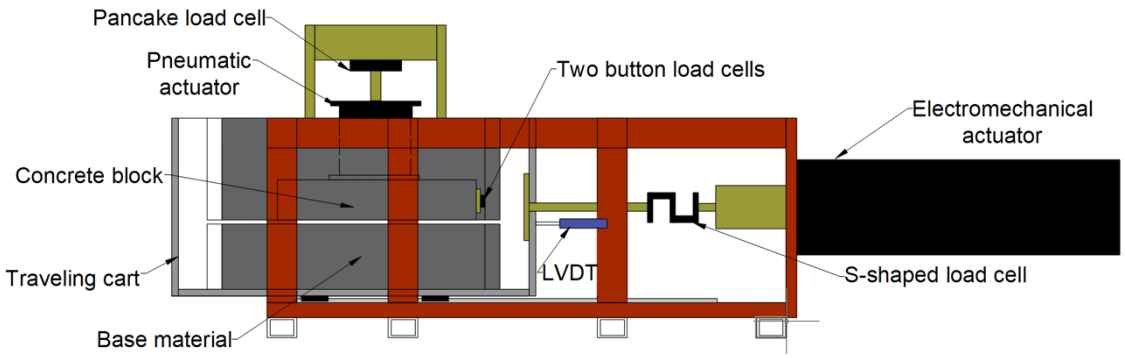

(a)

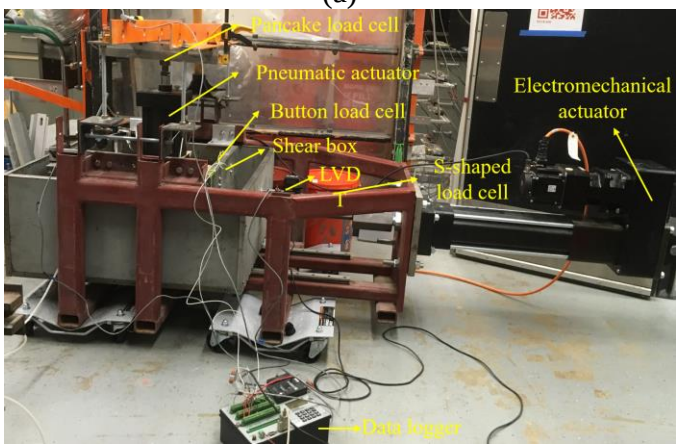

(b)

Figure 3.2: Phase I unit-cell direct shear test setup and instrumentation: (a) A scheme; (b) A photo.

3.2.2 Test Parameters and Procedure

Eleven test series involving different combinations of base and interface materials were conducted, as presented in Table 3.1. The bases and interface materials used in Phase I are shown in Figure 3.3 and Figure 3.4, respectively.

Direct shear tests were conducted with three predetermined normal stresses of 0.5 psi, 1.17 psi, and 2 psi, representing the weight of a concrete pavement with thickness values of 6 in., 14 in., and 24 in., respectively. The first two thicknesses corresponded to the range of conventional CRCP, while the third was selected to generate a higher level of normal stress for a better characterization of the shear strength failure envelope. The thickness of the concrete block employed in the tests was 3 in, with dead weight added by a vertical actuator to achieve the target normal stress at the interface.

For simplicity in testing, precast concrete blocks were used in some specimens with bond breakers (Series 1-3). The effects of using a precast concrete block (no bond with the base/interface material) on the interface restraint were also investigated by comparing the results of Series 3a and 3b. For

most of the test series, cast-in-place (CIP) concrete was used on top of the base or interface material to be as representative of field conditions as possible.

Tests were conducted with monotonically increasing displacements, at a rate of 0.0236 in./min until a 1 in. maximum displacement was reached or an obvious steady shear stress was observed.

Table 3.1: Phase I Test Matrix.

Series	Base type	Interface material	Concrete block	Normal stress (psi)
1	AASHTO Gravel No.8	None	Precast	0.5, 1.17, 2
2	Grade 3 Aggregate	None	Precast	0.5, 1.17, 2
3a	Grade 3 Aggregate	Two PE sheets	Precast	0.5, 1.17, 2
3b	Grade 3 Aggregate	Two PE sheets	CIP	1.17
4	Type B HMA base	None	CIP	1.17
5	Type B HMA base	Two PE sheets	CIP	0.5, 1.17, 2
6	CSB	None	CIP	1.17
7	CSB	1-in.-thick Type D HMA	CIP	1.17
8	CSB	Woven geotextile	CIP	1.17
9	CSB	Non-woven geotextile	CIP	1.17
10	CSB	One PE sheet	CIP	0.5, 1.17, 2
11	CSB	Two PE sheets	CIP	0.5, 1.17, 2

(a)

(b)

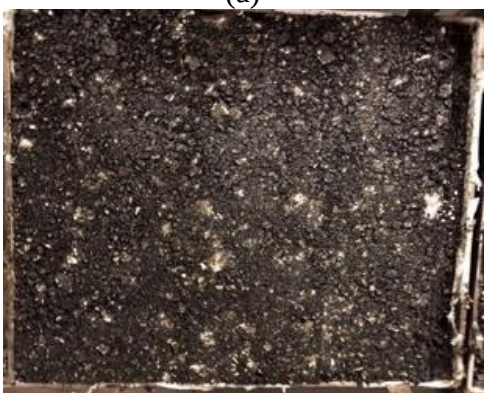

(c)

(d)

Figure 3.3: Phase I bases: (a) AASHTO Gravel No.8; (b) TxDOT Grade 3 Aggregate; (c) HMA; (d) CSB.

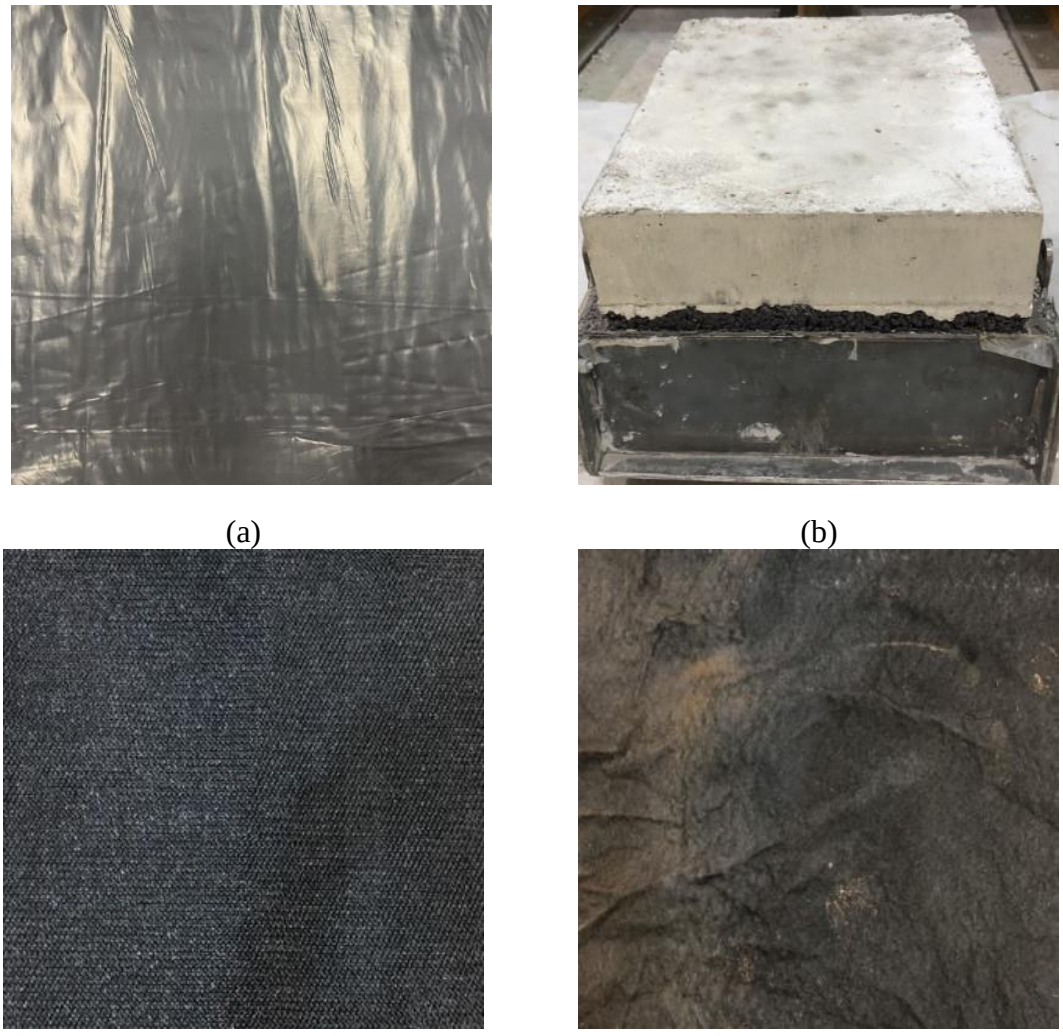

Figure 3.4: Phase I interface materials: (a) PE sheet; (b) 1-in.-thick HMA; (c) Woven geotextile; (d) Non-woven geotextile.

3.2.3 Test Specimens and Material Properties

Granular Base

The specimens comprised a concrete block/slab on top of a base material (and an interface layer if applicable). In Phase I, the granular bases were directly prepared inside of the bottom half shear box in two uniform 2.5-in.-thick lifts. For each lift, the materials were uniformly spread, and then properly compacted to the target relative density using a tamper. The concrete specimens had manageable dimensions of 15 in. × 15 in. × 3 in. The concrete-slab specimens were properly positioned against the walls of the shear box in the loading direction in order to make sure that the horizontal force transferring mechanism was properly established during the direct shear tests.

AASHTO Gravel No.8 base materials comprised uniformly graded gravels with the mean grain size of 0.28 in, and more details of the grain size distribution were presented by Mohamed (2017). TxDOT Grade 3 Aggregates had larger size particles and were comprised of angular crushed rocks.

The measured densities for AASHTO Gravel No.8 and TxDOT Grade 3 Aggregate base specimen were 104.6 pcf and 100.5 pcf, respectively.

Cement Stabilized Base

In Phase I, the stabilized bases (CSB and HMA) were constructed and cured in an additional steel box with the dimensions of 16 in. × 18 in. × 4.75 in, which was then placed into the bottom shear box for testing.

The guidelines of base construction in the State of Texas (TxDOT Item 276, 2014) were followed for the preparation of the CSB specimens in the laboratory. The components of CSB were proportionally combined in a mixer. The CSB specimens were constructed in two consecutive layers with a thickness of 2.5 in. For each layer, the mixed materials were placed into the steel base mold and then were spread uniformly. Each layer was compacted immediately after placing until a smooth surface was attained. Due to the relatively small-scale of Phase I specimens, a plate compactor with planer dimensions a bit smaller than the base mold was mainly used for compaction. A metal tamper driven by a jack hammer was used as well to compact the edges and corners.

Class L CSBs are used for rigid pavements in the State of Texas to ensure long-term strength and stability (TxDOT, 2019). The cement content by weight of CSB was 5%. CSB cylindrical specimens were prepared for unconfined compressive strength testing in accordance with ASTM D558 (2017). The CSB mixture was placed in three layers into a 4 × 4.6 in. cylinder mold, with each layer compacted by 25 blows of a 5.50 lbf rammer dropped from 12 in. The CSB compressive strength obtained at 7 days after placement, based on ASTM D1633 (2017), was 900 psi, which satisfied the minimum specimen strength requirement of 500 psi established in TxDOT Item 276 (2014).

Hot Mix Asphalt Base

The guidelines of the base construction in the State of Texas (TxDOT Item 341, 2014) were followed for the preparation of the HMA specimens in the laboratory. In Phase I, the procedure to prepare HMA specimens was similar to CSB specimens. In the case of CSB topped with a 1-in.-thick HMA layer, the surface of the CSB specimen was coated with a thin layer of MC-30 cutback asphalt before a thin Type D HMA layer was constructed on top of it following TxDOT Item 300 (2014). This procedure represented in-field construction steps to provide waterproofing and adhesion for a subsequent asphalt layer.

Table 3.2: HMA mix aggregate gradations.

	Sieve size (in.)	1-1.2	1	3/4	3/8	#4	#8	#30	#50	#200
Type B (base)	Percent passing (%)	100	99.2	93.2	74.5	49.7	35.0	22.4	16.1	5.0
Type D (interface)		100	100	100	93.9	61.0	39.4	23.8	16.6	4.5

Table 3.3: HMA mix characteristics.

	Asphalt content (%)	Theoretical maximum specific gravity	Void in mineral aggregates (%)
Type B (base)	4.5	2.569	13
Type D (interface)	5	2.549	15

Table 3.2 lists the aggregate gradation for the Type B and Type D HMA, which are typically used for the base and interface layer, respectively. In Table 3.3, the mix characteristics for the Type B and Type D HMA are provided.

Concrete Blocks

The concrete mix design for the slabs is presented in Table 3.4. The mix had a water/cement ratio of 0.49, a specified slump of 5 in. and a measured slump that ranged from 4 in. to 6 in. The concrete compressive strengths measured on the 28th day after casting, in accordance with ASTM C39 (2021), ranged from 4000 psi to 5000 psi, which satisfied the minimum requirement of 4000 psi (TxDOT Item 360, 2014).

Table 3.4: Concrete mix design.

Material type	Cement	Fly ash	Coarse aggregate	Fine aggregate	Water
Weight (lbf/yd^3)	412	138	1700	1351	200

3.3 Experimental Results and Discussion

3.3.1 Shear Stress-Displacement Relations

The concrete slab-base interaction may vary significantly depending on the types of base and interface materials. The shear force and shear displacement for each test series were recorded during testing. Assuming a uniform distribution of shear stresses over the entire interface contact area, the corresponding shear stress was obtained by dividing the total shear force by the contact area. The shear stress versus displacement relationships are presented as follows.

Granular Base

The shear stress versus displacement relationships for granular bases are presented in Figure 3.5. The purpose of conducting direct shear tests on the AASHTO Gravel No.8 base with a precast concrete block (Series 1) was to provide a baseline. As shown in Figure 3.5(a), the shear stress increased until the preliminary displacement was reached, followed by a plateau where steady sliding occurred.

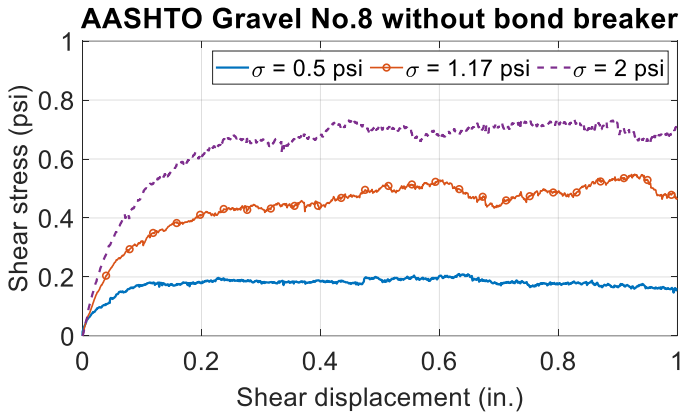

(a)

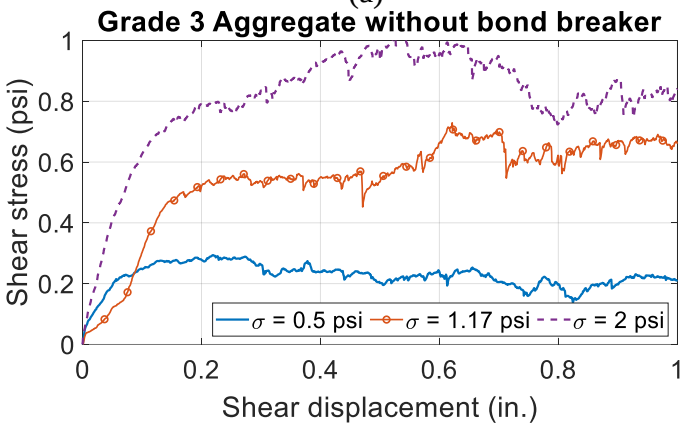

(b)

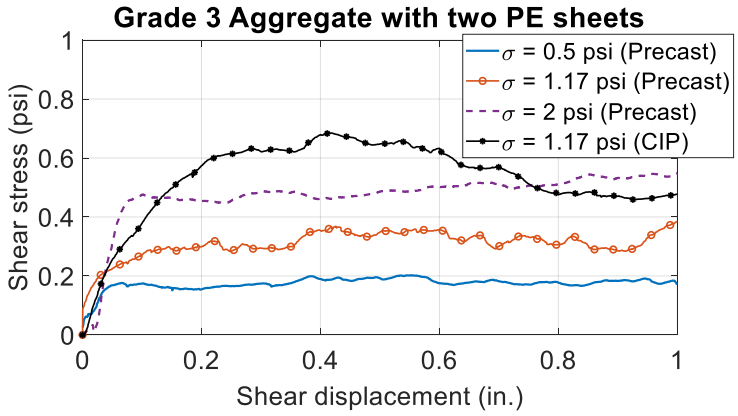

(c)

Figure 3.5: Shear stress-displacement relationship for granular bases: (a) AASHTO Gravel No.8 base without bond breaker (precast concrete); (b) Grade 3 Aggregate base without bond breaker (precast concrete); (c) Grade 3 Aggregate base with two PE sheets.

As shown in Figure 3.5(b), the shear response between the precast concrete block and Grade 3 Aggregate base (Series 2) did not feature a clear plateau as was observed with the AASHTO Gravel No.8 base. This difference in response was mostly attributed to the sharpness of crushed rock aggregates and the significantly larger size of Grade 3 aggregates. As a result, the increased

sharpness in the Grade 3 aggregates tended to result in a more uneven surface even after compaction, which can create some spurious interlocking between the aggregates and the concrete block. The effects of interlocking forced the concrete block to climb over the aggregates, instead of letting the block travel horizontally until eventually the aggregates cannot bear the pressure and popped out of place or got crushed. Such events can be easily identified at points where there was a gradual increase in shear stress followed by a sudden drop. The initial plateau values (before 0.3 in. displacement) were selected based on visual monitoring paired with measurements.

The Grade 3 Aggregate base with two PE sheets (Series 3a) were tested for three normal stress levels using a precast concrete block, as shown in Figure 3.5(c). The curve presented a pattern of an initial ascending branch and a plateau. The curve was smoother than Figure 3.5(b), where no bond breaker was used.

An additional test using a CIP concrete block (Series 3b) was conducted with a normal stress of 1.17 psi, and the relationship is also plotted in Figure 3.5(c) for comparison. For the tests involving a CIP concrete specimen, the peak shear strength was reached at approximately 0.4 in. displacement. After the peak, the shear stress gradually decreased until a plateau occurred at a displacement of approximately 0.8 in. Evaluation of the results from Series 3a and 3b reveal that the coefficient of friction of the interface was 1.5 times higher for the tests involving a CIP concrete specimen than when using a precast concrete block. This was likely due to the matching texture of the concrete cast against the interface generating a rougher profile, whereas the precast concrete block tended to slide on the high points of the base.

It was concluded that testing involving precast concrete test specimens is not representative of the overall interface behavior expected in the field, even in the presence of interface materials acting as bond breakers. This is because the specimens fail to capture the adhesive component with the interface material that adds to the mechanical interlock generated when concrete is directly cast. Therefore, in subsequent test series, concrete specimens were directly cast over the interface to better represent the expected field conditions.

Hot Mix Asphalt Base

The shear stress versus displacement relationships for HMA bases are shown in Figure 3.6. In the test involving concrete specimens placed on the HMA base (Series 4), the test was initially conducted with a normal stress of 1.17 psi, which corresponded to the most common CRCP thickness of 14 in. The result is shown in Figure 3.6(a). The setup was unable to fail the concrete-HMA interface without exceeding the capacity of the loading equipment, which indicated the existence of a strong bond at the interface.

In the case of HMA with two PE sheets (Series 5), the same specimen was used in the subsequent tests at different normal stresses with a testing order consisting of 2 psi, 1.17 psi and 0.5 psi. As shown in Figure 3.6(b), a well-defined peak strength was observed in the test conducted with a normal stress of 2 psi. The peak was attributed to the interlocking likely generated by the matching profile of the CIP concrete bottom surface and the HMA base top surface due to the self-weight of fresh concrete. For the other two normal stresses, peak strength values were reached by the maximum displacement of the test setup (1 in.), which was likely due to that the interlocking that developed in the initial test (2 psi) may have been lost during the subsequent tests.

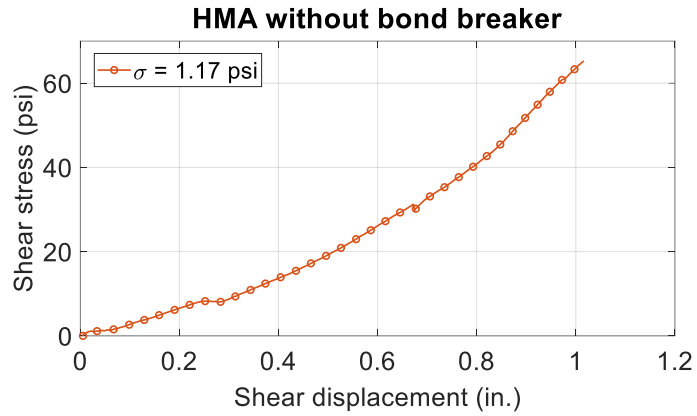

(a)

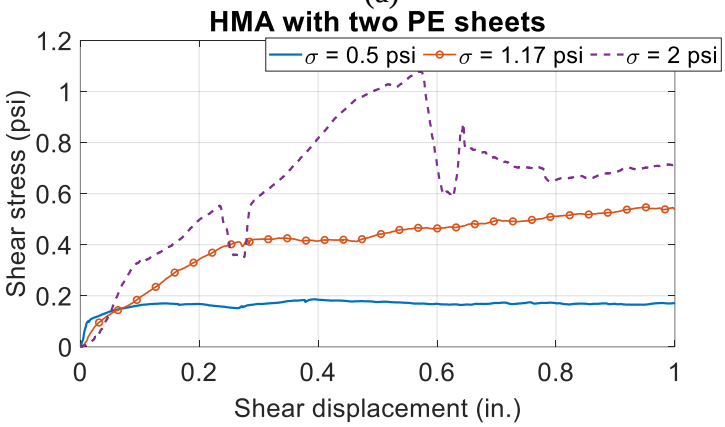

(b)

Figure 3.6: Shear stress-displacement relationship for HMA bases: (a) HMA without bond breaker; (b) HMA with two PE sheets.

Cement Stabilized Base

The shear stress versus displacement relationships for CSBs are shown in Figure 3.7 and Figure 3.8. Figure 3.7(a) shows the shear stress-displacement relationships for the interface test results that led to comparatively high shear stresses, namely, CSB without bond breaker, CSB with woven or non-woven geotextile. All test results involve CIP concrete placed directly over the interface. In the test involving concrete placed on CSB (Series 6), the maximum force was limited by the capacity of the test setup, so ultimate failure at the slab-base interface was not reached before stopping the test. Such results reveal that a strong adhesion has developed at the interface. Similarly, interface failure was not reached for the tests involving a non-woven geotextile placed between the CSB and concrete (Series 9). The CSB and woven geotextile specimen (Series 8) eventually failed at the interface, but at a relatively high shear stress of 45 psi. The use of a 1-in.-thick HMA layer (Series 7) resulted in a significant decrease in the interface strength, but still resulted in a peak strength of 9 psi, indicating the existence of adhesion at the CSB-HMA interface. As depicted in Figure 3.7(b), at approximately 0.32 in. shear displacement the bond was broken and the shear stress dropped significantly from its peak value to a plateau of approximately 1.4 psi. The concrete block was observed to slide along with the thin HMA layer relative to the CSB.

The results from tests conducted with a normal stress of 1.17 psi indicated that the 1-in.-thick HMA layer, woven and non-woven geotextiles investigated in this study were not suitable to function as bond breakers for the concrete slab-base interface. This is because if used in the transition slab of a seamless bridge system, this type of interface would generate high axial forces and lead to severe cracking issues. Therefore, no further tests were conducted involving these interface conditions with other normal stresses.

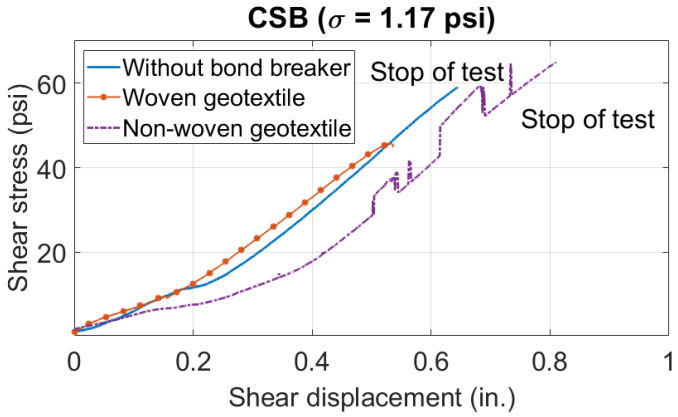

(a)

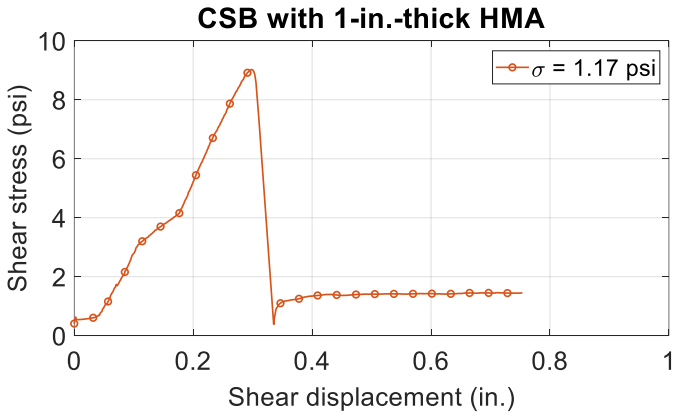

(b)

Figure 3.7: Shear stress-displacement relationship for CSB (with strong bond): (a) CSB with strong interfaces; (b) CSB with 1-in.-thick HMA layer.

As presented in Figure 3.8(a) and (b), for the CSB with PE sheets (Series 10 and 11), the shear stress-displacement relationships present similar trends as those observed in the HMA with PE sheets. The peak strength was observed in the first test with a normal stress of 2 psi, which was due to the initial interlocking. The peak strengths for the cases of 1.17 psi and 0.5 psi normal stresses were not completely reflected since the initial interlocking was disturbed in the first test. At relatively large displacements, the shear stress reached a plateau. The slight fluctuation was observed in the steady status, which could be caused by the undulation due to the local roughness/unevenness of the CSB surface or the mismatching of the initial interface profile. Similar to the Grade 3 Aggregate, the first plateau was selected as the steady shear strength.

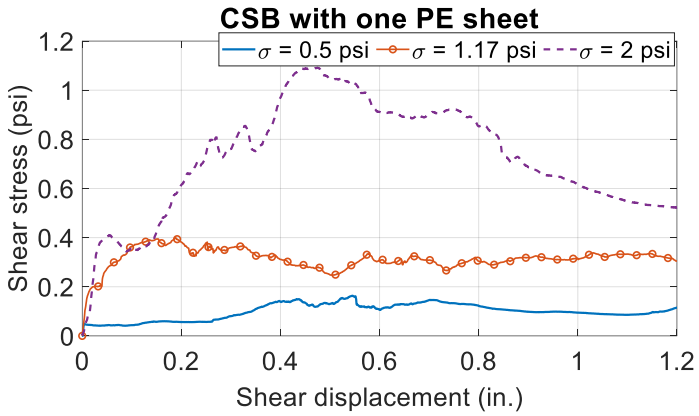

(a)

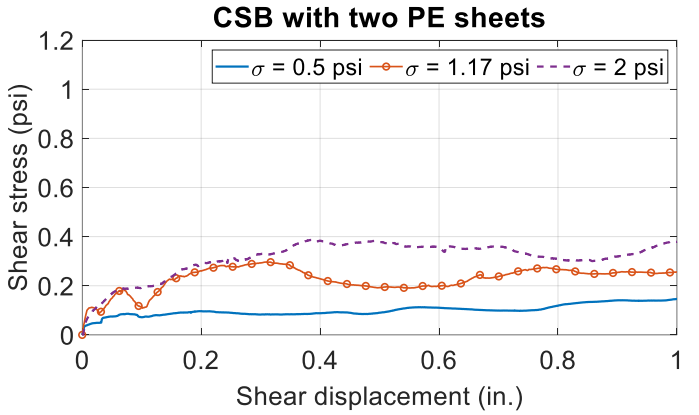

(b)

Figure 3.8: Shear stress-displacement relationship for CSB (with bond breakers): (a) CSB with one PE sheet; (b) CSB with two PE sheets.

3.3.2 Shape of Shear Stress-Displacement Relations

The shape of the shear stress-displacement curve depends on the concrete slab-base interface conditions. In summary, the curves for all test series can be ultimately categorized into two types, as presented in Figure 3.9. The first type (Figure 3.9(a)) exhibits a plateau at a relatively large displacement, which corresponds to a steady ultimate interface shear strength. The second type (Figure 3.9(b)) typically exhibits a pattern involving a well-defined interface peak shear strength followed by a drop and finally a steady (or residual) strength. Similar findings were reported in previous studies (Chan Suh et al. 2002). The first type is common for loose untreated bases, whereas the second type is usually observed in stabilized bases. This study further examined the shape of the shear stress-displacement relationships for the concrete slab-base interface with different types of interface materials.

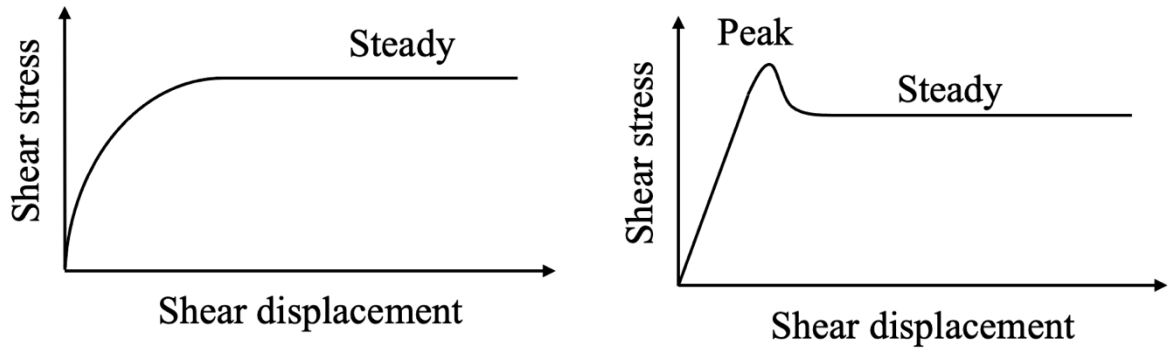

(a) (b)

Figure 3.9: Typical shapes of shear stress-displacement relationship at the concrete slab-base interface.

In this study, the first type of response was observed with a precast concrete specimen on granular bases, either without a bond breaker or with a bond breaker consisting of two PE sheets (i.e., Series 1, 2 and 3a). The second response type was observed for the rest of the series, which involved a CIP concrete specimen on granular/stabilized bases, either with or without bond breakers. For some strong interfaces that could not be failed (Series 4, 6, 8 and 9), only an initial portion of the stress-displacement curve was obtained. The peak in the second type of curve can be attributed to two sources of interface resistance. One source was the interlocking effect of the matching profiles between the top surface of the base and bottom surface of the CIP concrete block. This interlocking effect explains the small peaks observed with PE sheets. The interface shear strength dropped 35% (from 1.12 psi to 0.7 psi) after the interlocking mechanism was broken for the HMA with two PE sheets. The second source of the initial peak in the shear stress-displacement response was the adhesion of the interface, which may contribute significantly to the interface shear strength. For the CSB with a 1-in.-thick HMA layer, the shear strength dropped 85% (from 9 psi to 1.4 psi) following the peak, indicating a notable initial adhesion component. Once the initial adhesion and/or interlocking mechanism was broken, the shear stress decreased and tended to exhibit a plateau.

3.3.3 Interface Shear Strength and Friction Coefficients

Table 3.5 summarizes the results of the Phase I testing program, in terms of the Mohr-Coulomb parameters defined for each interface condition. The shear strength at failure used in the strength envelope corresponds to the steady interface shear strength, which has also been identified in the literature as the large-displacement interface shear strength.

For the tests for which ultimate failure could not be achieved at the interface within the loading capacity of the testing device (i.e., Series 4, 6 and 9), only a lower bound of the apparent coefficient of friction, μ_{app}, was calculated based on the maximum shear stress. The use of PE sheets significantly decreased the shear strength at the CIP concrete-CSB and CIP concrete-HMA interface by effectively eliminating the adhesion. This is evidenced by the small values of the intercept coefficient a of the resulting Mohr-Coulomb relation, as shown in Table 3.5. The coefficient of friction provided by two layers of PE sheets was slightly lower than that obtained using only one layer.

Table 3.5: Phase I frictional characteristics of concrete slab-base interaction.

Series	Base type	Interface material	Concrete	Mohr-Coulomb parameters	
				μ	a (psi)
1	AASHTO Gravel No.8	None	Precast	0.36	0.04
2	Grade 3 Aggregate	None	Precast	0.38	0.05
3	Grade 3 Aggregate	Two PE sheets	Precast	0.19	0.09
3b	Grade 3 Aggregate	Two PE sheets	CIP	$\mu_{app\_peak\ (\sigma=1.17psi)} = 0.57$ $\mu_{app\_steady\ (\sigma=1.17psi)} = 0.40$	
4	Type B HMA base	None	CIP	$\mu_{app\_peak\ (\sigma=1.17psi)} > 54$	
5	Type B HMA base	Two PE sheets	CIP	0.35	0
6	CSB	None	CIP	$\mu_{app\_peak\ (\sigma=1.17psi)} > 50$	
7	CSB	1-in.-thick Type D HMA	CIP	$\mu_{app\_peak\ (\sigma=1.17psi)} = 7.7$ $\mu_{app\_steady\ (\sigma=1.17psi)} = 1.2$	
8	CSB	Woven geotextile	CIP	$\mu_{app\_peak\ (\sigma=1.17psi)} = 39$	
9	CSB	Non-woven geotextile	CIP	$\mu_{app\_peak\ (\sigma=1.17psi)} > 56$	
10	CSB	One PE sheet	CIP	0.2	0.03
11	CSB	Two PE sheets	CIP	0.15	0.02

For tests that were conducted with three normal stress levels (Series 1, 2, 3a, 5, 10, and 11), shear strength envelopes were obtained by plotting three sets of normal stresses and shear stresses at failure. Figure 3.10 and Figure 3.11 plot the shear strength envelope for granular and stabilized bases, respectively. Two Mohr-Coulomb model parameters at the interface, coefficient of friction μ and intercept a, were calculated as the slope and intercept by linearizing the strength envelope. The coefficient of determination R^2 is also given, which indicates the goodness of fit of the linear regression model.

For the AASHTO Gravel No.8 without bond breaker involving the use of a precast concrete, as presented in Figure 3.10(a), the interface μ was 0.36, corresponding to an interface friction angle of $20°$, and the intercept a was 0.04 psi. Mohamed (2017) characterized the shear strength properties of the AASHTO Gravel No.8 using the same large-scale direct shear test setup with the normal stresses of 3.48 psi and 7.54 psi. The materials were prepared at the same relative density of 70%. The peak friction angle was identified as 30.9°. The friction angle at the precast concrete-AASHTO Gravel No.8 interface is close to 2/3 of the internal friction angle of AASHTO Gravel No.8.

The shear strength envelopes for the precast concrete block on top of the Grade 3 Aggregate without bond breaker and with two PE sheets are presented together in Figure 3.10(b) for comparison. The interface friction coefficient μ was decreased from 0.38 to 0.19 with the use of two PE sheets. The coefficient of friction at the precast concrete-Grade 3 Aggregate interface was slightly larger than that at the precast concrete-AASHTO Gravel No.8 interface, which could be explained by the rougher interface due to the larger size and angular shape of Grade 3 Aggregates.

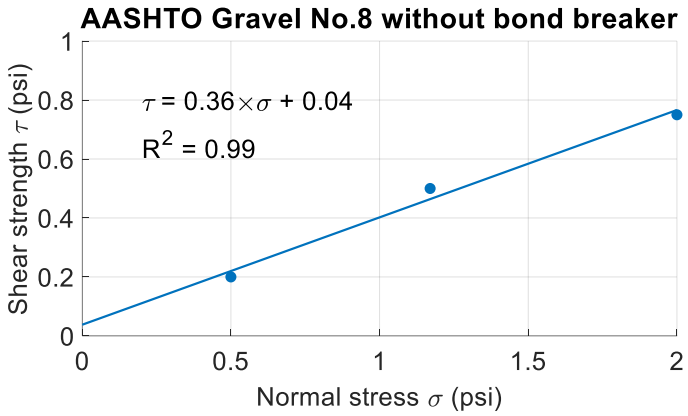

(a)

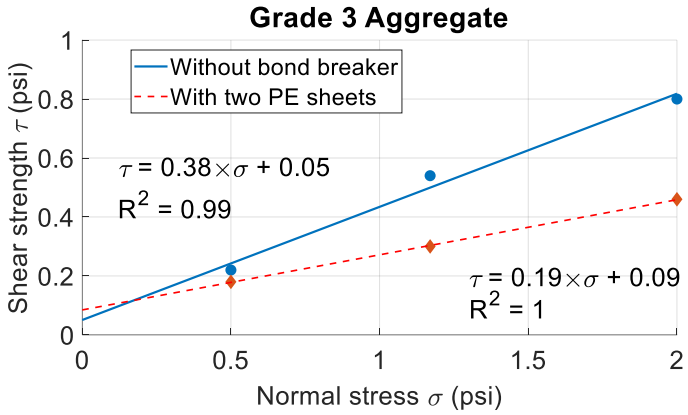

(b)

Figure 3.10: Steady shear strength envelopes for granular bases: (a) AASHTO Gravel No.8 base without bond breaker using a precast concrete; (b) Grade 3 Aggregate base without bond breaker and with PE sheets using a precast concrete.

The use of PE sheets significantly decreased the shear strength at the CIP concrete-CSB and CIP concrete-HMA interface by eliminating the adhesion. For example, in the case of HMA with two layers of PE sheet, the shear stress decreased from 63.4 psi to 0.41 psi for the case with 1.17 psi normal stress. The shear strength envelope for the CIP concrete block on top of HMA with two PE sheets is shown in Figure 3.11(a). The interface μ was 0.35. The shear strength envelopes for the CIP concrete block on top of CSB with one and two PE sheets are plotted together in Figure 3.11(b) for comparison. The interface μ was 0.2 and 0.15 for one and two PE sheets, respectively. With the same bond breaker, the interface μ was lower when the base was CSB than that when the base was HMA, which was likely attributed to a smoother finished surface of CSB.

In the above conditions, the linear regression model resulted in a non-zero but very small value of intercept a. In these cases, the relatively small intercept likely indicates the interlocking instead of adhesion at the interface because the use of polyethylene sheets completely breaks the bond. The steady shear strength increased proportionally as the normal stress increased, indicating that the major component of the residual shear resistance was pure friction in the case with the use of a bond breaker.

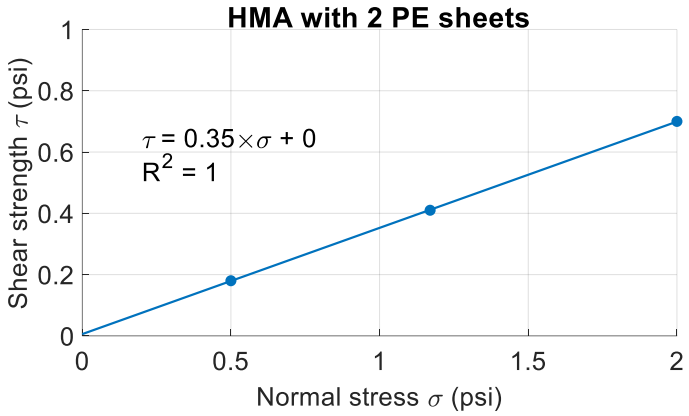

(a)

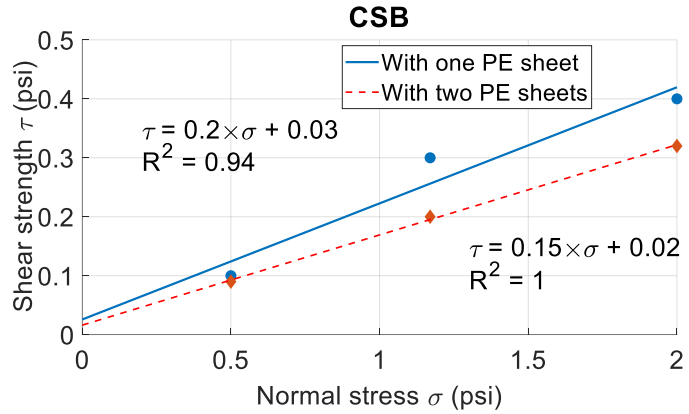

(b)

Figure 3.11: Steady shear strength envelopes for stabilized bases: (a) HMA base with two PE sheets; (b) CSB with one and two PE sheets.

3.3.4 Sliding Planes

For test specimens that have a bond breaker at the interface, the shear failure may occur at the concrete block-bond breaker interface or the base-bond breaker interface. In some cases, this failure may also occur at the bond breaker-bond breaker interface (applicable in the case of two PE sheets) or within the bond breaker itself (applicable in the case of CSB with a 1-in.-thick HMA layer). Eventually, the shear failure occurs at the weakest interface. The location of sliding plane when the steady shear strength was reached was observed in this study. Table 3.6 summarizes the sliding planes for different interface materials in Phase I.

For tests with two PE sheets, despite the type of bases (Grade 3 Aggregate base, HMA, or CSB), the sliding was observed to occur between the two sheets. Specimens with a single PE sheet exhibited initial slip at the sheet-base interface, but ultimately slid between the sheet and CIP concrete due to the deterioration of the bond.

Table 3.6: Phase I sliding planes.

Interface material (base)	Sliding plane
Two smooth PE sheets (Grade 3 Aggregate, CSB, HMA)	Between two sheets

One smooth PE sheet (CSB)	Initially, sheet-base; after a few cycles, sheet-CIP concrete.
1-in.-thick HMA (CSB)	Thin HMA layer-base
Woven geotextile (CSB)	Woven geotextile-base

Typically, for stabilized bases, the sliding plane was observed very close to the interface but was within the base material due to the strong bond at the interface. However, the sliding surface may be different if a thin layer of asphalt is applied over stabilized bases. In the case of CSB with a 1-in.-thick HMA layer (Series 7 in Phase I), it was observed that the concrete block with the thin layer of HMA slid together with respect to the CSB, as shown in Figure 3.12(a). Similar phenomena were reported in the investigation of a 0.75-in.-thick asphalt stabilized base over the CSB by Wesevich et al. (1987) and a 1.5-in.-thick HMA bond breaker over the lean concrete base by Chan Suh et al. (2002).

For the CSB with a woven geotextile, sliding occurred at the interface between the CSB and woven geotextile, whereas the concrete block remained attached to the geotextile, as shown in Figure 3.12(b). In this case, cement paste from the concrete was observed to have permeated the geotextile and bonded with the CSB during casting, which caused the comparatively high interface shear strength.

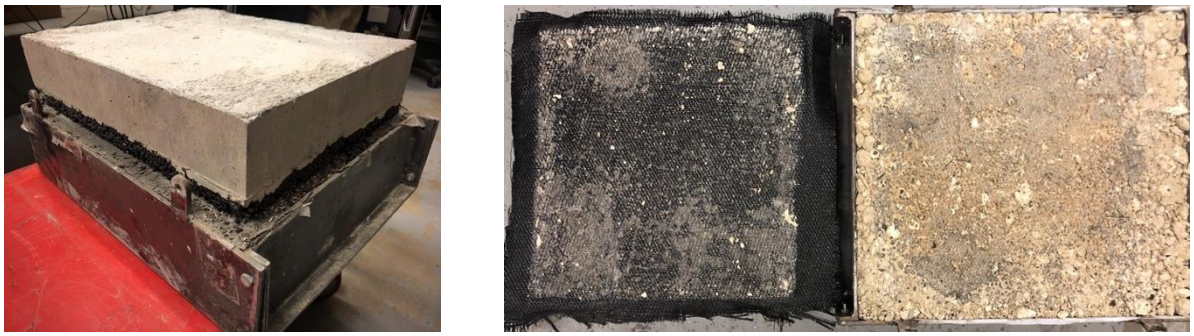

(a) (b)

Figure 3.12: Sliding planes in Phase I: (a) CSB with a 1-in.-thick HMA; (b) CSB with a woven geotextile.

3.3.5 Summary

This chapter summarizes the results of the Phase I experimental study, which provided a preliminary investigation the concrete pavement-base interaction through unit-cell direct shear tests. The bases investigated included granular bases and stabilized bases (HMA and CSB), which are commonly used in the U.S. The testing program explored the effectiveness of different interface materials employed as bond breakers. The interface materials included a 1-in.-thick HMA layer, woven-geotextile, non-woven geotextile, and one or two smooth PE sheets. Shear stress versus displacement (up to 1 in.) relationships with three normal stress levels of 0.5 psi, 1.17 psi and 2 psi, representing the weight of a 6-in.-, 14-in.- and 24-in.-thick concrete pavement, respectively, were reported for each type of interface condition. The response of the interfaces was

characterized by frictional and adhesive parameters based on the Mohr-Coulomb failure criteria. The main conclusions of this experimental study are summarized, as follows:

- Tests involving the use of a precast concrete were not representative of the overall interface behavior expected in the field as it failed to capture the adhesive and/or interlocking component of CIP concrete.
- Concrete-base interfaces with a 1-in.-thick HMA layer, woven geotextile and non-woven geotextile presented a strong adhesion and relatively high shear strength. As a result, these interface materials were not suitable to be used as bond breakers in the transition slab of seamless bridge-pavement systems.
- The use of polyethylene sheets eliminated the adhesion at the interface. For the CSB with PE sheets, the coefficients of friction for two PE sheets and one PE sheet were approximately 0.15 and 0.2, respectively.
- For bases with or without a bond breaker involving the use of a CIP concrete, the shear stress-displacement response at the concrete slab-base interface can be characterized by a peak shear strength followed by a drop to a large-displacement shear strength. The peak interface shear strength can be attributed to two sources: 1) an interlocking effect of the matching profiles between the top surface of the base and bottom surface of the CIP concrete block; and 2) the adhesion of the interface.

4. Phase II: Large-Scale Push-Off Test (Task 3.2)

4.1 Overview

Phase II testing examined the shear responses of a selected number of interface conditions identified in Phase I testing that were deemed most suitable for the transition slab in seamless bridge applications. While Phase I examined a large variety of interface conditions at a relatively small scale with a simple loading scheme, the Phase II program focused on fewer interface conditions but provided more representative data by considering a larger scale and a cyclic loading scheme.

Based on an assessment of the Phase I test results, the only bond breakers to fully eliminate the bond with the CIP concrete were the specimens with one or two polyethylene (PE) sheets at the interface. Consequently, PE sheets were further examined in Phase II with large-scale slab segments. Furthermore, the following two types of PE sheets with surface roughness were added to the test program: 1) a 40-mil-thick spike high-density polyethylene (HDPE) sheet with single-sided 18-mil asperities; and 2) a 60-mil-thick double-sided textured linear low-density polyethylene (LLDPE) sheet with 16-mil asperities. LLDPE sheets generally have higher tensile strength and resistance to harsh environments compared to the smooth PE in Phase I. LLDPE sheets are also more flexible than HDPE sheets, which simplifies handling during construction. Another practical bond breaker included in Phase II was suggested by the monitoring panel and consisted of asphalt-saturated organic felt paper, which is impermeable and has previously been used in bridge applications as bearings for pan girders. The specific material tested was Type II felt paper (ASTM D4869, 2016).

This chapter outlines the description of the testing program and results from Phase II, including the cyclic shear stress-displacement relations, interface shear strengths and coefficients of friction for each interface condition. The effects of cyclic movements and scales on the interface shear strength are discussed, and the sliding plane and visual inspection on the post-test interface conditions are also provided.

4.2 Experimental Program

4.2.1 Test Setup and Instrumentation

The Phase II experiments involved large-scale push-off tests on concrete slabs subjected to fully-reversed cyclic displacement demands, as depicted in Figure 4.1.

To facilitate the testing program, two identical self-reacting test frames, one of which can be seen in Figure 4.2(a), were designed and fabricated to conduct the push-off tests. Each frame accommodated two test specimens. The mechanism for the large-scale tests, with various components labeled, is depicted in Figure 4.2(b). The test setup consisted of a vertical support frame and a lateral reaction frame. Test specimens included a compacted base (8 ft. × 6 ft. × 7 in.) inside of a wooden box, a CIP concrete slab (5 ft. × 2 ft. × 6 in.) and an interface material between the base and slab. The specimens were prepared on top of the support frame. The reaction frame consisted of two identical wide flange beams, one on each side of the wooden box, perpendicular to the loading direction. The lateral beams restrained the movement of the base and are bolted to the bottom beams to transfer the horizontal force.

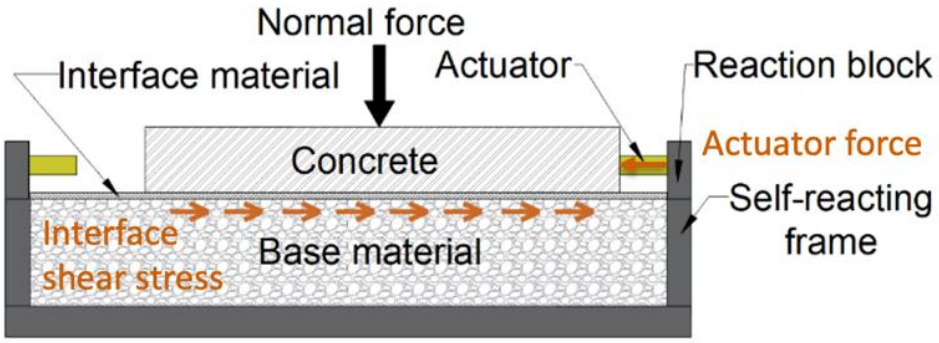

Figure 4.1: A scheme of Phase II large-scale push-off test.

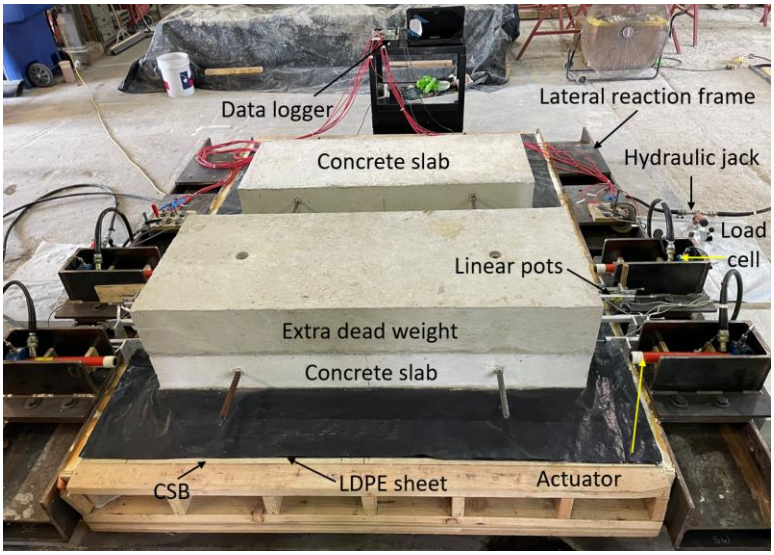

(a)

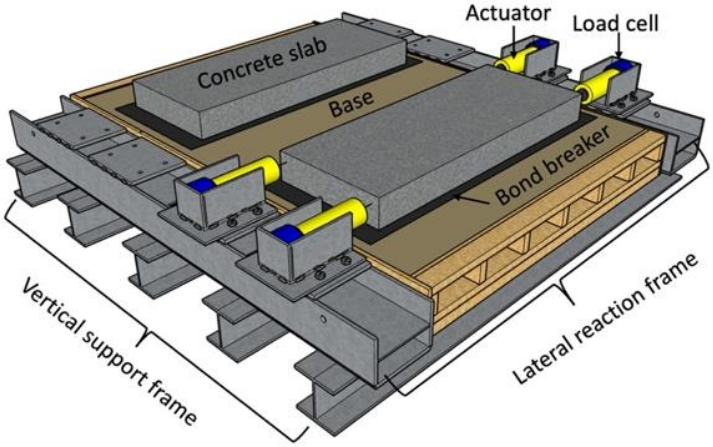

(b)

Figure 4.2: Phase II large-scale push-off test setup and instrumentation.

During testing, the horizontal actuator force and the relative displacement of the concrete slab with respect to the base were recorded using a CR3000 data logger at a frequency of 5 Hz. Two single-

acting hydraulic cylinders were used on each side to push the concrete slab in two opposite directions consecutively. When the cylinders on one side pushed the slab, the cylinders on the opposite side were fully retracted and were not in contact with the slab. The use of two cylinders on each side produced uniform sliding of the slab and mitigated rotational effects around the vertical axis of the concrete slab during testing. The instrumentation is also shown in Figure 4.2. The force applied by the hydraulic cylinders was measured via load cells with a capacity of 2 kips, and the interface shear force was calculated as the sum of the two load cell readings. A total of four linear potentiometers with a range of 4 in. were mounted on the lateral reaction frame (two on each side) to measure the displacement of the concrete slab relative to the base. The relative horizontal displacements were obtained by averaging the four readings.

4.2.2 Test Parameters and Procedure

Table 4.1 summarizes the test matrix for Phase II, which focused on CSB with different types of bond breakers.

Table 4.1: Phase II Test Matrix.

Series	Base type	Interface material
1	CSB (#1 & #2)	Two smooth PE sheets
2	CSB (#1 & #2)	One smooth PE sheet
3	CSB (#1)	Single-sided spike HDPE sheet
4	CSB (#1)	Double-sided textured LLDPE sheet
5	CSB (#1)	Felt paper
6	CSB (#2) with 1-in.-thick Type D HMA	Double-sided textured LLDPE sheet
7a	CSB (#2) with 1-in.-thick Type D HMA	Felt paper
7b	CSB (#2) with 1-in.-thick Type B HMA	Felt paper

Two CSB specimens with identical mix designs were prepared in Phase II, as pictured in Figure 4.3(a) and (b). The CSB for the two specimens were cast in two separate mixes. Although the mix designs were identical, the separate mixes produced a noticeable difference in the finished surface. Test Series 1 and 2 were repeated on both CSB Specimens #1 and #2. Due to the observable difference in CSB finishes, the results provide insight into the effects of the variances in the CSB finished surfaces on the coefficient of friction. The results in Test Series 1 and 2 were compared to those obtained in Phase I to identify potential differences caused by the sample size.

Additionally, CSB topped with a 1-in.-thick HMA layer was also considered as a base type (Series 6 and 7). In some U.S. states (Roesler et al., 2016), a thin HMA layer is routinely constructed under CRCP, so continuing a thin HMA layer to the transition slab might be a preferable construction procedure to accommodate the difference in thickness, as shown in Figure 4.4. Test Series 6 and 7 provide the concrete slab-base interactions with different types of bond breakers for such conditions. Furthermore, Type B and Type D HMA are usually used for the HMA base and thin interface layer, respectively. Test Series 7a and 7b specifically investigate the effects of Type D and Type B HMA on interface characteristics. Figure 4.3(c) presents the surface of Type B and Type D HMA layers on top of the CSB specimen. The selected interface materials are shown in Figure 4.8.

(a)

(b)

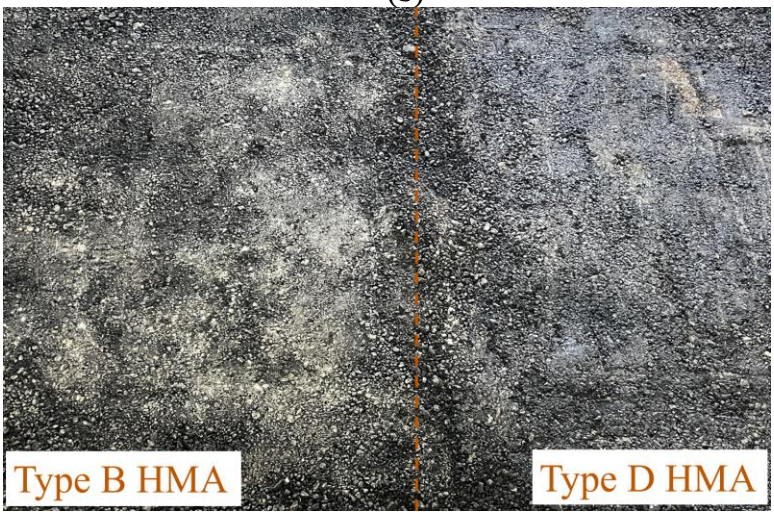

(c)

Figure 4.3: Phase II bases: (a) CSB specimen #1; (b) CSB specimen #2; (c) 1-in.-thick HMA layer on top of CSB.

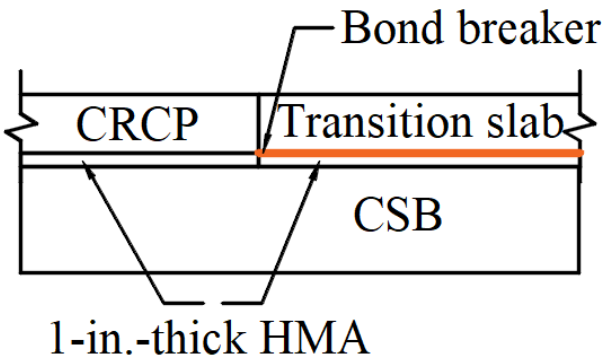

Figure 4.4: Arrangement of bond breakers from CRCP to transition slab.

For each interface condition, push-off tests were conducted with three normal stresses, consistent with Phase I, of 0.5 psi, 1.17 psi, and 2 psi, representing the weight of a concrete pavement with the thickness of 6 in., 14 in., and 24 in., respectively. The concrete slab specimen had a thickness of 6 in. corresponding to the 0.5 psi normal stress level. Two additional concrete slabs with identical plane dimensions, but different thicknesses of 8 in. and 10 in., were constructed for additional normal stress levels, which were reached by stacking the slabs as seen in Figure 4.2(a).

The concrete slab was quasi-statically loaded with cyclic movements. The loading protocol consisted of eight cycles of fully reversed horizontal displacements at an amplitude of 1 in. representing expansion-contraction cycles. The initial monotonically increasing displacement in the slab was used to characterize the basic frictional behavior of the interface and capture the peak strength. At the end of the initial monotonic test, the load was reversed to quantify the residual friction resistance in the opposite direction. Subsequent cyclic tests contributed to identifying and quantifying possible variations of the friction resistance with increasing deformation demands, including possible changes in the friction resistance of the bond breakers.

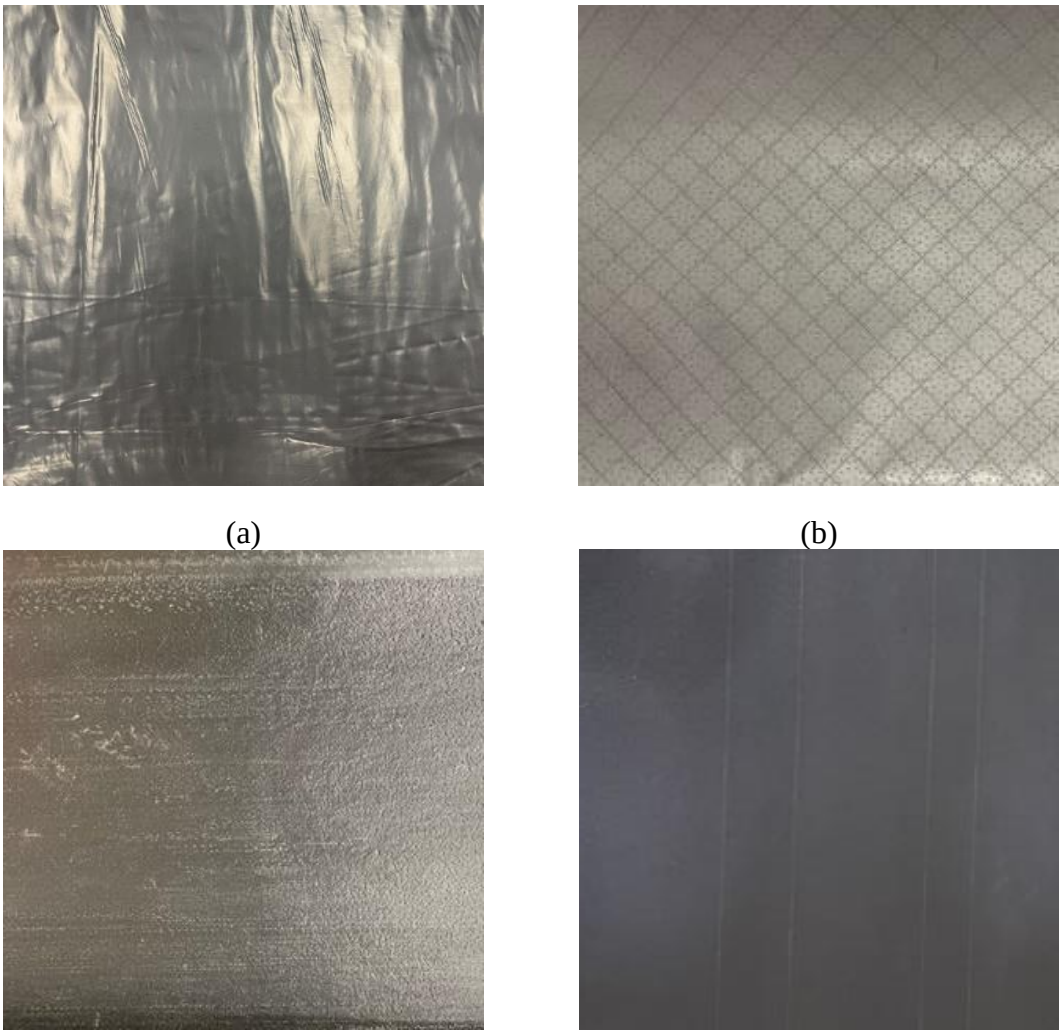

(a) (b)

(c) (d)

Figure 4.5: Phase II interface materials: (a) Smooth PE sheet; (b) Spike HDPE sheet; (c) Textured LLDPE sheet; (d) Felt paper.

4.2.3 Test Specimens and Material Properties

Cement Stabilized Base

In Phase II, plant-mixed CSB materials were delivered to the laboratory in a ready-mix truck. The cement content of the CSB by weight was 7%. The construction steps are shown in Figure 4.6. Two uniform layers with a thickness of 3.5 in. were constructed in sequence. For each layer, the mixed materials were placed into the formwork using a loader and then were spread uniformly using shovels. Each layer was compacted immediately after placing with the use of a plate compactor for several passes. The CSB surface was bladed to the design thickness of 7 in. and was compacted again until a smooth surface was attained.

The CSB compressive strengths obtained at seven days for specimens #1 and #2 were 790 psi and 1000 psi, respectively, which satisfied the minimum specimen strength requirement of 500 psi established in TxDOT Item 276 (2014).

(a) (b)

(c) (d)

Figure 4.6: Construction of CSB specimens in Phase II: (a) Place the mixed materials; (b) Spread the mixed materials; (c) Compact using a plate compactor; (d) Blade the surface.

Hot Mix Asphalt Base

The HMA mix that was utilized was identical to that used in Phase I. The procedure to prepare the 1-in.-thick HMA layer was similar to CSB specimens. Figure 4.7 shows the construction steps of a HMA specimen.

(a) (b)

Figure 4.7: Construction of HMA specimens in Phase II: (a) Apply a prime coat on CSB prior to the construction of HMA layer; (b) Compact using a plate compactor.

Concrete Slab

The concrete mix utilized was identical to that used in Phase I. The concrete compressive strengths measured on the 28th day after casting ranged from 4000 psi to 5000 psi, which satisfied the minimum requirement of 4000 psi (TxDOT Item 360, 2014).

4.3 Experimental Results and Discussion

4.3.1 Cyclic Shear Stress-Displacement Relations

CSB with Two Smooth PE Sheets

For the CSB tests with two PE sheets, the same specimen was used in the subsequent push-off tests at different normal stresses of 0.5 psi, 1.17 psi, and 2 psi. The cyclic shear stress versus relative displacement relationships for three normal stresses are presented in Figure 4.8. With a normal stress, σ = 0.5 psi, cyclic movements with an increasing amplitude from 0.25 in. to 2.0 in. were used as a trial loading protocol to investigate the effects of slip histories on the interface friction characteristics. Similarly, with a normal stress, σ = 1.17 psi, the amplitude of horizontal movements was 1.0 in. for the initial few cycles and was increased to 1.5 in. when a slightly increasing trend at the 1 in. displacement was observed. For the rest of Phase II tests, a loading protocol of fully reversed cyclic movements with 1 in. amplitude was established and applied.

The peak was observed in the initial cycle with a normal stress, σ = 0.5 psi, as shown in Figure 4.8(a). This peak was most likely due to the effects of interlock between the bottom surface of the CIP slab and the top of the base. Peaks were also observed in subsequent cycles, but with smaller magnitudes, for two possible reasons: 1) a reduction in surface roughness due to erosion; and/or 2) the interlocking effects decreased as the initial profiles became more dissimilar. The shear stress-displacement relationship plateaued following movement beyond the initial location. The shear stresses gradually decreased for a few cycles and no significant changes were observed in subsequent cycles.

For each normal stress level, aside from some isolated cases, the push-off tests were generally conducted for eight cycles. After the first few cycles, the tests were repeatable with slight variations over cycles. It was noticed that for σ = 1.17 psi, the peaks were not as obvious in the second half in cycles 7 and 8 as they were in the previous cycles. After a few days, the concrete slab was lifted and the PE sheets were stretched with an attempt to release any potentially stored energy in the system. The concrete slab was put back to the original location and additional cyclic tests were conducted. As shown in Figure 4.8(b), the peak at the initial spot appeared in cycle 9, showing good consistency with previous cycles. The possible reason for the disappearance of the peaks in cycles 7 and 8 may be a small mismatch with the original interface profile as the concrete slab was displaced.

It should be noted that the Phase II series of push-off tests with one and two PE sheets were conducted with two CSB specimens with noticeable surface differences. Figure 4.9 compares the shear stress-displacement relations when using CSB specimen # 1 and CSB specimen #2 with three normal stress levels. The responses with each normal stress level were consistent between the two specimens.

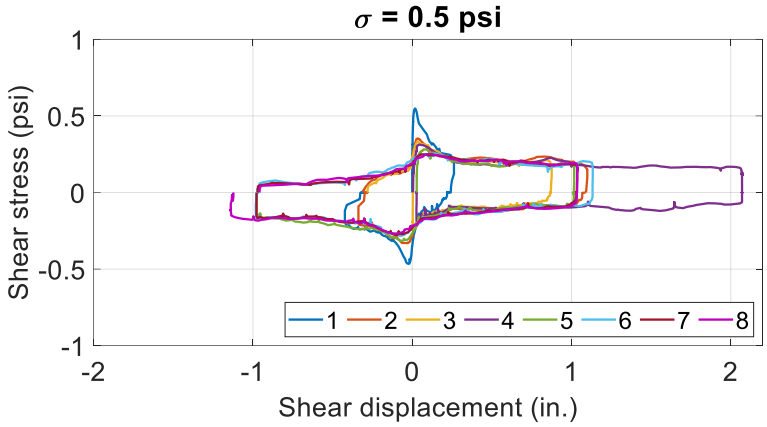

(a)

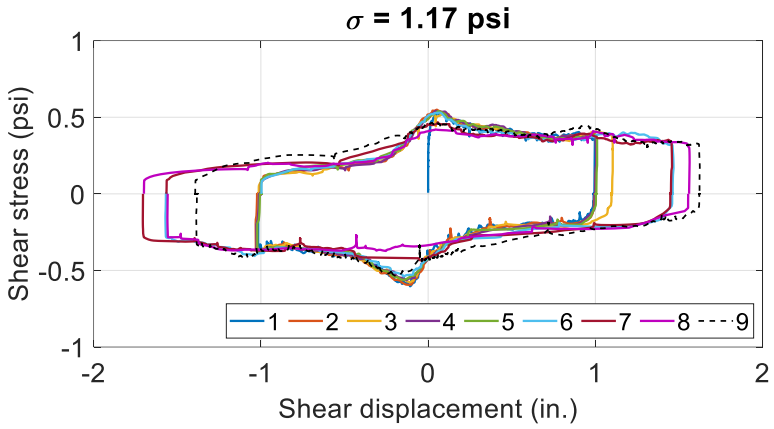

(b)

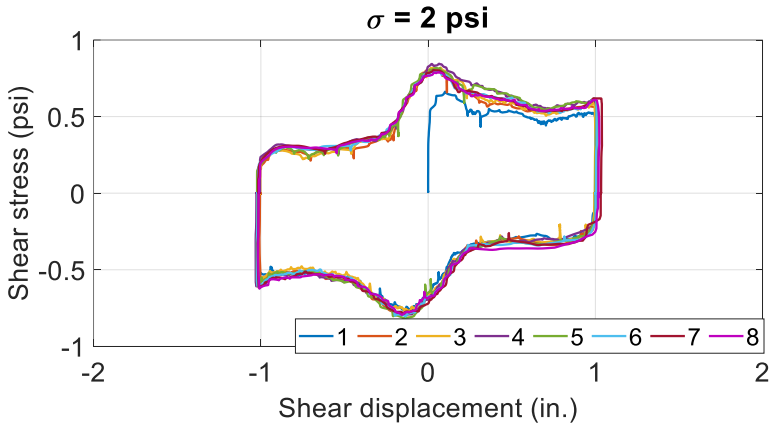

(c)

Figure 4.8: Cyclic shear stress-displacement relationship for CSB with two PE sheets.

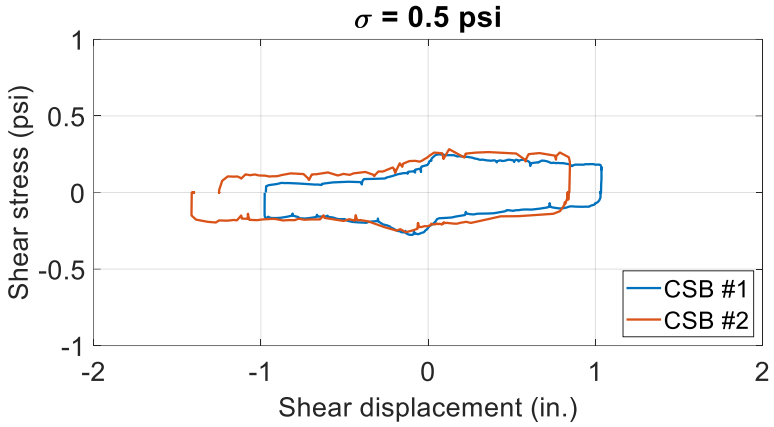

(a)

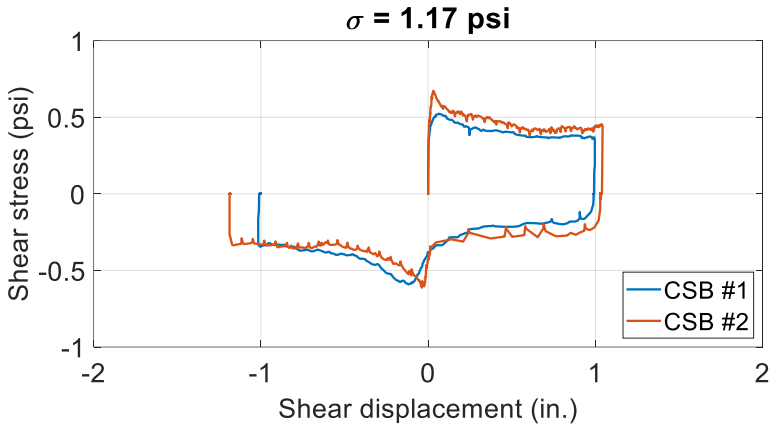

(b)

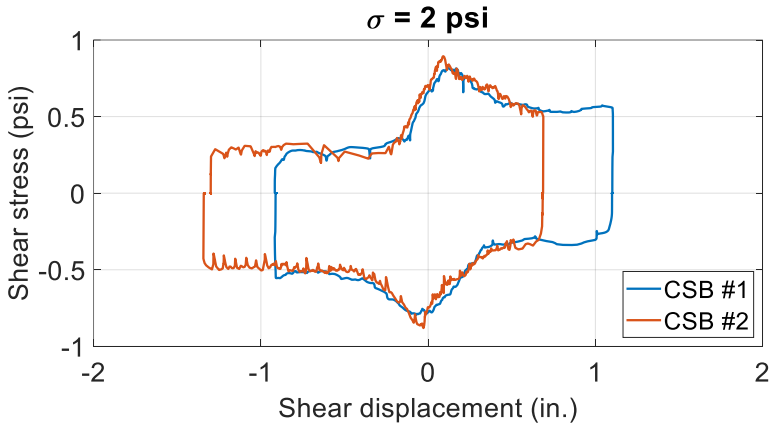

(c)

Figure 4.9: Effects of CSB surfaces on shear stress-displacement relationships for CSB with two PE sheets.

CSB with One Smooth PE Sheet

For the CSB with one PE sheet, the cyclic shear stress-displacement relationship with normal stresses of 0.5 psi, 1.17 psi, and 2 psi are presented in Figure 4.10. The cyclic behavior observed

with a smooth PE sheet was similar to that observed with two PE sheets presented in Figure 4.8. The obvious peak was observed in the first test with a normal stress σ = 0.5 psi. After the initial interlocking was overcome, the shear stress decreased significantly and then gradually became steady. The fluctuations in the curve are attributed to the complicated interface profile. The steady shear strength can be obtained by averaging the values in forward and reverse directions.

It is interesting that the shear strength in the reverse directional movement was smaller compared to the forward directional movement. This phenomenon was also observed in the case of CSB with two PE sheets. To further investigate this phenomenon, the three-dimensional digital image correlation (DIC) technique was used to measure the vertical displacement of the concrete slab during tests. The DIC results indicated several local inclined movements of the concrete slab, which were likely caused by small undulations of the CSB surfaces, settlement of CSB, or creep effects of CSB. These directional effects due to the complicated interface profile can result in "upward" or "downward" slopes that occur locally around the interface of the CIP concrete slab and the CSB, which explains the difference in the shear stress two directions.

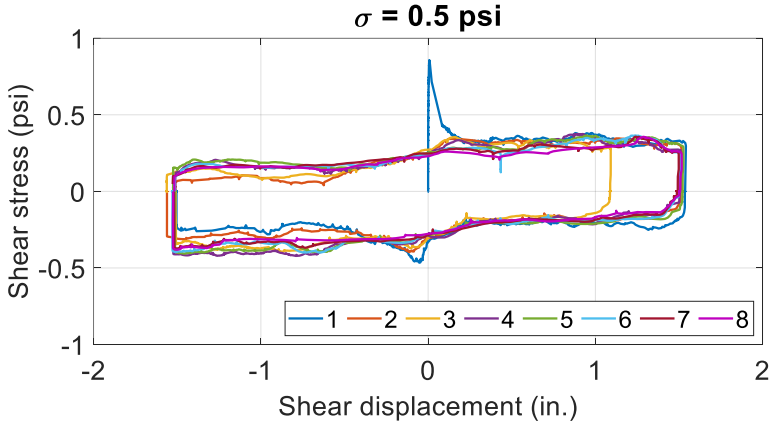

(a)

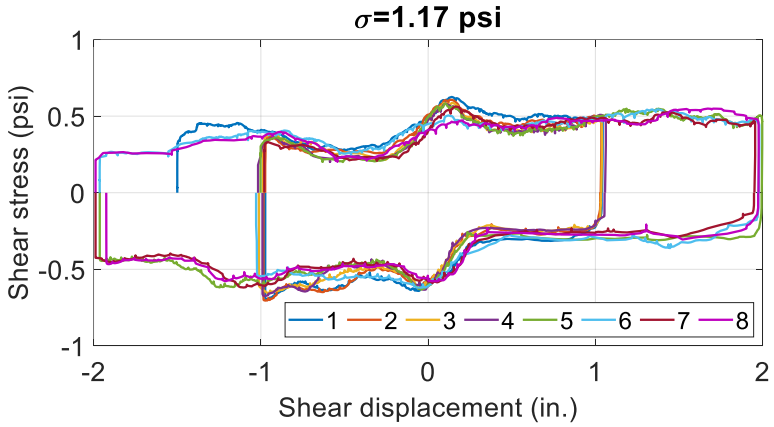

(b)

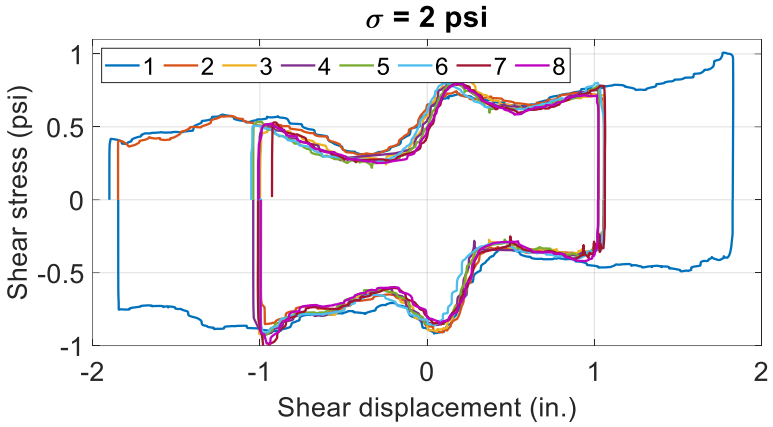

(c)

Figure 4.10: Cyclic shear stress-displacement relationship for CSB with one PE sheet.

Table 4.2 compares the measured and the corrected steady shear strengths with a normal stress, σ = 1.17 psi. The measured steady shear strength was corrected by accounting for the slope of the concrete movements characterized by the DIC results, which was an upward slope angle of 3.9° in the movement range of [0, 2] in. and a downward slope angle of 6.6° in the movement range of [-2, 0] in. The corrected steady shear strengths in forward and reverse directional movements after considering the slope of concrete movement showed good consistency. These directional effects can be eliminated by averaging the shear strengths in both directions.

Table 4.2: Comparison of measured and corrected steady shear strength.

Steady shear strength (psi)	Movement in [0, 2] in.		Movement in [-2, 0] in.	
	Forward	Reverse	Forward	Reverse
Measured	0.22	0.43	0.28	0.49
Corrected	0.35	0.35	0.36	0.36

Figure 4.11 compares the shear stress-displacement relationships when using CSB specimen # 1 and CSB specimen #2 for three normal stress levels. The results from the two different specimens agreed well with each other.

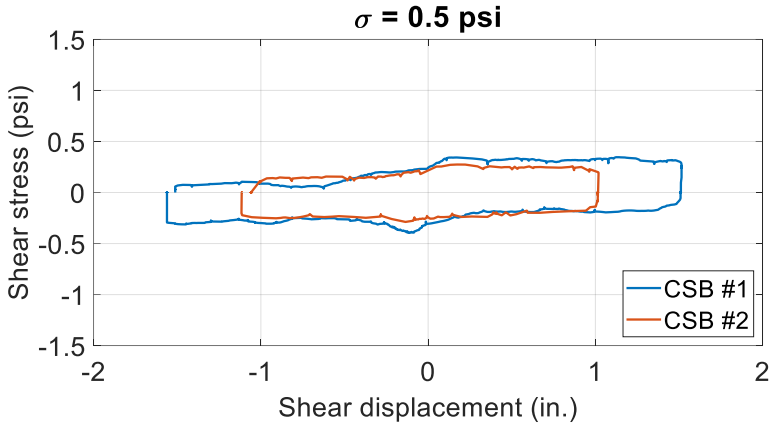

(a)

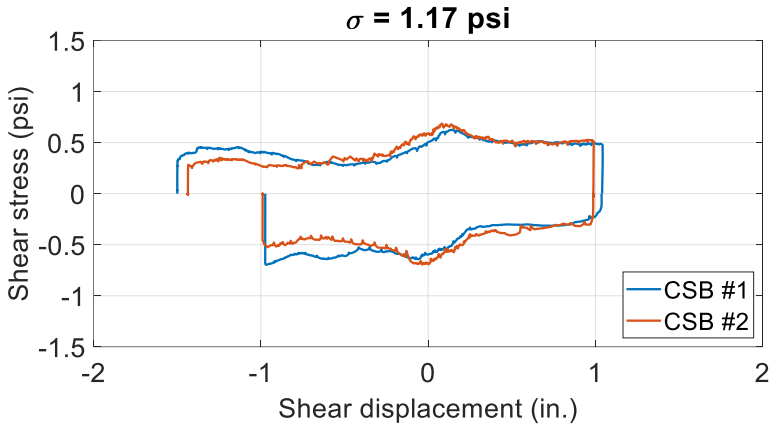

(b)

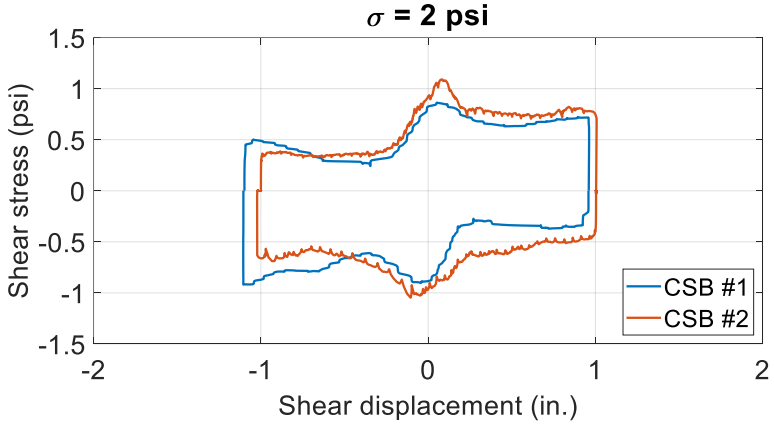

(c)

Figure 4.11: Effects of CSB surfaces on shear stress-displacement relationships for CSB with one PE sheet.

CSB with One Spike HDPE sheet

The cyclic shear stress-displacement relationships for tests of the specimen with a single-sided spike HDPE sheet on CSB with normal stresses of 0.5 psi, 1.17 psi, and 2 psi, are presented in Figure 4.12. The cyclic behavior observed with a spike HDPE sheet was similar to that observed with PE sheets.

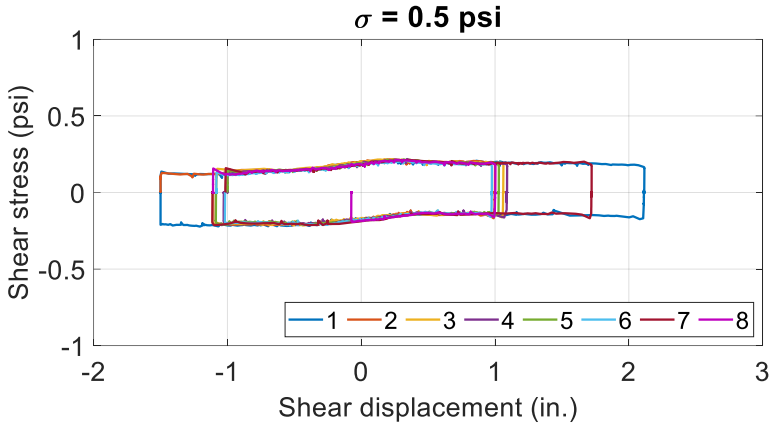

(a)

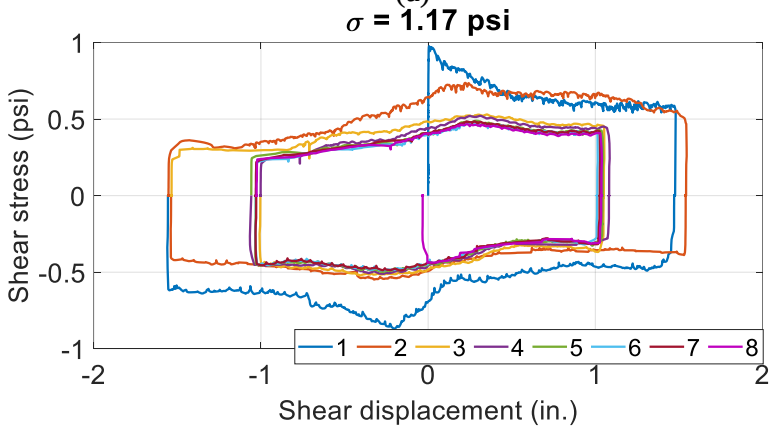

(b)

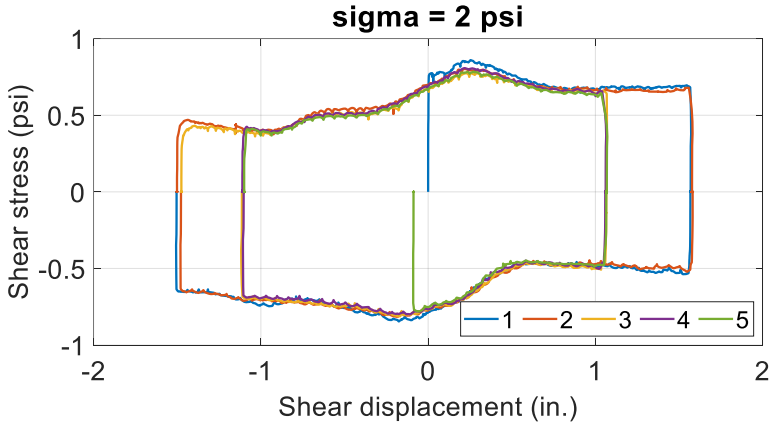

(c)

Figure 4.12: Cyclic shear stress-displacement relationship for CSB with a spike HDPE sheet.

The same specimen was used in the subsequent push-off tests at different normal stresses with a testing order consisting of 1.17 psi, 2 psi, and 0.5 psi. The normal stress of 1.17 psi is likely the most representative thickness that will be used in the field (thickness of 14 inches). The testing order is important to note since the effects of adhesion or interlock are generally the most significant on the first test. A significant peak was observed in both directions in the first test with

a normal stress, σ = 1.17 psi, and the peak value became smaller in the following cycles. The steady shear strength started to decrease in the second half of the second cycle of movements. After that, there were insignificant variations for the cyclic responses.

CSB with One Textured LLDPE Sheet

The cyclic shear stress-displacement relationships with normal stresses of 0.5 psi, 1.17 psi, and 2 psi applied to the specimen with a double-sided textured LLDPE sheet on CSB, are presented in Figure 4.13.

The same specimen was used in the subsequent push-off tests at different normal stresses with a testing order of 1.17 psi, 2 psi, and 0.5 psi. The peak was observed in the initial cycle with a normal stress, σ = 1.17 psi. The shear stresses gradually decreased for a few cycles, and there were no significant changes for the subsequent cycles of the tests. Directional effects of the shear stresses in the forward and reverse movements were also observed.

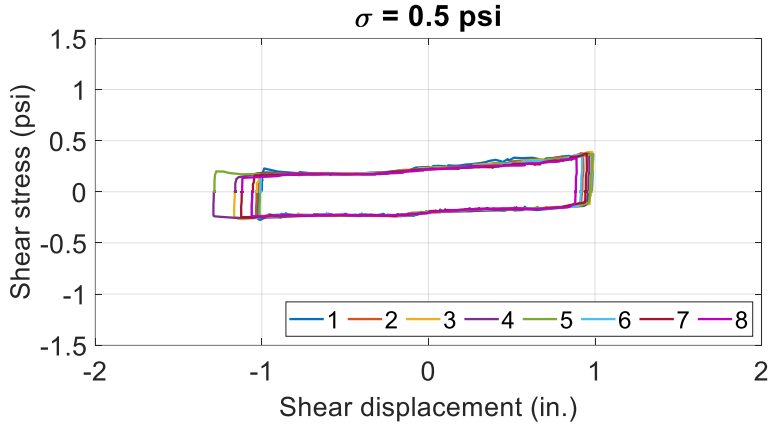

(a)

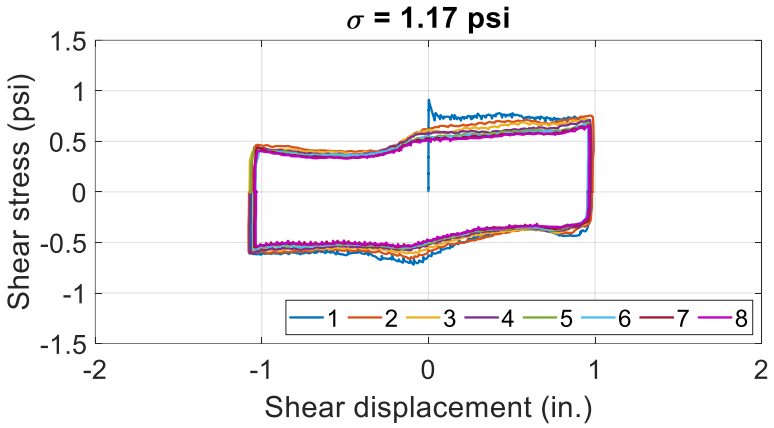

(b)

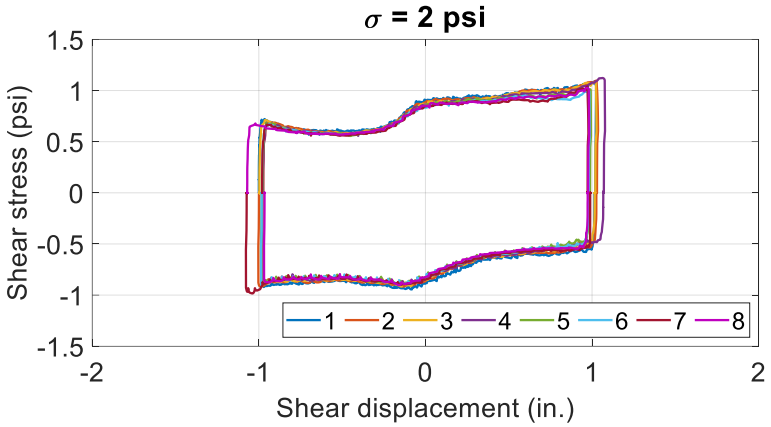

(c)

Figure 4.13: Cyclic shear stress-displacement relationship for CSB with a textured LLDPE sheet.

CSB with Felt Paper

For the tests on CSB with felt paper, the same specimen was used in the subsequent push-off tests at different normal stresses of 0.5 psi, 1.17 psi, and 2 psi. Due to the observed behavior, the tests on the specimen with CSB and felt paper were conducted in three different sequences:

- Sequence 1: 1.17 psi, 2 psi, and 0.5 psi
- Sequence 2: 0.5 psi, 1.17 psi, and 2 psi
- Sequence 3: 2 psi, 1.17 psi, and 0.5psi.

Following curing of the CIP slab, the normal stress of 1.17 psi was used in the first test, followed by the test with 2 psi, then the test with 0.5 psi. Following the first sequence of tests, two additional test sequences were conducted as outlined below. Figure 4.14 plots the cyclic shear stress-displacement relationship with different normal stresses in the first sequence of tests.

A significant peak was observed in the initial cycle, as shown in Figure 4.14(b). The initial peak was attributable to a certain amount of initial bond due to the slight adhesive features of felt paper as well as interlocking effects. Once the initial peak was overcome, the shear stress-displacement curve featured a plateau. In subsequent cycles, there were no obvious peaks as the concrete block moved beyond its initial placement and the curves were repeatable.

In addition, the difference of the steady shear strength between the forward and reverse directional movements was insignificant. The lack of a significant difference in cyclic direction may be due to the thicker texture of the felt paper compared to the PE sheets, so the interface friction was less affected by the small undulations of the CSB surface. This also explained the phenomenon of no obvious peaks at the initial spot in the subsequent cycles.

One exception was that a relatively high shear stress was observed in the first cycle with a normal stress, σ = 0.5 psi. This test was conducted right after the tests with a normal stress, σ = 2 psi by removing the concrete slabs on top for dead weights. The peak may still reflect the shear stress level with a higher normal stress level than 0.5 psi. To further investigate this phenomenon, two additional series of tests were conducted: 1) (Sequence 2) increasing sequences of normal stresses:

0.5 psi, 1.17 psi, and 2 psi; 2) (Sequence 3) decreasing sequences of normal stresses: 2 psi, 1.17 psi, and 0.5 psi. The shear stress-displacement relationships for two series are shown in Figure 4.15(a) and (b).

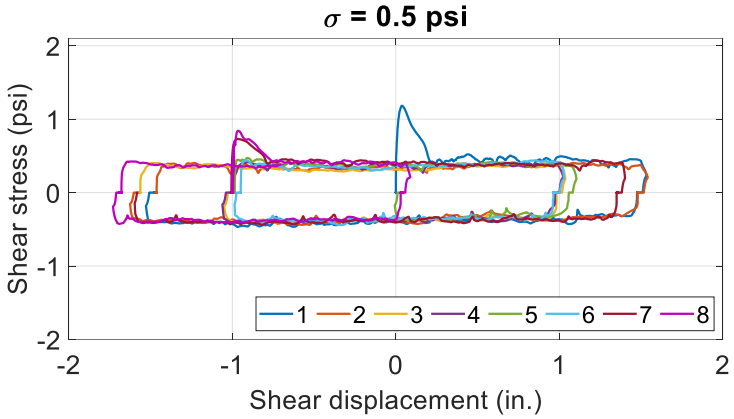

(a)

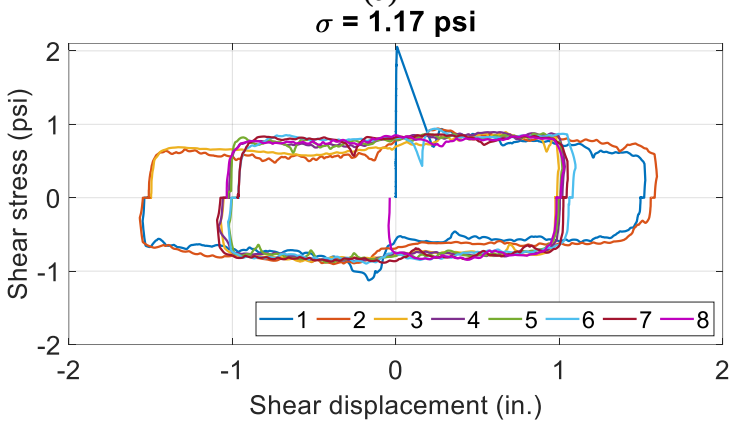

(b)

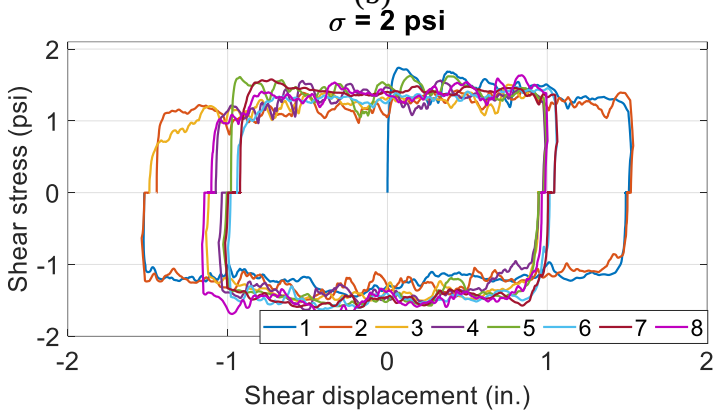

(c)

Figure 4.14: Cyclic shear stress-displacement relationship for felt paper on CSB (Sequence 1: 1.17 psi, 2 psi, 0.5 psi).

As shown in Figure 4.15(b), the peaks occurred when the normal stress was decreased from 2 psi to 1.17 psi and from 1.17 psi to 0.5 psi, while there were no obvious peaks when the tests were conducted with increasing normal stress levels, as shown in Figure 4.15(a). This was consistent with the prior observations. Although the extra concrete slabs were removed to reduce the normal stress level, the changes of the interface interaction components were not fully reflected in the first cycle. There were remaining effects of normal stress levels on the interface restraint.

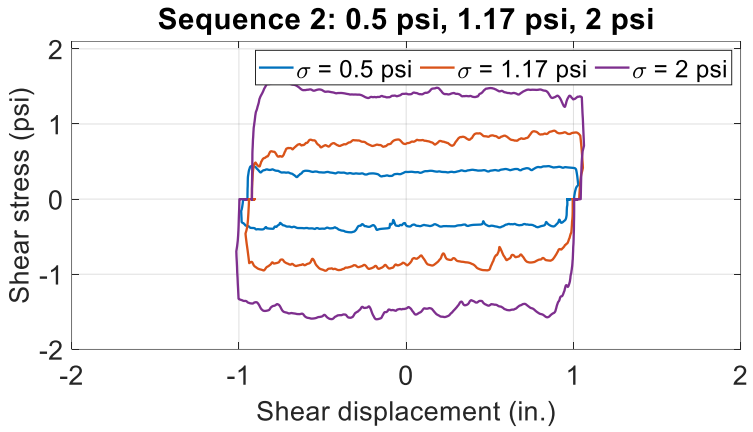

(a)

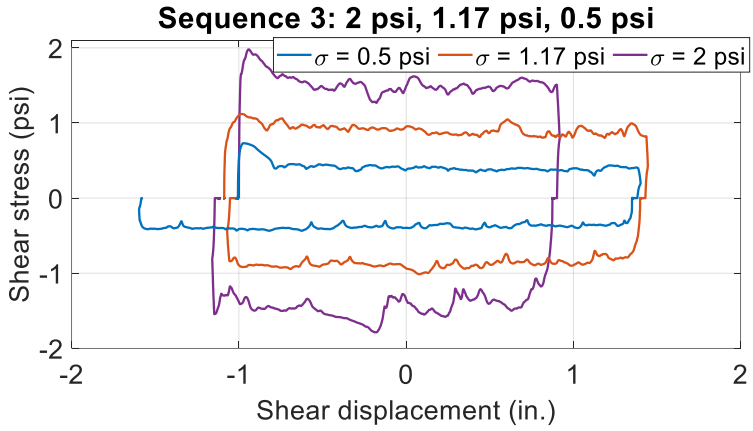

(b)

Figure 4.15: Effects of sequences of normal stress level for CSB with felt paper (Sequence 2 and 3).

It should be noted that there was a residual displacement in the reversed direction after unloading at the end of each half-cycle, as shown in Figure 4.14 and Figure 4.15. The interface was visually inspected after the completion of the cyclic tests by lifting the concrete slab, as shown in Figure 4.16. It was observed that the felt paper was tightly attached to the concrete slab, as shown on the left of Figure 4.16(a). There was some tearing of the felt paper, and small pieces spalled off from the felt paper as a result of the repeated cyclic movements, as shown in Figure 4.16(b). It also occurred in previous interface conditions of polyethylene sheets on CSB but with a much smaller value. The residual displacement may be possibly related to the accumulation of felt paper debris at the interface.

(a)

(b)

Figure 4.16: Visual inspection of the felt paper-CSB interface: (a) Felt paper attached to concrete slab; (b) Pieces of felt paper on CSB.

In order to further investigate this problem, an additional test was conducted after cleaning up the small pieces both on the concrete and CSB side, as shown on the right of Figure 4.16(b). Figure 4.17 compares the shear stress-displacement relations before and after cleaning the small pieces of felt paper. It was observed that the residual displacement almost disappeared. A possible explanation was that there were small local slopes due to the undulations of the CSB surface. Once the shear force was removed, the concrete slab slightly moved in the reverse direction due to the self-weight, which likely explained the small residual displacements for PE sheets. In the case of the felt paper, as the cyclic movements increased, the felt paper pieces spalled off and accumulated at the interface, which likely behaved as “rollers” and resulted in a larger reversed movement.

However, the shear strength at the interface was not significantly affected by the damage of the felt paper over cycles.

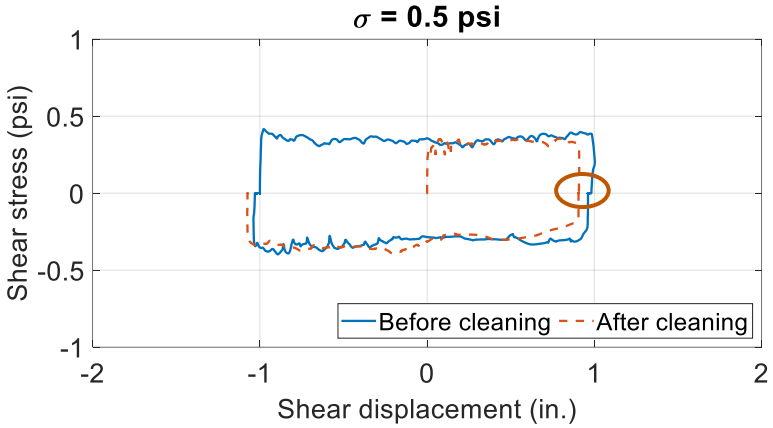

Figure 4.17: Effects of spalling pieces for CSB with felt paper.

Another interesting phenomenon was observed on the peak strengths over time. Figure 4.18 compares the shear stress-displacement relationship for the initial cycle and an intermediate cycle (at the same day), and the cycle after two weeks. The initial peak was attributed to the interlocking and initial adhesion at the interface. After a few cycles, there were no obvious peaks. However, the peak appeared after the specimens were sitting for a short period of time, which could possibly suggest that the adhesion built up at the CSB-felt paper interface over time. This was possibly related to the adhesive features of the felt paper. However, there were not significant variations of the steady shear strength over time.

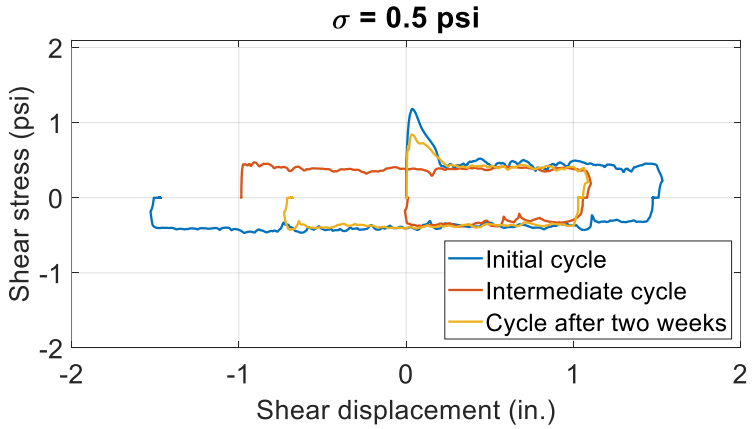

Figure 4.18: Peak strength over time for CSB with felt paper.

HMA with One Textured LLDPE Sheet

The cyclic shear stress-displacement relationship with normal stresses of 0.5 psi, 1.17 psi, and 2 psi normal stresses when a double-sided textured LLDPE sheet was used on CSB topped with a 1-in.-thick Type D HMA layer, are presented in Figure 4.19.

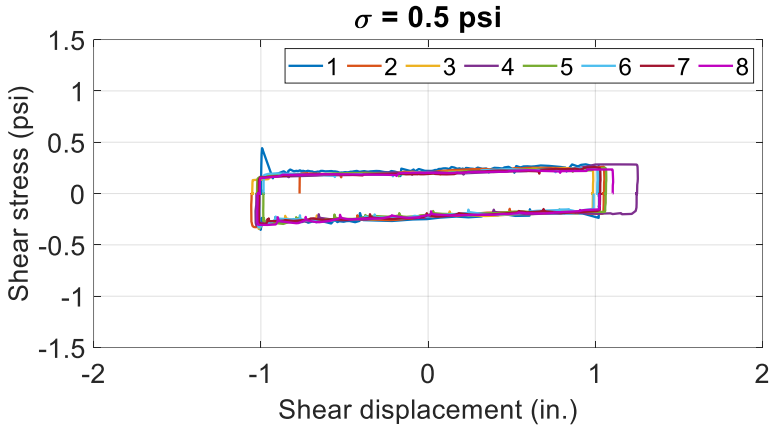

(a)

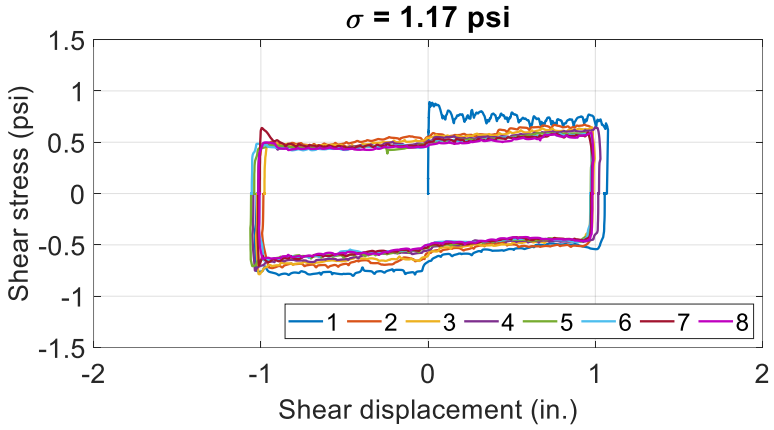

(b)

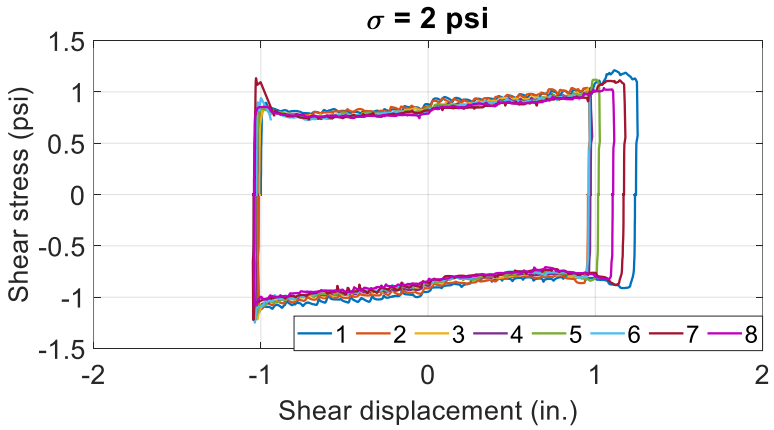

(c)

Figure 4.19: Cyclic shear stress-displacement relationship for HMA layer with a textured LLDPE sheet.

The same specimen was used in the subsequent push-off tests at different normal stresses with the normal stress testing order consisting of 1.17 psi, 2 psi, and 0.5 psi. The cyclic behavior for the HMA with a textured LLDPE sheet was very close to that for the CSB with a textured LLDPE sheet. The peak was observed in the initial cycle with a normal stress of σ = 1.17 psi. The shear

stresses gradually decreased for a few cycles, and there were no significant changes for the subsequent cycles of the tests.

One exception was that the peak strengths appeared again for the cycles that were conducted in a while from previous tests, as seen in the cycle 7 for σ = 1.17 psi and σ = 2 psi, and cycle 1 for σ = 0.5 psi. Similar phenomenon was observed for the felt paper on CSB, as shown in Figure 4.18. A likely source of the behavior attributed to the adhesive features of the felt paper, which was an asphalt-saturated material.

HMA with Felt Paper

The cyclic shear stress-displacement relationship with normal stresses of 0.5 psi, 1.17 psi, and 2 psi normal stresses when the felt paper was used on CSB topped with a 1- in.-thick Type D HMA layer, are presented in Figure 4.20.

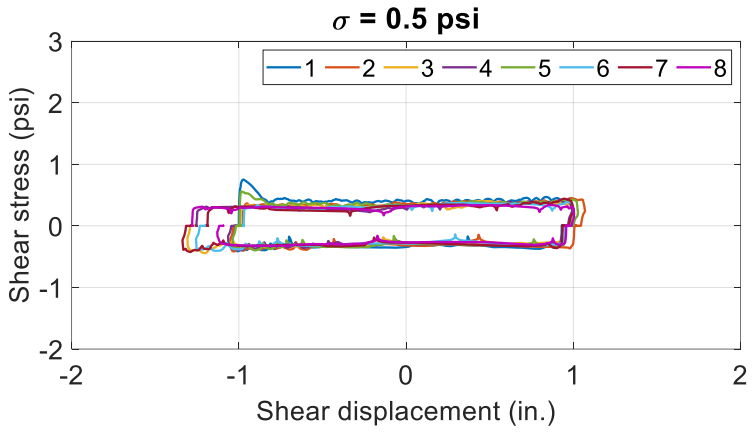

(a)

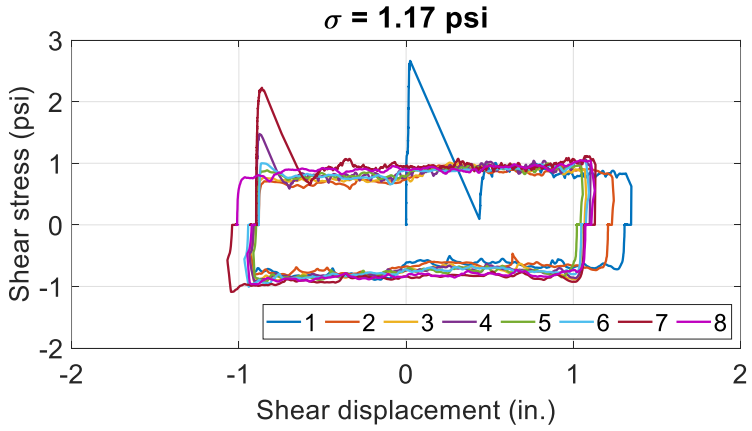

(b)

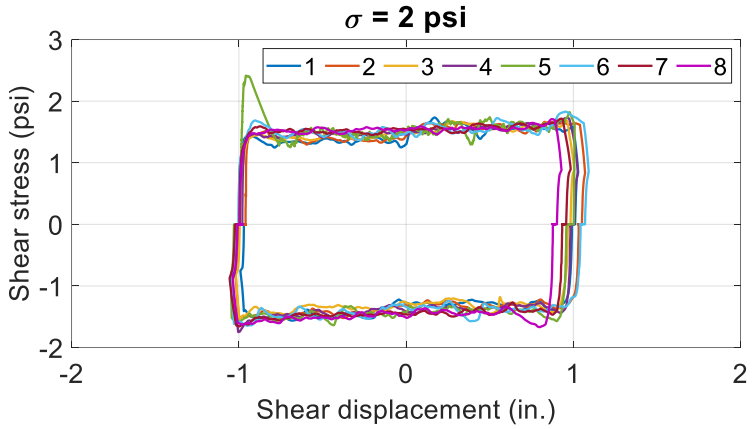

(c)

Figure 4.20: Cyclic shear stress-displacement relationship for HMA layer with felt paper.

The same specimen was used in the subsequent push-off tests at different normal stresses with a testing order consisting of 1.17 psi, 2 psi, and 0.5 psi. The cyclic behavior was very close to the CSB with felt paper. There was a significant peak in the initial cycle, which was attributed to the bond and interlocking at the interface. The peak strength was even higher than that for the CSB, which was likely due to a comparatively rougher surface of the HMA and adhesive features of the HMA itself. The built-up adhesion at the interface over time was more obvious than the felt paper on CSB or the textured LLDPE sheet on CSB topped with HMA layer, which was likely because that both felt paper and HMA layer were adhesive. The directional effects on the shear stresses in the forward and reverse directions were not obvious as compared to the PE sheets, which was likely due to a thicker texture of the felt paper. A relatively large residual displacement occurred as observed for the felt paper on CSB.

Figure 4.21(a) compares the steady shear strength envelopes between Series 7(a) and 7(b), in which Type B and Type D HMA was used under the felt paper, respectively. The shear strengths for each normal stress level agreed well with each other and the resulting coefficients of friction are relatively close.

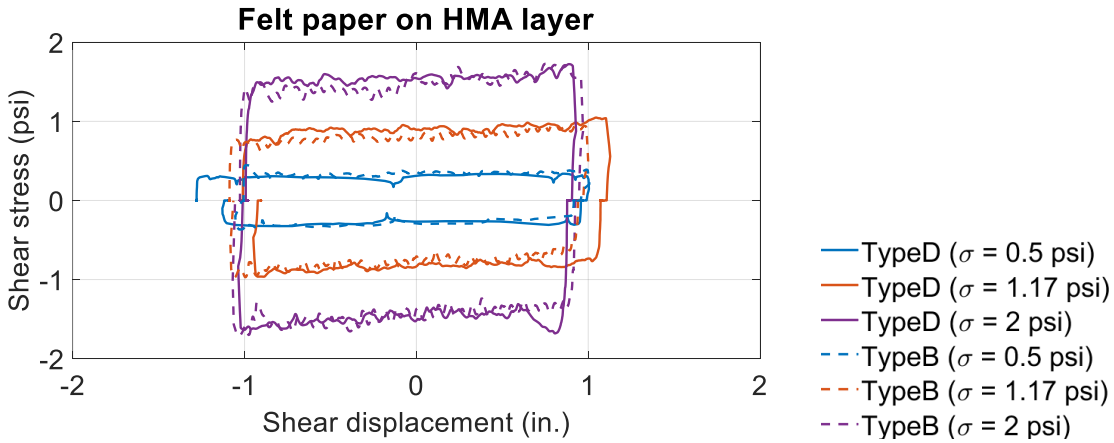

Figure 4.21: Effects of HMA type on the shear stress-displacement relations using a felt paper.

4.3.2 Interface Shear Strength and Friction Coefficients

Figure 4.22 plots the linearized steady shear strength envelope for the interfaces in Phase II using the Coulomb-friction model. As the figure shows, the linear regression line fits well with the test data, which indicates the absence of adhesion at the slab-base interface. The coefficient of friction is given by the slope of the linear regression line in Figure 4.22. The smooth PE sheets provided the lowest coefficient of friction (ranging from 0.2 to 0.3). The shear strength of one PE sheet was approximately 25% higher than the case with two sheets. With the small surface asperities of the spike HDPE sheet, the coefficient of friction increased slightly to a value of 0.3 compared to the smooth PE sheets. The use of a double-sided textured LLDPE sheet further increased the coefficient of friction to approximately 0.4. Felt paper provided a higher coefficient of friction (approximately 0.7) as compared to the polyethylene sheets. The coefficient of friction obtained with textured LLDPE and felt paper was slightly higher when the CSB surface was topped with a thin Type D HMA layer, as Figure 4.22 indicates. This effect was attributed to a rougher plane of the HMA surface in contact with the interface material as compared to the CSB.

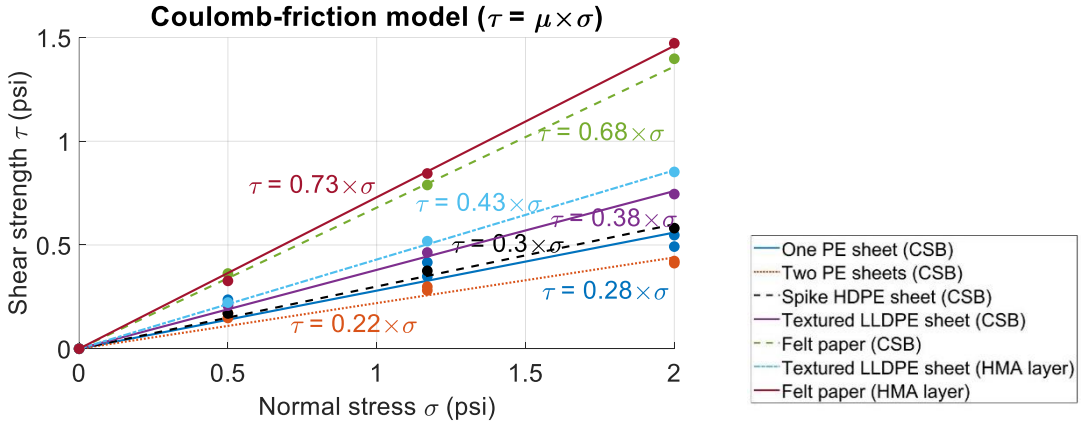

Figure 4.22: Phase II steady shear strength envelopes for different bond breakers.

As discussed previously, the Phase II series of push-off tests with one and two PE sheets were conducted with two different CSB specimens. This resulted in six sets of data points (σ, τ) per test series, two for each level of normal stress. The six data points obtained for each series are plotted together in Figure 4.22 to obtain the shear strength envelopes. The measured shear strength with each normal stress level was consistent between the two specimens. The consistency of the shear stress data indicated that the small variations in CSB textures did not significantly affect the coefficient of friction at the interface.

Figure 4.23 compares the steady shear strength envelope for Type D HMA and Type B HMA with felt paper. The shear strengths for each normal stress level agreed well with each other and the resulting coefficients of friction were relatively close. As shown in Table 3.2 and Table 3.3, the differences in the aggregate gradation and asphalt content between the thin HMA layer (Type D) and HMA base (Type D) are not significant. The results indicate that the concrete slab-thin HMA layer interface interaction on top of the CSB is equivalent to that of the concrete slab-HMA base for the same type of bond breaker.

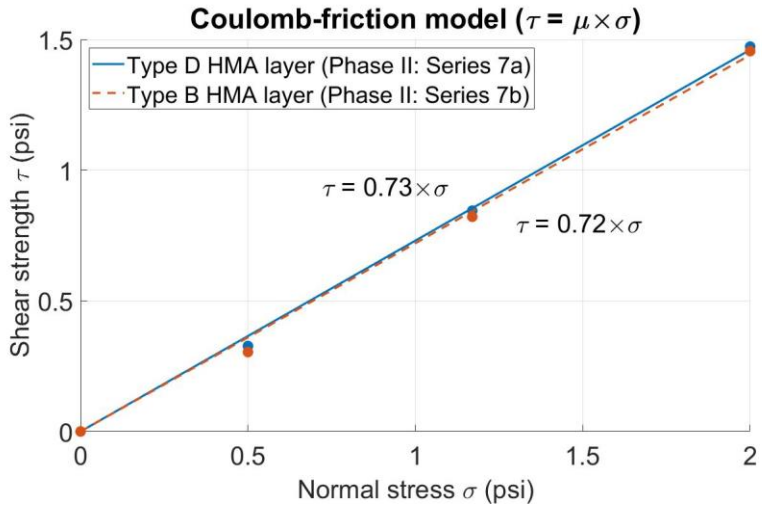

Figure 4.23: Effects of HMA type on the steady shear strength envelope using a felt paper.

4.3.3 Effects of Cyclic Movements

In Phase II, the effects of cyclic displacement histories that simulate the annual expansion-contraction cycles on the concrete slab-base interaction with different types of bond breakers were investigated. Figure 4.24 and Figure 4.25 plot the changes in shear strength obtained at different cycles of loading for different bond breakers on CSB and on CSB topped with a 1-in.-thick HMA layer, respectively.

The values of the peak and steady shear strength within each cycle are presented in Figure 4.24(a) and (b) for one and two smooth PE sheets, respectively. The peak strengths obtained for both the forward and reverse sliding movements are plotted for each cycle, as well as the average steady shear strengths in both directions. The peak shear strength in the initial cycle of the first test conducted at a normal stress of 0.5 psi was significantly higher than that in subsequent cycles. After five cycles, the peak shear strength stabilized, which can be attributed to a certain smoothing of the profile reducing the effects of interlock. Variation in the steady shear strengths with the number of cycles was insignificant and similar trends were observed for other bond breakers.

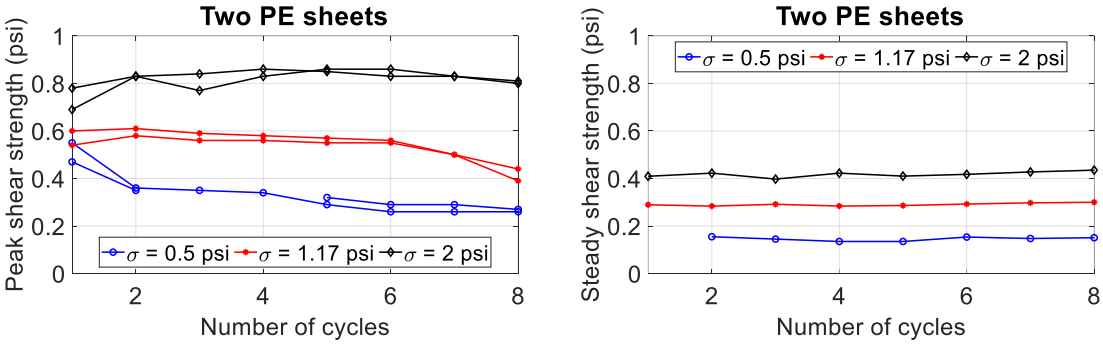

(a)

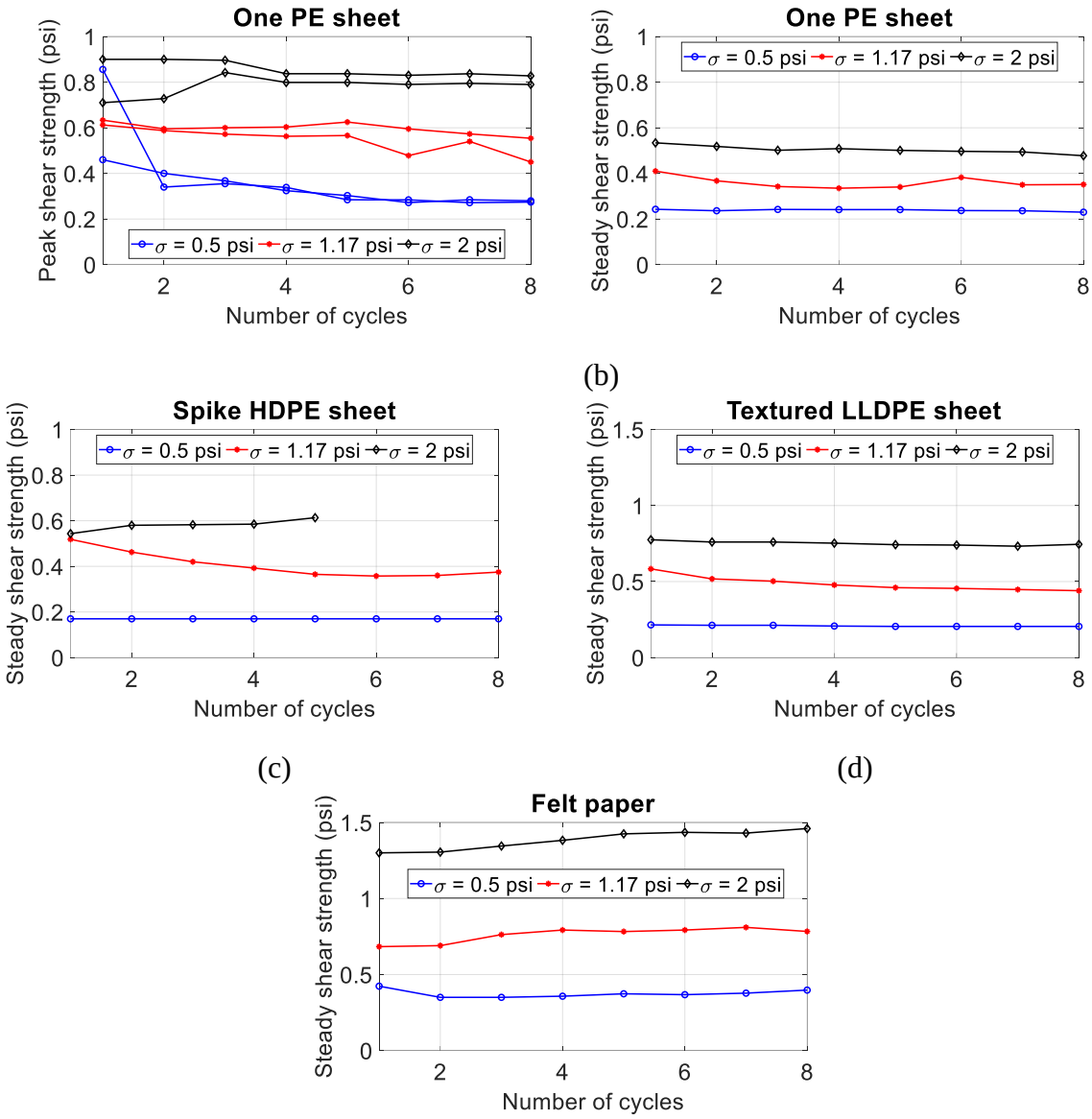

Figure 4.24: Effects of number of cycles on shear strengths for different bond breakers on CSB: (a) Two PE sheets; (b) One PE sheet; (c) Spike HDPE sheet; (d) Textured LLDPE sheet; (e) Felt paper.

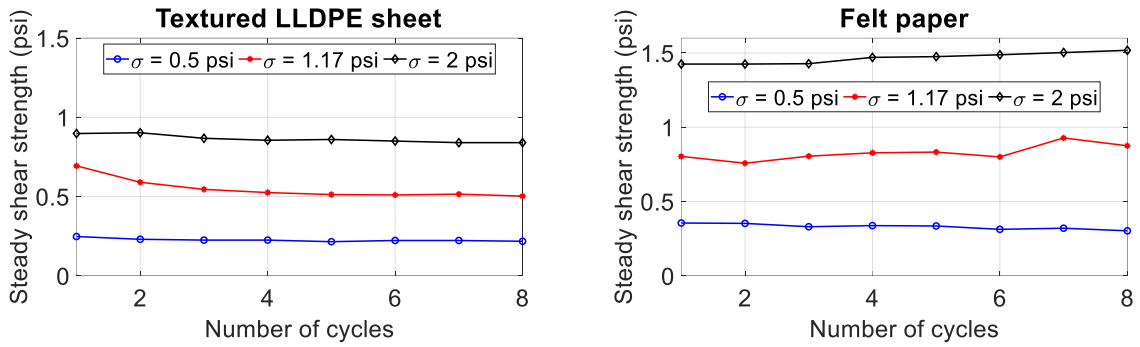

(a) (b)

Figure 4.25: Effects of number of cycles on shear strengths for different bond breakers on CSB topped with a thin HMA: (a) Textured LLDPE sheet; (b) Felt paper.

4.3.4 Effects of Scale

As previously stated, one and two layers of smooth PE sheets on CSB were tested in both Phase I and Phase II. The dimensions of the concrete specimens increased from 15 in. × 15 in. × 3 in. in Phase I to 60 in. × 24 in. × 6 in. in Phase II, which is an increase of more than 540% in the contact surface area. The steady shear strength envelopes were plotted together in Figure 4.26 for comparison. The steady shear strengths observed in Phase II were approximately 25% to 30% higher than those observed in Phase I. These differences are attributed to the rougher finished surfaces of the bases as well as the larger contact surface areas leading to increased interlock in Phase II. Due to the small-scale specimens used in Phase I, the CSB was compacted via a metal tamper plate driven by a jackhammer, which may have resulted in fewer surface undulations. In Phase II, compaction was carried out with several passes of a plate compactor, which produced surfaces that are likely more consistent with those found in practice. While the Phase I unit-cell direct shear tests were useful in providing a preliminary characterization of interface restraint for different bond breakers, the Phase II large-scale push-off tests are considered more representative of field conditions and thus provide a more accurate characterization of the slab-base interaction.

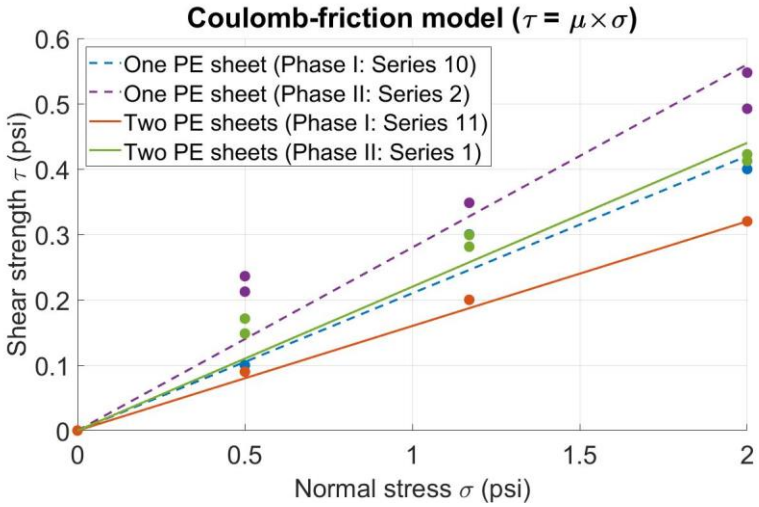

Figure 4.26: Steady shear strength envelope for different scales.

4.3.5 Sliding Planes

Table 4.3 summarizes the sliding (failure) planes for the different interface materials in Phase II.

Table 4.3: Phase II sliding planes

Interface material (base)	Sliding plane
Two smooth PE sheets (CSB)	Between two sheets
One smooth PE sheet (CSB)	Initially, sheet-base; after a few cycles, sheet-CIP concrete.
Single-sided spike HDPE sheet (CSB)	
Double-sided textured LLDPE sheet (CSB/HMA)	Sheet-base
Felt paper (CSB/HMA)	Felt paper-base

As shown in Table 4.3, sliding in specimens with a double-sided textured LLDPE sheet occurred between the base and interface material given that the interface with CIP concrete achieved some level of bond when concrete was cast against the interface material. Specimens with a single PE and HDPE sheets also exhibited initial slip at the sheet-base interface, but ultimately slid between the sheet and CIP concrete due to the deterioration of the bond. Specimens with a single PE sheet exhibited initial slip at the sheet-base interface, but ultimately slid between the sheet and CIP concrete due to the deterioration of their bond. For CSB or HMA layer with a felt paper, the sliding plane was the interface between the CSB and felt paper.

4.3.6 Visual Inspection of Post-Test Interface Conditions

In Phase II, the interface surfaces were visually inspected after the cyclic tests were completed, as shown in Figure 4.27. For the CSB with smooth PE sheets, wrinkles and tearing were observed at several locations of the sheet, and the CIP concrete specimen was completely unbonded from the sheet and its bottom surface was relatively smooth, as shown in Figure 4.27(a). Local unevenness on the bottom surface of the concrete slab reflected the matching profile of the base surface. As shown in Figure 4.27(b) and (c), the spike HDPE sheet and textured LLDPE sheet presented significantly less damage, owing to the relatively larger thickness and density. Hence, the spike HDPE and textured LLDPE sheets are expected to provide the best performance not only in terms of interface strength but also durability among the investigated polyethylene sheets. For the CSB with felt paper, the felt paper was bonded tightly to the concrete slab with some tearing while small spalling pieces of felt paper were observed, as shown in Figure 4.27(d). Similar tearing and paper spalling were observed for the felt paper on CSB topped with a thin HMA layer, as shown in Figure 4.27(e). The spalling pieces were attached to the HMA surface due to the adhesive condition of both the felt paper and HMA. Overall, the effects of the cyclic movements on the interface restraint were insignificant despite the observed damages to the bond breakers.

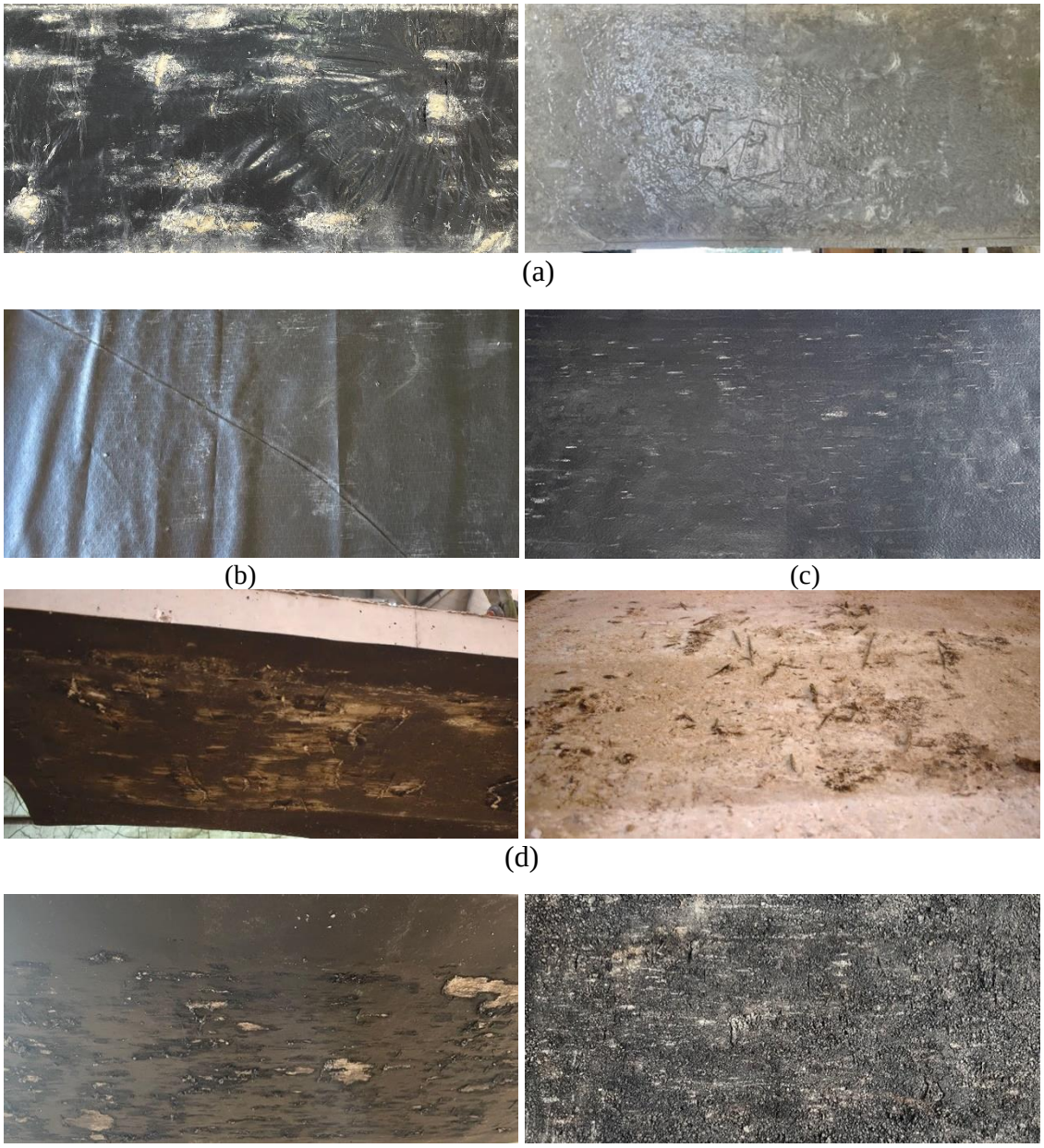

Figure 4.27: Visual inspection of bond breakers after cyclic tests: (a) Smooth PE sheet; (b) Spike HDPE sheet; (c) Textured LLDPE sheet; (d) CSB with felt paper; (e) HMA with felt paper.

To reflect significant long-term damage to the bond-breaker that may happen over the service life of the seamless bridge, an extreme condition was idealized in which the bond-breaker was completely removed. Such a test simulates extreme damage where the bond breaker was to be totally eroded in places. For the specimen with the polyethylene sheet on the CSB, the specimen was lifted and the sheet was removed. The pavement was then tested with concrete on the CSB base. For this specimen, the friction coefficient changed from 0.28 to 0.51. While the coefficient of friction of approximately 0.50 is representative of the conditions that might occur long-term, additional studies on the long-term performance are likely prudent.

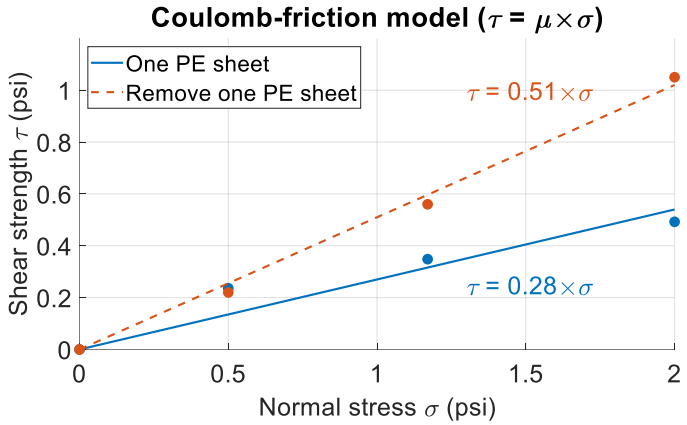

Figure 4.28: Comparison of shear strength envelopes after removing one PE sheet.

4.4 Summary

The concrete slab-base interaction, which significantly affects the behavior and design of the seamless bridge-CRCP system, was experimentally characterized through a comprehensive two-phase experimental program: Phase I unit-cell direct shear tests and Phase II large-scale push-off tests. This chapter presents the Phase II tests which provided comprehensive experimental data about the response of candidate interface conditions for the transition slab of the seamless system. The bases included in the testing program were CSB and CSB topped with a thin HMA layer, which are commonly used in the U.S. under CRCP. The interface materials included one or two smooth PE sheets, spike HDPE sheet, textured LLDPE sheet and felt paper. The tests provided data on the cyclic shear stress versus displacement (with a magnitude of 1 in.) relationships of the different interfaces when subjected to three normal stress levels of 0.5 psi, 1.17 psi, and 2 psi, representing the weight of a 6-in.-, 14-in.-, and 24-in.-thick concrete pavement, respectively. The coefficients of friction for each interface were determined based on a Coulomb-friction model. The effects of cyclic displacements on the shear strengths were investigated. Post-test interface conditions were examined by a visual inspection. The main conclusions of Phase II results are summarized as follows:

- The use of polyethylene sheets and felt paper eliminated the adhesion at the interface. These interface materials presented $\tau - \sigma$ relations that could be represented well with the classic Coulomb-friction model. The coefficient of friction at large displacements provided by these bond breakers is listed in descending order, as follows: felt paper (approximately 0.7); textured LLDPE sheets (approximately 0.4); spike HDPE sheets (approximately 0.3); and smooth PE sheets (approximately 0.25).
- The concrete specimen-base interfaces with effective bond breakers presented a shear stress-displacement response characterized by a peak shear strength followed by a drop to a large-displacement shear strength. The contributions to peak interface shear strength can be attributed to two sources: 1) an interlocking effect due to the matching profile of the fresh concrete and base generated during casting; and 2) different levels of adhesion of the interface material to the base. The magnitude of peak strength was found to decrease after the first cycle of loading due to the abrasion of the interface, while the shear strength at large displacements was essentially independent of the number of cycles.

- Small wrinkles, tearing, and spalling of interface materials were observed by the visual inspection after the tests. There were fewer damages to the textured LLDPE sheet and spike HDPE sheet than to the smooth PE sheet due to the increased thickness and density. Overall, despite the damage to the interface materials, the cyclic behavior was repeatable after a few cycles.
- Based on their ability to eliminate adhesion and their adequate range of friction coefficients, felt paper and double-sided textured LLDPE sheets have been identified as adequate bond breakers for the transition slab in seamless bridge-CRCP systems.

5. Numerical Modeling of the Axial Response of Seamless Bridge-Pavement Systems (Task 5)

5.1 Overview

The behavior of the seamless bridge-pavement system was investigated through numerical modeling. Although full-scale experiments of a bridge with seamless connection are desirable, such experiments are not practical in a laboratory setting. Although the research study that this technical memorandum is a part of, does include plans to instrument and monitor a bridge in the field, a bridge for such a study has yet to be identified. Therefore, the use of numerical models provides valuable insight into the system behavior that can later be confirmed with data from a field instrumentation. The data from these computer-based numerical models provides important guidance on future design of seamless bridge-pavement systems.

This chapter presents analysis results of the axial (longitudinal) response of the seamless system through finite element (FE) modeling. Nonlinear FE models of the entire seamless bridge-pavement system were developed to study the interaction between the bridge structure, the CRCP and the pavement base due to thermal contraction and expansion of the bridge and the pavement, and concrete shrinkage. Due to this interaction, tensile and compressive forces are introduced in the transition slab. This interaction also modifies the distribution of longitudinal forces within the bridge structure. Numerical models were developed for prototype bridge-pavement systems, and parametric studies were conducted to identify the main characteristics affecting the transition length and the amount of reinforcement required in the transition slab. The parameters investigated include the coefficient of friction at the concrete slab-base interface, reinforcement ratio and slab thickness of the transition zone, and temperature change. A series of axial analyses were also conducted for standard bridges in Texas with various bridge configurations, including the span length, number of spans, number of girders, and girder size. The potential design issues related to the seamless bridge connection for standard bridges and CRCPs in Texas were identified based on the results of these analyses. Based on the results of experimental testing and numerical studies, proper bond breakers under the transition zone for a seamless system were recommended. The numerical models were also used to investigate the seamless connection concept for jointed concrete pavement or flexible pavement.

5.2 Development of the FE Model

5.2.1 General Modeling Scheme

The finite element models of the entire seamless bridge-CRCP system with axial loading were developed using the commercial FE package Abaqus (Abaqus, 2017). Nonlinear static analyses were performed with Abaqus/Standard to account for nonlinearities in the material and concrete slab-base interface responses.

Figure 5.1 shows a scheme of the proposed FE model for studying the axial behavior of the seamless bridge-CRCP system. The various structural components that lead to restraint in the longitudinal direction of the slab/bridge are represented as a spring element. Assuming a symmetric configuration of the bridge-pavement system with respect to the center of the bridge, and thus a symmetric response with respect to this same point, only half of the entire system was modeled. As shown in Figure 5.1, using a three-span bridge as an example, the FE model included

half of the bridge, a transition zone comprising of a transition slab and an approach slab, and the pavement-base interaction.

All the bridge elements contributing to the axial response of the seamless system were accounted for, including the bridge decks over girders, link slabs between two adjacent simply supported spans, prestressed concrete girders, bearings, and pier columns. Fully composite behavior was assumed between the girders and decks. The abutment and pier foundations were treated as rigid foundation elements due to very large stiffnesses in the longitudinal direction.

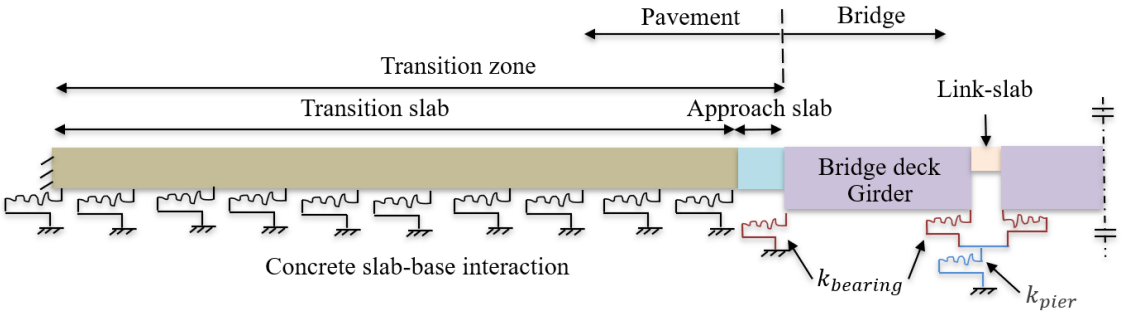

Figure 5.1: A scheme of the structural model for the seamless system with axial loading.

To study the axial response of the entire seamless system, one-dimensional (1D) models employing line elements and springs were developed to achieve a computationally efficient analysis. Two-node linear line elements (T2D2) were used to model the axial behavior of the bridge superstructure and the pavement. Truss elements were used to model the reinforcing steel and concrete separately for the reinforced concrete elements, including the pavement, bridge decks, and link slabs to consider their longitudinal contributions. A perfect bond was assumed between the steel and the concrete. The shear stiffness of the bearings was represented with linear springs. The pier columns were represented as linear springs with an equivalent stiffness for translational movements. Nonlinear springs were used to model the concrete slab-base interaction (friction) in the shear direction within the transition slab. The concrete slab-base interaction was ignored for the approach slab considering the separation from the base with the differential embankment settlement.

The bridge girders were assumed to remain elastic and were modeled using the gross section properties considering no cracking under service conditions. This assumption was deemed appropriate due to the beneficial effects of the girder prestressing that extends the useful life of the tensile regions of the girder. Nonlinear material constitutive laws of concrete were used to capture the cracking response of the transition zone and bridge decks. An elastic-perfectly plastic model was used for the reinforcing steel.

A uniform mesh size of 3 in. was used. The translational movements in both longitudinal and vertical directions were restrained at the end of the transition zone. At the other end of the model, i.e., the center of the bridge, boundary conditions that only allowed the symmetrical translations were applied due to the symmetry of the structural configurations and loadings. The axial effects are possibly due to the temperature changes, concrete shrinkage and creep effects.

5.2.2 Material Modeling

The concrete damaged plasticity model was used to represent the nonlinearity of the concrete. The model uses a plasticity-based, damage model to represent concrete tensile cracking and compressive crushing (Abaqus User's Manual, 2017). For simplicity, in this technical memorandum, only the plasticity of concrete was considered without defining the damage variables for compression and tension. Figure 5.2 plots the nonlinear uniaxial compressive and tensile stress-strain laws used for the concrete model. The concrete compressive law is based on the Thorenfeldt's curve (Thorenfeldt et al., 1987). The concrete compressive stress-strain relationship is given by Eq. 5.1:

$$f_c = f_c' \times \frac{n\left(\frac{\varepsilon_c}{\varepsilon_c'}\right)}{n-1+\left(\frac{\varepsilon_c}{\varepsilon_c'}\right)^{nk}}, \quad \text{Eq. 5.1}$$

in which:

$n = 0.8 + \frac{f_c'}{2500}$,

$\varepsilon_c' = \frac{n}{n-1} \times \frac{f_c'}{E_c}$,

$E_c = 40000\sqrt{f_c'} + 1000000$,

$k = \begin{cases} 1, & |\varepsilon_c| < \varepsilon_c' \\ 0.67 + \frac{f_c'}{9000} \geq 1, & otherwise \end{cases}$,

where:

f_c = concrete compressive stress (psi),
ε_c = concrete compressive strain,
f_c' = concrete compressive strength (psi),
n = curve fitting factor,
ε_c' = strain corresponding to f_c',
E_c = modulus of elasticity (psi),
k = factor describing the post-peak decay.

The concrete tensile stress-strain model used in this technical memorandum was proposed by Vecchio and Collins (1986), as shown in Eq. 5.2. Prior to the cracking of concrete, a linear elastic behavior is assumed with the same modulus of elasticity as that for compression. For cracked reinforced concrete, the concrete between cracks can carry post-cracking tensile stresses due to the interaction with the reinforcement, which are referred to as tension-stiffening effects (Lin, 2010). In this model, tension-stiffening effects are considered by defining the nonlinear post-failure strain-softening behavior.

$$f_t = \begin{cases} E_c\varepsilon_t, & 0 \leq \varepsilon_c \leq \varepsilon_{cr} \\ \frac{f_t'}{1+\sqrt{c_T\varepsilon_t}}, & \varepsilon_c \geq \varepsilon_{cr} \end{cases}, \quad \text{Eq. 5.2}$$

where:

f_t = concrete tensile stress (psi),
ε_t = concrete compressive strain,
f_t' = concrete tensile strength (psi),
ε_{cr} = concrete cracking strain ($\varepsilon_{cr} = \frac{f_t'}{E_c}$),

c_T = factor controlling tension stiffening ($c_T = 200$).

Eq. 5.3 shows the conversion between the concrete tensile strength and compressive strength for different conditions, where f_c' and f_t' are expressed in psi. Generally, Eq. 5.3(a) and (b) are used for concrete subjected to pure tension and pure flexure, respectively. In this technical memorandum, Eq. 5.3(c) defines a tensile strength within the range of values that might be used based upon either pure axial tension or pure flexure, which was deemed reasonable for the components where concrete is subjected to combined axial and flexural effects. Eq. 5.3(a) was used to determine the concrete tensile strength of the transition pavement, bridge decks and link slabs for the axial analysis of the entire system.

$$f_t' = \begin{cases} 4\sqrt{f_c'},\ pure\ tension, & \text{Eq. 5.3(a)} \\ 7.5\sqrt{f_c'}, pure\ flexure, & \text{Eq. 5.3(b)} \\ 6\sqrt{f_c'}, tension - flexure. & \text{Eq. 5.3(c)} \end{cases}$$

The concrete damaged plasticity model describes the stiffness degradation of concrete by defining the damage parameter d, which has the value ranging from zero (no damage) to one (complete damage). The degraded unloading/reloading stiffness of concrete is defined as $E = (1 - d)E_c$, where E_c is the initial stiffness of concrete without damage. The weakened unloading response of concrete in compression and tension is also shown in Figure 5.2(a) and (b), respectively. The compressive and tensile damage parameters d_c and d_t (Zheng et al., 2016) are defined in Eqs. 5.4(a) and (b), separately, as follows:

$$d_c = 1 - \frac{f_c}{E_c \varepsilon_c^{pl}\left(\frac{1}{b_c} - 1\right) + f_c}, \quad \text{Eq. 5.4(a)}$$

$$d_t = 1 - \frac{f_t}{E_c \varepsilon_t^{pl}\left(\frac{1}{b_t} - 1\right) + f_t}. \quad \text{Eq. 5.4(b)}$$

where b_c and b_t is the ratio of plastic strain ε^{pl} to inelastic strain ε^{in} for concrete in compression and tension, respectively. b_c was taken as 0.7 (Birtel and Mark, 2006), assuming that most of the inelastic compressive strain is maintained after unloading. Once concrete tensile damage initiates, the stiffness significantly reduces with a small residual strain (Birtel and Mark, 2006). In this study, b_t was taken as 0.2 to keep residual strains small upon crack while avoiding numerical convergency issues.

The input parameters to the concrete damaged plasticity model included inelastic strains for tension and compression, which are defined as the total strain minus the elastic strain corresponding to the undamaged material. Five additional parameters are required to define the yield surface in multi-axial stress conditions (dilation angle, flow potential eccentricity, ratio of initial biaxial compressive yield stress to initial uniaxial compressive yield stress, ratio of the second stress invariant on the tensile meridian to the compressive meridian at initial yield, and visco-plastic regularization parameter). The values taken for those parameters are described in detail in Section 6.2.2, where the concrete is subjected to two-dimensional stresses. In the current analysis, concrete is subjected to uniaxial compression/tension and therefore the response is

independent of these five parameters. Finally, the coefficient of thermal expansion of concrete was taken as 6.5×10^{-6}/°F.

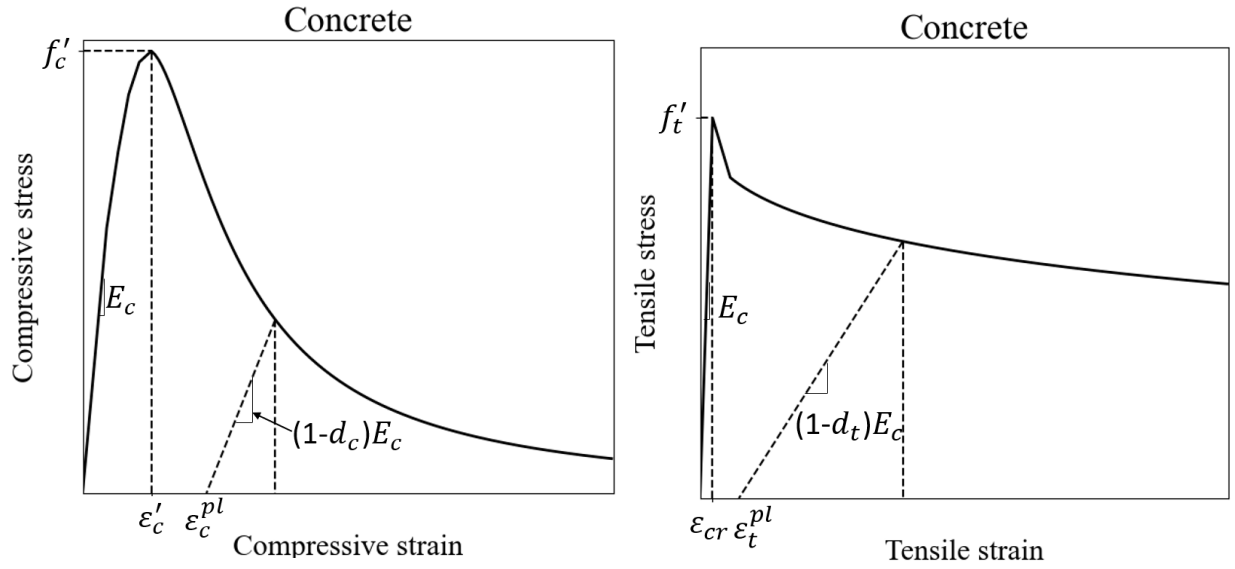

(a) (b)

Figure 5.2: Concrete constitutive laws with damage: (a) Compression; (b) Tension.

A bi-linear elastic perfectly plastic stress-strain relationship was used for reinforcing steel. As shown in Figure 5.3, the stress-strain relationship features an elastic region (modulus of elasticity: 29000 ksi) up to the yield strain ε_y and yield stress f_y, following a plateau, which represents the yielding stage. The coefficient of thermal expansion for steel was taken as 6.5×10^{-6}/°F.

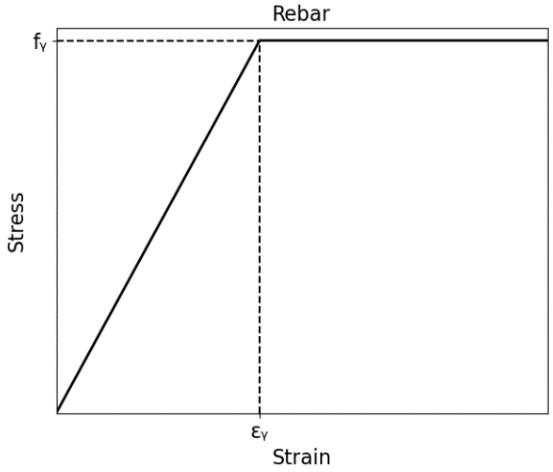

Figure 5.3: Reinforcing steel constitutive law.

5.2.3 Concrete Slab-Base Interaction

The studies on the concrete slab-base interaction considered the effect of the bond breakers based on the experimental investigations were outlined previously in Chapters 3 and 4. Specifically, the interface response at the concrete slab-base interface with the use of the most promising bond breakers, i.e., felt paper and double-sided textured LLDPE sheet, are characterized by an initial

cycle in which the shear stress-displacement relation consists of an increasing branch up to the peak and a small drop followed by a plateau. For the subsequent cycles, the relationship generally consists of a plateau without an obvious peak.

To model the frictional characteristics at the concrete slab-base interface with bond breakers, the shear stress-displacement relationships obtained from the experimental testing were simplified to a tri-linear curve for the initial cycle and a bi-linear curve for the subsequent cycles, as shown in Figure 5.4(a) and (b), respectively. The values of the peak shear strength, τ_p, the steady shear strength, τ_s, the displacement for initial sliding, u_0, and the displacement corresponding to the onset of the steady stage, u_s, were identified from the experimental results as presented in Chapter 4. The simplified multi-linear shear stress-displacement relationships are able to capture the major characteristics of the friction and adhesion/interlock for the first cycle, and primarily friction for the subsequent cycles.

Springs elements were used to simulate the nonlinear responses shown in Figure 5.4 in the tangential direction at the concrete slab-base interface. The shear stress-displacement relations obtained from testing were converted into shear force-displacement relations based on the tributary area of slab represented by an individual spring.

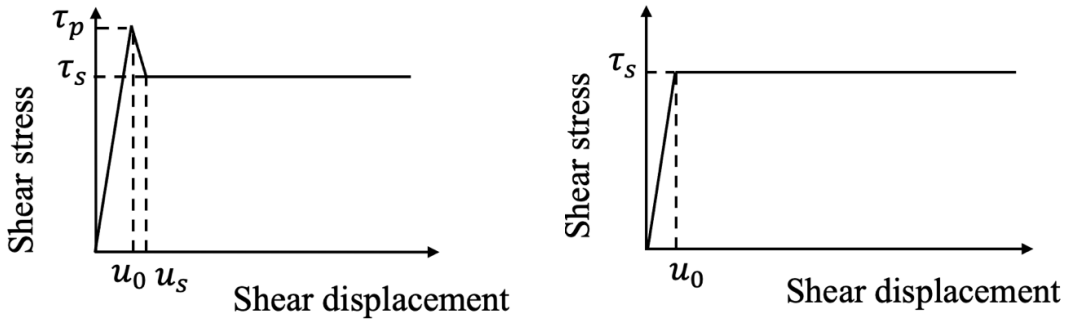

(a) (b)

Figure 5.4: Simplified concrete slab-base interaction with bond breakers: (a) Initial cycle; (b) Subsequent cycles.

5.2.4 Boundary Conditions

The following boundary conditions were applied at the center of the bridge and the end of the transition zone. The translational movements in the longitudinal direction at the right end of the model representing the middle point of the bridge were restrained, taking advantage of the symmetry of the system. On the pavement side, it is anticipated that the movements of the pavement due to the thermal movements of the bridge and pavement itself is completely dissipated at a sufficient distance from the bridge end. The concrete pavement beyond the transition zone can be treated as conventional CRCP, in which thermal movements are distributed among closely spaced transverse cracks without moving longitudinally. Two possible boundary conditions at the end of the pavement were considered, as shown in Figure 5.5.

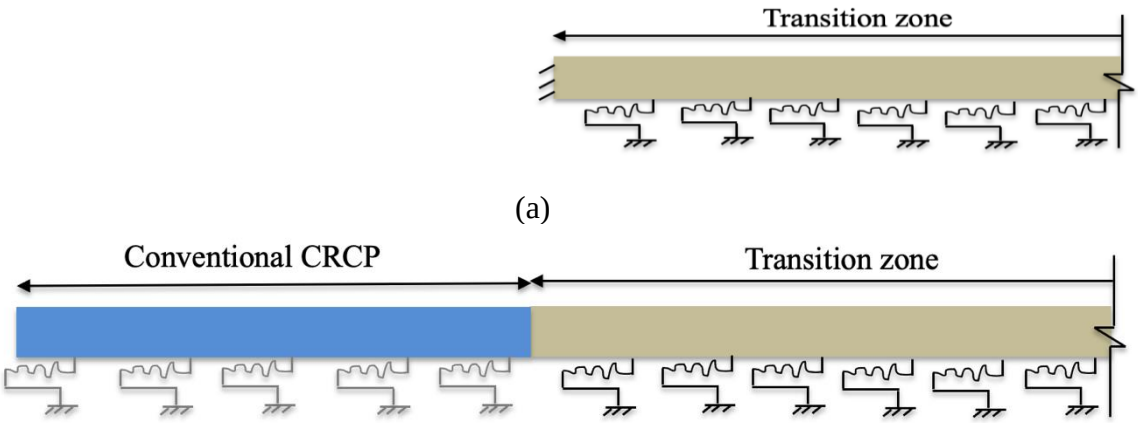

Figure 5.5: Two boundary conditions at the pavement side: (a) Transition zone with restrained translational movements; (b) Transition zone connected with CRCP.

For the case in Figure 5.5(a), the translational movements at the end of the transition zone are restrained to represent the zero-displacement status. The case in Figure 5.5(b) is a direct representation of real conditions, which models a conventional CRCP at the end of the transition zone. For modeling purposes, only a limited length of the conventional CRCP beyond the transition zone was included. Bond breakers were only used for the transition zone, whereas the interface shear strength for the conventional CRCP was assumed strong. The effects of the two boundary conditions on the axial response of the seamless system were investigated and are presented in Section 5.4.2.

5.2.5 Loading Considerations

The actions to be considered for a seamless bridge-CRCP system mainly included imposed deformations due to daily and seasonal temperature changes and concrete shrinkage. Since the seamless system involves both the bridge structure and pavement, design specifications for the bridge and pavement were reviewed to determine the magnitude of these actions.

Uniform temperature changes were assumed in the pavements without considering the impact of temperature gradient through the thickness, which are likely insignificant. The temperature variations that an element experiences are determined by the instantaneous ambient temperature at a given time relative to the concrete placement temperature when the closure-pour is made. TxDOT Item 422 Concrete Superstructures and Item 360 Concrete Pavement in Standard Specifications for Construction and Maintenance of Highways, Streets, and Bridges (2014, TxDOT) require placing concrete only when the placement temperature is between 50°F and 85°F for the bridge superstructure, and between 40°F and 95°F for the pavement. According to the AASHTO LRFD Bridge Design Specifications (2020), the design ambient temperatures are considered to vary in the range of 30°F to 110°F for bridges. TxDOT CRCP-ME Design Software (Ha et al., 2012) considers the ambient temperature in a range from 40°F to 120°F for concrete pavements.

Table 5.1 summarizes the design ambient temperature range, and concrete placement temperature range as specified for the bridge and pavement. The corresponding maximum temperature increase

and decrease are also provided. The maximum temperature increase is expected to occur in summer when the concrete is placed during winter, which is calculated as the upper bound of the ambient temperature minus the lower bound of the concrete placement temperature. In contrast, the maximum temperature decrease is correspondingly calculated as the difference in the lower bound of the ambient temperature relative to the upper bound of the concrete placement temperature.

Table 5.1: Specifications of the design temperature range for pavement and bridge.

	Ambient temperature (°F)	Concrete placement temperature (°F)	Max. increase ΔT (°F)	Max. decrease ΔT (°F)
Pavement	50-120	40-95	80	-45
Bridge	30-110	50-85	60	-55

The temperature requirements for the bridge and pavement as per the various design specifications have some differences. The deviations in the thermal considerations for design are likely due to the differences in structural types, structural functions, construction requirements, and other factors. Considering the extremes for the placement temperature relative to the maximum design values for bridge/pavement expansion produces a maximum temperature increase of 80°F for pavements and 60°F for bridges. Similarly, for contraction in the bridge/pavement, it produces a maximum temperature decrease of 45°F for pavements and 55°F for bridges. Generally, a worst-case scenario was assumed in this study with a maximum temperature increase of 80°F and a temperature decrease of 55°F for both the pavement and bridge in the analysis and design of a seamless bridge-pavement system. This assumption was further investigated and confirmed in Section 5.5.5, where the axial responses were examined when the thermal loadings differed between the pavement and bridge.

Restrained concrete shrinkage is another source of concrete cracking. Concrete volume shrinkage consists of plastic shrinkage, autogenous shrinkage, and drying shrinkage, among which the drying shrinkage is the most dominant component (Yousefpoursadatmahalleh, 2015). Restraint from the base material and the reinforcing steel, differential shrinkage strains between the concrete cast-in-place (CIP) decks and other precast members results in tensile stresses in the concrete. Ge et all. (2021) instrumented and monitored the response of four bridges during and post-construction, which showed that the restrained concrete shrinkage is the dominant factor for the bridge deck crack initiation. AASHTO LRFD Bridge Design Specifications (2020) assume the concrete drying shrinkage strain after one year to be -0.5×10^{-3}. TxDOT CRCP-ME Design Software (Ha et al., 2012) considers the ultimate drying shrinkage for CRCP in the range of -0.7×10^{-3} to -0.4×10^{-3}. Concrete may shrink some amount for both the bridge and pavement before they are seamlessly connected. In this study, a drying shrinkage of -0.5×10^{-3} was explicitly applied for the concrete pavement and bridge CIP decks. The drying shrinkage was ignored for precast girders assuming that concrete shrinkage is almost complete before casting the composite concrete bridge deck.

Another time-dependent effect of concrete is creep, which is defined as the increase in strain with constant compressive stresses. Concrete creep effects in precast girders were ignored in this study

assuming that most creep deformations in the girders are small after placement and curing of the bridge deck.

Depending on the loading conditions, different concrete models were used. In the case of temperature change only, the concrete elements are subjected to monotonic loading. The axial behavior of the seamless system is not affected by the concrete stiffness degradation. To save computational costs, only the plasticity of concrete was considered for those analyses.

It should be mentioned that in the case of concrete shrinkage and temperature decrease, the concrete is in tension when the concrete is subjected to shrinkage and the tensile strain continues to increase due to the subsequent temperature decrease. As a result, monotonically tension loading is expected for concrete elements and thus the plasticity of concrete was considered only. In the case of concrete shrinkage and temperature increase, the concrete is tension due to shrinkage and the subsequent temperature increase will cause the unloading of concrete followed by the reverse loading in compression. To represent the concrete behavior with stiffness degradation, damage parameters for concrete in compression were defined.

5.3 Analysis of Prototype Seamless Bridge System in Australia

A seamless bridge-CRCP prototype system designed in Australia was analyzed with the modeling strategy proposed in Section 5.2. The system with seamless connection for a typical 393-ft.-long bridge was previously analyzed by Bridge et al. (2005) using a simple elastic model. Gross composite section properties were used for bridge elements and pavements in compression. For concrete in tension, after cracking, the tension-stiffening effects were taken into account by increasing the elastic modulus of the steel as a uniform smeared stiffness over the full length of the reinforcement between cracks. The axial response obtained using these proposed simulation methods agreed well with results from post-construction monitoring in actual seamless bridge systems (Griffiths et al., 2005).

In this section, the analysis results of this prototype seamless bridge in Australia using the models described in Section 5.2 are presented and compared with the analytical results of Bridge et al. (2005). Given the shortage of field data on the actual response of a seamless bridge-CRCP system, this comparison served as an indirect validation of the proposed nonlinear finite modeling scheme.

5.3.1 Model Description

Computational models were developed based on the data reported by Bridge et al. (2005) complemented by details obtained from design drawings of actual seamless bridges in WM7 project in Australia (Griffiths, personal communication, 2019).

In the numerical models, for a 393-ft.-long bridge, the transition zone was simulated as 393 ft. long, including a 360-ft.-long transition slab and a 33-ft.-long approach slab. A 295-ft.-long conventional CRCP was included at the end of the transition zone with restrained longitudinal movements. The transition slab had a uniform thickness of 9.5 in, which was the same as the thickness of the conventional CRCP it connected to. The reinforcement distribution within the transition zone were not reported in the publications, and therefore were assumed based on the design drawings of an actual seamless system of the same bridge length in WM7. Figure 5.6 presents the variation in the longitudinal reinforcement ratio along the conventional CRCP and

transition zone. The transition slab consisted of five segments with varying lengths and reinforcement amounts, which were utilized with a goal to optimize the design based on the varying axial demands. Two layers of longitudinal reinforcement were used in the transition slab with a gradually increasing reinforcement ratio of 0.75%, 1.05%, 1.34%, 1.72%, and 2.09% from the conventional CRCP to the approach slab. The respective length for each segment was 164 ft., 49 ft., 49 ft., 49 ft., and 49 ft. The transition segment near the conventional CRCP had a similar reinforcement ratio as that for a conventional CRCP, which was approximately 0.67%.

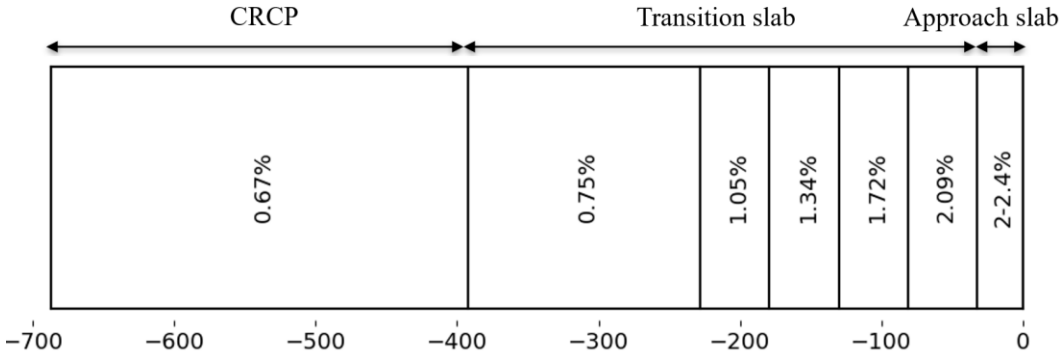

Figure 5.6: Configuration of the transition zone and CRCP of the Australia seamless bridge.

The thickness of the approach slab gradually increased from 9.5 in. at the end of the transition slab to 14 in. at the bridge abutment. The pavement thickness near the bridge abutment was increased to accommodate the flexural effects. The approach slab was modeled as four segments with the same length but increasing reinforcement ratio from 2% to 2.4% toward the bridge abutment.

The configuration of the bridge was also assumed based on design drawings of the same actual seamless bridge in WM7. The bridge was non-skewed with three spans. The bridge deck was 9.8 in. thick and 56 ft. wide, supported by 9 T-shaped precast concrete girders with each gross area of approximately 7950 in^2. The "unusual" thickness of 9.8 inches is due to the SI-US units conversion (250 mm thick slab). Link slabs were used between two adjacent bridge spans to form a continuous bridge deck. The link slab was assumed to be 4 ft. long and 9.8 in. thick. The reinforcement amounts for the bridge decks over girders and link slabs were assumed as 0.5% and 3.4%, respectively. Within 6 ft. of the bridge deck near the abutment, the longitudinal reinforcement was assumed continuous from the approach slab to accommodate large axial forces and bending moments in this region, resulting in a locally-increased reinforcement ratio to 2%.

Although the actual bridge has 9 girders and a width of 56 ft., for simplicity the bridge was idealized as a "unit" width section of 1 in. to study the basic behavior. The girder depth was approximately equivalent to 10 in. assuming a uniform distribution of the total axial stiffnesses provided by 9 girders over the entire bridge width. The equivalent stiffnesses of the bearing and pier column in the longitudinal direction for a-unit-wide (1 in.) model were determined using the method reported in Malviya (2021). The modeled shear stiffness of each elastomeric bearing was 5000 lbf/in. according to the technical data sheet. The equivalent stiffness of the bearings was approximately equivalent to 67 lbf/in. assuming a uniform distribution of the total shear stiffness provided by 9 bearings over the entire width. The pier column was considered as a cantilever beam with a fixed end at the base. The lateral stiffness of pier column is defined in Eq. 5.5:

$$k_{pier} = \frac{3EI}{l^3}, \quad \text{Eq. 5.5}$$

where:

k_{pier} = lateral stiffness (lbf/in.),

E = modulus of elasticity (psi) (E_c= 40000$\sqrt{f_c'}$ + 1000000),

I = area moment of inertia of the beam section (in^4) (for circular sections, $I = \frac{\pi D^4}{64}$, D is the diameter of the circle),

l = length of the cantilever beam (in.).

The pier was 17.4 ft. high and its cross-section was circular with a diameter of 3 ft. The concrete compressive strength for piers was 4.65 ksi. Correspondingly, the lateral stiffness of each pier was calculated as 101285 lbf/in. The stiffness of piers for a unit-wide bridge was approximately equivalent to 904 lbf/in. assuming a uniform distribution of the total lateral stiffnesses provided by 6 piers over the entire bridge width.

The concrete compressive strengths for bridge girders, bridge decks, and pavement were taken as 7.25 ksi, 5.8 ksi, and 4.65 ksi, respectively, based on the specified values in the design drawings. The concrete tensile strength was determined using Eq. 5.3(a). Young's modulus of reinforcing steel is 29000 ksi and the assumed nominal yield strength was taken as 60 ksi.

To model the concrete slab-base interaction within the transition zone, for simplicity, a constant coefficient of friction μ was assumed. Two different levels of coefficient of friction (μ = 0.5 and μ = 1.5) were considered following the same assumptions as in Bridge et al. (2005). A bi-linear shear stress-displacement relationship at the interface was assumed considering a small initial displacement of 0.015 in. The friction was ignored for the approach slab considering the separation from the base due to potential (and likely) differential embankment settlement in the region near the abutment.

Table 5.2 lists the total environmental strains due to thermal variations, concrete shrinkage, and creep, which were used for the axial analysis and design in Australia (Bridge et al., 2005). The strains for the pavement and bridge in the case of expansion (temperature increase) and contraction (temperature decrease) conditions were specified separately. When the temperature increases, the bridge and pavement expand resulting in compressive stresses in the materials. In contrast, when the temperature decreases, the bridge and pavement contracts, causing tensile stresses. The environmental strains were converted to the equivalent temperature changes, which were applied to both concrete and reinforcing steel elements to model the corresponding deformations.

Table 5.2: Thermal loadings used by Bridge et al. (2005) in Australia.

Loading	Pavement	Bridge
Expansion	100 $\mu\varepsilon$ (micro strain)	200 $\mu\varepsilon$
Contraction	300 $\mu\varepsilon$	650 $\mu\varepsilon$

5.3.2 Model Results and Comparison with Previous Analyses

Figure 5.7 and Figure 5.8 compare the results obtained with the proposed FE model and those of Bridge et al. (2005) for expansion and contraction, respectively. The horizontal axis represents locations on the conventional CRCP, transition zone, and bridge, from left to right. The origin represents the bridge abutment position, with the pavement on its left and the bridge on its right. Only the comparison of the results along the CRCP and transition zone is presented due to the unavailability of results along the bridge from the published papers by Bridge et al. (2005). The vertical axis plots the axial force, longitudinal displacement, and material stress at each location. Particularly, concrete compressive stresses are presented for the expansion condition, and maximum steel stresses are presented for the contraction condition. The material strains in the plot are the net strains, i.e., the strains due to stresses. Conventions for the presentation of axial analysis results are defined as: tension is positive and compression is negative. A positive displacement value represents the movement toward the bridge center, whereas a negative value indicates the movement away from the bridge center. Results for two frictional resistances are included.

Overall, the FE model results agree well with the analysis results obtained by Bridge et al. (2005). Both boundary conditions result in similar axial forces and longitudinal displacements. The longitudinal forces transferred through the concrete slab-base interaction within most of the transition zone are identical as evidenced by the similar slope of the axial force diagram. Small differences were obtained at the end of the transition zone due to the small relative displacement which did not fully activate friction in the method proposed here. The jagged pattern of the maximum steel stress within the transition zone, which reflects the gradual increase of reinforcement ratio in tune with the increasing demand, was well captured. There are other slight differences in the responses, which are likely due to other differences in the material laws or modeling assumptions regarding design aspects. For example, the reinforcement amount used for each member was indirectly obtained from design drawings, which may not be exact.

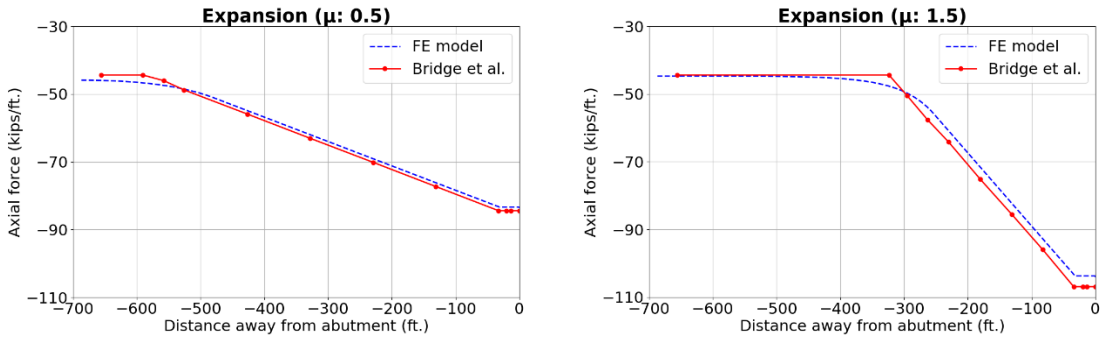

(a)

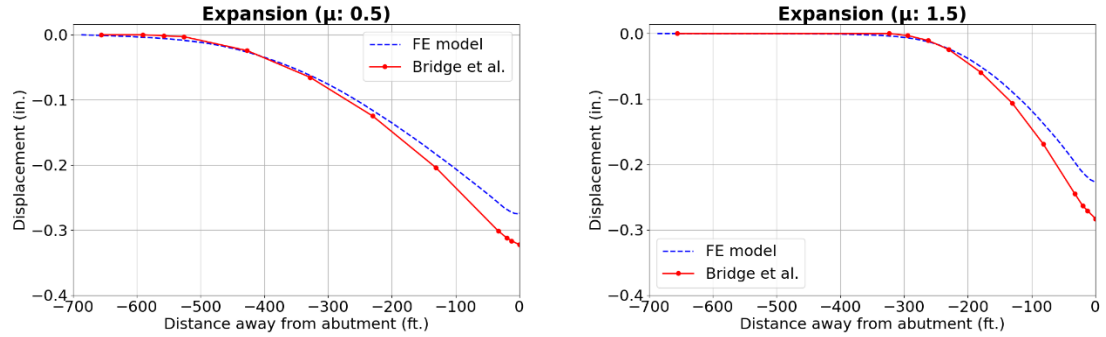

(b)

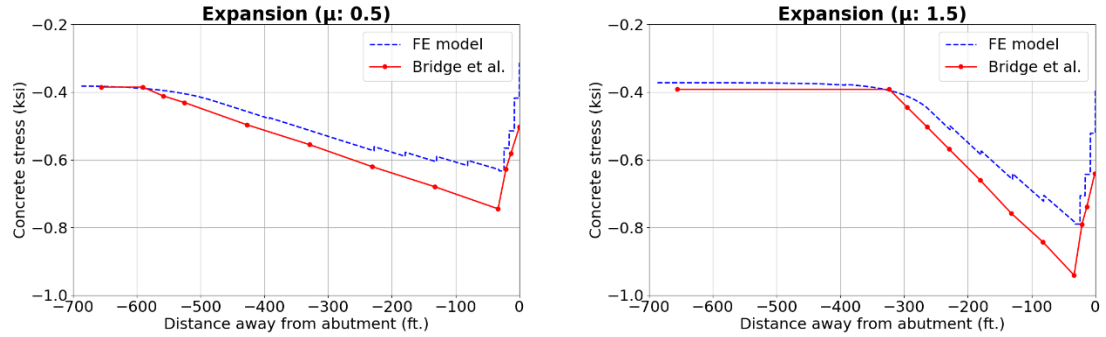

(c)

Figure 5.7: Comparison of results by FE model and Bridge et al. (2005) (temperature increase): (a) Axial force; (b) Longitudinal displacement; (c) Concrete stress.

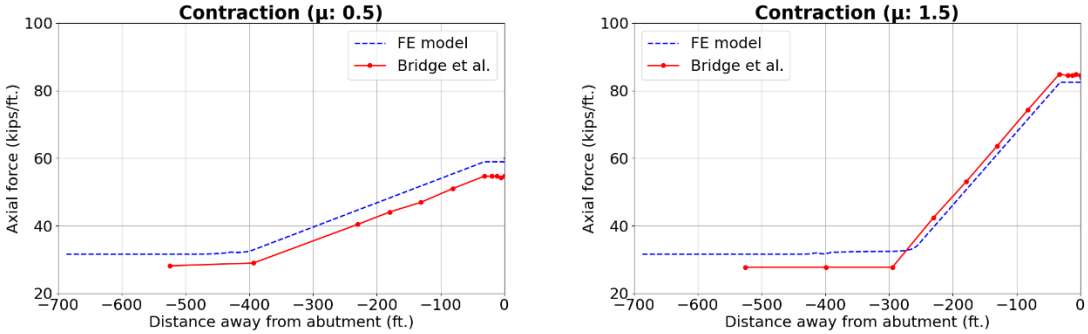

(a)

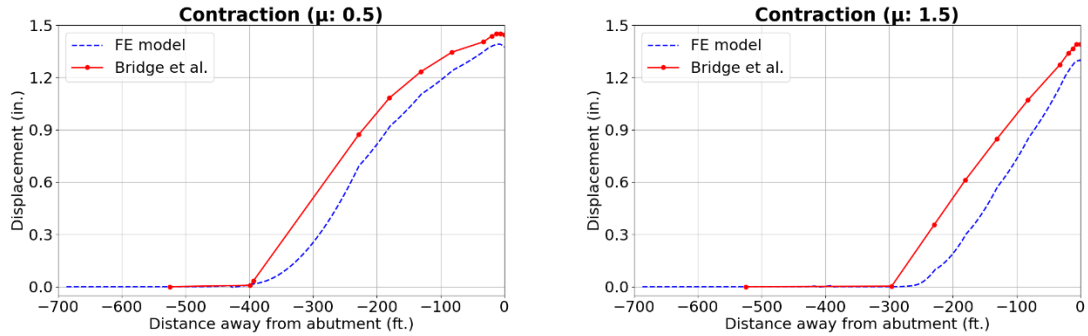

(b)

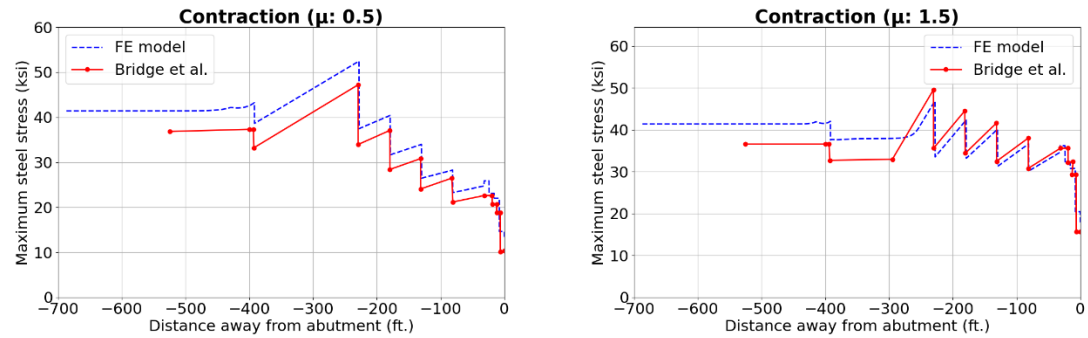

(c)

Figure 5.8: Comparison of results by FE model and Bridge et al. (2005) (temperature decrease): (a) Axial force; (b) Longitudinal displacement; (c) Maximum steel stress.

5.4 Analysis of Prototype Seamless Bridge System in Texas

5.4.1 Model Description

To investigate the axial behavior of a prototype seamless bridge-CRCP system in Texas, a structural model with typical TxDOT pavement and bridge design details was created using the modeling scheme described in Section 5.2.

The prototype bridge that was studied had three spans each 100 ft. long. The total width of the bridge was 40 ft. The prototype bridge was assumed to use typical TxDOT designs for multiple-span bridges employing precast prestressed concrete girders, as shown in Figure 5.9. In Texas, the

standard concrete decks make use of partial-depth Precast Concrete Panels (PCPs) of 4 in. thick with a thick Cast-in-Place (CIP) concrete layer of 4.5 in. thick. Most prestressed concrete girder bridges make use of continuous concrete decks that are composite with simply-supported concrete girders, and the link slab regions where the bridge decks are continuous between two adjacent simply-supported spans use the poor-boy continuous construction technique, as presented in Figure 5.9. Since girders contribute significantly to the stiffness of bridge superstructures, the link slabs are significantly less stiff due to the discontinuity of bridge girders at these locations. A typical construction procedure for these link slab regions in Texas is to place crack formers to control the cracking pattern while keeping the longitudinal reinforcement ratio essentially the same throughout the bridge deck.

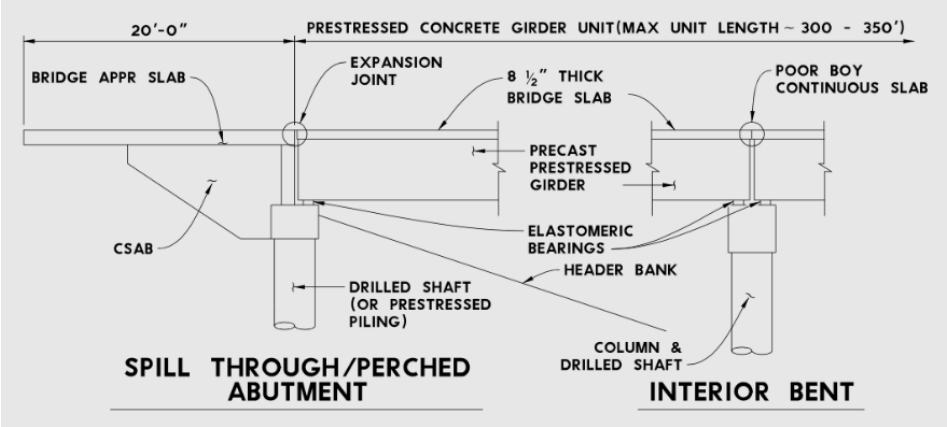

Figure 5.9: Details of bridges in Texas.

The effective axial stiffness is primarily provided by the bridge girders and the CIP portion of the decks due to the discontinuity of partial-depth PCPs and their reinforcement in the longitudinal direction. Therefore, in the model, the PCP portion of the bridge decks was ignored for the axial analysis. The bridge decks were modeled considering only the 4.5-in.-thick CIP portion.

The bridge deck was assumed to be supported on five Tx54 precast prestressed concrete girders with each gross area of about 817 in^2. Link slabs were modelled as 2 ft. long and 8.5 in. thick. The longitudinal reinforcement ratio was assumed as 0.7% for the bridge decks. The link slabs are expected to take higher axial forces due to the seamless connection compared to conventional jointed bridges. Therefore, the reinforcement ratio in these regions was modelled with a significant increase to 2.5%.

For the 1-in.-wide model, the equivalent depth of the girder, longitudinal stiffness of the bearings and pier columns were assumed using the method described in Section 5.3.1 assuming a uniform distribution of stiffnesses over the entire bridge width. The equivalent girder depth was determined as 8.5 in. The equivalent stiffnesses of the elastomeric bearing and the pier column were calculated as 117 lbf/in. and 2137 lbf/in., respectively.

For the analysis and design, a sufficiently long portion of the transition zone where the slab thickness, reinforcement amount and the use of bond breakers are different from the conventional CRCP was simulated. The transition zone consisted of a 30-ft.-long approach slab and a 600-ft.-long transition slab. The thicknesses of the transition slab and approach slab were modeled as 11 in., which is within the typical thickness ranges of CRCP in Texas (7 in. to 13 in.). The transitions

slab was divided into three segments. The reinforcement ratio for each segment was 0.75%, 1.1%, and 1.45% toward the approach slab. The corresponding length for each segment was 430 ft., 100 ft., and 70 ft. A constant reinforcement ratio of 2% and uniform thickness was used for the approach slab for simplicity. The details of the length and reinforcement amount for each segment are shown in Figure 5.10. The reinforcement quantities in the pavement and link slabs were determined based on preliminary analyses to limit the tensile stress in the reinforcing steel to an acceptable level, as discussed later. A constant coefficient of friction $\mu = 0.8$ was assumed for the transition slab only.

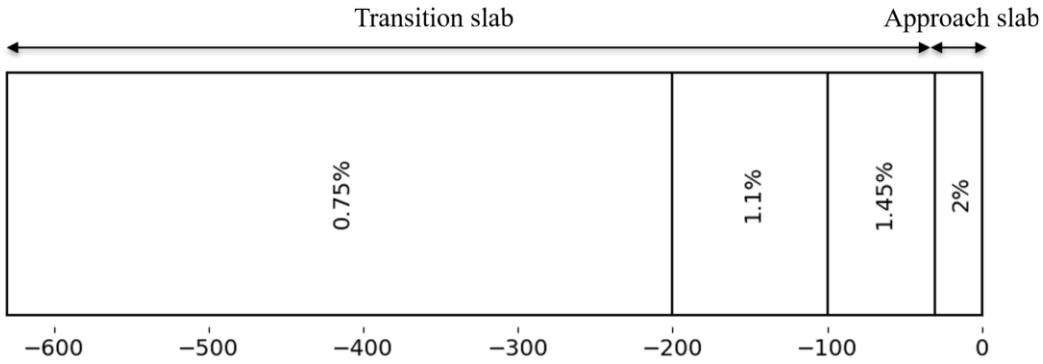

Figure 5.10: Configuration of the transition zone.

The concrete compressive strength for the bridge girders was taken as 8 ksi while a value of 4 ksi was taken for the bridge deck and pavement. The elastic modulus of the reinforcing steel is 29000 ksi and the nominal yield strength was taken as 60 ksi. Two loading conditions were considered: expansion (temperature increase of 80°F) and contraction (temperature decrease of 55°F). The uniform temperature change was equally applied to the pavement and bridge. Concrete shrinkage was explicitly considered to investigate its effects on the axial response.

5.4.2 Boundary Condition Effects

To seek the appropriate boundary conditions and investigate the effects on the system response, two models were developed with different boundary conditions as described in Figure 5.5. One model employed restrained translational movements at the end of the transition zone, which is referred to as “Transition slab with fixed end” model. The other model included the same length of the transition zone and an extra 600 ft. long CRCP at the end of the transition slab with a free end, which is referred to as “Transition slab with CRCP”. A constant coefficient of friction of 0.8 was used for the transition slab in the two models. In the second model, a higher coefficient of friction was assumed for the conventional CRCP to represent the interaction for a typical concrete slab-CSB interface of large interface restraint without bond breakers. AASHTOWare Pavement Design Software (Roesler et al., 2016) recommends the range of design values for friction coefficients between CRCP and different types of bases. When cement stabilized base is used beneath CRCP, the friction coefficient from low to high is 3.5, 8.9, and 13. These high values of the apparent coefficient of friction are explained by large contribution of adhesion to the shear resistance of the interface. The coefficient of friction varies over a wide range, due to variations on the material mix and properties, surface roughness and construction methods. This study assumed a constant apparent friction coefficient of 3.5 to represent the interaction at the interface between the concrete pavement and CSB topped with a 1-in.-thick HMA relieving layer.

Figure 5.11 and Figure 5.12 compare the distribution of total axial force and longitudinal displacement of the system with two different boundary conditions in the cases of expansion and contraction, respectively. The horizontal axis follows the conventions as defined before, with the origin denoting the bridge abutment position. The shaded area in light orange represents the bridge region. Only the results for half of the bridge are included, and a symmetric axial behavior was assumed for the other half. Both boundary conditions result in the same behavior in the transition zone and bridge deck. The minimum required length of the transition zone can be determined based on its response. In the case of expansion, approximately 450 ft. to 500 ft. of the transition zone is required to fully dissipate the movements caused by the bridge-pavement interaction. The seamless connection does not affect the pavement beyond this point. In the case of contraction, the axial force gradually decreases from the bridge abutment to the transition zone and keeps constant starting at approximately 300 ft. away from the abutment. The pavement stops moving beyond this point as well.

The model including CRCP provides additional information about the response of the CRCP. The absence of restraint at the end of CRCP results in a zero axial force but a relatively large displacement. For example, it will have a longitudinal displacement of -1.7 in. and 0.3 in. when experiencing an 80°F temperature increase and a 55°F temperature decrease, respectively. This behavior is not affected by the presence of the bridge or transition zone, and is consistent with the expected movements in CRCP joints, as discussed in Section 5.7.

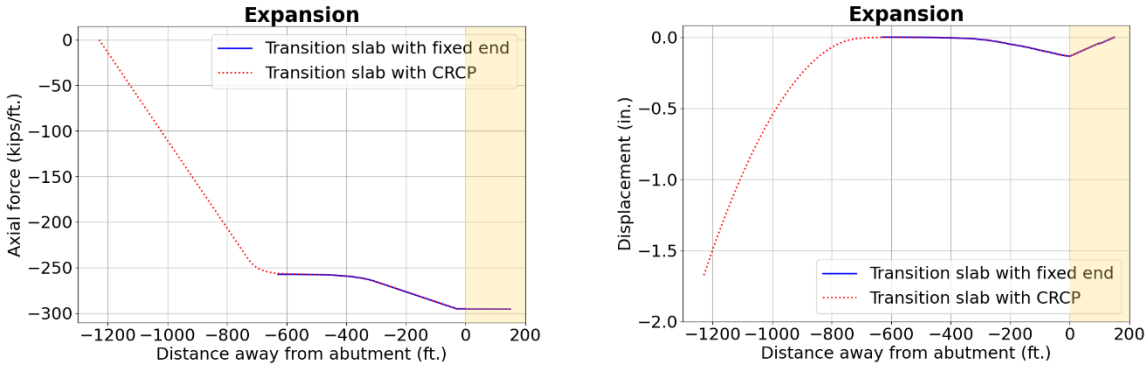

(a) (b)

Figure 5.11: Comparison of boundary conditions (temperature increase): (a) Axial force; (b) Longitudinal displacement.

It can be concluded that if the transition zone is modeled longer than the minimum required length to dissipate the bridge-pavement interaction, the boundary condition with restrained movements at the end of the transition zone can accurately represent the restraint provided by the conventional CRCP without need of explicitly including the CRCP portion. Therefore, for the numerical modeling discussed in the following subsection, the end of the transition zone was assumed to be restrained regarding the translational movements for simplicity.

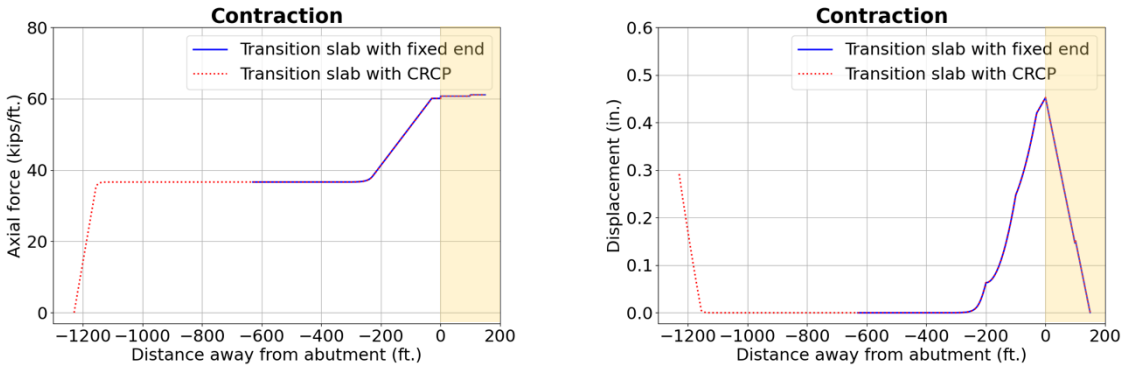

(a) (b)

Figure 5.12: Comparison of boundary conditions (temperature decrease): (a) Axial force; (b) Longitudinal displacement.

5.4.3 Axial Response with Thermal Effects

Figure 5.13 demonstrates the axial behavior of the transition zone and bridge in the case of expansion. The results are presented in terms of the total axial force, longitudinal movement, and material strain and stress, which are plotted along the transition zone and bridge deck. The axial force is for the entire section, whereas the concrete and reinforcement material stresses are plotted only for the reinforced concrete decks. This is because the bridge decks tend to crack when subjected to tension, whereas the bridge girders are expected to remain elastic.

When the temperature increases, the bridge expands and moves away from the center of mass. Since the bridge is stiffer than the pavement, the pavement will be pushed away from the bridge center by the bridge expansion. This can be seen by a negative value of the longitudinal displacement for both the transition zone and the bridge. The displacement is maximum at the bridge abutment, which is approximately 0.13 in. The frictional forces are developed at the concrete slab-base interface due to the movement of the transition pavement. The movement of the transition zone gradually decreases to zero due to the restraint by the frictional forces.

Additional compressive forces are generated within the transition zone and bridge due to the seamless connection. The magnitude of the axial force per unit width is maximum at the bridge abutment, which is approximately 295 kips/ft, and gradually decreases to a constant value of 258 kips/ft. The variation of the axial force within the transition zone is caused by the accumulation of the concrete slab-base interaction. The axial force is constant for the approach slab (within 30 ft. long of the bridge abutment) due to the assumed frictionless behavior as a result of the anticipated differential embankment settlement.

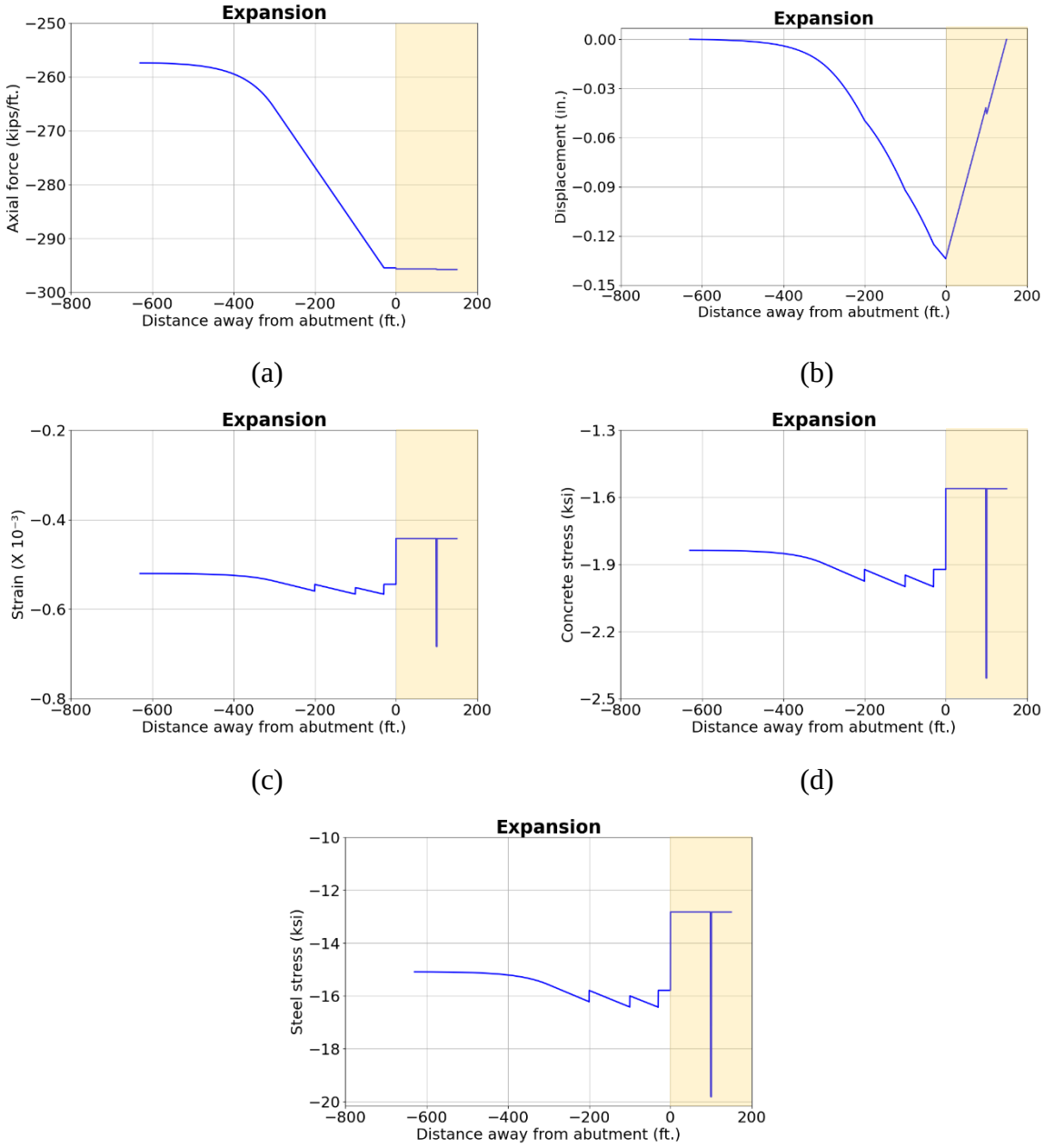

Figure 5.13: Axial response (temperature increase): (a) Axial force; (b) Longitudinal displacement; (c) Strain; (d) Concrete stress; (e) Steel stress.

At approximately 600 ft. away from the bridge abutment on the pavement side, the displacement decreases to zero and the axial force decreases to a constant value. This observation indicates that after 600 ft. long of the transition zone, the additional axial effects caused by the bridge-pavement interaction are completely dissipated. Beyond this point, the reinforced concrete pavement is not affected by the bridge with the temperature increase. This, therefore, provides an indication of the minimum required length of the transition zone.

The dissipation of bridge effects on the pavement response can also be confirmed by the fact that the response of the reinforced concrete pavement beyond the minimum transition length is the same as that of a conventional CRCP. Considering a typical section of CRCP with the same uniform temperature increase of 80°F, the axial force N acting on the CRCP section that has longitudinal deformations completely restrained can be calculated from Eq. 5.6:

$$F = A_c f(\varepsilon_c) + A_s f(\varepsilon_s), \quad \text{Eq. 5.6}$$

in which:

$\varepsilon_{th} = \alpha \Delta T$,

$\varepsilon = \varepsilon_{total} - \varepsilon_{th}$,

where:

α = coefficient of thermal expansion (/°F),
ΔT = temperature change,
ε_{th} = thermal strain,
ε_{total} = total strain,
ε = strain related to stress (subscript c for concrete and subscript s for steel),
E = modulus of elasticity (E_c = 3530 ksi, and E_s = 29000 ksi),
f = compressive stress,
A = area for a unit width (A_c = 11 in^2, and A_s = 11×0.75% = 0.0825 in^2).

Substituting α = 6.5×10^{-6} and ΔT = 80°F into the equation, the thermal strain is calculated as $\varepsilon_{th} = \alpha \Delta T$ = 5.2×10^{-4} for both concrete and steel. The strain related to stress is thus obtained as $\varepsilon_c = \varepsilon_s$ = -5.2×10^{-4} considering that the total strain is zero. The concrete and steel compressive stresses are calculated by multiplying the modulus of elasticity by the strain due to stress since they are in the elastic range, which are $f_c = E_c \varepsilon_c$ = -1.84 kips, and $f_s = E_s \varepsilon_s$ = -15 ksi. The axial force per unit width, F, calculated using Eq. 5.6 is -258 kips/ft., which is the same as the simulated result for the pavement beyond the transition zone. The strain, concrete stress, and steel stress are the same as well.

The variation of the axial force along the bridge superstructure is generally minor, indicating that only a small portion of the axial force is transferred from the bridge superstructure to the substructure through the relatively flexible bearings that support the girders. The sharp increase in strain at the link slabs reflects the significant decrease in stiffness in this region. However, it is not generally critical in the case of expansion loading conditions since concrete is very strong in compression.

In contrast, considering the expansion behavior, the concrete is in tension and cracks tend to occur in the reinforced concrete pavement and bridge deck. Limiting crack widths is vital for the service life of structures. Therefore, it is necessary to investigate the cracking response and estimate the crack width to ensure the serviceability limit state. Crack development, crack width, and spacing are affected by many factors, such as the rebar diameter and spacing, and concrete cover. Frosch (1999) proposed Eq. 5.7 to estimate the crack width, which is currently used by the AASHTO Bridge Design Specifications (2020).

$$w = 2 \frac{f_s}{E_s} \beta \sqrt{d_c^2 + \left(\frac{s}{2}\right)^2}, \quad \text{Eq. 5.7}$$

where:

w = most probable crack width (in.),
f_s = rebar stress under service loading (ksi),
E_s = elastic modulus of reinforcing bar (ksi),
d_c = thickness of cover from extreme tension fiber to closest bar center (in.),
s = bar spacing (in.),
$\beta = 1.0 + 0.08d_c$.

However, the original work in the development of Eq. 5.7 did not clearly state whether the rebar stress should be taken as the average steel stress through the cracked regions or the maximum steel stress at cracks. For reinforced concrete sections, at cracks, the concrete stress diminishes to zero and all tension forces are carried by the steel. Between adjacent cracks, due to the tension stiffening effects, the concrete can carry some tensile forces. The concrete stress and rebar stress obtained from the proposed numerical model represent the average steel stresses in cracked regions. However, the rebar stress is maximum at cracks, which can be calculated by dividing the total axial force for the cracked section by the rebar area. Ge (2021) studied the relationship between the rebar stress and the crack width by conducting direct tension tests on reinforced concrete specimens with various concrete properties and reinforcement ratios. The measured crack widths generally matched the predictions based on Eq. 5.7 when the maximum rebar stress was used.

The current structural design standard limits the maximum rebar stress to control the crack opening for serviceability limit states. Therefore, it is important to assess the maximum rebar stress at cracks. As per the AASHTO LRFD Bridge Design Specifications (2020), the maximum steel stress should not exceed 60% of the yield strength for reinforced concrete structures. For reinforced concrete pavement, it is common to limit the maximum steel stress below two-thirds of the yield strength (Roesler et al., 2016). Accordingly, this study establishes the acceptable limit for the maximum steel stress at 40 ksi and 36 ksi for the pavement and bridge deck, respectively, considering the use of Grade 60 steel.

Figure 5.14 presents the axial force, longitudinal displacement, strain, concrete stress, average steel stress, and maximum steel stress along the transition slab and bridge deck (including the link slabs) in the case of temperature decrease. Since the bridge girders generally remain elastic under the serviceability conditions, the material stresses are demonstrated for the bridge deck only. When the temperature decreases, the bridge contracts toward the center of mass. The transition pavement is therefore pulled toward the bridge center of mass as well since the stiffness of the bridge is generally larger than that of the pavement. This movement is indicated by positive displacements. The displacement is maximum at the bridge abutment, with a value of approximately 0.45 in. The displacement of the pavement is gradually dissipated by the concrete slab-base interaction within approximately 300 ft. into the transition zone measured from the end of the bridge (i.e., the abutment).

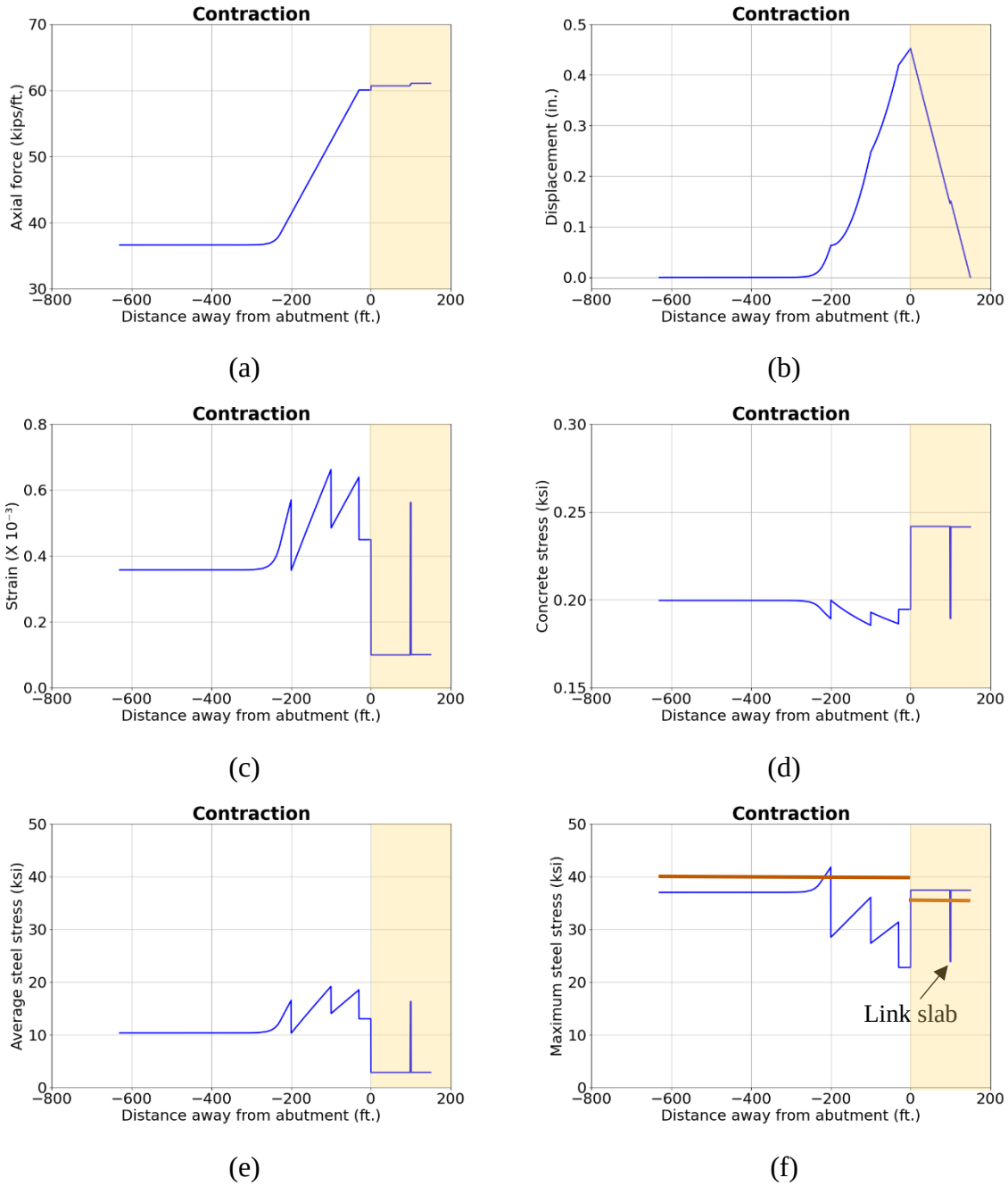

Figure 5.14: Axial response (temperature decrease): (a) Axial force; (b) Longitudinal displacement; (c) Strain; (d) Concrete stress; (e) Average steel stress; (f) Maximum steel stress.

Additional tensile forces are generated within the transition zone and bridge due to the seamless connection. The transition slab was designed to have three regions with increasing reinforcement amounts as it reaches the approach slab corresponding to the increasing axial force demand. As a result, the strain does not vary largely within the transition slab, which tends to generate similar cracking patterns. The sudden drop of the strain at the end of each segment is caused by the increase in the reinforcement amount and thus the increase in stiffness. The strain at the link-slab location over the interior supports is significantly increased as compared to that for the portions of the

bridge decks that are directly over girders, which reflects the large reduction of stiffness within the link slabs due to the discontinuity of bridge girders. The maximum steel stress differs from the average steel stress in the transition zone, bridge decks, and link slabs, indicating the likely occurrence of cracking in the concrete slab/deck. The average steel stress in the link slabs is much higher than that in the bridge decks over girders. However, the maximum steel stress in the link slabs is lower than that in the bridge decks. This is due to the heavy reinforcement ratio of 2.5% assumed for the link slabs. The acceptable limits for the maximum steel stress at 40 ksi and 36 ksi for the pavement and bridge deck, respectively, are also plotted in the figure. The reinforcement arrangement can be adjusted further to satisfy the design criterion and for optimization purposes as well.

The minimum required length of the transition zone can be determined based on the axial force and displacement distribution along the pavement. From the two examples for the compressive/tensile axial behavior demonstration, as shown above, a 600 ft. long and a 300 ft. long transition slab is engaged to completely dissipate the movement due to the bridge-pavement interaction in the case of expansion and contraction, respectively. The reinforcement amount in the transition zone can be determined based on the tensile demand in the case of contraction since the response of the system is critical.

The design of the seamless bridge-pavement system depends on the construction time. If the seamless bridge-pavement system is constructed in winter, for example, in January, the system generally experiences a net temperature increase in the summer, which requires a relatively long transition zone to dissipate the thermal movements but is favorable for the behavior to avoid concrete cracking. In contrast, if the seamless bridge is constructed in summer, a subsequent temperature decrease experienced by the system will cause cracking in the concrete. A shorter transition zone but larger reinforcement amount is needed.

5.4.4 Axial Response with Thermal and Shrinking Effects

To investigate the effects of shrinkage on the axial behavior of the seamless system, analyses were conducted by considering shrinkage in combination with temperature variations. Expansion (temperature increase of 80°F) and contraction (temperature decrease of 55°F) conditions were considered. The ultimate drying shrinkage strain was converted to temperature variations by a factor of the thermal expansion coefficient, which was applied to concrete elements.

Figure 5.15 and Figure 5.16 demonstrate the axial behavior of the transition zone and bridge deck for the above loading considerations. The response without shrinkage effects is also plotted for comparison.

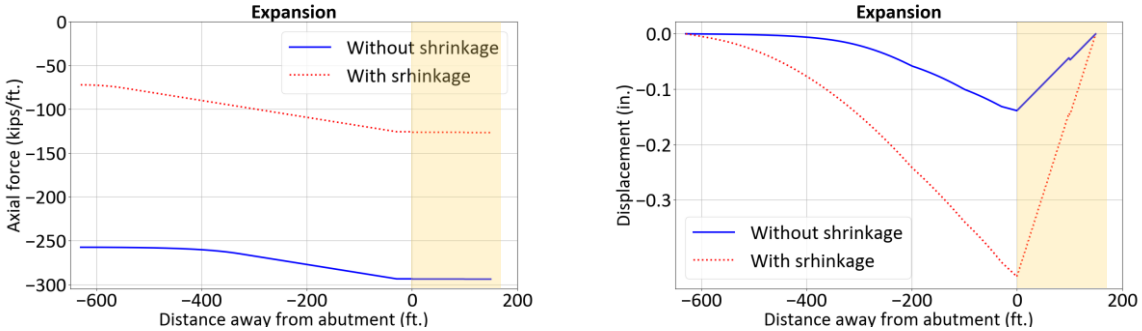

(a)

(b)

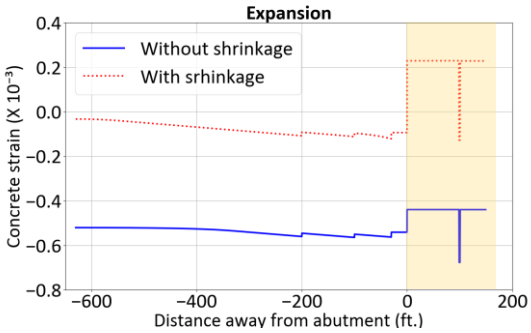

(c)

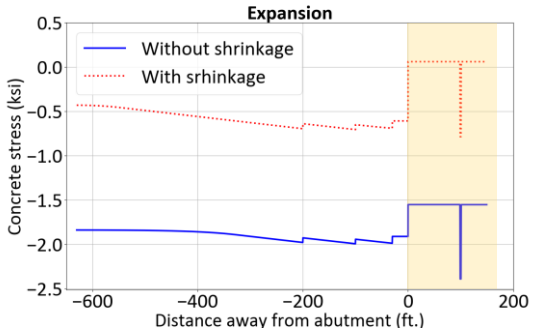

(d)

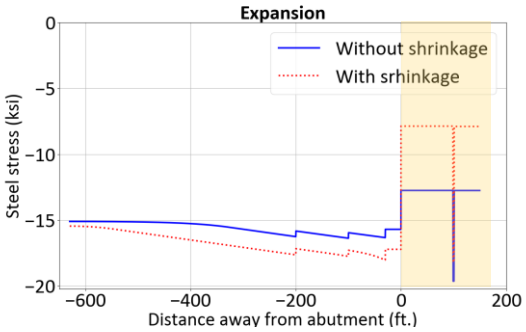

(e)

Figure 5.15: Axial behavior demonstration (temperature increase and concrete shrinkage): (a) Axial force; (b) Longitudinal displacement; (c) Strain; (d) Concrete stress; (e) Steel stress.

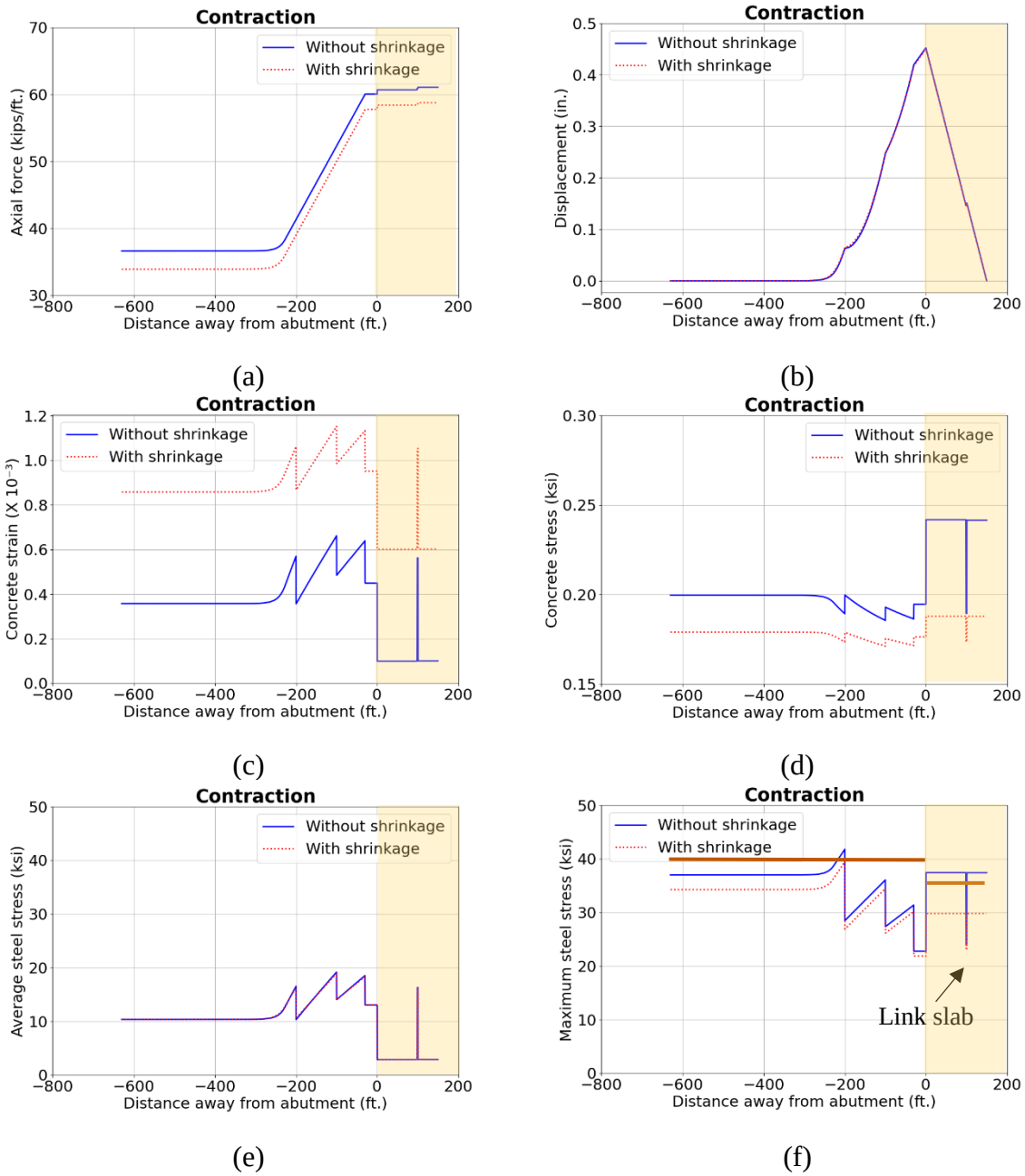

Figure 5.16: Axial behavior demonstration (temperature decrease and concrete shrinkage): (a) Axial force; (b) Longitudinal displacement; (c) Strain; (d) Concrete stress; (e) Average steel stress; (f) Maximum steel stress.

With the temperature increase, the bridge and pavement tend to expand. However, the shrinkage causes the concrete volume to decrease. The effects of shrinkage counteract the effects of temperature increase. With shrinkage, the concrete net compressive strain decreases due to the counteracting effects, as shown in Figure 5.15(c). In the bridge deck regions, the concrete exhibits tension as a result of combined thermal and shrinkage effects (see Figure 5.15(d)), whereas the reinforcing steel is in compression (see Figure 5.15(e)). The overall compressive force demand in the system is lower compared to the case with the temperature increase effects alone, as indicated in Figure 5.15(a). Although combined stresses in the concrete change from compression to tension

in some regions, the tensile strain demand is much lower compared to that with the combined effects of temperature decrease and shrinkage. For the case considered, the material stress is not generally a concern when adding the shrinkage effects.

The concrete shrinkage strains tend to increase the total strain with contraction of the pavement and bridge with the temperature decrease and the concrete net tensile strain therefore increases, as shown in Figure 5.16(c). Once the concrete cracks, the average concrete stress in the cracked region decreases as the concrete tensile strain increases. With the concrete shrinkage effects, the concrete net tensile strain is larger and correspondingly the concrete net tensile stress is smaller for all the cracked components, as indicated in Figure 5.16(d). Because the cracking of concrete leads to the reduction of the section stiffness, the axial force demand is slightly lower with the shrinkage effects (see Figure 5.16(a)). The maximum steel stress decreases as well, as shown in Figure 5.16(f). Therefore, ignoring the shrinkage effects for the analysis and design of the seamless system tends to be conservative. The relative stiffness of the bridge and pavement elements is not significantly affected by the shrinkage effects. The displacement and average steel stress are nearly the same regardless of consideration of shrinkage.

5.4.5 Effects of Cyclic Interface Behavior

As observed in the experimental testing in Chapters 3 and 4, at the concrete slab-base interface with bond breakers, the peak strength typically occurs in the initial cycle due to the mechanical interlocking or adhesion. In the subsequent cycles, the shear stress is generally steady without an apparent peak. The peak strength affects the interface restraint for the first time the transition slab moves with temperature changes. For the rest of the service life of structures, the restraint from the base is controlled by the constant steady coefficient of friction. This section investigates the effects of the shear stress-displacement relationship for both the initial and subsequent cycles of bridge expansion and contraction, particularly the peak strength, on the axial behavior of the seamless system.

As discussed in Section 5.2.3, the shear stress-displacement relationships can be simply represented by multi-linear curves. As an example, the test data for felt paper at the concrete-CSB interface as described in Section 4.3.1 with a normal stress, $\sigma \approx 1$ psi, were considered. The normal stress corresponds to an 11-in.-thick concrete pavement. The shear stress-displacement relationships for the initial and subsequent cycles were simplified as shown in Figure 5.17. For the initial monotonic movement, the peak strength is 2 psi corresponding to a very small initial displacement of 0.015 in., and then suddenly drops to 0.8 psi and keeps constant at 0.8 psi starting from the displacement of 0.03 in. The coefficient of friction for the peak and steady stage is correspondingly 2.0 and 0.8, respectively. In the subsequent cycles, constant shear strength of 0.8 psi is used with an initial displacement of 0.015 in. It corresponds to a constant coefficient of friction of 0.8.

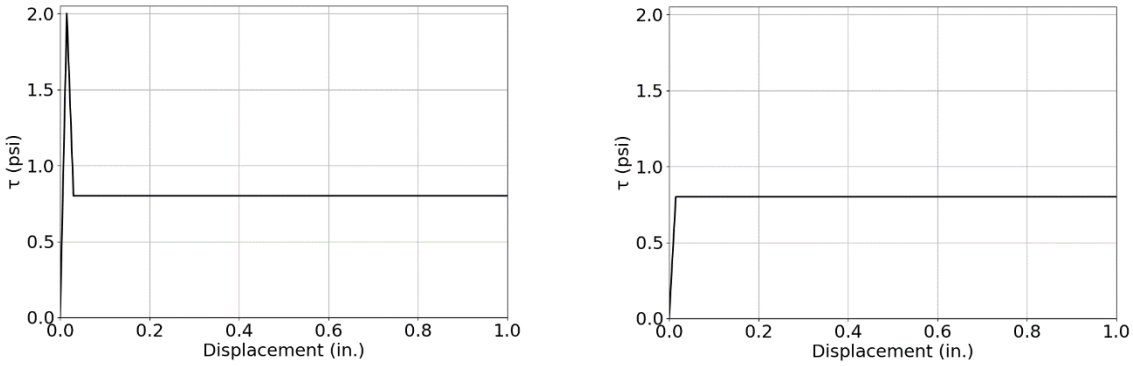

(a) (b)

Figure 5.17: Simplified shear stress-displacement relationships: (a) Initial cycle; (b) Subsequent cycles.

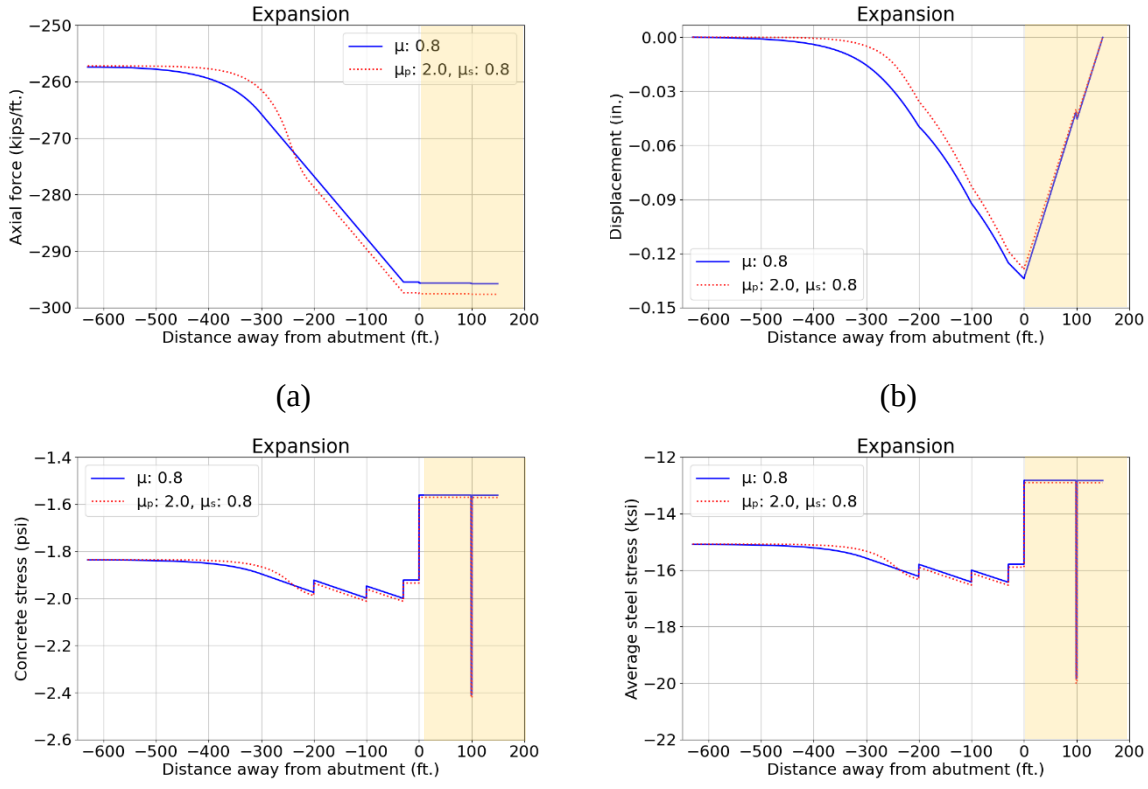

(a) (b)

(c) (d)

Figure 5.18: Results for different cyclic interface behavior (temperature increase): (a) Axial force; (b) Longitudinal displacement; (c) Concrete stress; (d) Steel stress.

Figure 5.18 and Figure 5.19 demonstrate the axial behavior of the transition zone and bridge deck in the respective cases of expansion (temperature increase of 80°F) and contraction (temperature decrease of 55°F). The peak in the shear stress-displacement relationship has a minor impact on the global axial behavior of the entire system. The peak strength may affect the local behavior near the end of the transition zone, where relatively small displacements can be expected. Most of the transition zone is governed by the constant steady shear strength. Therefore, the axial force that is

transferred by the concrete slab-base interaction within the transition zone is similar between the two interface models. The material stress level is close for most regions, especially the critical regions where higher demands are expected. Therefore, a general interface condition simplified with a steady coefficient of friction can be used for the analysis and design of the seamless system.

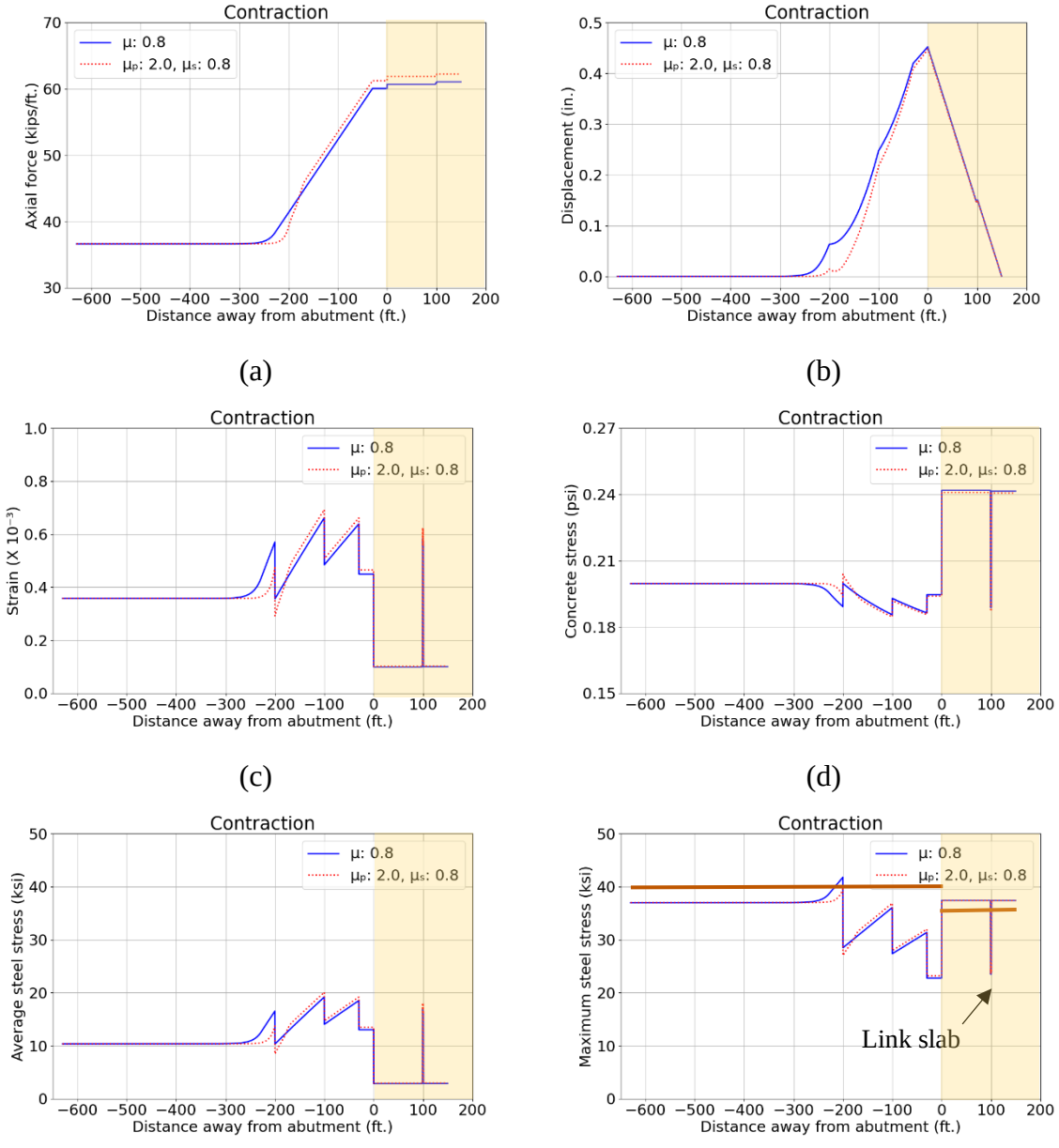

Figure 5.19: Results for different cyclic interface behavior (temperature decrease): (a) Axial force; (b) Longitudinal displacement; (c) Concrete strain; (d) Concrete stress; (e) Average steel stress; (f) Maximum steel stress.

5.5 Numerical Parametric Study

5.5.1 Overview

The axial responses of the seamless bridge-CRCP system are dependent on the imposed strains, relative stiffness of the bridge and pavement elements, and concrete slab-base interaction. This section presents parametric studies for the axial behavior of the transition zone and bridge elements with thermal changes when varying the configurations of the transition pavement. The different magnitudes of the temperature fluctuations for the bridge and pavement were also considered to identify the worst-case scenario. Through the parametric studies, the main characteristics affecting the effective transition length and the amount of reinforcement required in the transition slab were identified. The resulting axial forces in the reinforced concrete slab and the distribution of axial forces within the bridge were analyzed to identify potential design implications, such as modified deformation or force demands in specific bridge elements (e.g., link slabs).

A simplified benchmark model was developed. The benchmark model was a three-span bridge with each span 100 ft. long, which was seamlessly connected with a 630-ft.-long transition zone consisting of a 600-ft.-long transition slab and a 30-ft.-long approach slab. The bridge details were the same as those of the model developed in Section 5.4.1. The thickness of the pavement was 11 in. The reinforcement ratio in the transition slab was assumed uniform within the transition slab to make the influence of each parameter straightforward. The reinforcement ratios in the transition slab and approach slab were 1% and 2%, respectively. A constant coefficient of friction of $\mu = 1.0$ was used for the transition slab. The parametric studies were only conducted for the case of temperature decrease (-55°F) for both the pavement and bridge.

Four parameters with varying magnitudes were considered: concrete slab-base interaction, reinforcement ratio of the transition slab, thickness of the transition slab, and temperature changes for the pavement and bridge. The axial responses with varying parameters were compared with that of the benchmark model.

5.5.2 Concrete Slab-Base Interaction

The impact of the coefficient of friction at the concrete slab-base interface in the transition slab was evaluated by considering values of 0.25, 0.5, 1.0, and 1.5. This parameter represents the apparent coefficient of friction, which is aimed to reflect the interface restraint due to all possible components, i.e., pure friction, mechanical interlocking, and adhesion. The axial force per unit width, longitudinal displacement, strain, concrete stress, average steel stress, and maximum steel stress for the transition zone and bridge deck in the contraction condition are compared for four values of coefficient of friction μ in Figure 5.20.

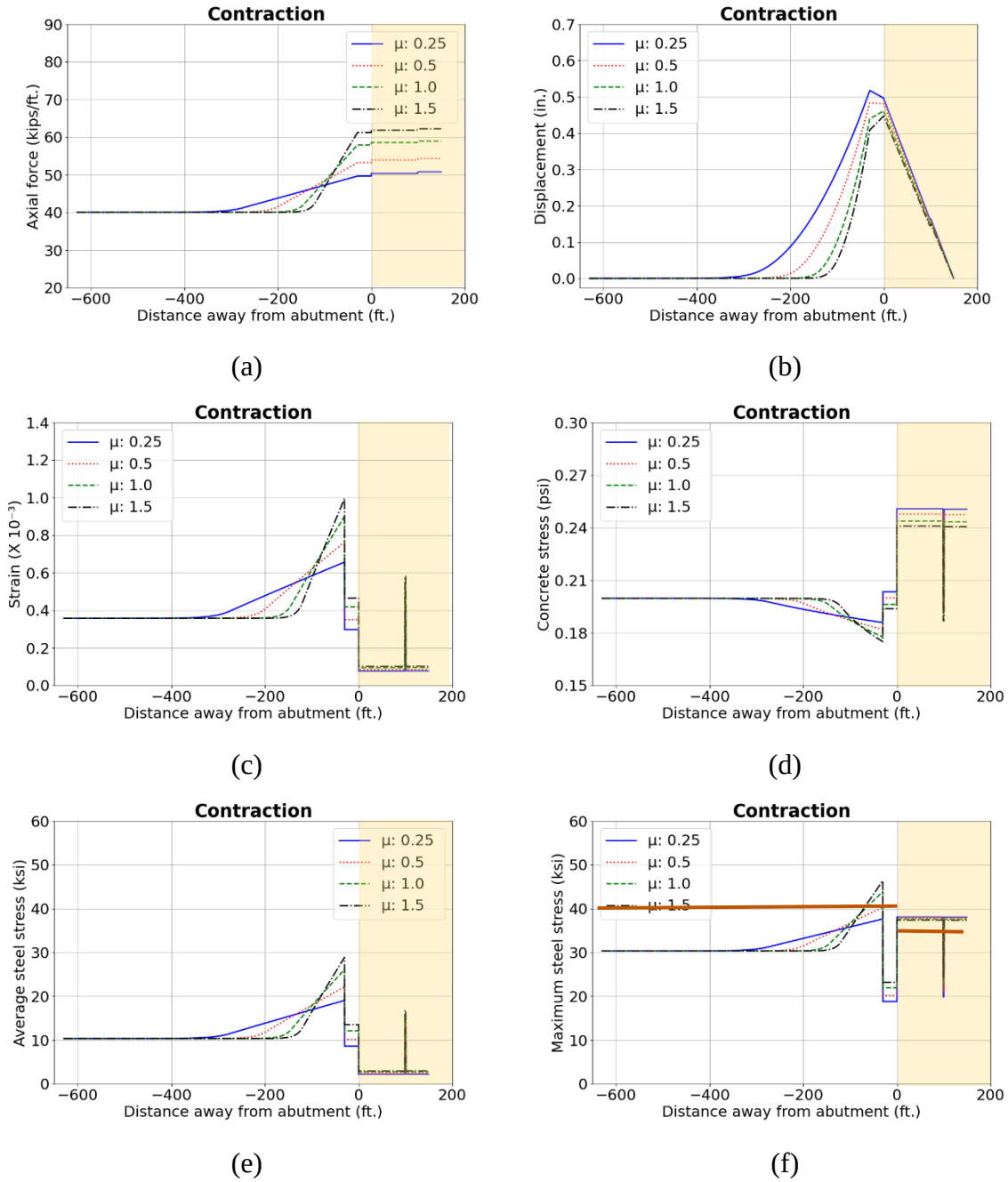

Figure 5.20: Results for different coefficients of friction: (a) Axial force; (b) Longitudinal displacement; (c) Concrete strain; (d) Concrete stress; (e) Average steel stress; (f) Maximum steel stress.

The interaction between the pavement and the base impacts the magnitude of the axial forces that are generated in the system as well as the length over which the movements are dissipated. A higher restraint tends to dissipate the movements within a shorter length. The required respective lengths of the transition zone for values of μ = 0.25, 0.5, 1.0, and 1.5 are approximately 350 ft., 250 ft., 200 ft., and 150 ft. for a total 300-ft.-long bridge. However, a higher restraint generates larger demand in the system. The increase of the interface restraint results in the increase of axial

force, tensile strain, average steel stress and maximum steel stress at cracks, especially in the vicinity of the bridge abutment. The tensile strain and average steel stress within the approach slab are kept low due to the use of relatively heavy reinforcement (2%). For μ = 1.0 and 1.5, the maximum steel stress within some regions of the transition slab exceeds the design limit, which is 40 ksi. Increasing the concrete slab-base interaction also tend to induce a larger strain demand in the link slabs, which are critical regions since the axial forces are only carried by the reinforced concrete slabs. The maximum steel stress within the link slabs is limited to values below 36 ksi, which satisfies the design criterion for the serviceability limit state. This was accomplished by providing a relatively large reinforcement ratio of 2.5%.

The global models developed in Abaqus contribute to determining the effects of different base materials and bond breakers in the response of the seamless system. Although the reinforcement ratio might be adjusted to satisfy the design requirements and optimize the use of materials, a general observation based on these parametric studies is that a lower bound coefficient of friction of approximately 0.5 (μ may be higher than this value but lower than 1) seems to provide a desired level of restraint, which could result in a reasonable length of the transition slab and a controllable cracking behavior. The serviceability status may be easily satisfied with a coefficient of friction as low as 0.25, but this may result in a relatively long transition slab that is not practical for actual field applications. If the interface restraint is too high (μ>1), serviceability limits for crack control will likely be exceeded due to large demands. Phase II experimental testing measured the coefficient of friction provided by different types of bond breakers on common bases. Based on the experimental testing results, double-sided textured linear low-density polyethylene sheet and felt paper are promising bond breakers to be used under the transition zone, which provides the coefficient of friction of approximately 0.4 and 0.7, respectively.

5.5.3 Thickness of Transition Zone

Utilizing larger slab thickness tends to lead to an increase in the stiffness of the pavement, which may affect the bridge-pavement interaction. Typically, CRCP is 7 to 13 in. thick if one layer of longitudinal reinforcement is used and could increase to 14 to 15 in. with two layers of reinforcement in some cases. The range of values of thickness of the transition zone was considered as 9 in., 11 in., and 13 in. to cover the most common range of typical CRCPs. Figure 5.21 compares the axial responses for the transition slab with four different thicknesses of the transition zone.

The pavement thickness significantly changes the relative stiffness of the bridge and pavement elements, thus affecting the system response. A thicker transition slab has a larger stiffness, which results in higher axial forces in the system. Correspondingly, the tensile strains in the bridge decks and link slabs increase as well. This may require an increase of the reinforcement amount in the link slabs to control the cracking, which is critical for the serviceability limit state. The tensile strain in a thicker transition zone may not necessarily increase as the increase in stiffness compensates for the increase in force demand. Actually, in this case, the strain is a bit lower for a pavement with a larger thickness with the same thermal loadings. More displacement occurs in the system when the pavement is much softer compared to the bridge elements. However, the required length of the transition zone is almost the same for four thicknesses, which is governed by the concrete slab-base interaction.

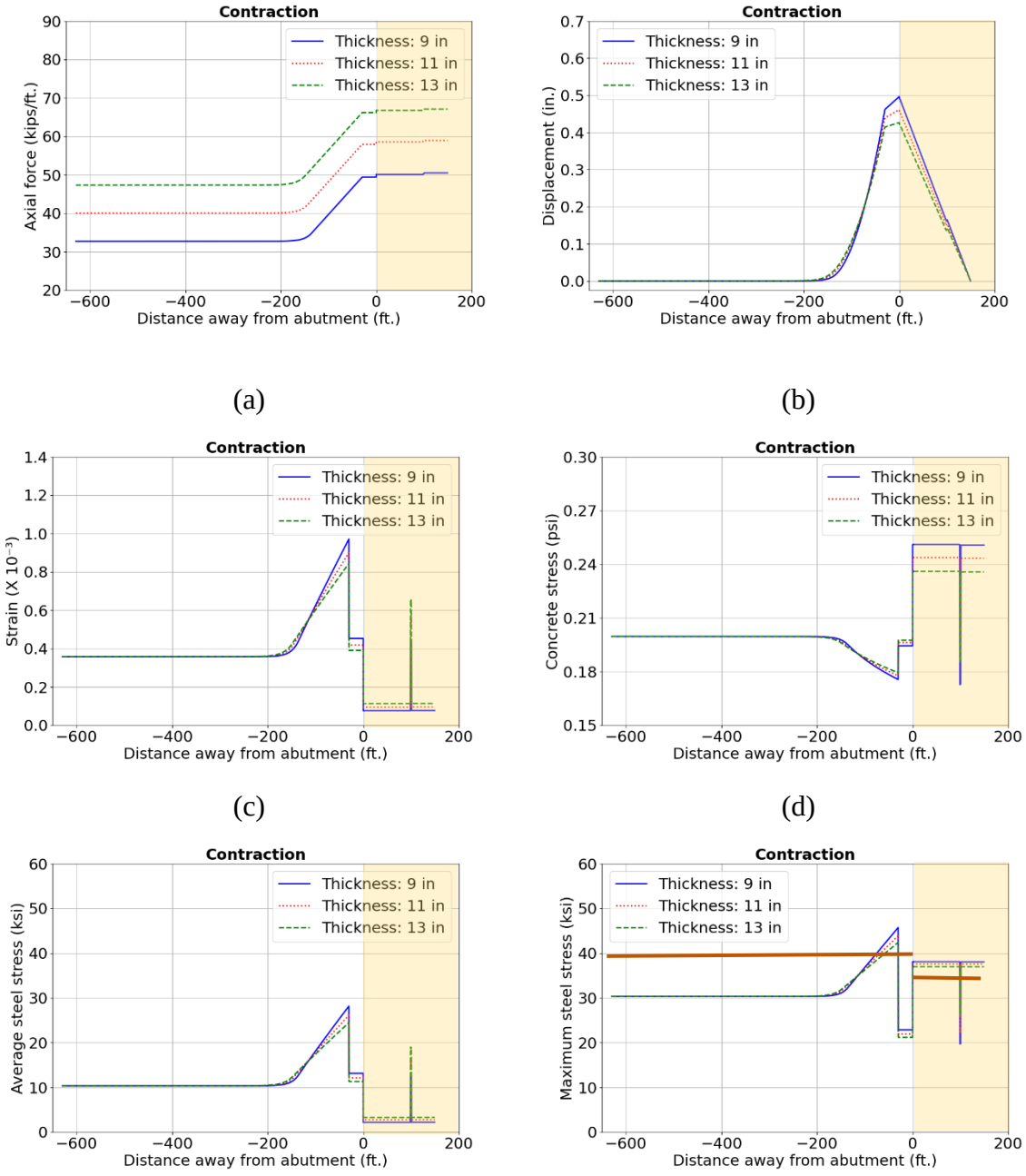

Figure 5.21: Results for different slab thicknesses: (a) Axial force; (b) Longitudinal displacement; (c) Concrete strain; (d) Concrete stress; (e) Average steel stress; (f) Maximum steel stress.

Generally, the transition slab thickness is designed to be consistent with the CRCP it connects to, which simplifies the construction procedure. The transition length and reinforcement details within the transition zone should be designed based on the specific thickness of the slab once it is determined since it can largely influence the force demand and stress distribution in the seamless system.

5.5.4 Reinforcement of Transition Slab

The amount of reinforcement in the transition slab also affects the stiffness of the pavement and controls the cracking behavior of the reinforced concrete. A report by the Federal Highway Administration (Roesler et al. 2016) has shown that desired crack patterns are developed in CRCP with a longitudinal reinforcement ratio in the range of 0.7%-0.8%. The reinforcement ratio in the transition zone is expected to be larger than that for a conventional CRCP considering the additional axial force due to the bridge-pavement interaction. The variation in the reinforcement ratio in the transition slab that was evaluated consisted of 1%, 1.5%, and 2%. The reinforcement ratio of the approach slab was kept at 2%. Figure 5.22 compares the axial responses for three levels of reinforcement ratio in the transition slab.

The effects of the reinforcement ratio of the transition slab on the axial response of the seamless system show a similar trend as that of the slab thickness. This is because both the slab thickness and the reinforcement ratio affect the axial stiffness of the reinforced concrete pavement to resist the movements caused by bridge expansion and contraction. The increase in reinforcement amount leads to the increase in axial stiffness of the pavement, which generates higher axial forces in the system with the same temperature changes. It places a higher tensile strain demand for the approach slab, bridge decks, and link slabs. For the transition slab, although the axial force increases, the strain demand decreases as the section with more reinforcement is stronger in resisting axial forces. Consequently, the maximum steel stress is lower for a transition slab with a higher reinforcement ratio.

The relative stiffness of the bridge and pavement influences the magnitude of the transition movement. The required length of the transition zone to dissipate the thermal movements is not affected by the reinforcement ratio of the transition slab. Instead, it is mainly controlled by the restraint at the concrete slab-base interface.

Using a constant reinforcement ratio in the transition zone may not be economical since the demand in the transition zone gradually increases with proximity to the bridge. The reinforcement amount can be reduced in the regions with a smaller demand. Dividing the transition zone into multiple regions with gradually varying reinforcement amounts which was used by Australia is generally a good practice to optimize the use of reinforcement. A higher reinforcement ratio in the approach slab serves two purposes: 1) to deal with the high axial demand since the movement and axial force are the largest in this region; 2) to have some reserved capacity for bending due to differential embankment settlement and vehicle loads.

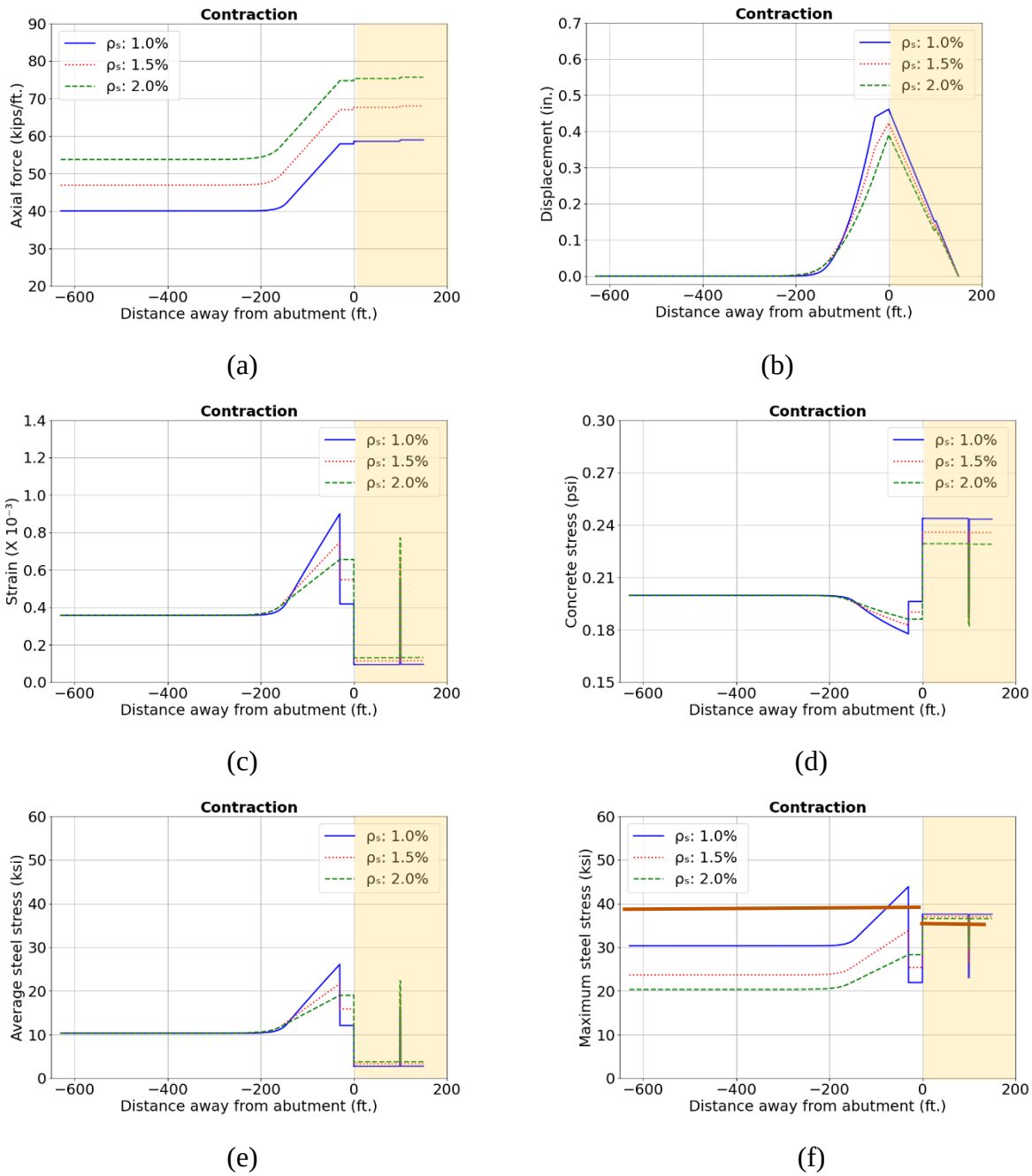

Figure 5.22: Results for different reinforcement ratios: (a) Axial force; (b) Longitudinal displacement; (c) Concrete strain; (d) Concrete stress; (e) Average steel stress; (f) Maximum steel stress.

5.5.5 Temperature Change

As described in Section 5.2.5, the respective values of the maximum temperature decrease to be considered in the design of a bridge and a pavement are 55°F and 45°F based on their specified ambient temperature and allowable concrete placement temperature range. In the previous analysis, a temperature decrease of 55°F was assumed for both bridge and pavement. This section also discusses the axial responses in the cases where differential thermal strains occur between the

bridge and pavement. The values of the temperature decrease were assumed as 35°F, 45°F, and 55°F for the pavement while keeping a temperature decrease of 55°F for the bridge. The conditions of temperature increase were not investigated because the concrete in compression is not critical for the design. Figure 5.23 compares the axial responses with three temperature change conditions.

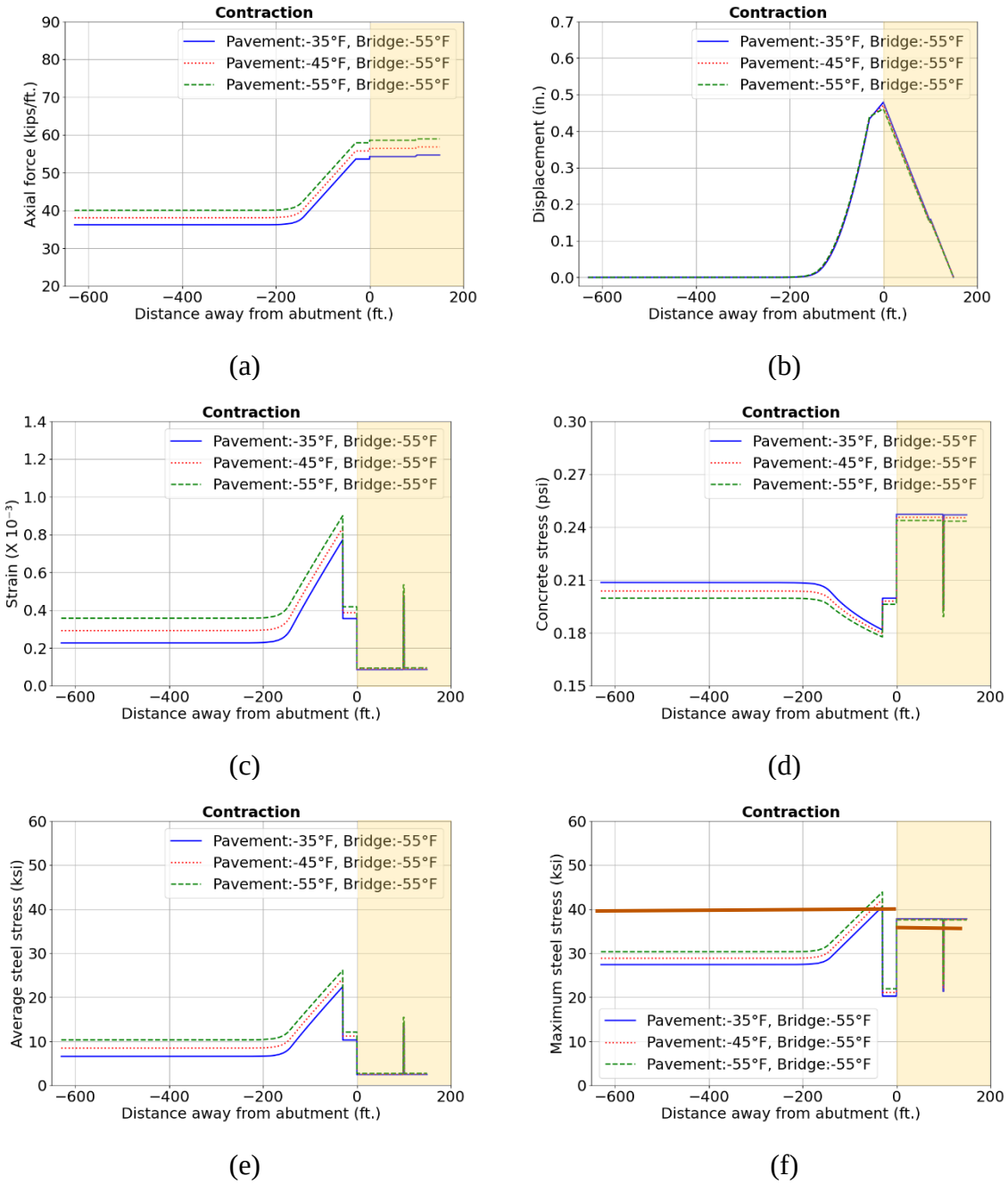

Figure 5.23: Results for different temperature changes: (a) Axial force; (b) Longitudinal displacement; (c) Concrete strain; (d) Concrete stress; (e) Average steel stress; (f) Maximum steel stress.

The tensile strains in the pavement are higher when a larger temperature change is experienced by the pavement. The tensile strains in the bridge are almost the same in three conditions because the temperature changes experienced by the bridge are the same. The axial force in the system is a bit higher when the pavement and bridge experience larger temperature changes. In conclusion, the response of a seamless system with a temperature decrease of $55°F$ for both the bridge and pavement is most critical and is assumed as the worst-case scenario for the design.

5.6 Analysis of Standard TxDOT Bridges

5.6.1 Overview

This section presents results from the axial analysis of seamless bridge systems considering standard TxDOT bridges and CRCP designs. The parametric studies are aimed to include the modeling variations that represent the range of common geometries involving the span lengths, number of spans, number of girders, and girder sizes (cross-sections) to compare the responses of different bridge configurations. For each bridge configuration, the responses with the concrete slab-base interaction provided by two promising bond breakers, i.e., double-sided textured linear low-density polyethylene sheet ($\mu = 0.4$) and felt paper ($\mu = 0.7$) were analyzed. Two loading conditions were applied: the maximum possible expansion (temperature increase), and the maximum possible contraction (temperature decrease). These parametric studies of bridge configurations provide insight into the expected behavior of the seamless system of standard TxDOT bridges and CRCPs with the use of the proposed bond breakers in the transition zone under the worst conditions.

The same pavement design was used for the transition zone between the bridge and CRCP, regardless of the bridge configuration. The transition pavement design was the same as that used in the models of Section 5.3, which divided the transition zone into three different segments, as shown in Figure 5.10. The reinforcement ratio and corresponding length for each segment were 0.75% and 430 ft, 1.1% and 100 ft. and 1.45% and 70 ft, with the 70 ft. region nearest the approach slab (bridge).

Table 5.3: Details of TxDOT bridge configurations for parametric analysis.

Girder Type	Span length (ft.)	# of spans	# of girders
Tx28 (A=585 in^2)	40 70	3	5
Tx34 (A=627 in^2)	40 80	3	5
Tx54 (A=817 in^2)	40 80 125	3	5
	125	4	5
	125	3	6

Table 5.3 summarizes the details of the bridge configurations for the parametric studies. TxDOT generally makes use of standard precast prestressed reinforced concrete girders for bridges, such as Tx28, Tx34, or Tx54. The integer represents the nominal depth of the girder. A three-span Tx54

bridge with a span length of 125 ft. is common and was considered as a prototype bridge for this study. Smaller girder sizes of Tx28 and Tx34 were also examined. The typical maximum span length associated with the respective girders are Tx28 – 70 ft., Tx34 – 80 ft., and Tx34 – 125 ft. Both three-span and four-span bridges were considered. The total bridge lengths varied from 120 ft. to 500 ft. Typical values for the overall bridge deck widths were taken as 40 ft. and 46 ft, which will likely make use of five and six standard girders, respectively. Therefore, the effects of the number of girders were also investigated. The cross-section area of each type of girder is also listed in the table. In total, 9 different bridge configurations were investigated.

5.6.2 Span Length

Figure 5.24 to Figure 5.29 show the axial responses for three-span Tx28, Tx34, and Tx54, bridges with different span lengths. The results for cases with both expansion and contraction are presented. The axial force per unit width and displacement are presented along the transition zone and half of the bridge. The maximum steel stress in the case of contraction is presented since it is one of the most important indicators for the design of a seamless bridge-pavement system. The effects of the concrete slab-base interaction are compared for values of the coefficient of friction of 0.4 and 0.7. The origin indicates the location of the bridge abutment, with the transition zone on its left and the bridge on its right. All figures for different configurations presented in this section are plotted with the same scale for comparison.

The change in the bridge span length impacts the interaction between the bridge and pavement when they are seamlessly connected. Increasing the span length leads to an increase in the force demand in the system. The axial force and strain demands increase for longer span lengths. In general, the concrete compressive stress is higher for expansion cases while the maximum steel stress is higher for contraction cases. In the case of Tx54 girders with a span length of 125 ft., the maximum steel stress near the end of the transition is a bit higher than the target value of 40 ksi. The reinforcement within this region might be increased to reduce the stress below the target value and satisfy the design criterion. Aside from this case, the maximum rebar stress can be controlled below 40 ksi for the pavement and 36 ksi for the bridge decks considering the single transition slab design proposed in this study. Similar trends are also observed for Tx34 and Tx28 bridges with different span lengths.

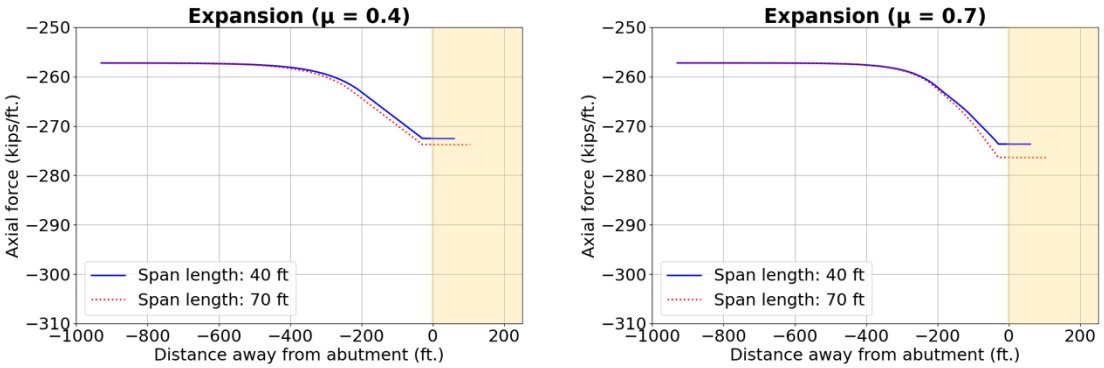

(a)

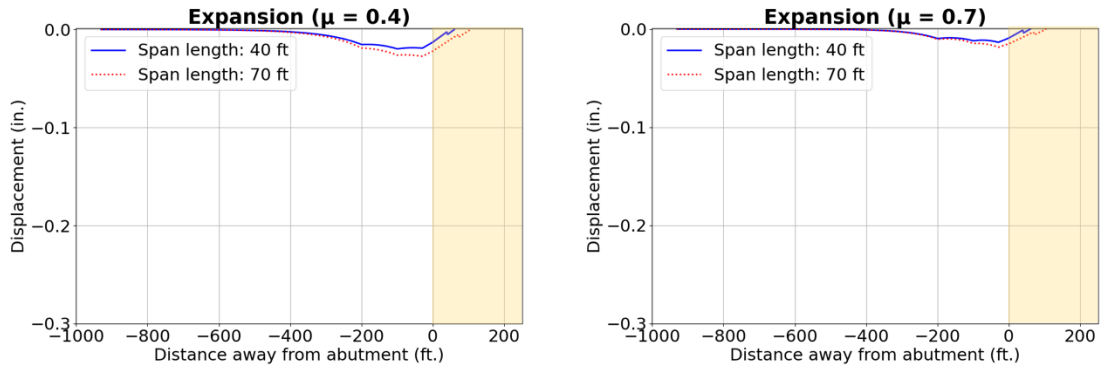

(b)

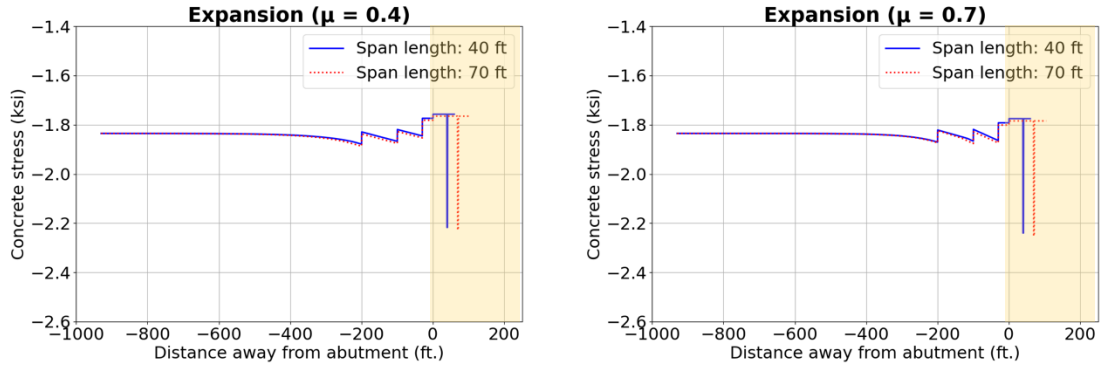

(c)

Figure 5.24: Results of Tx28 bridges with different span lengths (temperature increase): (a) Axial force; (b) Longitudinal displacement; (c) Concrete stress.

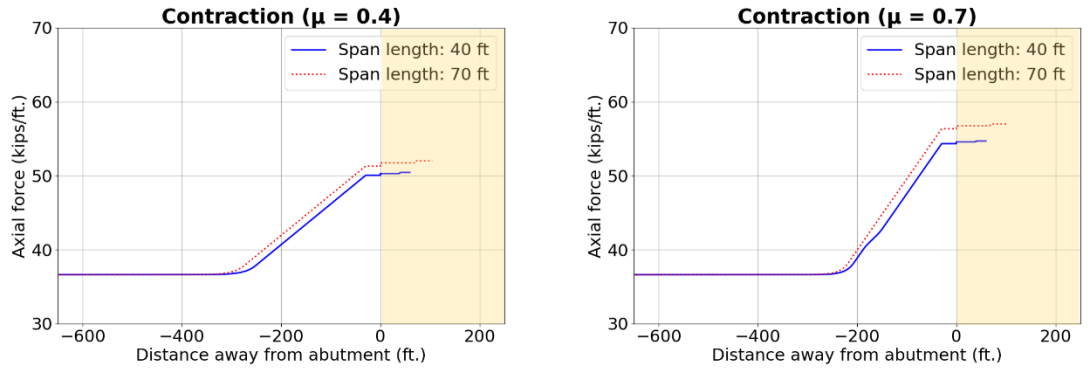

(a)

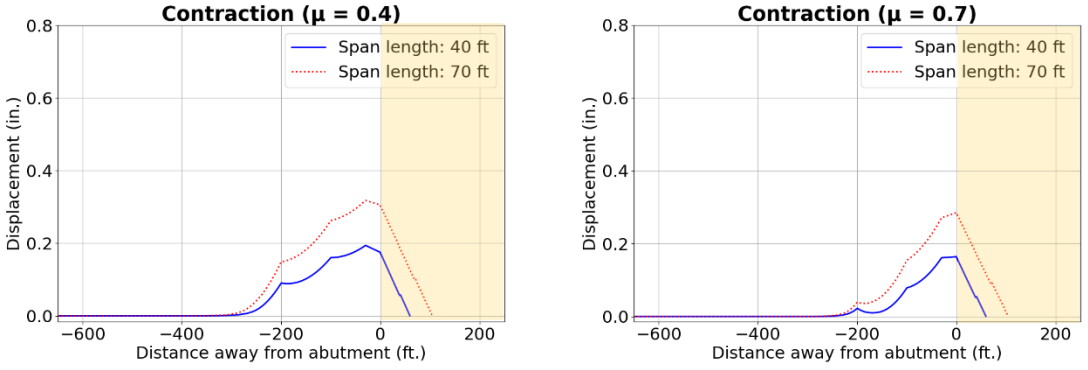

(b)

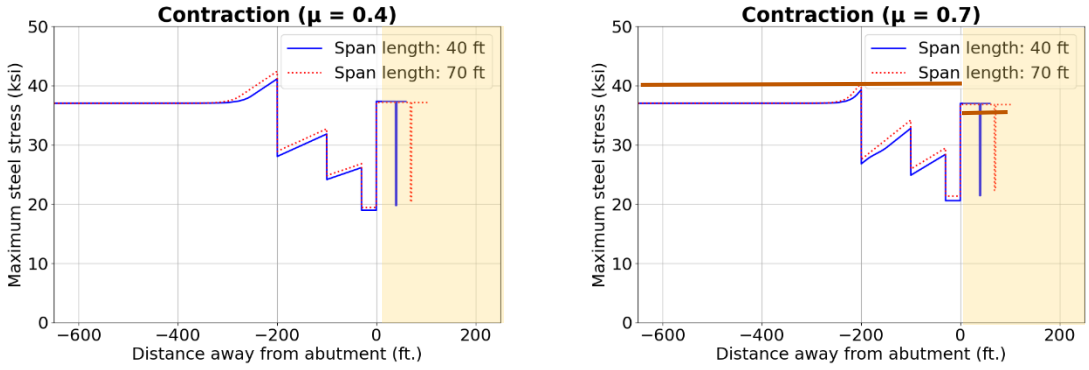

(c)

Figure 5.25: Results of Tx54 bridges with different span lengths (temperature decrease): (a) Axial force; (b) Longitudinal displacement; (c) Maximum steel stress.

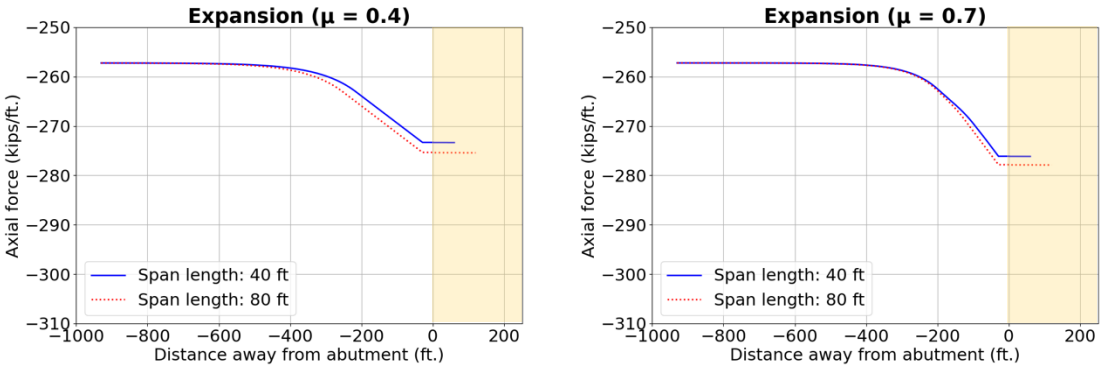

(a)

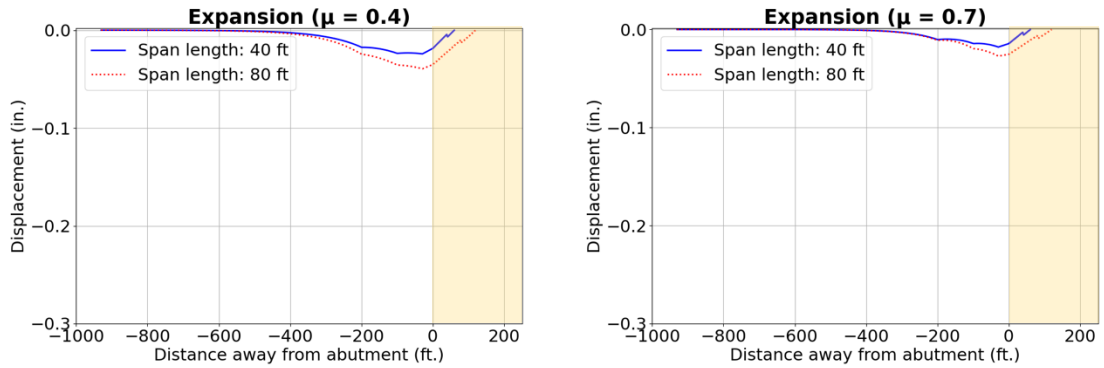

(b)

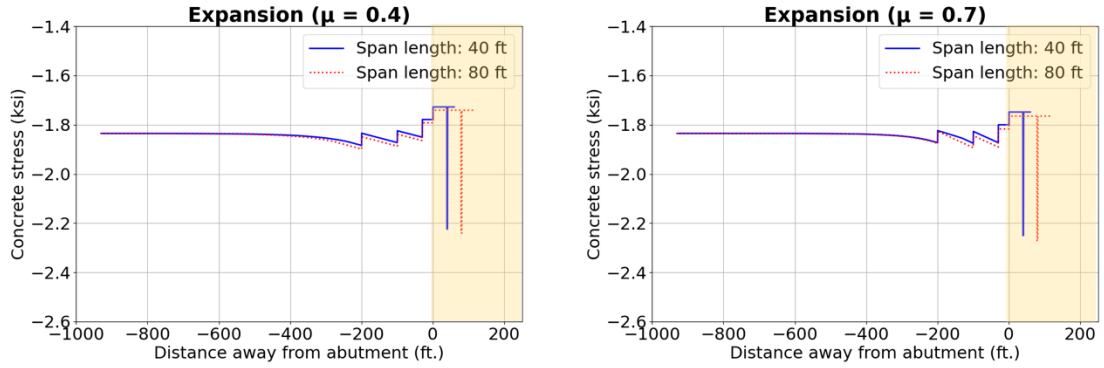

(c)

Figure 5.26: Results of Tx34 bridges with different span lengths (temperature increase): (a) Axial force; (b) Longitudinal displacement; (c) Concrete stress.

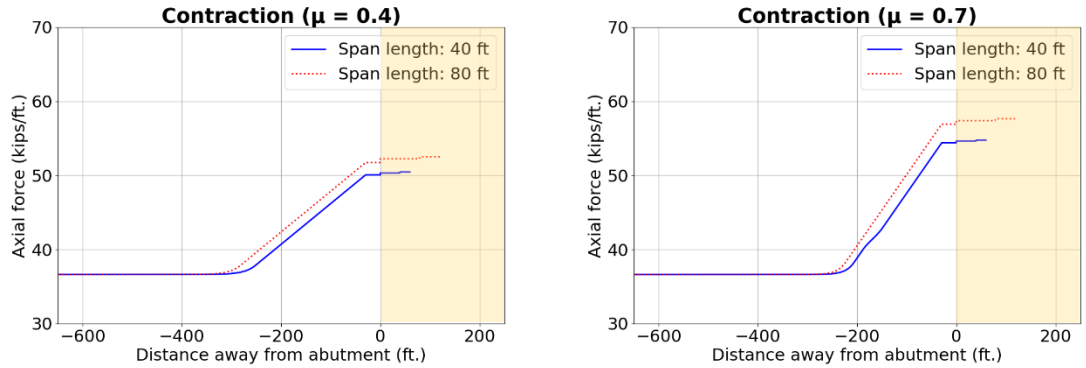

(a)

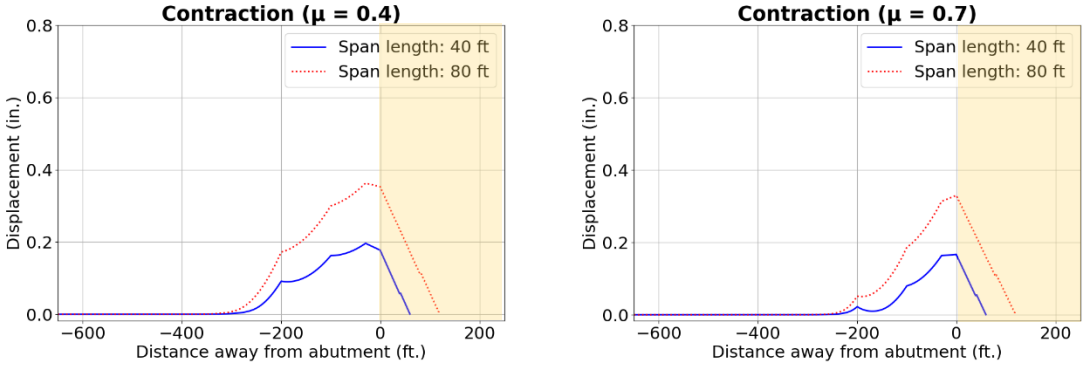

(b)

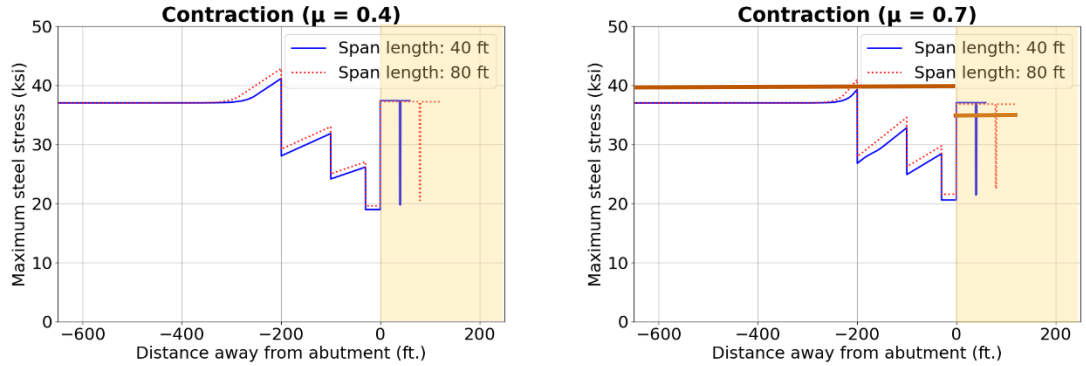

(c)

Figure 5.27: Results of Tx34 bridges with different span lengths (temperature decrease): (a) Axial force; (b) Longitudinal displacement; (c) Maximum steel stress.

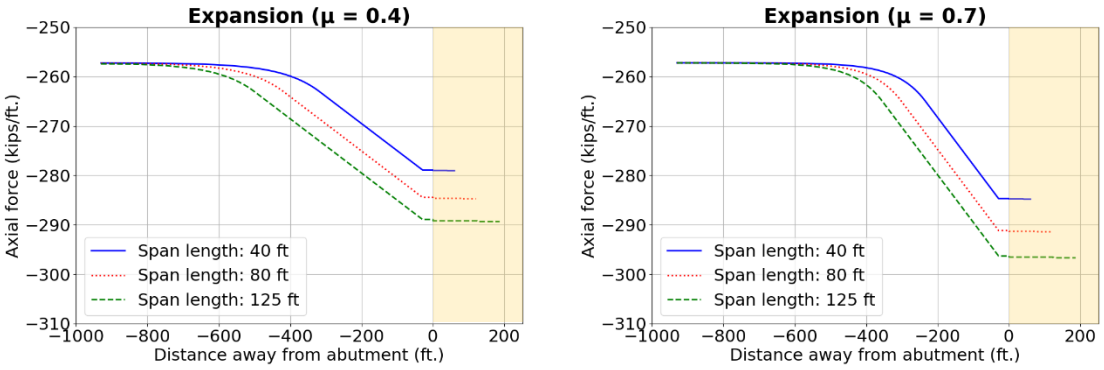

(a)

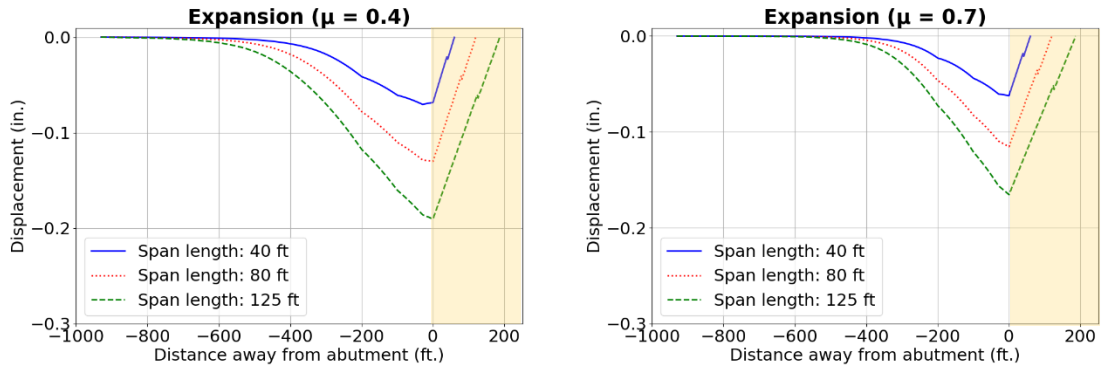

(b)

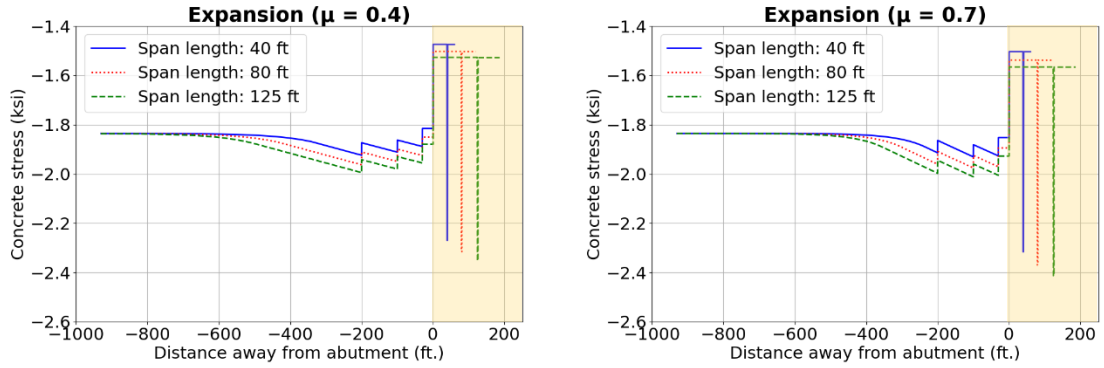

(c)

Figure 5.28: Results of Tx54 bridges with different span lengths (temperature increase): (a) Axial force; (b) Longitudinal displacement; (c) Concrete stress.

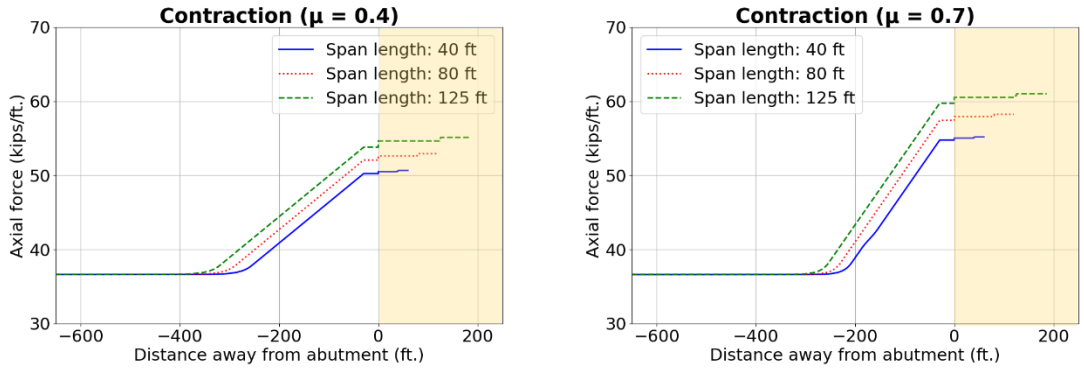

(a)

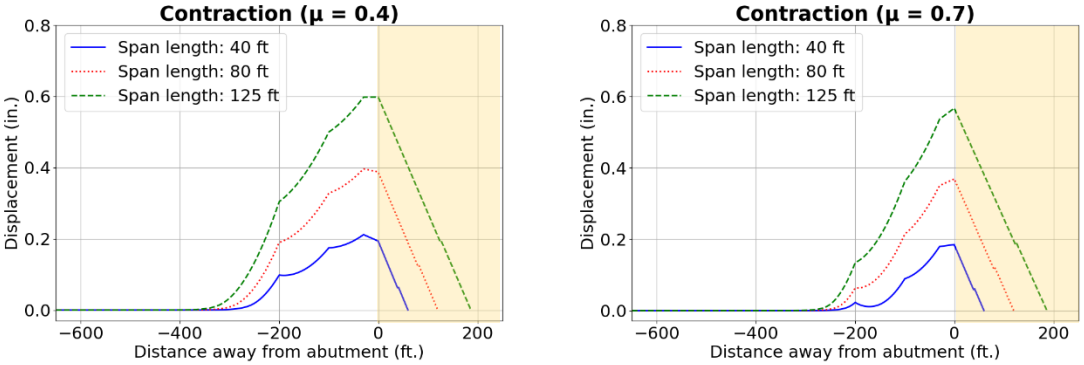

(b)

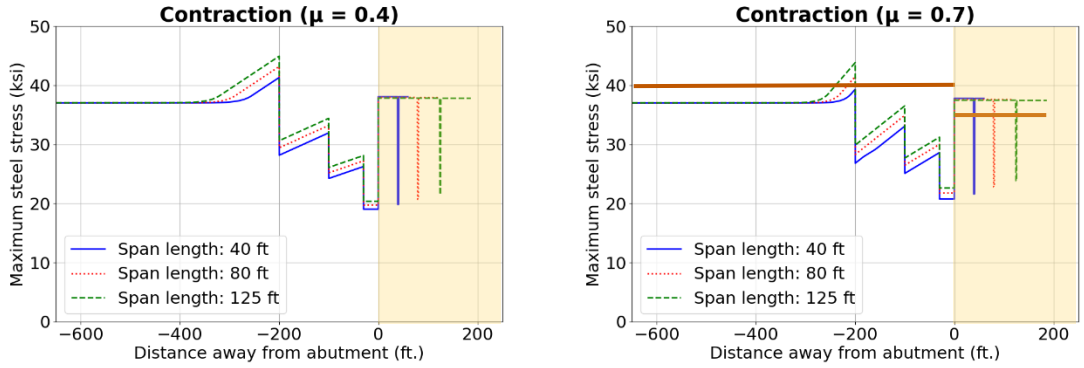

(c)

Figure 5.29: Results of Tx54 bridges with different span lengths (temperature decrease): (a) Axial force; (b) Longitudinal displacement; (c) Maximum steel stress.

5.6.3 Number of Spans

In this sub-section, the effects of the number of spans on the axial response of the seamless system were investigated for the bridges with the Tx54 girders. Specifically, bridges with 3 and 4 spans were analyzed which are reasonably common bridges constructed in Texas. Figure 5.30 and Figure 5.31 show the results for the cases of expansion and contraction, respectively. The effects of concrete slab-base interaction are compared for a coefficient of friction of 0.4 and 0.7.

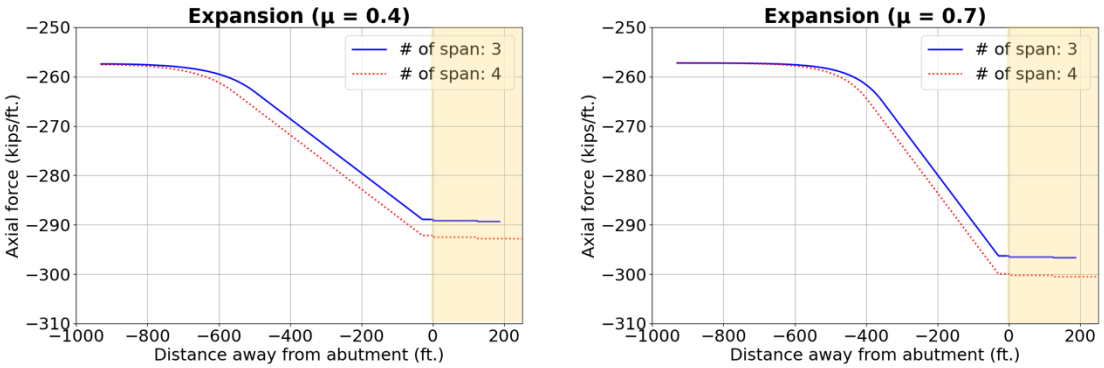

(a)

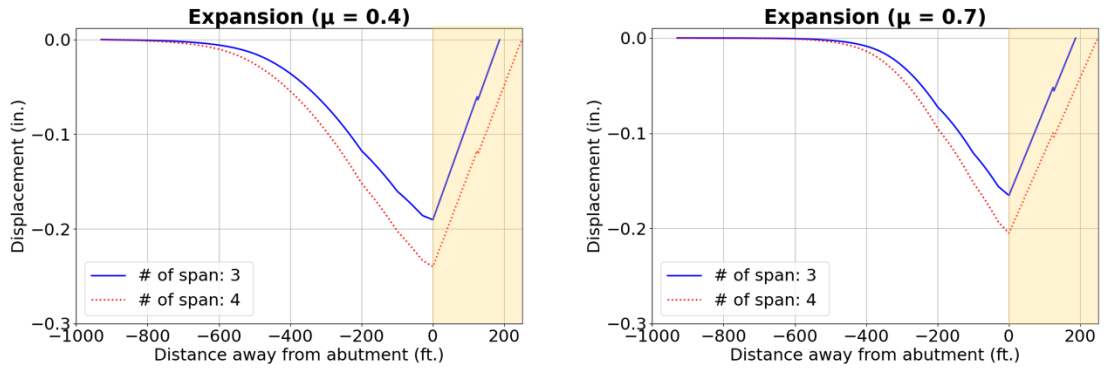

(b)

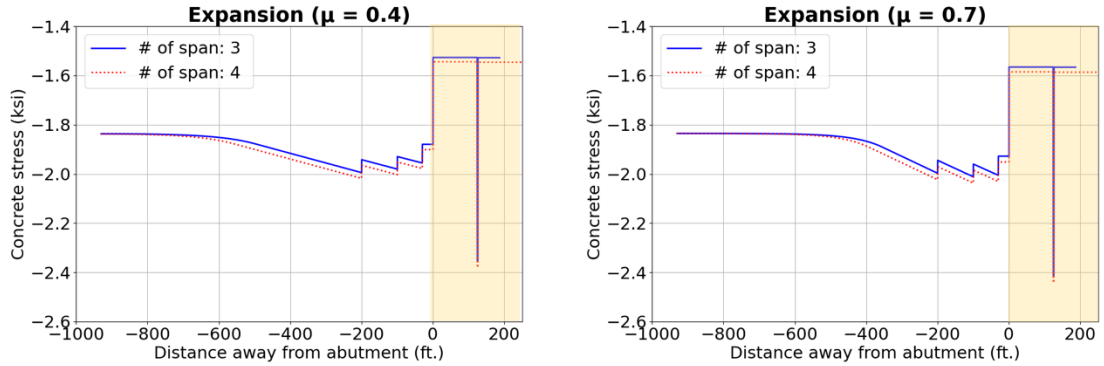

(c)

Figure 5.30: Results of Tx54 bridges with different numbers of spans (temperature increase): (a) Axial force; (b) Longitudinal displacement; (c) Concrete steel stress.

The increase in the number of spans generally results in larger force demands in the system similar to the behavior observed with increases of the bridge span length. The larger number of spans leads to the rise of the compression or tension forces, strain, and concrete compressive stresses/maximum steel stresses in the system.

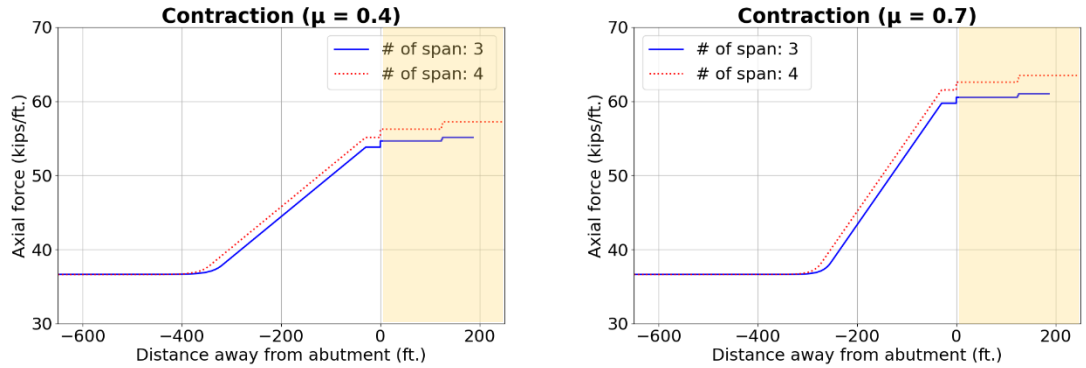

(a)

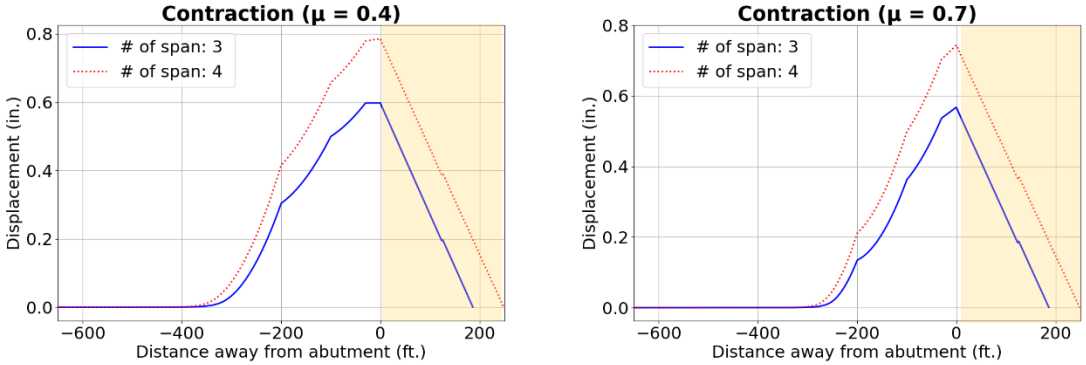

(b)

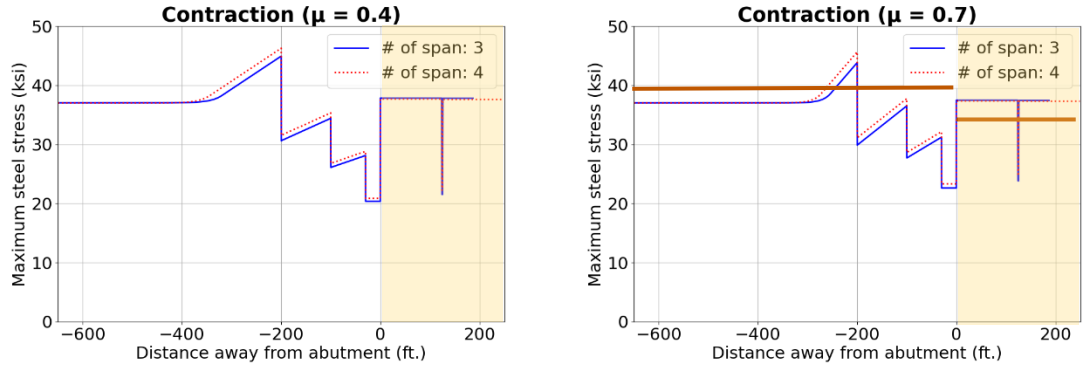

(c)

Figure 5.31: Results of Tx54 bridges with different numbers of spans (temperature decrease): (a) Axial force; (b) Longitudinal displacement; (c) Maximum steel stress.

5.6.4 Number of Girders

The axial analyses of the seamless system with different number of girders were conducted using the bridges with the Tx54 girders. Bridge widths of 40 ft and 46 ft were used, which is consistent with many bridge geometries. Correspondingly, 5 or 6 girders are used to support bridge decks of those widths. Figure 5.32 and Figure 5.33 show the results in the case of expansion and contraction, respectively. The effects of concrete slab-base interaction are compared for a coefficient of friction of 0.4 and 0.7.

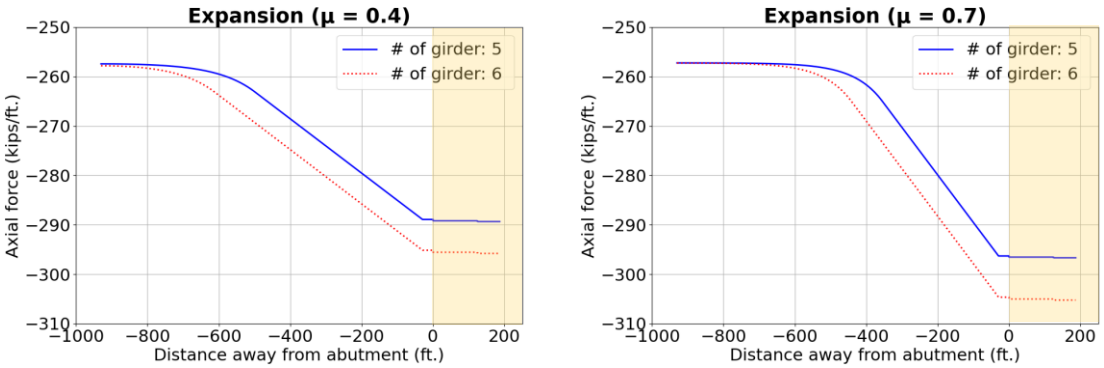

(a)

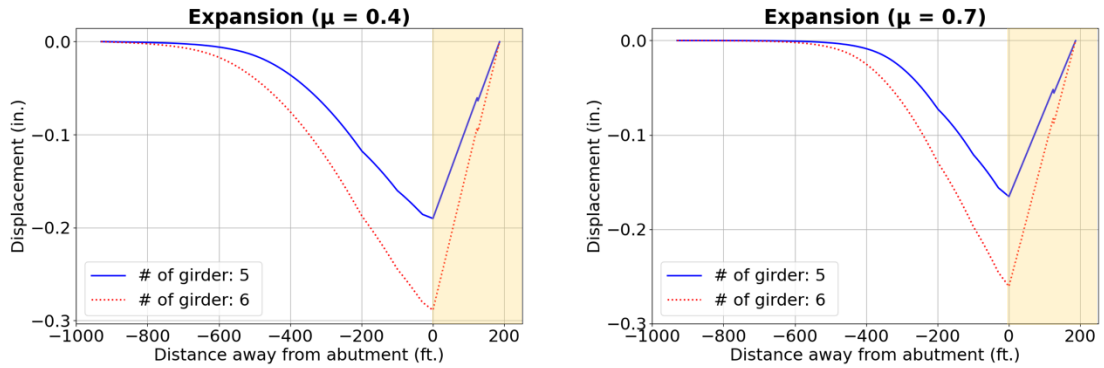

(b)

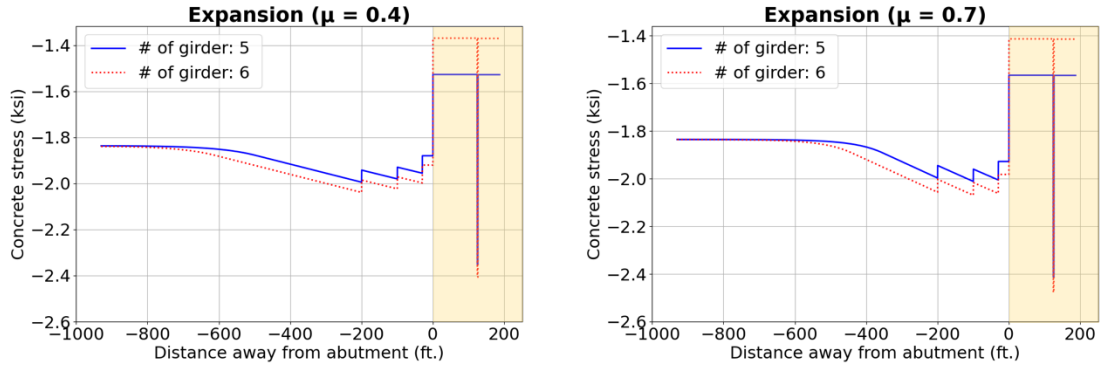

(c)

Figure 5.32: Results of Tx54 bridges with different numbers of girders (temperature increase): (a) Axial force; (b) Longitudinal displacement; (c) Concrete stress.

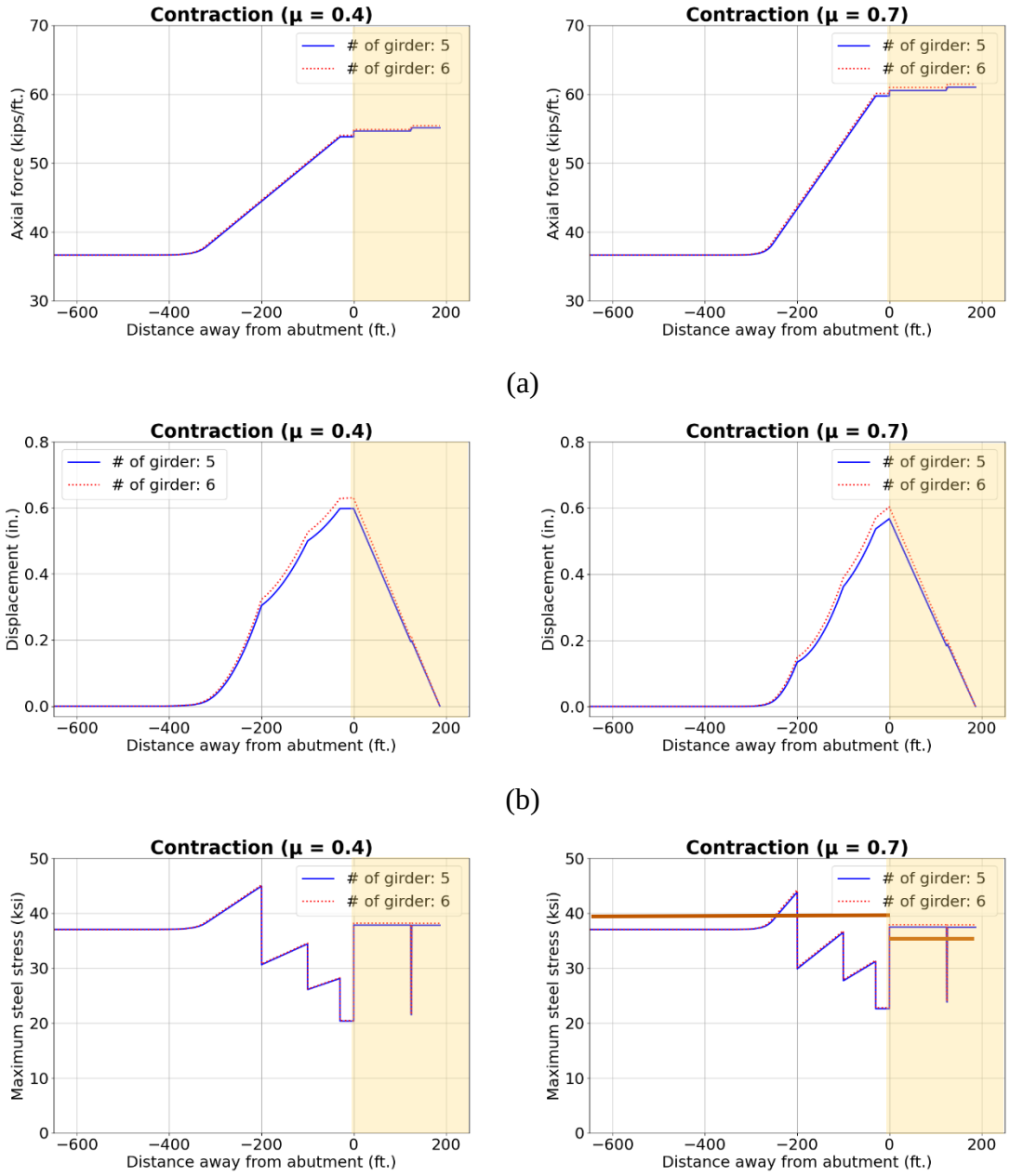

Figure 5.33: Results of Tx54 bridges with different numbers of girders (temperature decrease): (a) Axial force; (b) Longitudinal displacement; (c) Maximum steel stress.

For the same bridge girder size, span lengths, and the number of spans, increasing the number of girders generally increases the stiffness of the bridge, which results in a higher demand for both the pavement and bridge for the expansion case, as shown in Figure 5.32. For the contraction conditions, however, the increase of demands when the number of girders increases to 6 is generally negligible as shown in Figure 5.33. This can be explained by the fact that when in tension, the overall stiffness of the system is mainly governed by the cracked elements (pavement and link slabs).

5.6.5 Girder Size

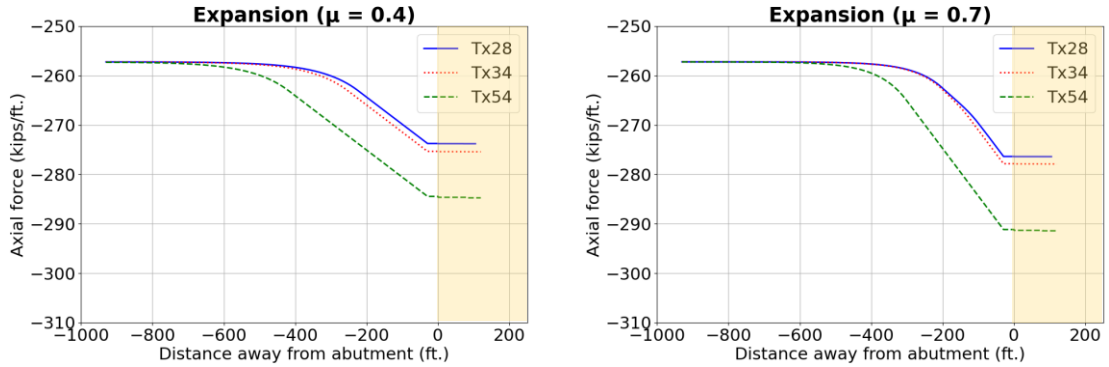

(a)

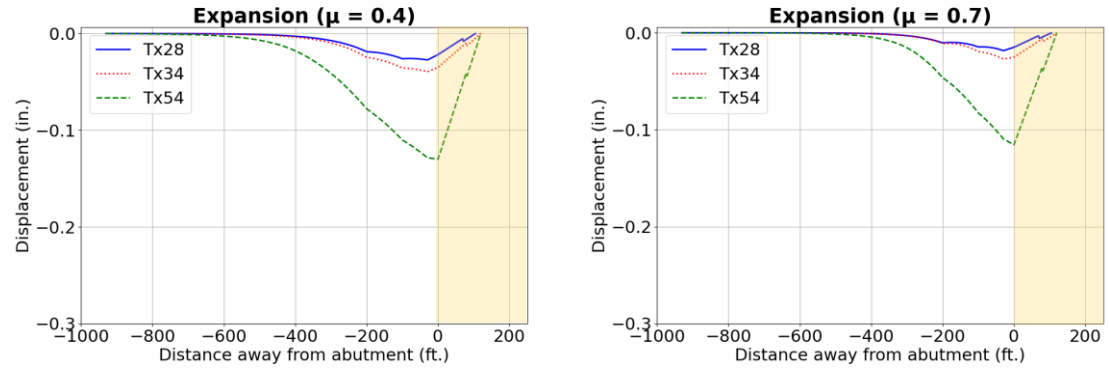

(b)

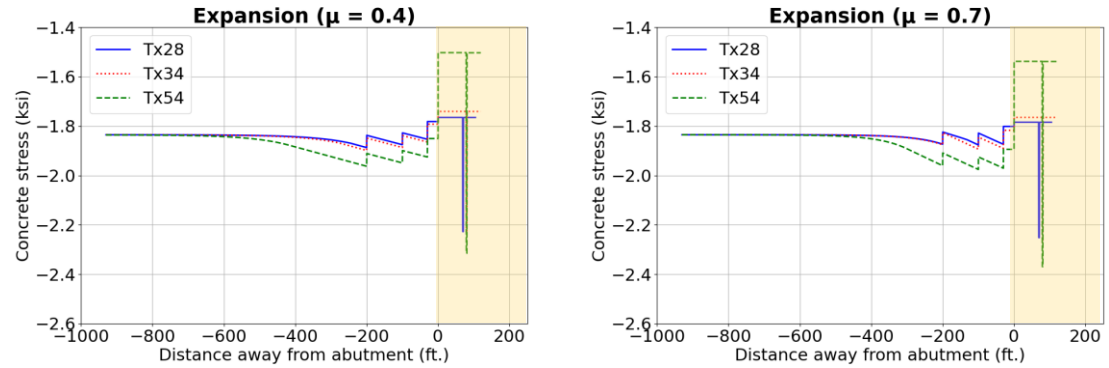

(c)

Figure 5.34: Results for bridges with different girder sizes (temperature increase): (a) Axial force; (b) Longitudinal displacement; (c) Concrete stress.

The axial stiffness of the bridge is generally dominated by the bridge girders. Using different girder sizes changes the relative stiffness of the bridge and pavement elements. As noted earlier, Tx54, Tx34, and Tx28 girders, which are commonly used in Texas, have cross-sections in descending order. Figure 5.34 and Figure 5.35 compare the axial responses for three girder sizes with a bridge span length of 80 ft. (70 ft. for the case of the Tx28 bridge). The effects of concrete slab-base interaction are compared for a coefficient of friction of 0.4 and 0.7.

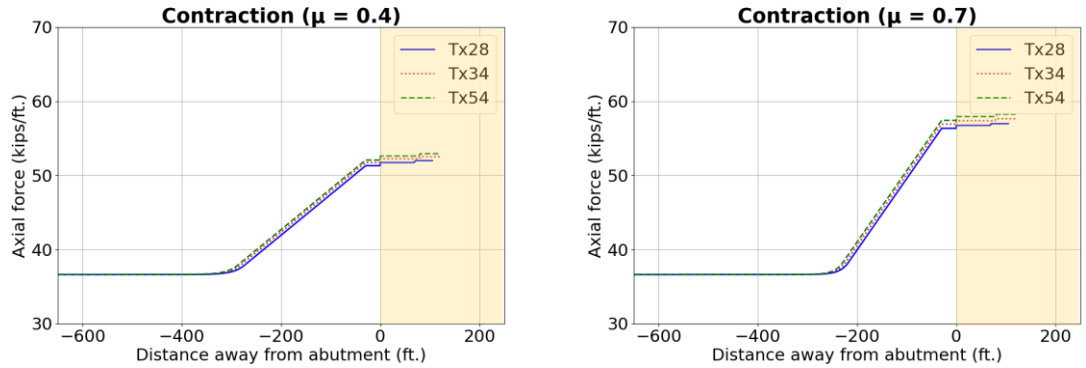

(a)

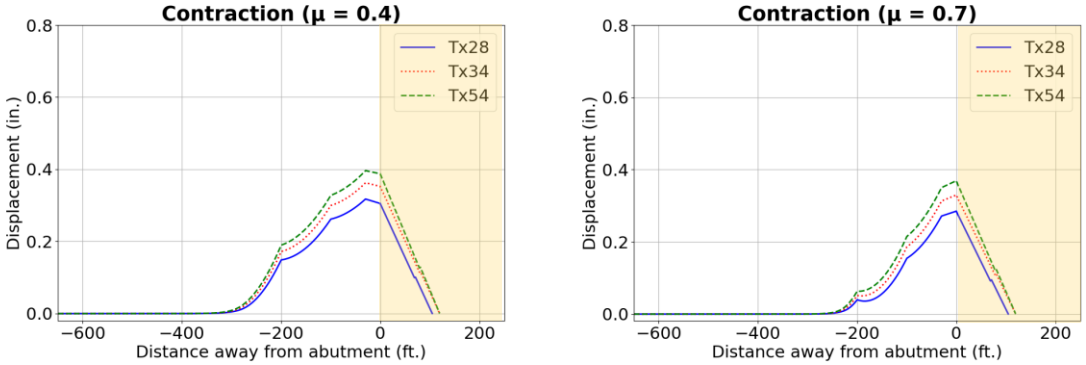

(b)

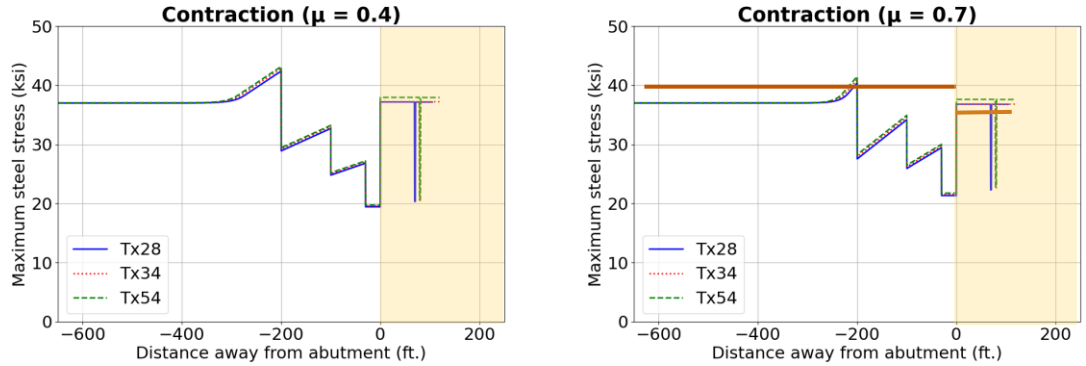

(c)

Figure 5.35: Results for bridges with different girder sizes (temperature decrease): (a) Axial force; (b) Longitudinal displacement; (c) Maximum steel stress.

The behavior between Tx28 and Tx34 bridges is very similar due to the relatively small differences in cross-section between these two types of girders. The use of Tx54 girders enlarges the axial demand in the system. Similar to the impact of the number of girders, the increase in demand is noticeable for the expansion case but not significant for the contraction case.

5.6.6 Final Remarks

In conclusion, using different bridge span lengths, number of bridge spans, number of bridge girders, and girder size will change the demand from the bridge side with temperature changes, which affects the bridge-pavement interaction. As a result, the compressive/tensile forces developed in the system and material stresses are influenced by these parameters. One exception is the number and size of girders for the contraction condition, as the difference in axial stiffness provided by the girders practically does not matter when cracking occurs in the pavement and link slabs.

By comparing the axial force and displacement plots for different bridge configurations in both conditions, it is generally true that a longer transition zone where the bond breaker is applied is needed for the bridge expansion condition than that for the bridge contraction condition. Considering the relative strength of concrete in compression, the design of the reinforcement amount in the transition zone is controlled by the bridge contraction condition. Table 5.4 summarizes the required length of the transition zone determined in the case of contraction for different bridge configurations.

Another relevant conclusion of the parametric analysis is that a single design of the transition slab, with a total length of 400 ft. and reinforcement ratios varying between 0.75% and 1.45%, and a 30-ft.-long approach slab with 2% reinforcement ratio would be appropriate for most of the bridge configurations analyzed here. While in some cases the design could be further optimized by reducing the amount of steel, this indicates that some level of standardization can be achieved for design guidelines of seamless systems if accepting some level of extra conservatism.

Table 5.4: Required length of the transition zone for different bridge configurations.

Girder type	Span length (ft.)	# of spans	# of girders	Total length (ft.)	Length of transition zone (ft.)	
					$\mu = 0.4$	$\mu = 0.7$
Tx54	40	3	5	120	320	250
	80			240	350	270
	125			375	380	300
	125	4	5	500	400	320
	125	3	6	375	380	300
Tx34	40	3	5	120	300	230
	80			240	320	250
Tx28	40	3	5	120	300	230
	70			210	320	250

It can be seen that for a bridge with a longer span length, more spans, more girders, or a larger girder cross-section area, a longer minimum transition zone is generally required. The required length of the transition zone in the case of $\mu = 0.4$ is approximately 1.3 times the length in the case of $\mu = 0.7$.

It should be noted that the derived minimum required length of the transition zone is based on the reinforced concrete pavement with a thickness of 11 in. using the preliminarily proposed reinforcement configuration. The bridge-pavement interaction due to the seamless connection is controlled by the relative stiffness of bridge and pavement elements, which determines the axial

behavior of the seamless system. For a different pavement thickness, the stiffness of the pavement and the frictional forces provided by the base may change, as discussed in Section 5.5.3.

5.7 Extended Application to JCP/Flexible Pavement

5.7.1 Background

Pavements are generally categorized into two types, rigid and flexible pavement, based on the flexural stiffnesses. Rigid pavement is composed of Portland cement concrete, whereas flexible pavement is surfaced with bituminous materials. The most common types of concrete pavements used in Texas are jointed concrete pavement (JCP) and CRCP (TxDOT, 2019). JCP deals with thermal stresses through transverse cracks but in a different pattern compared to CRCP. For CRCP, continuously longitudinal reinforcement is provided with a goal of limiting cracking to closely spaced cracks (common crack spacing ranges from 1.5 to 6 ft.), which limits the crack width and ensures the efficient load transfer between two adjacent CRCP panels. However, JCP typically consists of uniformly spaced joints so that the number and location of transverse cracks are pre-determined. Typically, the spacing of transverse cracks is approximately 15 to 20 ft. (Roesler et al., 2016). The adjacent plain concrete segments are joined by dowel bars.

The present study focuses on the application of the seamless connection technology applied with CRCP, as shown in Figure 5.36(a), but a similar concept could be applied to flexible pavements and JCP. The original seamless bridge-CRCP system makes the system fully jointless by eliminating both the expansion joints originally located at the bridge abutment and the end of the approach slab. The key longitudinal load-transfer mechanism relies on the concrete slab-base interaction within the transition zone, which is a particularly designed continuous reinforced concrete pavement between the bridge and the conventional CRCP. The investigation of boundary conditions as presented in Section 5.4.2, demonstrates that the same behavior of the transition zone and bridge will be obtained if a certain length of conventional CRCP with an unrestrained end is connected at the end of the transition zone. With an additional length of CRCP, the strong restraint from the base helps restrain the movement of the transition zone and the effects of the bridge-pavement interaction can be dissipated through the transition zone, and the movements obtained at the end of the CRCP are solely due to the local contraction/expansion of the pavement itself.

The use of CRCP with an unrestrained end can achieve the same objective of dissipating bridge movements over a transition slab and is not limited to roadways that use CRCP. The proposed load-transfer mechanism provided by the interaction at the concrete slab-base interface could be potentially extended to the circumstances that the pavement is JCP or flexible pavement, as shown in Figure 5.36(b). This concept requires only the use of CRCP (with and without bond breakers) near the bridge.

This section outlines results of a study focused on the theoretical feasibility of extending the seamless connection technique to JCP or flexible pavements. The axial behavior of the transition zone connected with an additional CRCP segment at its end is demonstrated. The required length of the CRCP segment in the cases of expansion and contraction is explored. The same model for the investigation of boundary conditions was used in the analysis. The difference between the transition zone and a short CRCP panel is mainly from whether a bond breaker is used between the base and concrete pavement. Under CRCP, a large apparent coefficient of friction was assumed to represent the strong restraint provided by the stabilized base without bond breakers. A relatively

low coefficient of friction was assumed for the transition zone, considering that a bond breaker is used to eliminate the adhesion at the interface. To demonstrate the axial behavior and investigate the effects of the length of the CRCP panel, the apparent coefficient of friction for the transition zone and CRCP was taken as 0.8, and 3.5, respectively. The effects of slab-base interaction for the CRCP were also investigated.

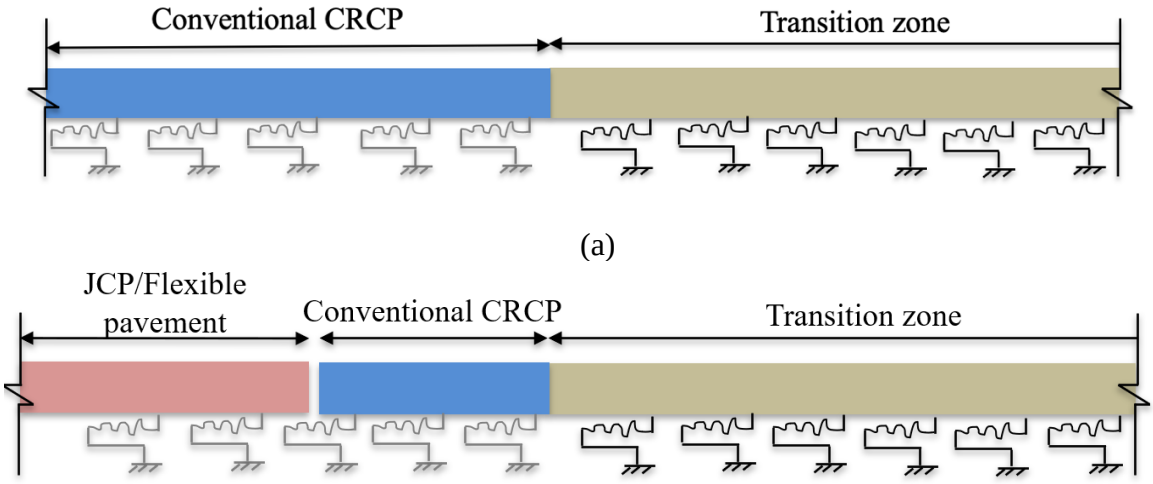

Figure 5.36: A scheme of seamless connection for CRCP and JCP/flexible pavement: (a) Seamless connection for CRCP; (b) Seamless connection for JCP/flexible pavement.

5.7.2 Axial Behavior

Figure 5.37 and Figure 5.38 show the axial response of the bridge deck, transition zone, and a certain length of CRCP in the case of expansion (temperature increase of 80°F) and contraction (temperature decrease of 55°F) conditions. The specific length of CRCP at the end of the transition zone is marked as shaded area in light green. It is noted that the respective length of the additional CRCP considered were 100 ft. and 600 ft. for expansion and contraction conditions. Trial tests were preliminarily conducted to determine the minimum required length of CRCP required to provide sufficient restraint to the transition zone. More details of the effects of the length of the CRCP are presented next.

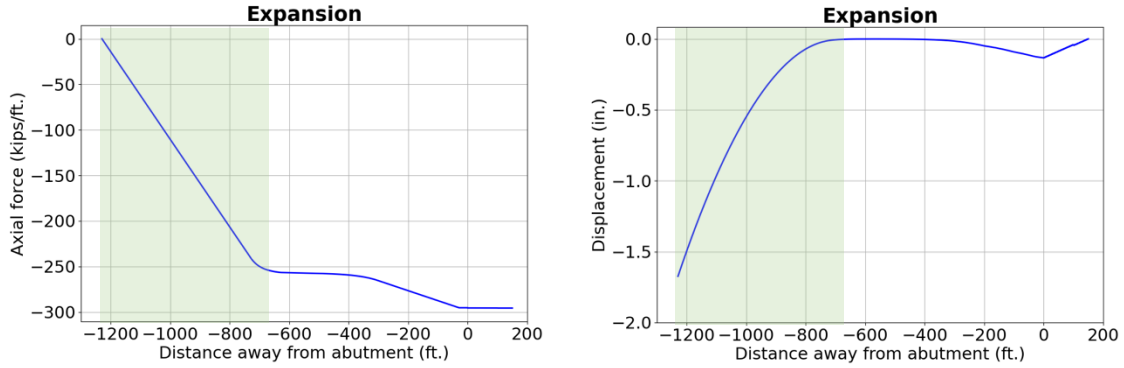

(a) (b)

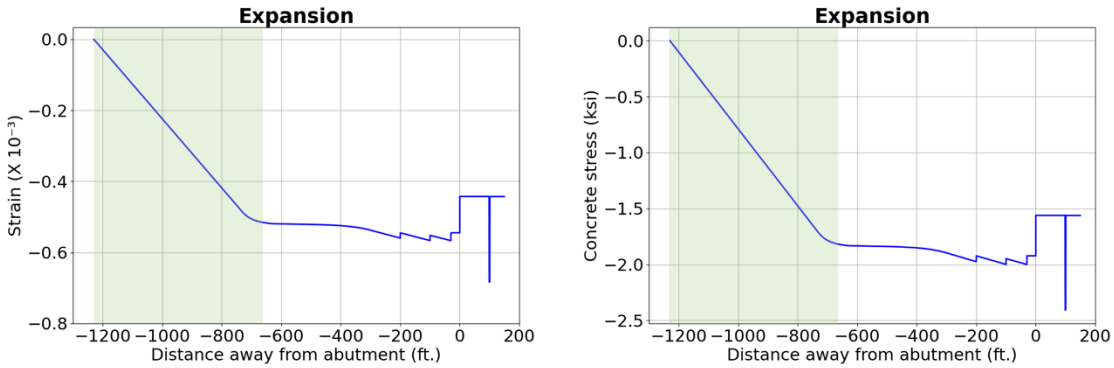

(c) (d)

Figure 5.37: Axial behavior of transition slab connected with CRCP (temperature increase): (a) Axial force; (b) Longitudinal displacement; (c) Strain; (d) Concrete stress.

In the case of bridge expansion, the bridge deck, transition zone, and CRCP are in compression. The restraint from the base and CRCP reduces the movement of the transition zone to zero at approximately 500 ft. The maximum expansion in the CRCP was approximately 1.6 in. at the end.

In the case of contraction, the bridge deck, transition zone, and CRCP are in tension. The effects of the bridge-pavement interaction on the pavement are dissipated within approximately 300 ft. of the transition zone. Concrete was still within the elastic range at a local region approximately 50 ft. long near the end of the CRCP, which is indicated by the same value of average steel stress and maximum steel stress. This is due to the boundary conditions at the end of CRCP that only provide support in the vertical direction. The CRCP contracts approximately 0.3 in. at the end.

Generally, if the additional CRCP segment is sufficiently long, the movement of the pavement in the case of bridge contraction or expansion can be entirely dissipated within the transition zone. A local behavior is expected at the end of the CRCP segment, which is typical for the ends of conventional CRCP.

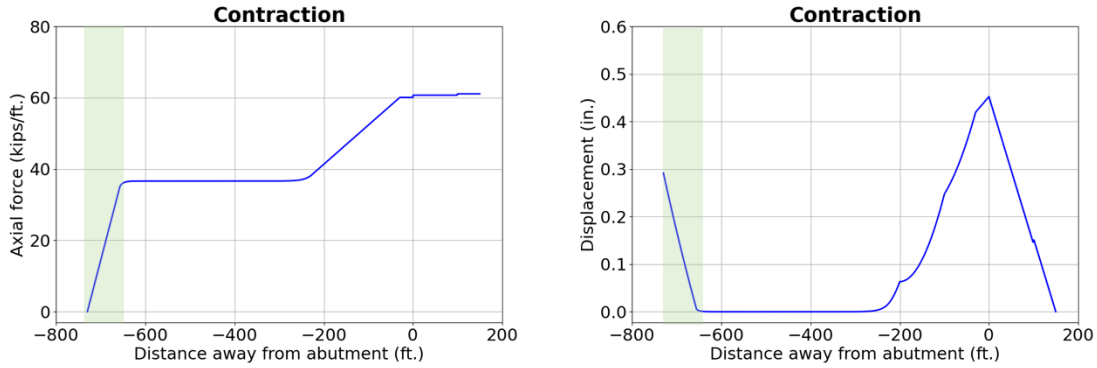

(a) (b)

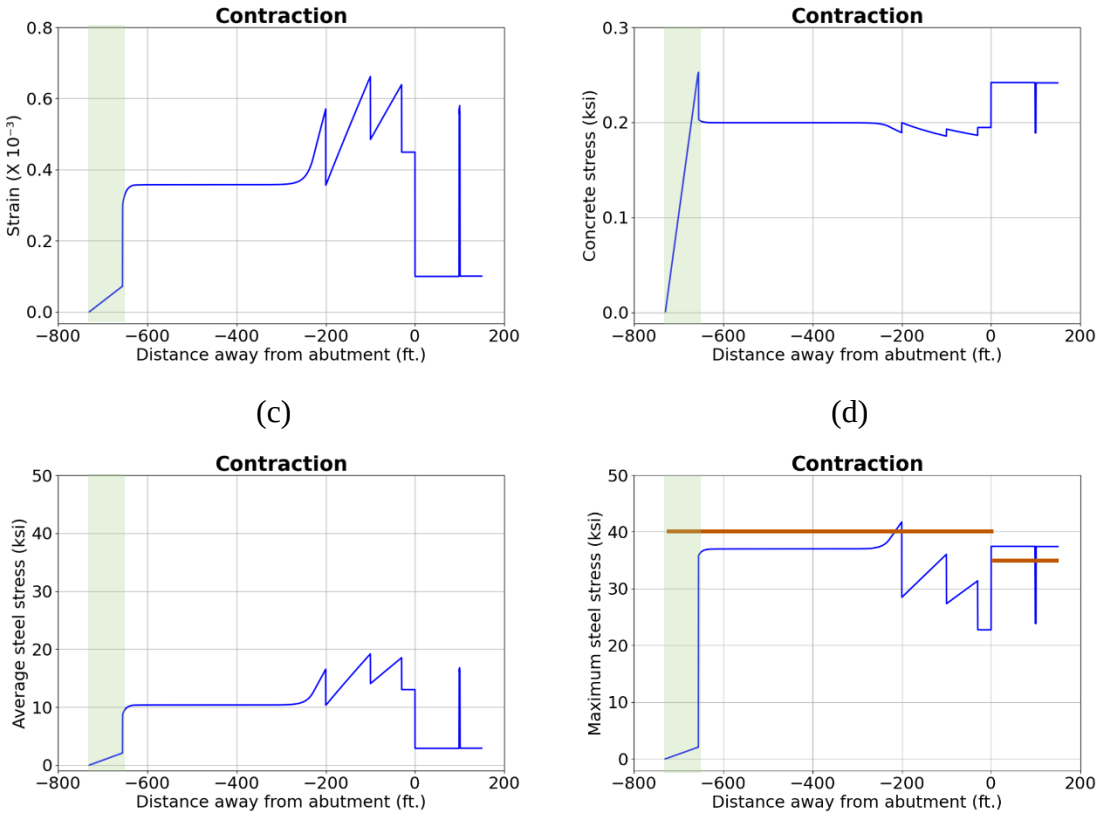

Figure 5.38: Axial behavior of transition slab connected with CRCP (temperature decrease): (a) Axial force; (b) Longitudinal displacement; (c) Strain; (d) Concrete stress; (e) Average steel stress; (f) Maximum steel stress.

5.7.3 Effects of Length of CRCP

The axial response is affected by the length of the additional CRCP segment at the end of the transition zone. The required CRCP during temperature increase is significantly longer than that during temperature decrease from the above case demonstrating axial behavior. For bridge expansion cases, the CRCP length was varied from 400 ft. to 700 ft. with an increment of 100 ft; for bridge contraction cases, the CRCP length was varied as 50 ft., 100 ft., and 150 ft. Figure 5.39 and Figure 5.40 present the axial response for different lengths of CRCP in the cases of expansion and contraction, respectively. The transition zone was 630 ft. long, and the location is marked as shaded area in light blue, with the bridge on the left end and CRCP with different lengths on the right.

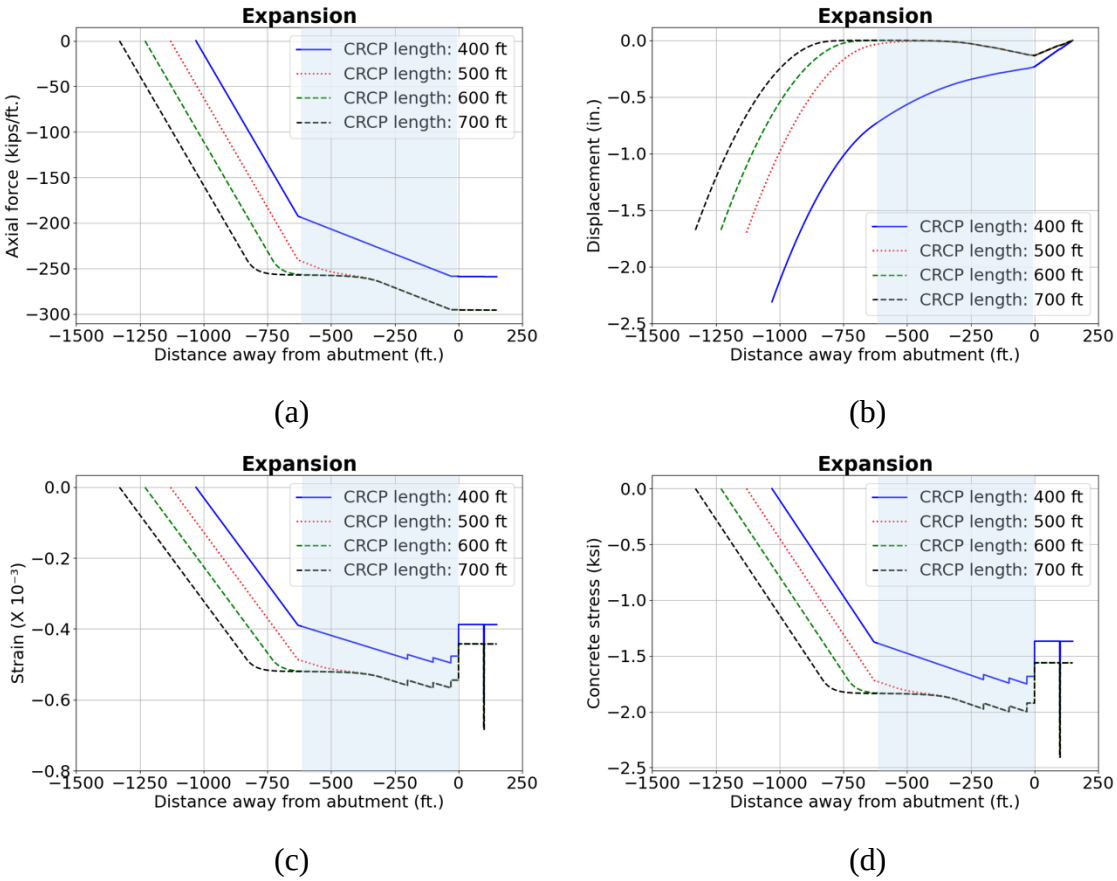

Figure 5.39: Results for different lengths of CRCP (temperature increase): (a) Axial force; (b) Longitudinal displacement; (c) Strain; (d) Concrete stress.

For the cases of expansion, the axial force in the system is relatively low if the CRCP is 400 ft. long. However, the CRCP fails to restrict the movement of the transition pavement as indicated by a diverged displacement distribution along the transition zone and CRCP. When the length of CRCP increases to 500 ft., the transition zone is generally restrained except for a small region near the end. When the length of CRCP is 600 ft., the transition zone is fully restrained. The responses in the transition zone and bridge deck are not affected when the CRCP length increases from 600 ft. to 700 ft.

For the cases of contraction, it can be determined that 100 ft. is the required length of the CRCP. If the length of the CRCP further increases, it does not change the response of the transition zone and bridge deck. When the CRCP is only 50 ft. long, after approximately 500 ft. of the transition zone, the effects of the bridge-pavement interaction disappear. However, the rest of the transition zone does not behave like a conventional CRCP. Due to the insufficient restraint from the CRCP segment at the end, the reinforced pavement from 500 ft. to 680 ft. away from the bridge abutment is in the elastic range and the displacement diverges.

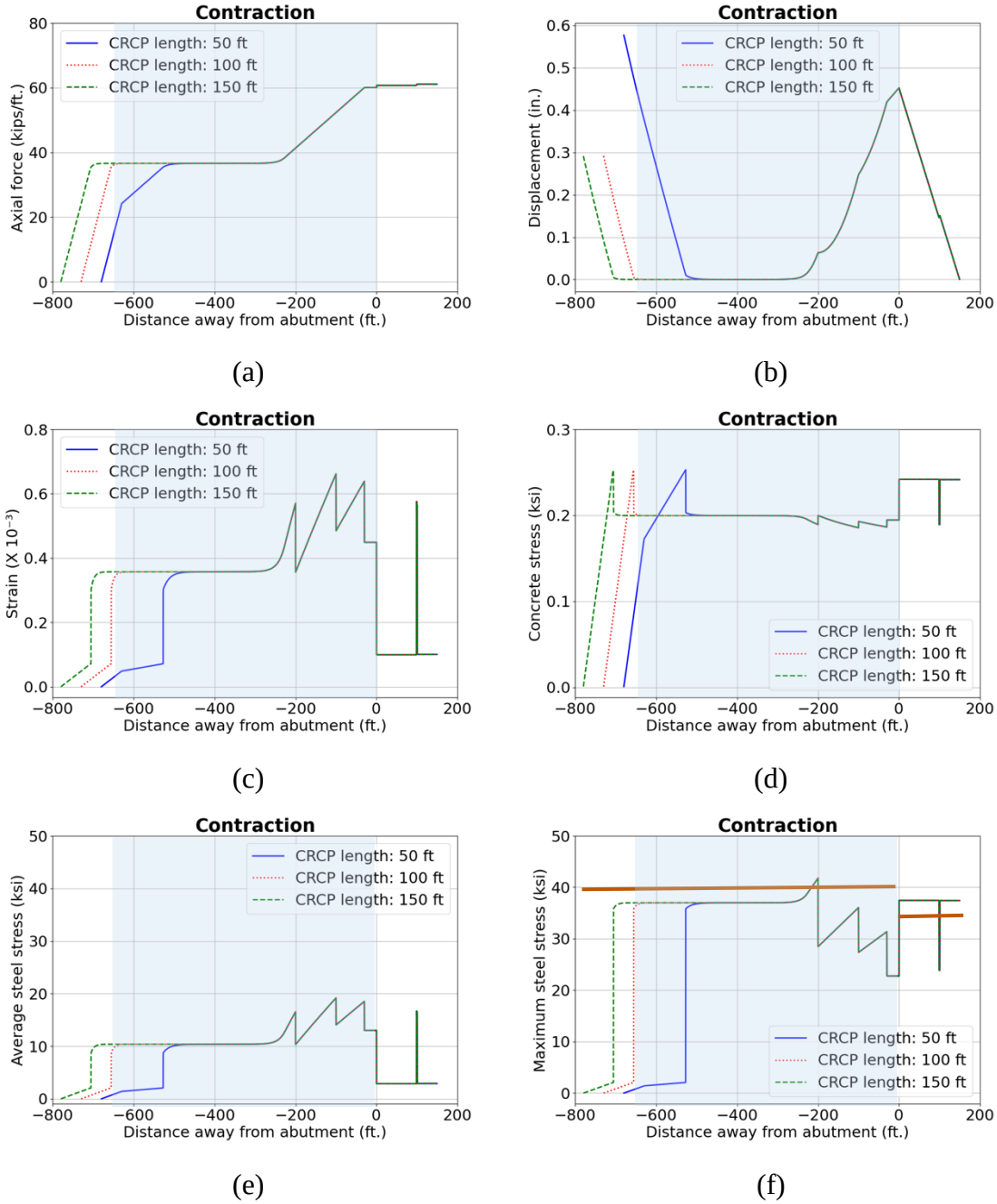

Figure 5.40: Results for different lengths of CRCP (temperature decrease): (a) Axial force; (b) Longitudinal displacement; (c) Strain; (d) Concrete stress; (e) Average steel stress; (f) Maximum steel stress.

It is observed that if the CRCP is longer than the required length, the local behavior at the end of the CRCP segment is independent of the length of the CRCP. For example, in the case of contraction, the diverged displacement occurs within approximately 80 ft. at the end of the CRCP and the end displacement is roughly 0.3 in. for both CRCP lengths of 100 ft. and 150 ft. This is representative of the local response at the ends of a conventional CRCP (Saraf et al., 2013). More details are presented in the following Section 5.7.4. Considering a very long conventional CRCP,

the pavement will expand or contract with temperature changes, concrete shrinkage, and creep. However, these deformations are restrained by the longitudinal reinforcement and the base and generate stresses in the pavement. CRCP accommodates the thermal movements and releases the restraint stresses by forming transverse cracks. As a result, the deformations are fully restrained by the concrete slab-base interaction and longitudinal reinforcement except for two local regions near the ends, where a displacement occurs due to a free end.

5.7.4 Discussion

A longitudinal displacement is expected to occur at the end of the short CRCP segment with temperature changes and concrete shrinkage when it is connected to the transition zone. The magnitude of the end displacement is controlled by the temperature changes, concrete shrinkage and creep, and concrete slab-base interaction. With the temperature decrease, an end displacement of approximately 0.3 in. occurs, which is relatively small. With the temperature increase, the end displacement can be as large as 1.6 in. Those results discussed above only considered the maximum temperature decrease and increase with neglecting the concrete shrinkage. If the concrete drying shrinkage is considered, the end displacement is expected to decrease for expansion conditions and increase for contraction conditions.

Saraf et al. (2013) collected field data and recorded the ambient temperature and the slab displacement at the transverse construction joints of CRCP. The results from the field monitoring showed that the concrete contracted as much as 0.2 in. over a period of two days, which was mainly due to concrete drying shrinkage. According to Zollinger and Tayabji (2007), typically, a 1 in. to 1.5 in. expansion space is necessary at CRCP ends when there is no attempt made to restrict CRCP end movements. This is consistent with the end movements predicted by the proposed models.

In any case, the local behavior near the end of the additional CRCP segment is consistent with the behavior of conventional CRCP. The current practices addressing the thermal movements at the end of the CRCP can be used for this application. Zollinger and Tayabji (2007) summarized the current practices for various pavement transition elements such as the junction between a continuously reinforced concrete pavement and a JCP or a flexible pavement (asphalt concrete pavement), and so on. The CRCP and JCP are usually connected by a dowel bar coated with epoxy to provide a proper load transfer between the two pavement types. A sealant can be used at this joint to fill the gaps. It also includes a thickness transition over a distance of 10 ft., as shown in Figure 5.41(a). Figure 5.41(b) demonstrates the details of the transition from CRCP to asphalt concrete pavement that has been used in the Houston District. It involves a thickened edge consisting of the compacted asphalt concrete (AC) backfill between the two pavements. However, uneven deformation may develop on the asphalt concrete pavement to accommodate the movements of the CRCP with temperature changes. Another concern is the non-uniform support due to the differential deflections of two types of pavements. Improvements for the transition between different types of pavements were also recommended by Zollinger and Tayabji (2007). For example, the use of a sleeper slab element at the joint may be effective at reducing the deflection and support discontinuity underneath two different types of pavement and enhance the performance.

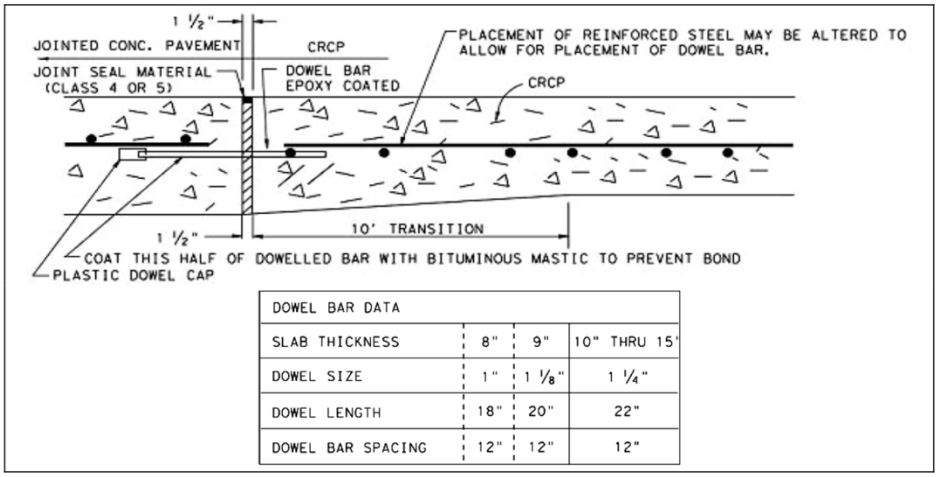

DOWEL BAR DATA			
SLAB THICKNESS	8"	9"	10" THRU 15"
DOWEL SIZE	1"	1 ⅛"	1 ¼"
DOWEL LENGTH	18"	20"	22"
DOWEL BAR SPACING	12"	12"	12"

(a)

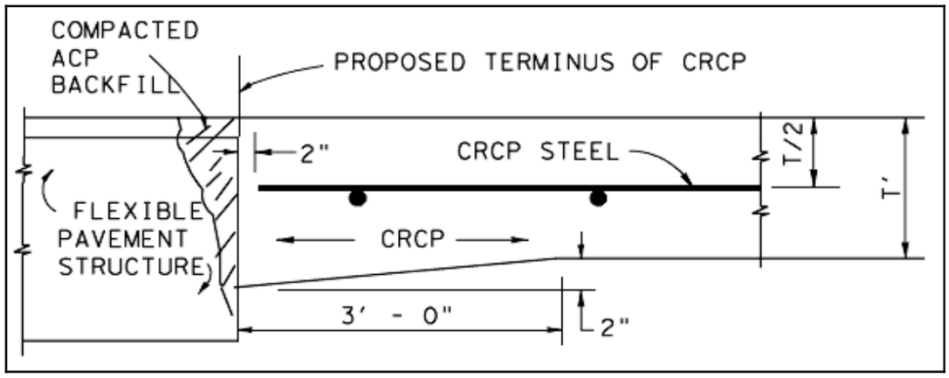

(b)

Figure 5.41: Current practice of transition details between pavements (Zollinger & Tayabji, 2007): (a) Transition details between CRCP and JCP; (b) Transition details between CRCP and flexible pavement.

In general, the seamless connection technology using a proper concrete-slab base interaction for load transferring can be applicable for the JCP or flexible pavement. It provides many benefits by eliminating the expansion joints over the abutment, such as reduction of the costs due to construction and maintenance, and improvement of durability.

5.8 Summary

In this chapter, axial analyses of the entire seamless bridge-CRCP system with temperature changes are presented using the nonlinear finite element models developed in Abaqus. One-dimensional finite element models were developed to simulate the axial behavior of the seamless system. All the elements contributing to the axial response were accounted for, including the pavement, concrete slab-base interaction, bridge superstructure, elastomeric bearings, and pier columns. Nonlinear models were used to represent the cracking response of the pavement and bridge decks, as well as frictional response at the concrete pavement-base interface.

The proposed modeling scheme was verified using previous analysis results of a seamless bridge in Australia. The numerical models have been used to study seamless system designs for typical

Texas bridges. Parameters of the transition zone configuration, including the concrete slab-base interaction, reinforcement ratio, and slab thickness of the transition zone, and that of the bridge configuration, including the span length, number of spans, number of girders, and girder size, were varied to investigate their effects on the transition length and the amount of reinforcement required in the transition slab and bridge decks. The extended application of the seamless connection technology for jointed concrete pavement or flexible pavement was also explored numerically. The main conclusions and findings are summarized as follows:

- The axial response of the seamless bridge-pavement system is mainly controlled by the magnitude of temperature changes. In the case of expansion (temperature increase), the bridge and pavement components are subjected to compression. In the case of contraction (temperature decrease), the system is in tension, which is more critical as the concrete in the transition zone and bridge decks are expected to crack. A simple design criterion based on the maximum tensile stress on reinforcing steel is used to control crack widths. The critical regions of the seamless system are mainly the approach slab in the vicinity of the bridge abutment, where the highest demand is expected, and the link slabs, where the stiffness sharply reduces due to the discontinuity of the bridge girders.
- The concrete shrinkage effects counteract the effects of the temperature increase, leading to smaller compressive stresses and even tensile stresses in some regions. The combined shrinkage effects and temperature decrease result in a smaller maximum steel stress at cracks compared to that in the case of temperature decrease alone, thus it is conservative to ignore the concrete shrinkage effects for design purposes.
- Through a series of parametric studies, it is identified that the concrete slab-base interaction significantly affects the tensile or compressive force introduced in the system and the required length of the transition zone. The target range of the friction coefficient at the concrete slab-base interface is approximately 0.5, and not higher than 1, to balance the transition slab length and reinforcement ratio for a typical bridge configuration in Texas.
- The axial response of the seamless system also depends on the relative stiffness of the bridge and pavement elements. The increase in the slab thickness and reinforcement ratio of the transition zone leads to a larger axial force and correspondingly higher strain in the bridge decks and link slabs, whereas the strain in the transition zone may decrease as the section is stiffer with either increased thickness or reinforcement amount. The parameters relevant to the bridge configuration also influence the axial response of the system. The increase of span length and number of spans leads to higher axial forces that are associated with larger longitudinal expansion/contraction of the bridge, and correspondingly higher material strain demands. Increasing the number and size of girders causes higher axial forces in the system as the bridge stiffness is increased for the expansion condition, whereas the influence is insignificant for the contraction condition as the difference in axial stiffness provided by the girders practically does not matter when cracking occurs in the pavement and link slabs.
- A single design of a 400-ft.-along transition zone with reinforcement ratios varying between 0.75% and 1.45%, and a 30-ft.-long approach slab with 2% reinforcement ratio are likely appropriate for most of the common Texas bridge configurations. While in some cases the design may be further optimized by reducing the amount of steel, this indicates that some level of standardization can be achieved for design guidelines of seamless systems if accepting some level of extra conservatism.

- The seamless connection technology can be adapted for circumstances where a jointed concrete pavement or flexible pavement is used on the pavement side. This is achieved by introducing a certain length of the conventional CRCP at the end of the transition zone. The bridge-pavement interaction is dissipated through the concrete slab-base interaction underneath the transition zone and the movement of the transition zone is further restrained by the short CRCP segment. Moderate displacements are expected to occur at the end of the additional CRCP segment, which is solely due to the local behavior at the ends of CRCP and is independent of the bridge movements. The current practices to deal with the movement at the local end of a CRCP could be used as a transition in this region.

6. Numerical Modeling of the Out-of-Plane Response of Transition Zone (Task 4)

6.1 Overview

As discussed in the previous chapters, the approach slab is subjected to the axial effects from the seamless-bridge interaction due to thermal deformations and concrete shrinkage. In addition, the approach slab is also potentially subjected to flexural stresses as a result of the out-of-plane effects caused by the combination of differential embankment settlement and vehicular loading. This chapter presents analyses of the out-of-plane response of the transition zone in a seamless bridge-pavement system using a continuum finite element (FE) model. The FE model proposed for the transition zone is capable of simulating concrete cracking and the concrete slab- base interaction.

Preliminary studies were first conducted with the out-of-plane analysis focused on the approach slab utilizing an idealized fixed-end boundary condition, assuming an infinite rotational restraint provided by the adjacent bridge superstructure. The effects of the magnitudes of the rotational restraint on the out-of-plane response of the approach slab were numerically investigated. The model was further refined by modeling the restraint by the bridge as a spring with an equivalent rotational stiffness representing the approximate stiffness of the bridge.

The response of the transition zone with the combined axial and out-of-plane effects were also evaluated using the same modeling scheme. The interaction of the bridge and pavement on the transition zone due to the axial effects were considered by applying a prescribed bridge longitudinal displacement at the seamless connection, which was based on the results of the axial analysis of the entire seamless bridge-pavement system using the 1D structural model proposed in Chapter 5.

Finally, parametric studies were conducted to investigate the response of the transition zone with different slab configurations (reinforcement ratio and slab thickness), and different levels of embankment settlement.

6.2 Development of the FE Model of Approach Slab

6.2.1 General Modeling Scheme

A two-dimensional (2D) plane stress FE model of the approach slab was developed to study the response with differential embankment settlement and vehicular loads. The model was created using the commercial analysis package Abaqus (Abaqus, 2017). Nonlinear static analysis was performed with Abaqus/Standard to account for material nonlinearities in the concrete and at the concrete slab-base interface.

The FE model included the approach slab made of reinforced concrete, a base layer and the concrete slab-base interface. Figure 6.1 shows the elements included in the approach slab model.

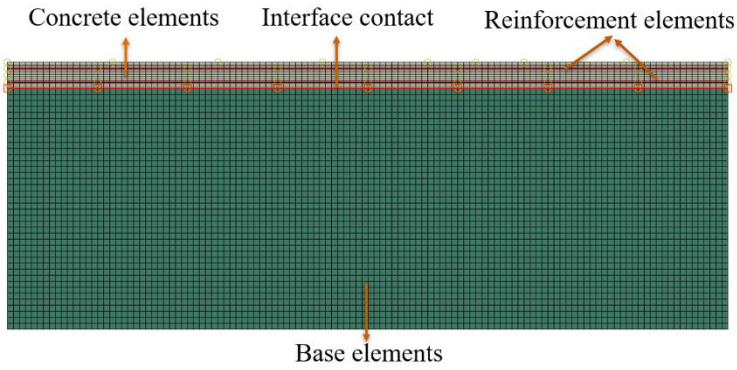

Figure 6.1: FE model details of the approach slab, base and interface.

Current TxDOT bridge design specifications (TxDOT, 2015) provide a standard approach slab design for conventional bridges (BAS-C approach slab). Figure 6.2 shows the design details of the BAS-C approach slab. The BAS-C approach slab is 20 ft. long and 13 in. thick, with #5 rebars at a maximum 12 in. spacing at the top layer (correspondingly, reinforcement ratio of 0.2%) and #8 rebars at a maximum 6 in. spacing at the bottom layer (correspondingly, reinforcement ratio of 1%). For the implementation of the seamless bridge connections, modifications are likely needed for the design of approach slabs because increased force demands are expected due to the interaction between the bridge and transition zone.

For modeling purposes, the approach slab was assumed to have a thickness of 13 in. and a length of 30 ft., which was deemed sufficient to include the portion of the approach slab that is likely to be subjected to bending due to vertical effects. For the out-of-plane analysis in the vertical direction, the base was modeled with a thickness of 10 ft. which was deemed sufficient to avoid the effects of boundary conditions. The longitudinal reinforcement ratio was increased to 2%, which was equally distributed among top and bottom layers of reinforcement. The concrete cover for both the top and bottom layer of the reinforcement was set as 3 in. This preliminary reinforcement amount was based upon the seamless connection design in Australia (Griffiths, personal communication, 2020).

Solid elements (CPS4R) were used to simulate the base and concrete elements of the approach slab, which are four-node bilinear quadrilateral plane stress elements with reduced integration and hourglass control. Two-node linear truss elements (T2D2) were used to simulate the longitudinal reinforcement of the approach slab. The reinforcement elements were embedded in the concrete elements with a perfect bond assumed between the steel and concrete. Concrete and steel reinforcement were modeled using the same nonlinear material laws employed in Chapter 5 for the axial analyses (damaged plasticity for concrete and elastic-perfectly plastic law for steel). Elastic material properties were assumed for the base elements to represent the subgrade/base stiffness.

As shown in Figure 6.1, a uniform mesh size of 3 in. was used for the base and reinforcement elements. The concrete elements were meshed with a size of 3 in. along the longitudinal direction and a finer size of 1 in. in the vertical direction to achieve a better resolution of the stresses along the cross-section.

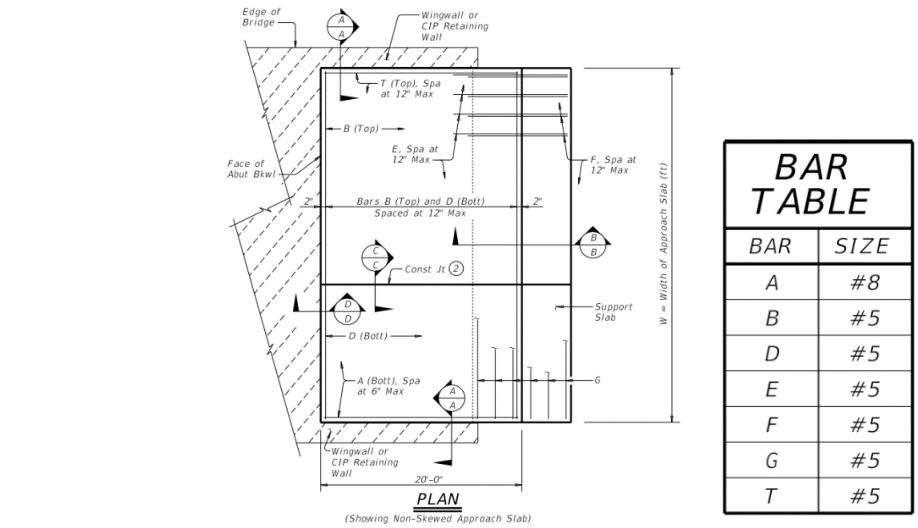

(a)

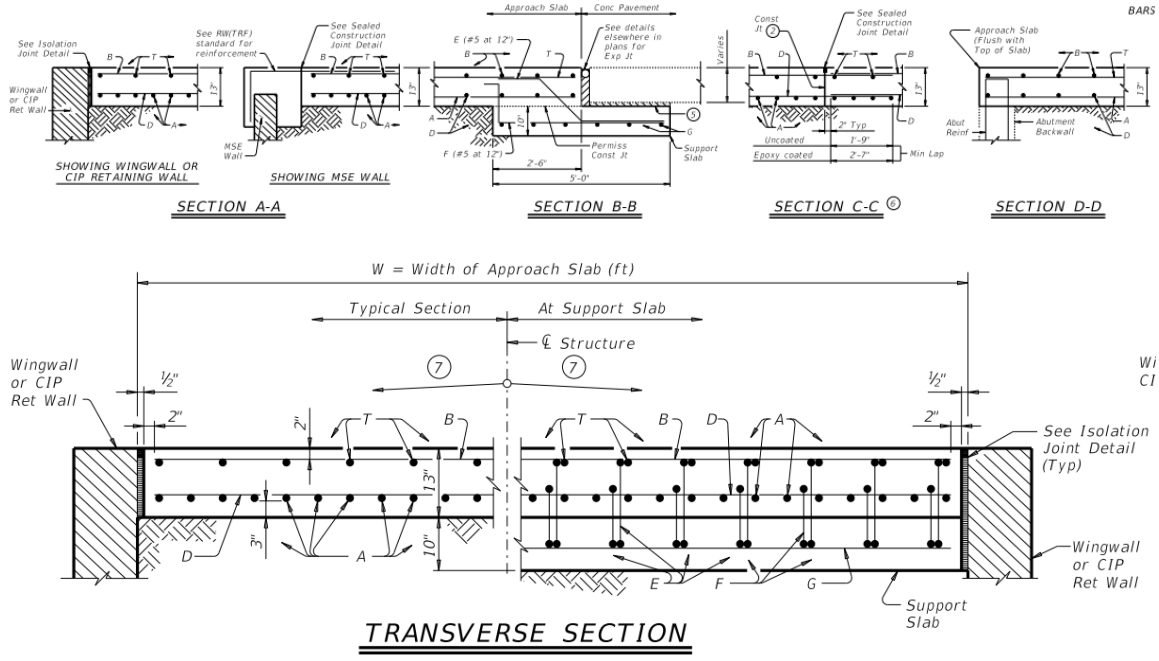

(b)

Figure 6.2: Standard design of the BAS-C approach slab in Texas (TxDOT, 2015): (a) Plan drawing and rebar table; (b) Section drawings.

A contact condition with elastic-damage constitutive laws in the tangential and normal directions was introduced at the slab-base interface. The elastic properties, damage initiation and damage propagation in the normal direction are capable of capturing the separation of the interface and loss of the support with the combination of the differential embankment settlement and vehicular loads. The relationship in the tangential direction associated with the longitudinal movements is able to simulate the longitudinal force transferring mechanism, which is mainly activated with the axial effects.

6.2.2 Material Modeling

The concrete damaged plasticity model was used to represent the nonlinearity of the concrete. For simplicity in the study, only the plasticity of concrete was considered without defining the damage variables for compression and tension.

The uniaxial compressive and tensile stress-strain curves for concrete were calibrated using the same models as for the axial analysis, as described in Section 5.2.2. The concrete compressive strength for the transition zone was taken as 4 ksi. Regarding the concrete tensile strength, Eq. 5.3(a) was used for the concrete in the transition slab where the response is controlled by pure axial effects. For the approach slab where response is controlled by the combined axial and flexural effects, Eq. 5.3(c) was used.

In addition, four parameters are required to define the yield surface in a multi-axial stress environment (Abaqus User's Manual, 2017). The dilation angle ψ, measured in the p-q plane, was assumed to be 30° based on previous research (Zheng et al., 2016; Sümer & Aktaş, 2015). Flow potential eccentricity that defines the rate at which the hyperbolic flow potential approaches its asymptote ε was taken as the default value of 0.1. The ratio of initial biaxial compressive yield stress σ_{b0} to initial uniaxial compressive yield stress σ_{c0}, $\frac{\sigma_{b0}}{\sigma_{c0}}$ was taken as the default value of 1.16, as recommended in the Abaqus User's Manual (2017). K_c is the ratio of the second stress invariant on the tensile meridian to the compressive meridian at initial yield and was made use of the default value of 2/3. In addition, a visco-plastic regularization of the concrete constitutive equations was used to improve convergence with the viscosity parameter assumed to be 0.001. The concrete compressive strength of the approach slab was taken as 4 ksi. The Poisson's ratio was taken as 0.2 while the coefficient of thermal expansion for concrete was taken as 6.5×10^{-6}/°F.

A bi-linear elastic perfectly plastic stress-strain relationship was used for reinforcing steel, as described in Section 5.2.2. The elastic modulus and the nominal yield strength of reinforcing steel were taken as 29000 ksi and 60 ksi, respectively. The Poisson's ratio was taken as 0.3 and the coefficient of thermal expansion for steel was taken as 6.5×10^{-6}/°F.

6.2.3 Concrete Slab-Base Interaction

A contact condition was used to model the concrete slab-base interface behavior. Surface-to-surface contact was assigned to the contact pairs, i.e., the bottom surface of the approach slab and the top surface of the base. Hard contact was assumed at the concrete slab-base interface to represent the pressure-overclosure relationship. This minimizes the penetration of the two surfaces in contact. Cohesive behavior was defined at the interface, which is based on a traction-separation approach. In the normal direction, zero stiffness was assumed to simulate the separation of the two surfaces.

The interface constitutive law in the tangential direction provided a simplified representation of the cyclic shear stress-displacement relations obtained from the experimental testing program outlined in Chapter 4. The investigation of the effects of cyclic interface behavior on the axial response of a seamless system, as presented in Section 5.4.5, indicates that a steady ultimate interface shear strength is representative of the general interface interactions for analysis and design purposes. Therefore, a constant coefficient of friction $\mu = 0.8$ was assumed for the approach slab based on the test data for the concrete-CSB interface with felt paper for the bond breaker (see conclusions of Chapter 4). Accordingly, the shear stress-displacement curve

corresponding to a 13-in.-thick slab was represented with the same simplified bi-linear relations used in the axial analyses, presented in Figure 5.17(b). The displacement at the onset of steady stage was taken as 0.015 in. based on test results.

The tangential behavior can be simulated by defining either frictional or cohesive behavior. In this study, cohesive behavior was used to avoid convergence problems even though the physical nature of the interaction is mainly frictional. The reason is that when using a frictional law, the shear force at each contact node is dependent on the normal force. Since normal pressures can vary significantly when the contact status changes from closure to opening, the use of frictional models can lead to convergence problems. Instead, a cohesive model was defined to represent the interface frictional behavior at the concrete slab-base interface for both axial and flexural analysis, by pre-defining the level of constant normal stress due to the slab weight. The initial stiffness was determined as the steady shear strength divided by the corresponding displacement. Damage was introduced and initiated when the shear stress exceeded the steady shear strength. The plateau was simulated by defining a relatively large displacement at failure for damage evolution.

6.2.4 Boundary Conditions and Loading Considerations

The boundary conditions of the approach slab are presented in Figure 6.3. The lateral sides of the base layer were restrained in the longitudinal direction and the bottom of the base layer was restrained in the vertical direction. At the end of the approach slab on the pavement side, the longitudinal movement was restrained, whereas the slab was free to move in the vertical direction as the base settles. At the other end of the approach slab that connects to the bridge deck, fully-restrained boundary conditions were assumed when analyzing the out-of-plane effects only. The vertical movement was also restrained assuming no settlement of the bridge abutment. As a result, no rotation was allowed at the bridge end of the approach slab. The boundary conditions in the rotational degree of freedom are discussed in Section 6.3.

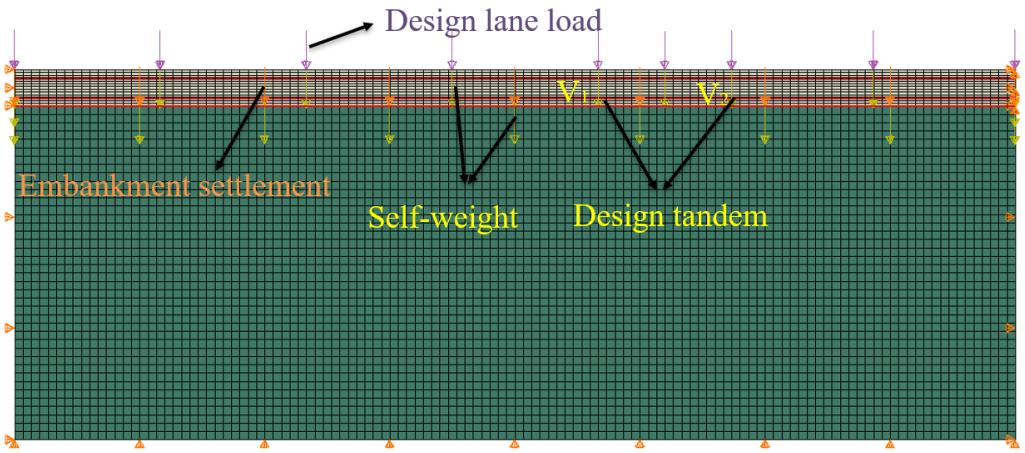

Figure 6.3: FE model details of the approach slab with boundary conditions and loads.

A 1 in. settlement relative to the bridge abutment was considered for the base layer underneath the approach slab for the out-of-plane analysis. This value is representative of the magnitude of embankment settlements commonly occurred in the field. Thus, this assumed settlement value was deemed reasonable for analysis purposes.

Vertical loads included dead load, i.e., the self-weight of the approach slab, and the vehicular live loads. The AASHTO LRFD Bridge Design Specifications (2020) define the vehicular live loading on the roadways of bridges for a standard design lane width of 12 ft., i.e., designated HL-93, which consists of a combination of the design truck or design tandem, and the design lane load. Figure 6.4(a) and (b) demonstrate the axle weights and spacing of the design truck and design tandem, respectively. The design lane load consists of a load of 0.64 kips/ft. uniformly distributed in the longitudinal direction. Transversely, the design truck/tandem and design lane load are assumed to occupy 10 ft. within a design lane. The extreme force effects are taken as the larger of the effect of the design tandem combined with the effect of the design lane load, and the effect of the design truck combined with the effect of the design lane load.

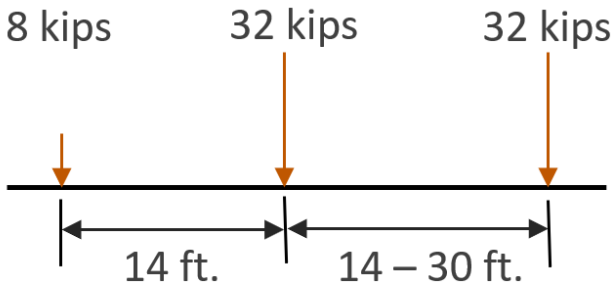

(a)

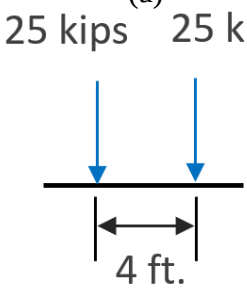

(b)

Figure 6.4: Weights and spacing of axles (Malviya, 2021): (a) Design truck; (b) Design tandem.

Considering the length of the approach slab and the spacing of axles for the design truck/tandem, the effects of the design tandem represented the controlling load that provides the largest impact on bending in the approach slab compared to the design truck. Therefore, a combination of design lane load and design tandem was applied as the vehicular live loads for the approach slab. The out-of-plane response of the approach slab varies as the design tandem loads move in the longitudinal direction. The locations of axles of the tandem corresponding to the worst-case scenario were determined based on an influence line analysis where for simplicity, fixed boundary conditions were assumed at both ends. Specifically, the focus of the analysis was directed at the magnitude of the negative bending moment at the bridge end. The bending moments are superimposed due to the vertical loads, including the design tandem, self-weight of the slab and embankment settlement, leading to concrete crack at the top near the bridge end.

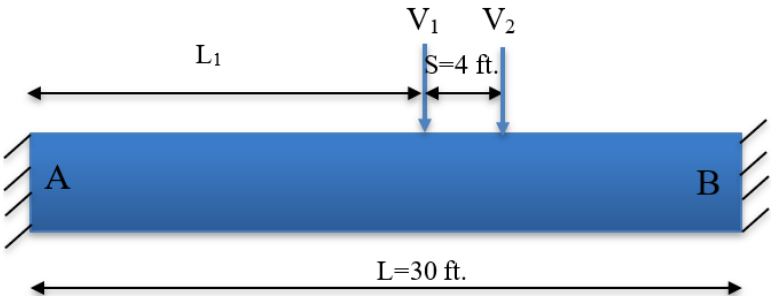

(a)

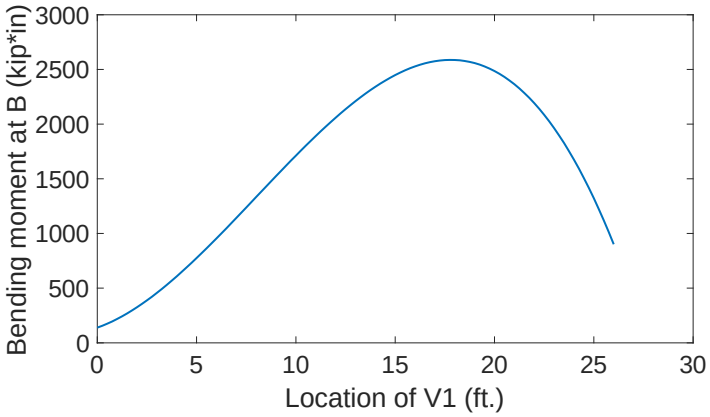

(b)

Figure 6.5: Axle locations of design tandem for the worst-case scenario: (a) A scheme of an approach slab subjected to design tandem loads; (b) Influence line.

Figure 6.5(a) presents a scheme of a 30 ft. long and 12 ft. wide approach slab subjected to the designated tandem load, where the axle loads V_1 and V_2 with a magnitude of 25 kips were applied at a specified spacing of 4 ft. The axle load V_1 was applied at a distance of L_1 away from the pavement end A. Figure 6.5(b) presents the influence line of the bending moment at the bridge end B when the axle locations varied along the approach slab. The worst-case scenario of the design tandem that resulted in the maximum negative bending moment at the bridge end of the approach slab was reached when two axles were 8.25 ft. and 12.25 ft. away from the bridge end.

The model simulated the response of the approach slab per unit width (1 in.). The unit weight of the reinforced concrete was taken as 150 pcf and was applied to the approach slab as a body force. A uniform displacement of 1 in. was applied at the top surface of the base layer to simulate the embankment settlement relative to the abutment. The vehicular loads for a design width of 12 ft. as discussed above were correspondingly scaled to a 1-in.-wide slab assuming a uniform distribution over the transverse direction for simplicity. Accordingly, a design lane load was applied as a uniform pressure of 0.37 psi at the top surface of the approach slab. The design tandem loads V_1 and V_2 with a magnitude of 174 lbf were applied at 8.25 ft. and 12.25 ft. away from the bridge end of the approach slab, respectively. All the loads mentioned above were unfactored considering serviceability limit states. The applied loads and displacements are also presented in Figure 6.3.

6.3 Out-of-Plane Analysis of Approach Slab

6.3.1 Response with Fixed Ends

The out-of-plane response of the approach slab when subjected to embankment settlement and vehicular loads was first investigated assuming fixed boundary conditions at both ends of the approach slab, which is the extreme case when no rotation is allowed. Figure 6.6(a) shows the contour plot of the vertical displacements of the approach slab and base. The contour plots in this technical memorandum use a deflection factor of 10 to assist in displaying the results more clearly. Under the vertical loads, a majority portion of the approach slab to the bridge end is separated from the base. The remaining approach slab near the pavement end is still supported by the base and is not subjected to bending.

Figure 6.6(b) plots the vertical displacement of the approach slab along the length. The horizontal axis represents the locations on the approach slab with the origin indicating the location of the bridge abutment. The graph shows that the unsupported length of the approach slab was approximately 5 ft. Figure 6.6(c) plots the opening at the concrete slab-base interface along the approach slab. Zero opening indicates that the contact pairs are in contact, whereas a positive value of the opening indicates the separation of two surfaces. The graph agrees with the observation from the vertical displacement plot that approximately 5 ft. of the approach slab adjacent to the bridge was separated from the base due to the loss of support. The remaining portion of the approach slab kept in close contact and settled with the base.

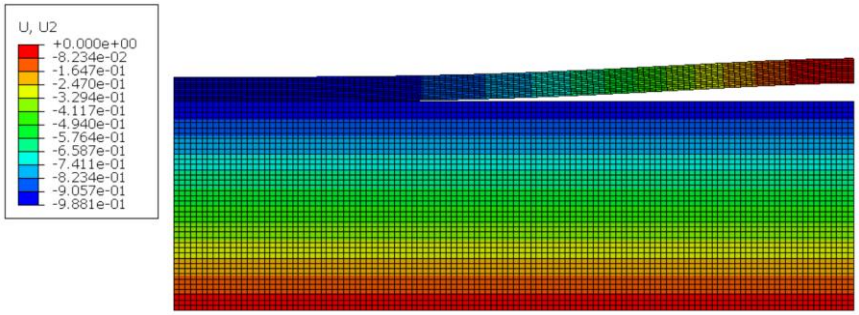

(a)

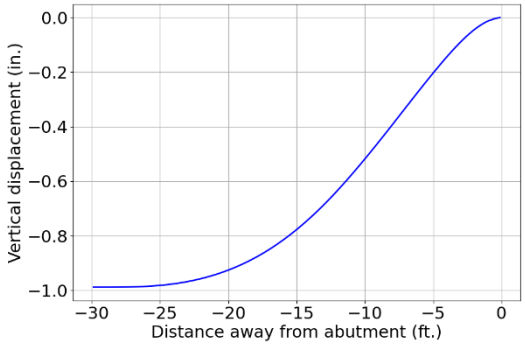

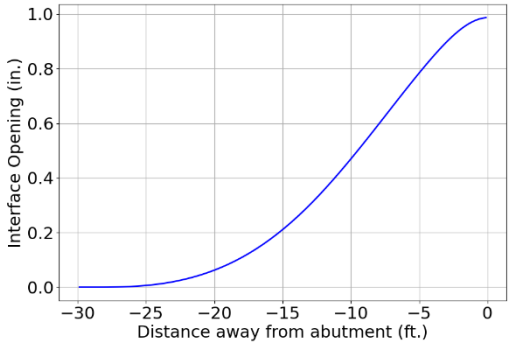

(b) (c)

Figure 6.6: Vertical displacements: (a) Contour plot of the approach slab and base (deflection scale factor: 10); (b) Vertical displacement of the approach slab; (c) Interface opening.

A two-dimensional (2D) plane stress FE model of the approach slab was developed to study the response with differential embankment settlement and vehicular loads. The model was created using the commercial general analysis package Abaqus (Abaqus, 2017). Nonlinear static analysis was performed with Abaqus/Standard to account for material nonlinearities in the concrete and at the concrete slab-base interface.

Figure 6.7(a) plots the distribution of concrete longitudinal stresses and Figure 6.7(b) plots the uniaxial steel stresses at the top and bottom layers. The region adjacent to the bridge abutment within approximately 7.5 ft. experiences negative bending which causes tension in the top of the slab. The remaining portion experiences positive bending, which results in tension in the bottom of the slab. The tensile steel stress induced by the out-of-plane effects is the largest at the top layer near the bridge end of the approach slab, which is approximately 25 ksi. These steel stresses correspond to average steel stresses between cracks, since the concrete was assumed to carry tensile stresses through a tension-stiffening law. The maximum tensile steel stresses at crack locations are larger, as described in Chapter 5.

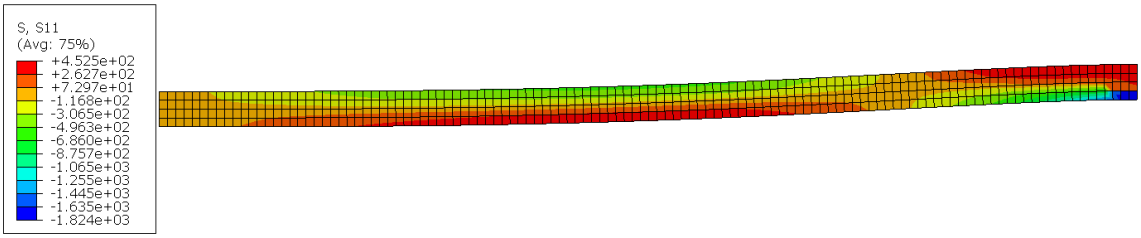

(a)

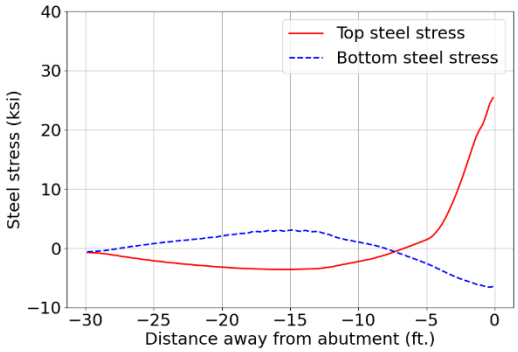

(b)

Figure 6.7: Material stresses of the approach slab: (a) Concrete longitudinal stress; (b) Steel stress.

The idealized fixed-end boundary conditions assume that no rotation is allowed at the end of the approach slab on the bridge side. However, this assumption is likely too simplified and results in an overestimation of the average steel stress. Since the approach slab continues to the bridge deck, the approach slab is not fully fixed from rotation, but instead has some flexibility based upon the rotational stiffness of the bridge at the support location. The restraint provided by the bridge is somewhere between zero (equivalent to a pinned end) and infinite (equivalent to a fixed end). In the following sub-section, the effects of the boundary conditions at the bridge end on the out-of-plane response of the approach slab are presented and a more realistic boundary condition is proposed.

6.3.2 Effects of Boundary Conditions

The boundary conditions at the bridge end of the approach slab for the rotational degree of freedom were modified using a rotational spring to represent the rotational restraint from the bridge. Figure 6.8 presents the boundary conditions of the approach slab with a rotational spring. At the section of the bridge end of the approach slab, the point at the middle height was fixed in both longitudinal and vertical directions, whereas the remaining points in the section were able to rotate around the mid-point as a rigid body. The magnitudes of the stiffness of the rotational spring k were varied between values of 0.1, 5×10^6, 10^7 and 10^{10} lbf·in/radian. These are fictitious values established with the sole purpose of providing a wide range of different rotational restraints at the end of the approach slab to study the impact on the bending induced stresses in the reinforcing steel.

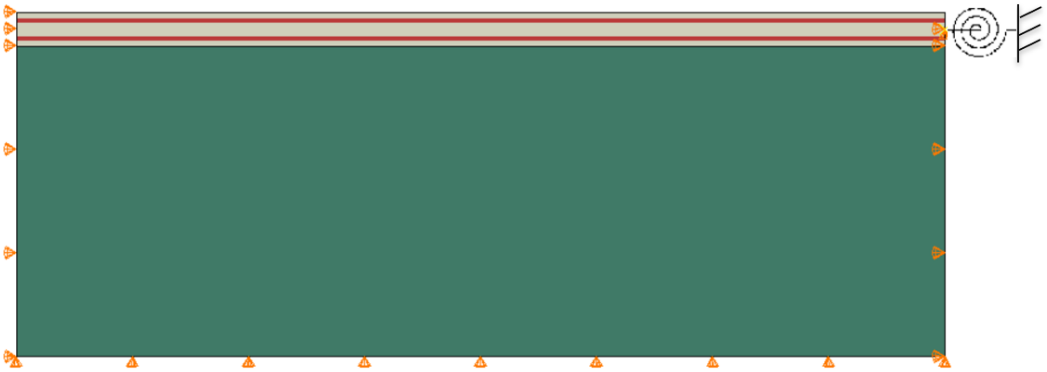

Figure 6.8: Boundary conditions of the approach slab with a rotational spring.

Figure 6.9 compares the response of the approach slab with different rotational restraints. The response of the approach slab with fixed ends is also presented for comparison. The magnitudes of the rotational restraint significantly affect the tensile steel stresses at the top layer, especially in the vicinity of the bridge abutment, where the tensile steel stress is expected to be the largest. The steel stresses at the bottom layer and the vertical displacements of the approach slab are also affected by the rotational stiffnesses of the spring, but the influences are generally mild, and these performances were deemed not critical. The following discussions are focused on the effects of the rotational restraints on the top layer tensile steel stresses.

When the rotational stiffness is relatively large, for example, $k = 10^{10}$ lbf·in/radian, the negative bending moment at the bridge end is significant, and for the problem studied leads to the largest tensile steel stress of approximately 25 ksi. It is noted that the response of the approach slab in this condition agrees with the response of the approach slab with idealized fixed ends, which is an extreme case representing the infinite rotational restraint. In contrast, when the rotational stiffness is relatively small, for example, $k = 0.1$ lbf·in/radian, the steel stress at the bridge end is almost zero. As expected, the flexural response approaches another extreme of the approach slab with a pinned end that allows free rotation.

The rotational stiffness of a real bridge is between two extreme conditions and the rotational restraint for the approach slab is limited. Correspondingly, the tensile steel stresses at the top layer are expected to be lower than that in the fixed-end condition. For example, when $k = 10^7$ lbf·in/radian, the tensile steel stress at the bridge end decreases from 25 ksi to 12.5 ksi; when $k = 5 \times 10^6$ lbf·in/radian, the tensile steel stress at the bridge end is only approximately 5 ksi. In

summary, the response of the approach slab, particularly the tensile steel stresses developed in the top layer near the bridge end are directly relevant to the rotational restraint provided by the bridge. A stiffer bridge imposes a larger rotational restraint on the approach slab when subjected to embankment settlement and vehicular loads, thus a larger bending moment and higher tensile steel stresses is developed.

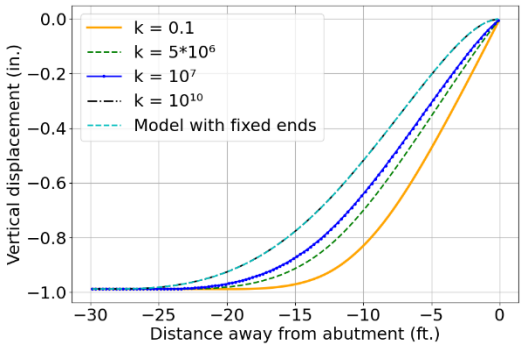

(a)

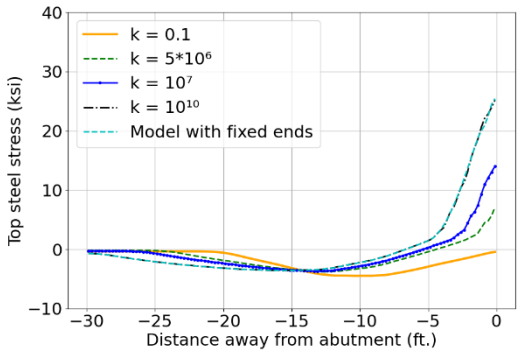

(b)

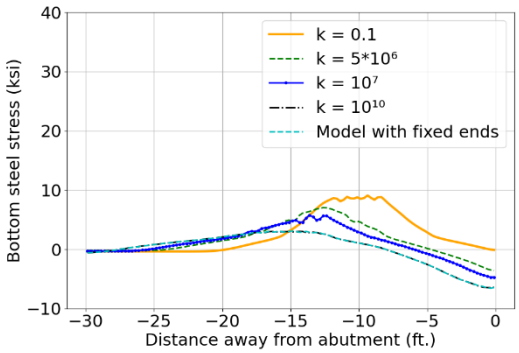

(c)

Figure 6.9: Out-of-plane response of the approach slab for different rotational restraints: (a) Vertical displacement; (b) Top steel stress; (c) Bottom steel stress.

6.3.3 Response with Actual Restraint

A more representative model including a bridge continuously connected with the approach slab, was developed to simulate the rotational restraint from a real bridge, as shown in Figure 6.10. The model simulated the response of the approach slab-bridge structure per unit width (1 in.). The purpose of this study was to determine which spring stiffness from the study outlined in the previous section is most representative of the actual conditions. The spring can then be selected for improved modelling efficiency in additional studies on the bending response. Assuming a symmetric configuration of the bridge-pavement structure with respect to the center of the bridge, and thus a symmetric response with respect to this same point, only half of the bridge was modeled.

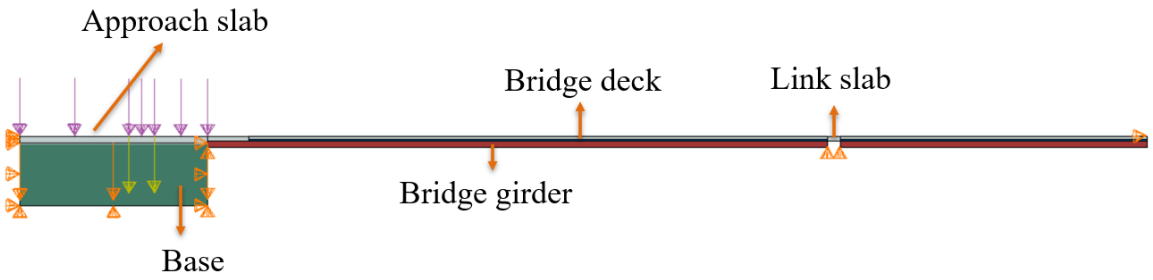

(a)

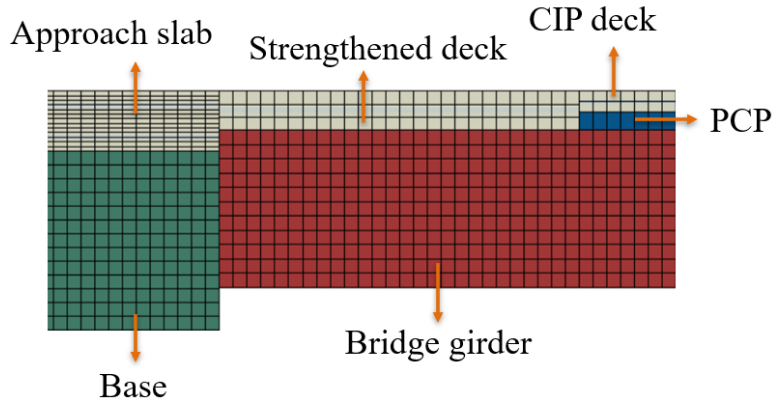

(b)

Figure 6.10: FE model details of the approach slab with a bridge: (a) Boundary conditions; (b) Mesh details of the primary elements at the seamless connection.

The modeling details of the approach slab and base were the same as used in the previous model for the out-of-plane analysis of the approach slab. The boundary conditions are demonstrated in Figure 6.10(a). The boundary conditions on the base layer and pavement side of the approach slab were consistent with previous models. At the other side of the model, i.e., the center of the bridge, the longitudinal translational movement was restrained, whereas the vertical translational movement was free, due to a symmetrical geometry. Simply-supported boundary conditions were applied at the girder.

The bridge elements in the model included bridge decks, girders and link slabs between two adjacent simply supported spans, as presented in Figure 6.10(a). The prototype bridge had three 100-ft.-long spans. The bridge was representative of common bridge configurations in Texas. The bridge decks were modeled as 8.5 in. thick, comprising of a partial-depth PCP and CIP portion of the concrete. Figure 6.10(b) presents a closer view of the primary elements at the seamless connection, through which PCP and CIP portion of the deck were displayed. The bridge girder generally contributes the majority of the rotational stiffness at the bridge section. Figure 6.11 presents the cross-section dimensions of typical I-girders used in Texas (TxDOT, a). The nominal depth of I-girders varies in the range of 28 in. to 70 in. The rotational stiffness of the bridge increases as the girder depth increases.

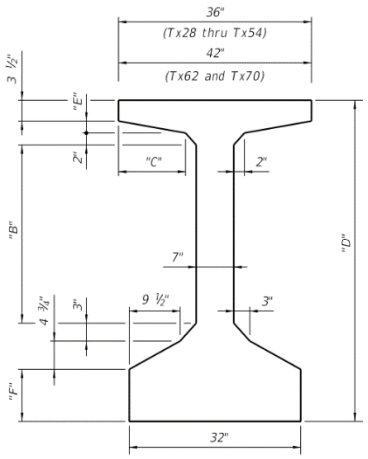

GIRDER DIMENSIONS							
Girder Type	"D" (in.)	"B" (in.)	"C" (in.)	"E" (in.)	"F" (in.)	Area (sq. in.)	Weight (plf)
Tx28	28	6	12 ½"	2"	6 ¾"	585	630
Tx34	34	12	12 ½"	2"	6 ¾"	627	675
Tx40	40	18	12 ½"	2"	6 ¾"	669	720
Tx46	46	22	12 ½"	2"	8 ¾"	761	819
Tx54	54	30	12 ½"	2"	8 ¾"	817	880
Tx62	62	37 ½"	15 ½"	2 ½"	8 ¾"	910	980
Tx70	70	45 ½"	15 ½"	2 ½"	8 ¾"	966	1,040

Figure 6.11: TxDOT I-girder cross-section dimensions (TxDOT, a).

For this analysis, the girder cross-section was simplified as an exact I-shape with the dimensions shown in Figure 6.12(a). The prototype bridge had a girder depth of 60 in., which was assumed to represent the upper range of likely girder depths and correspondingly represented a relatively large rotational restraint provided by common Texas bridges. The tributary deck width over a supporting girder was assumed to be 90 in. For simplicity, the I-shape girder was equivalently converted to a rectangular girder, assuming a uniform distribution of the section flexural stiffness over the tributary width. As a result, the depth of the equivalent rectangular girder was taken as 34 in. Link slabs were modeled as 2 ft. long and 8.5 in. thick.

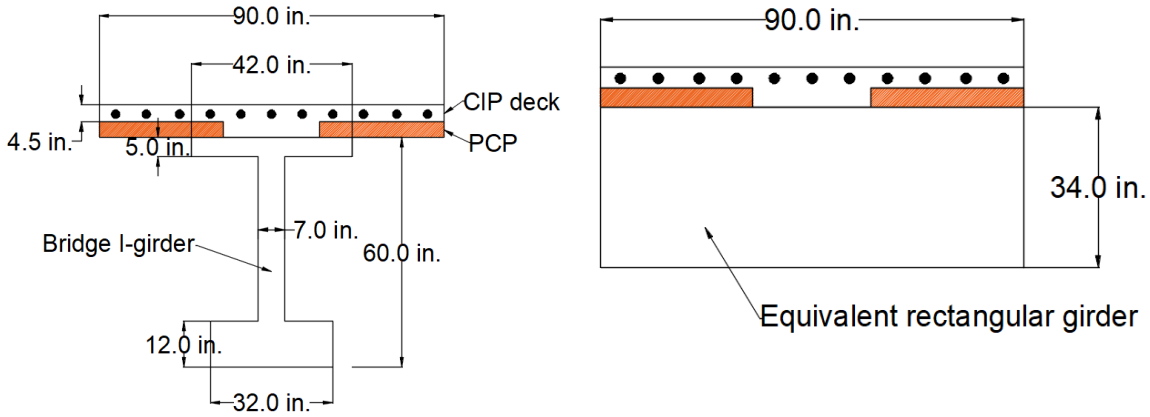

(a) (b)

Figure 6.12: Cross-section of the prototype bridge for a tributary width: (a) Bridge deck over I-girder; (b) Bridge deck over equivalent rectangular girder.

As demonstrated in Figure 6.10(b), a small portion of the bridge deck near the abutment was strengthened. This local bridge deck region was subjected to increased demands due to the combined axial and out-of-plane effects. For the seamless bridges of the WM7 project constructed in Australia, the longitudinal reinforcement at the top layer within the approach slab continued to the bridge deck of the end-span for a short distance of 6.5 ft. until a construction joint (CJ) was employed (Griffiths, personal communication, 2020). The reinforcement ratio within this region

was approximately 2%, which was a significant increase compared to a ratio of approximately 0.78% for the remaining bridge decks over the girders.

This local bridge deck was simulated as 6.5 ft. long and was strengthened by utilizing a full-depth CIP concrete section instead of a combined PCP and CIP section and higher longitudinal reinforcement amounts. The simple practice of continuing the top layer longitudinal reinforcement of the approach slab to the strengthened deck as employed in the Australia seamless bridge was used. The corresponding reinforcement ratio of the strengthened deck was approximately 1.5%, whereas 0.7% was used for the remaining bridge decks over the girders.

The bridge girders were assumed to remain elastic and were modeled using the gross section properties. Concrete nonlinear constitutive laws were used for the bridge decks over the girders and link slabs to capture the cracking behavior. The concrete compressive strengths for the bridge girders, bridge decks and approach slab were taken as 8 ksi, 4 ksi, and 4 ksi, respectively. The elastic modulus of the reinforcing steel is 29000 ksi and the nominal yield strength was taken as 60 ksi.

Figure 6.13 illustrates the contour plot of the vertical displacements of the system. In Figure 6.13, the geometry of the system is magnified (×2) in the vertical direction to assist in displaying the results more clearly. The primary behavior of interest due to the out-of-plane effects is the flexure within the approach slab and strengthened bridge deck near the abutment which are subjected to negative bending moment. Figure 6.14(a) presents the concrete longitudinal stresses within those two interested regions. The concrete in the top is subjected to tension. Figure 6.14(b) and (c) plot the steel stresses of the approach slab and strengthened bridge deck, respectively. The tensile steel stress within the approach slab is the largest at the bridge end with an approximate value of 10 ksi, which is a significant decrease relative to the value of 25 ksi estimated by the model with an idealized fixed-end boundary condition previously outlined in Section 6.3.1. The strengthened deck has the same level of tensile steel stresses at the bridge abutment end.

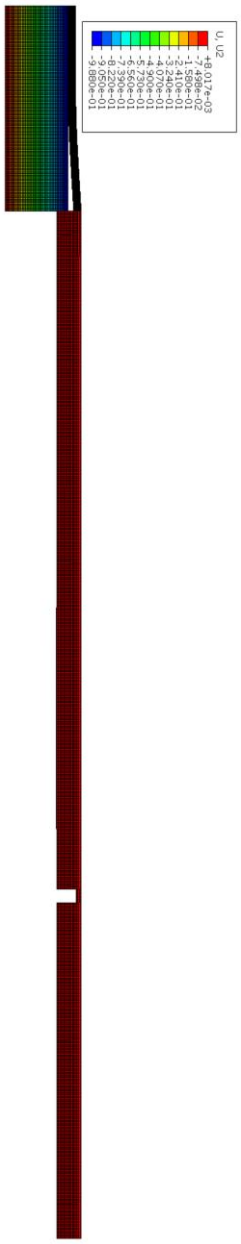
U, U2
+9.017e+03
+7.484e+02
-1.580e+01
-2.410e+01
-4.074e+01
-4.906e+01
-5.738e+01
-6.570e+01
-7.390e+01
-8.222e+01
-9.054e+01
-9.886e+01

(a)

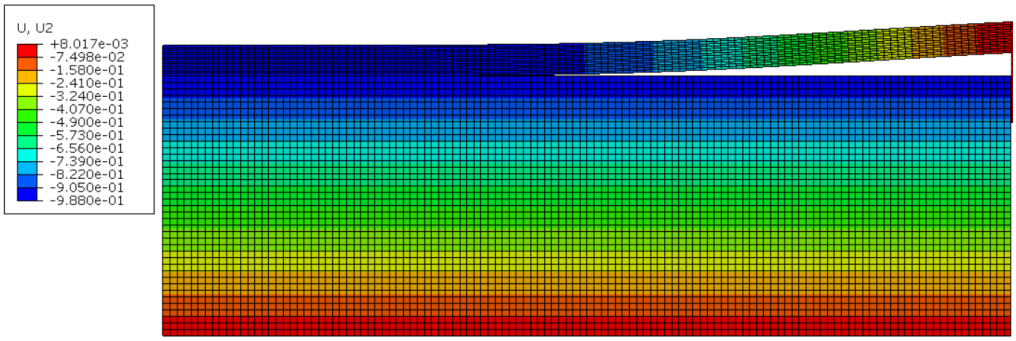

(b)

Figure 6.13: Contour plot of the vertical displacement (deflection scale factor: 10): (a) The approach slab-bridge structure; (b) Zoomed transition zone.

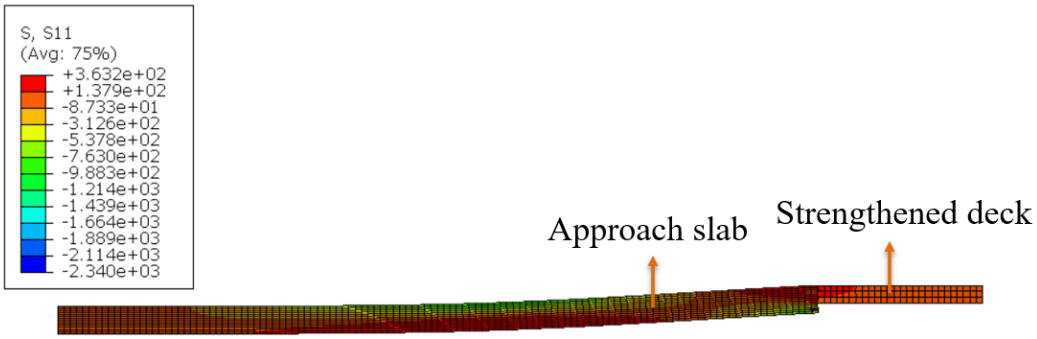

(a)

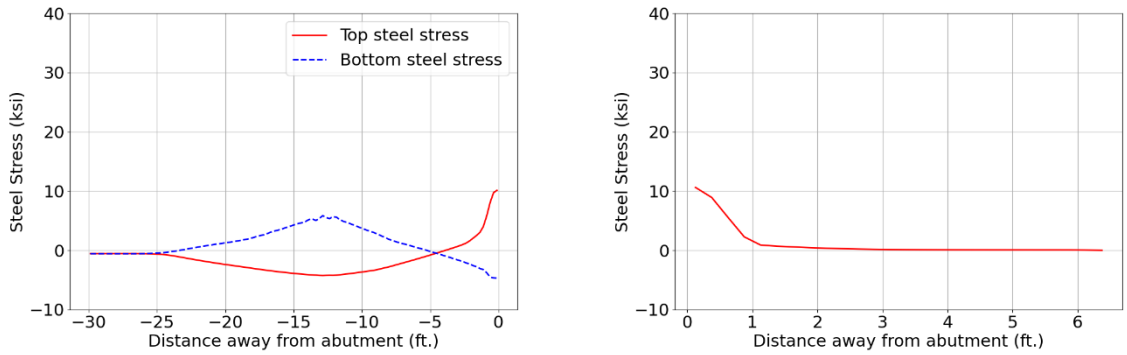

(b) (c)

Figure 6.14: Material stresses of the approach slab-bridge structure: (a) Concrete longitudinal stress near the bridge abutment; (b) Steel stress of the approach slab; (c) Steel stress of the strengthened bridge deck.

Figure 6.15 compares the response of the approach slab for models with the range of end restraints discussed in Section 6.3.2 consisting of: 1) the modelled bridge (best estimate of the restraint and therefore labeled "Model with actual restraint"); 2) three different rotational springs simulating the restraint of the bridge; and 3) full fixity. The response of the approach slab with bridge modelled produced results within the range when the rotational stiffness varied between 5×10^6 and 10^7

lbf·in/radian. Therefore, the rotational stiffness of 10^7 lbf·in/radian is deemed to be a reasonable representation for the estimation of the rotational restraint provided by the bridge. For the subsequent modeling of the transition zone subjected to the combined axial and out-of-plane effects, a rotational spring was employed at the bridge end of the approach slab with a stiffness of 10^7 lbf·in/radian.

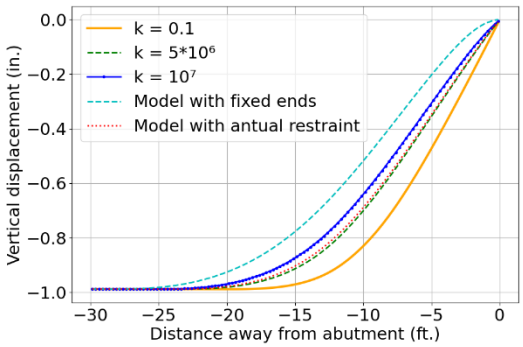

(a)

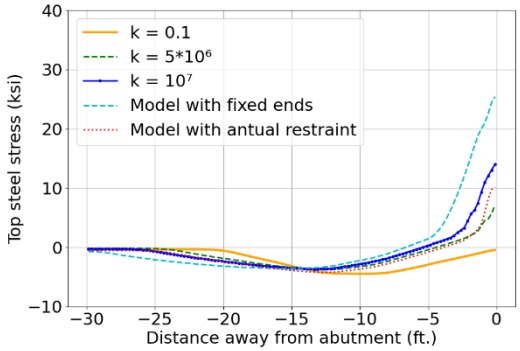

(b)

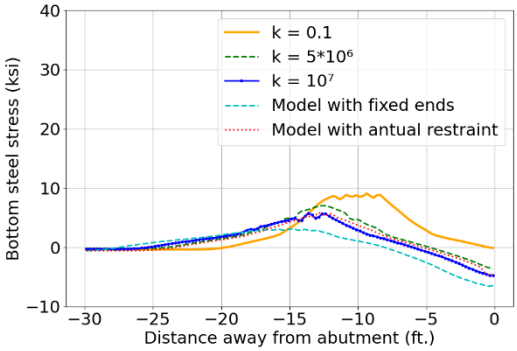

(c)

Figure 6.15: Comparison of response of the approach slab with actual restraint and different rotational restraints: (a) Vertical displacement; (b) Top steel stress; (c) Bottom steel stress.

6.4 Combined Axial and Out-of-Plane Analysis of Transition Zone

While the last section focused on the impact of flexural stresses in the transition zone from vehicular loads and embankment settlement, the flexural stresses need to be combined with axial force effects. The approach slab is subjected to both axial effects due to the thermal deformation of the bridge and pavement itself, and out-of-plane effects due to the embankment settlement and vehicular loads. The stress demands corresponding to the axial effects and the flexural effects were characterized separately in Chapter 5 and Section 3 of the present chapter, respectively. The approach slab is in tension when the temperature decreases and in compression when the temperature increases. The axial force is the largest near the bridge abutment. With the out-of-plane effects alone, the critical region is the top side near the bridge abutment, where the concrete is anticipated to crack, and a relatively large tensile stress is induced in the longitudinal reinforcement. The response of the approach slab near the bridge end due to the axial effects

corresponding to a temperature decrease and out-of-plane effects will superimpose, causing even larger tensile steel stresses in the top approach slab near the bridge abutment.

As mentioned, the reported tensile stress for the out-of-plane effects alone corresponds to the average stress between cracks. The tensile steel stress at cracks is higher than the average steel stress since concrete carries no tensile forces at cracks. The design criteria of a seamless bridge-pavement system for the serviceability limit state established in Section 5.4.3 state that the maximum steel stress at cracks should be controlled below 40 ksi and 36 ksi for the pavement and bridge deck, respectively, to control the crack width within an acceptable limit. A final design of the approach slab should ensure that the maximum steel stress at cracks with the combined axial and out-of-plane effects satisfies the design limits.

This section discusses the response of the approach slab with the combined axial (temperature decrease) and out-of-plane effects using a 2D continuum model of the transition zone.

6.4.1 Model Description

A 2D continuum model of the transition, which comprised a transition slab and an approach slab made of reinforced concrete, a base layer, and the concrete slab-base interaction was developed for the combined axial and out-of-plane analysis, as presented in Figure 6.16(a). The modeling scheme described in Section 6.2 was employed for this analysis.

The model simulated the response of the transition pavement per unit width (1 in.). The approach slab had the same configuration (30 ft. long and 13 in. thick, reinforcement ratio of 2% equally distributed among top and bottom layers) as in the previous models presented in Section 6.2.1. The length and reinforcement ratio of the transition slab were consistent with those used for the axial analysis of a prototype seamless bridge-pavement system in Texas as described in Section 5.4. The transition slab was simulated as 600 ft. long, which consisted of three segments (as marked by the dashed lines in Figure 6.16(a)). The reinforcement ratio for each segment is also presented in Figure 6.16(a). The corresponding length for each segment was 430 ft., 100 ft., and 70 ft. The thickness of the transition slab was 13 in. as well. The base layer was modeled with a thickness of 10 ft.

A uniform mesh size of 3 in. was used for the base, reinforcement and concrete elements in the transition slab. For the approach slab, the concrete elements were meshed with a size of 3 in. along the longitudinal direction and a finer size of 1 in. in the vertical direction to achieve a more refined representation of stresses along the cross-section. Figure 6.16(b) shows the mesh details of different types of elements in the model.

The concrete compressive strength of the transition zone was taken as 4 ksi. A constant coefficient of friction $\mu = 0.8$ was assumed for the transition slab, which is consistent with the approximate measured value for the felt paper bond breaker on CSB. Considering that the majority of the approach slab was separated from the base under the vertical loads, the interface between the approach slab and base was assumed frictionless considering a separation of two surfaces due to the embankment settlement.

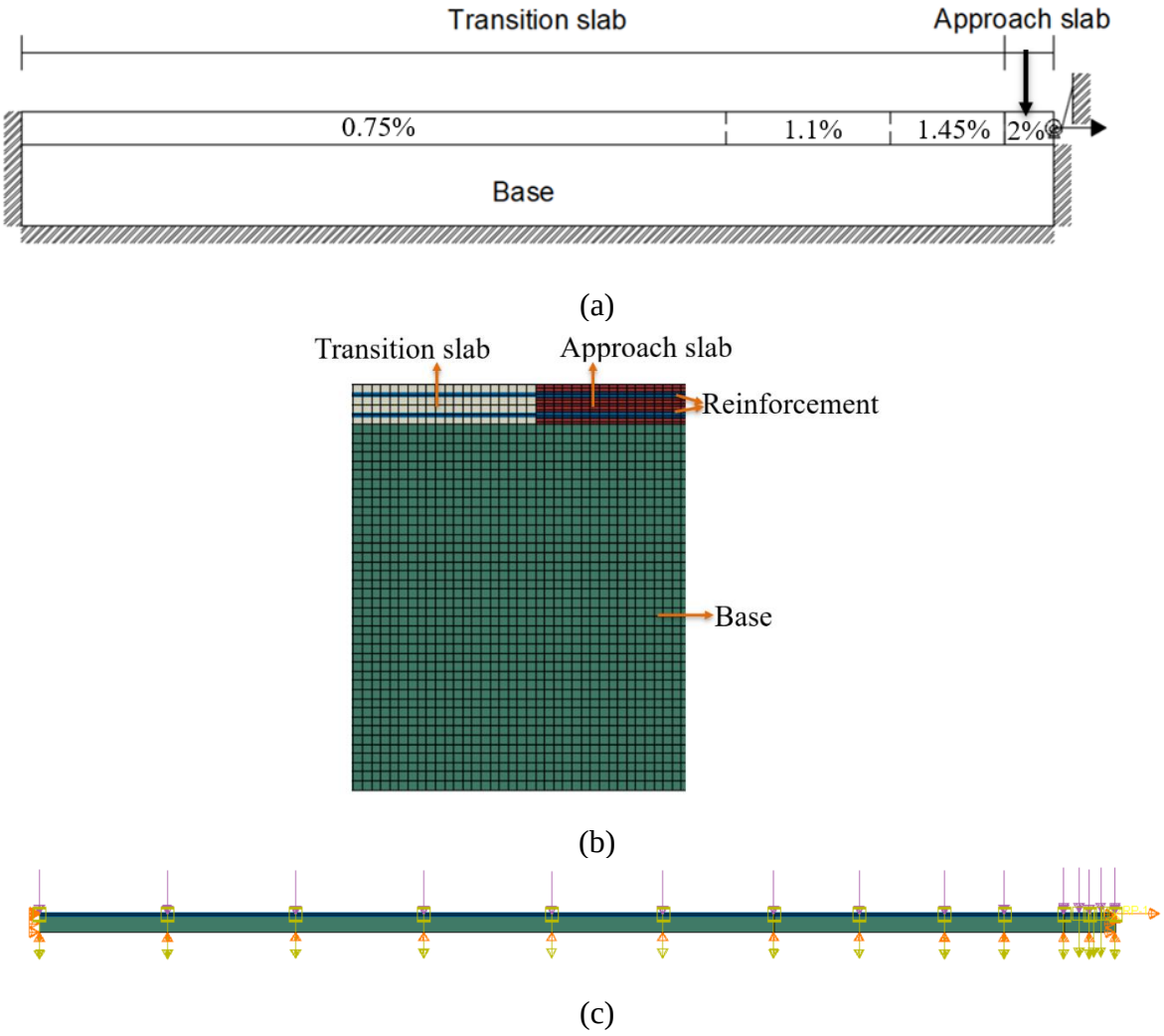

Figure 6.16: FE model details of the transition zone: (a) A sketch with boundary conditions (not scaled in dimensions); (b) Mesh details; (c) Details of boundary conditions and loads.

Boundary conditions are also illustrated in Figure 6.16(a) and (c). The base layer was longitudinally restrained on both lateral sides and vertically restrained on the bottom. The transition zone was longitudinally restrained at the pavement end, whereas it could move vertically as the base settled. On the bridge end of the approach slab, the point at the middle height of the approach slab was restrained in the vertical direction, whereas the remaining sections can rotate controlled by a rotational spring with a stiffness of 10^7 lbf·in/radian. In the longitudinal direction, a prescribed movement was defined as discussed in detail in the following paragraph.

Four loadings were considered including the self-weight of the transition zone, axial effects due to the temperature change and bridge movement, embankment settlement and vehicular loads. The different loads were applied in separate steps. For the axial effects, with the temperature decrease, the transition zone was subjected to its thermal contraction and bridge contraction as well. The longitudinal movement of the bridge over the abutment was obtained from the axial analysis of the entire system with the same temperature decrease using the analytical method developed in

Chapter 5. The shrinkage effects were not considered based on the findings in Chapter 5. In summary, in addition to a uniform temperature decrease (-55°F) applied for both the concrete and reinforcement elements of the transition pavement, a longitudinal movement of approximately 0.41 in. representing the bridge contraction was applied at the middle height of the bridge end. For the out-of-plane effects, the 1 in. embankment settlement was applied at the top surface of the entire base layer. The vehicular loads including the design tandem and design lane load as specified in Section 6.2.4 were applied for the approach slab only. Figure 6.16(c) presents the loading details of the model. Note that the temperature change is not explicitly displayed in this figure.

6.4.2 Response with Axial Effects

Figure 6.17(a) and (b) plot the average steel stress and maximum steel stress along the entire transition zone when the system was subjected to a uniform temperature decrease of 55°F and a longitudinal displacement of 0.41 in. toward the bridge. The horizontal axis represents the locations on the transition slab and approach slab from left to right. The origin represents the bridge abutment position. The values of the maximum steel stress at crack locations were calculated by dividing the total tensile force in the section (that of concrete and steel) by the steel area, as described in Chapter 5.

Considering the axial effects, the maximum steel stresses at cracks within the transition zone are below the limit of 40 ksi, which is also marked in Figure 6.17(b). For the approach slab, due to the axial effects alone, the average and maximum steel stresses are approximately 8 ksi and 22 ksi, respectively.

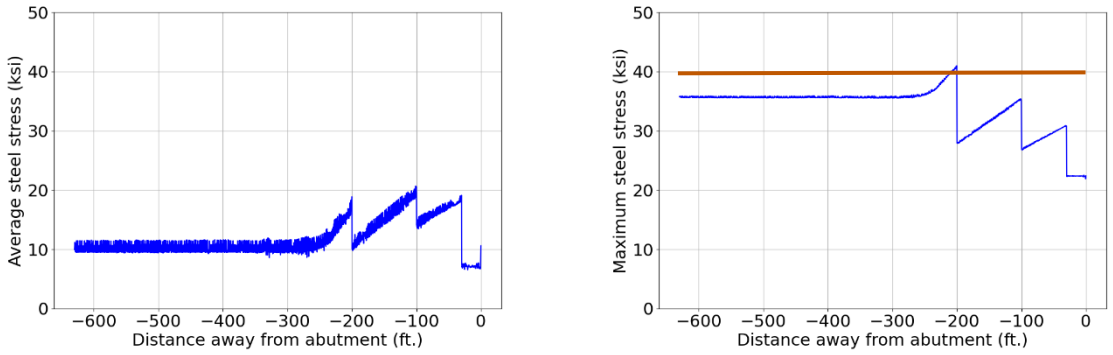

Figure 6.17: Axial response of the transition zone: (a) Average steel stress; (b) Maximum steel stress.

6.4.3 Response with Combined Effects

The response of the transition slab is mostly controlled by the axial effects. Considering the response of the approach slab when subjected to the embankment settlement and vehicular loads, a small portion of the approach slab near the pavement end is supported by the base layer without being subjected to the out-of-plane effects. Therefore, the focus on the behavior is directed at the response of the approach slab with the combined axial and out-of-plane effects.

After the axial effects were applied, the embankment settlement and vehicular loads were applied sequentially in two separate steps. Figure 6.18 presents the response of the approach slab in the two loading conditions: 1) axial and settlement; and 2) axial, settlement and vehicular loads. The first loading condition considered the thermal effects and embankment settlement only, which are generally deemed as long-term effects for the seamless system. The second loading condition can be considered as a worst-case scenario when the vehicular loads are temporarily imposed to the system in addition to the maximum level of the long-term effects.

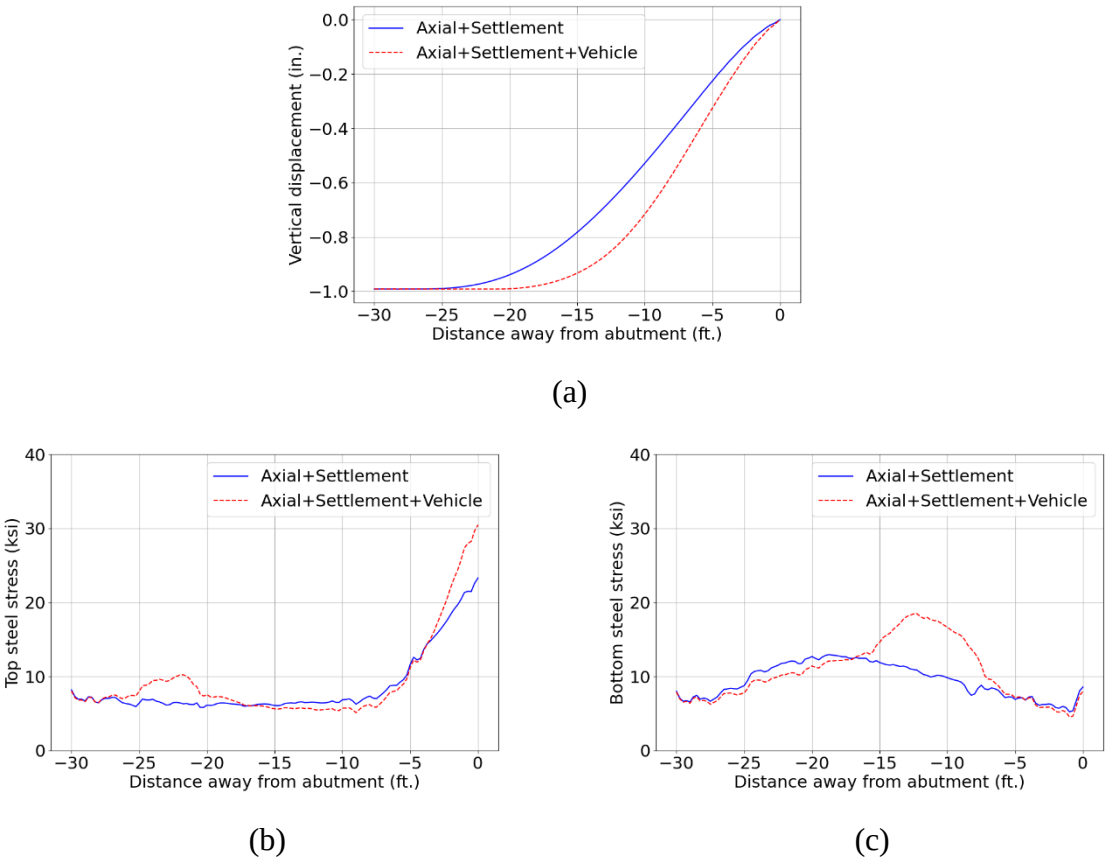

Figure 6.18: Combined axial and out-of-plane response of the approach slab: (a) Vertical displacement; (b) Top steel stress; (c) Bottom steel stress.

The vertical displacement plot in Figure 6.18(a) where a small portion of the approach slab near the pavement end has no deflection confirms that the transition slab is not affected by the out-of-plane effects. Once the base layer settles 1 in., the average tensile steel stress is the largest near the abutment with an approximate value of 22 ksi. When the approach slab is further subjected to vehicular loads, the approach slab deflects more. The negative bending moment at the bridge end of the approach slab is also increased when the vehicular loads are additionally applied. As a result, the largest average tensile steel stress increases to approximately 30 ksi, as shown in Figure 6.18(b).

The average tensile stress developed in the top layer of longitudinal reinforcement near the bridge abutment due to the axial effects only is 8 ksi. A previous analysis of the approach slab due to the

out-of-plane effects only as discussed in Section 6.3.3 evaluates this value as approximately 11 ksi. The average tensile steel stress near the bridge abutment increases to 30 ksi with the combined effects. These results indicate that the axial effects and out-of-plane effects on the response of the approach slab are not a case of simple linear superposition. The fact that the combined effects in the tensile reinforcing steel is larger than the sum of the two separate effects is explained by the evolution of cracking in the reinforced concrete section. With combined loading conditions, the propagation of concrete cracking from the top surface of the approach slab with increasing loads leads to a gradual reduction of the section stiffness and a shift of the neutral axis, which results in an increase of tensile steel stress compared to the cases of simple superposition.

The maximum tensile steel stress at the top layer longitudinal reinforcement near the bridge abutment due to the combined axial and out-of-plane effects was estimated based on the results of the analyses. It was calculated by dividing the total tensile force of the cracked reinforced concrete section by the steel area. For concrete, only a portion of the area subjected to tension is considered to be effectively transmitted to steel at crack locations, according to the tension-stiffening provisions in fib Model Code for Concrete Structures 2010 (fib, 2013). The effective concrete area in tension $A_{c,ef}$ (Figure 6.19) in a slab subjected to bending is defined in Eq. 6.1:

$$A_{c,ef} = \min\left(2.5 \times \left(c + \frac{\varphi}{2}\right), \frac{(h-x)}{3}\right), \qquad \text{Eq. 6.1}$$

where:

c = concrete cover,
φ = diameter of the tensile rebar,
h = entire depth of the section,
x = the distance between the neutral axis and the compressive side of the cross-section.

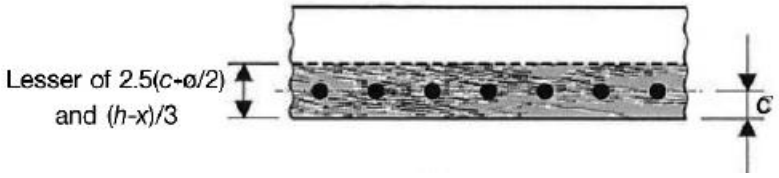

Figure 6.19: Effective concrete area in tension in a slab subjected to bending (fib, 2013).

The maximum steel stress at cracks for a reinforced concrete slab subjected to bending is defined in Equation 6.2:

$$f_{s,max} = (f_{c,ave}A_{c,ef} + f_{s,ave}A_s)/A_s, \qquad \text{Eq. 6.2}$$

where:

$f_{s,max}$ = maximum tensile steel stress at cracks,
$f_{c,ave}$ = average concrete longitudinal stress in tension,
$f_{s,ave}$ = average steel stress in tension,
A_s = tensile rebar area.

Figure 6.20 presents the contour plot of the concrete longitudinal stresses of the approach slab of 4 ft. long near the bridge abutment. At this region, the top of the approach slab is subjected to

flexure and tension. The neutral axis is located at a distance of 10 in. from the tensile side. It was assumed that #6 rebars were used, which has a diameter of 0.75 in. The concrete cover was 3 in. The entire depth of the section was 13 in. Correspondingly, the effective concrete area was determined as 3.33 in^2 based on Eq. 6.1, which was controlled by the value of $\frac{(h-x)}{3}$. The reinforcement area in the top layer was 0.13 in^2. At the local section near the bridge end of the approach slab, the average concrete stress is approximately 250 psi (as shown in Figure 6.20), and the average tensile steel stress is approximately 30 ksi. Based on Eq. 6.2, the maximum steel stress due to the combined axial and out-of-effects was estimated as 36.4 ksi, which is below the stress limit of 40 ksi.

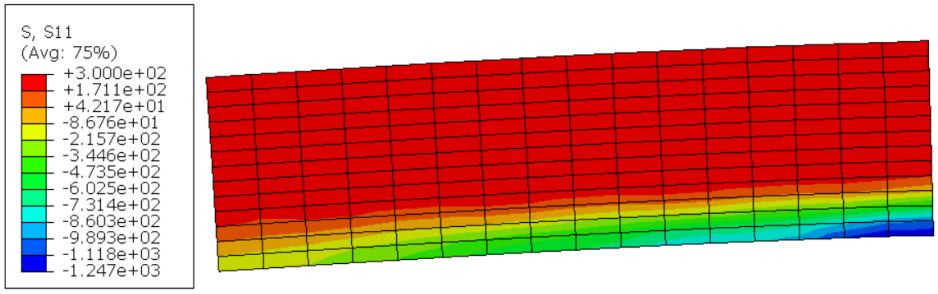

Figure 6.20: Longitudinal concrete stress contour plot of a local region of the approach slab (approximately 4 ft. long from the bridge abutment).

6.5 Numerical Parametric Study

6.5.1 Overview

This section investigates numerically the effects of key design parameters, namely the reinforcement ratio and thickness of the approach slab, on the response with the combined axial and out-of-plane effects. The response of the approach slab with various levels of the embankment settlement was also investigated. This numerical parametric study complements those findings of the Chapter 5 on the effects of the configurations of the transition zone (such as slab thickness, reinforcement ratio) and bridge (span length, number of spans, number of girders, girder size) on the axial response of the entire seamless bridge-pavement system.

The FE model of the transition zone as described in Section 6.4 was used as a benchmark model for the numerical parametric study. The approach slab was 30 ft. long and 13 in. thick with reinforcement ratio of 2% uniformly distributed among top and bottom layers. The axial effects including a uniform temperature decrease of 55°F and a longitudinal displacement of 0.41 in. toward the bridge were applied. The approach slab was subjected to a 1 in. embankment settlement and vehicular loads. The out-of-plane response of the approach slab with varying magnitudes of the parameters were compared with that of the benchmark model.

6.5.2 Reinforcement Ratio of Approach Slab

As discussed in Section 5.5.4, the reinforcement amount in the transition zone affects the stiffness of the pavement and controls the cracking behavior of the reinforced concrete. The response of the approach slab when subjected to the combined axial and out-of-plane effects as shown in Section 6.4 indicates that the bottom longitudinal reinforcement at approximately middle span of the

approach slab is in tension but it is not critical due to a smaller negative bending moment and thus a lower stress level compared to those near the bridge end. It is more concerned at the bridge end, where the maximum tensile steel stress at the top layer is approximately 34 ksi. Therefore, in this parametric study, the reinforcement ratio of the top layer steel of the approach slab was increased from 1% for the benchmark model to values of 1.5% and 2%. The reinforcement ratio of the bottom layer steel was kept at 1%.

Figure 6.21 plots the axial response of the approach slab with different ratios of the top layer reinforcement. The effects of the reinforcement ratio on the axial response agree with the observations using a 1D structural model as discussed in Section 5.5.4. The increase in reinforcement leads to the increase in axial stiffness of the pavement, which generates slightly higher axial forces in the system. Nevertheless, the axial strain of the approach slab decreases as the reinforcement amount in this region increased. A higher reinforcement ratio is beneficial in cracking control as indicated by a lower maximum steel stress at cracks.

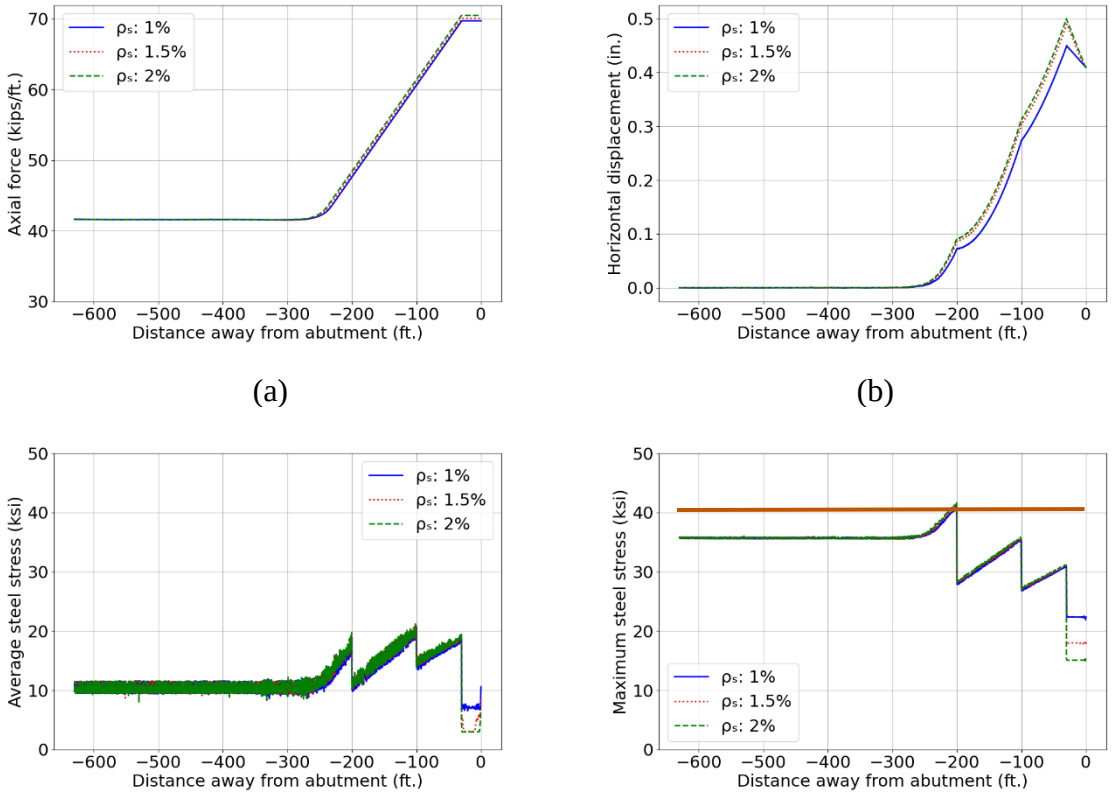

Figure 6.21: Axial response of the approach slab for different reinforcement ratios at the top layer: (a) Axial force; (b) Longitudinal displacement; (c) Average steel stress; (d) Maximum steel stress.

For the response of the combined axial and out-of-plane effects, Figure 6.22 compares the vertical displacement, average steel stresses at the top and bottom layers of the approach slab when varying the top layer reinforcement ratio. Figure 6.23 plots the corresponding concrete longitudinal stress contour of the local 4 ft. long approach slab near the bridge abutment.

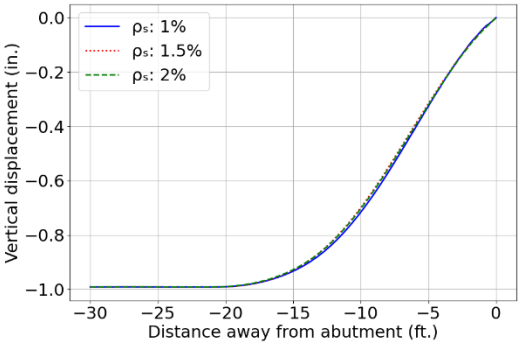

(a)

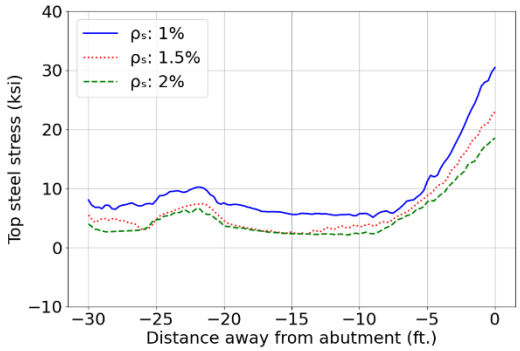

(b)

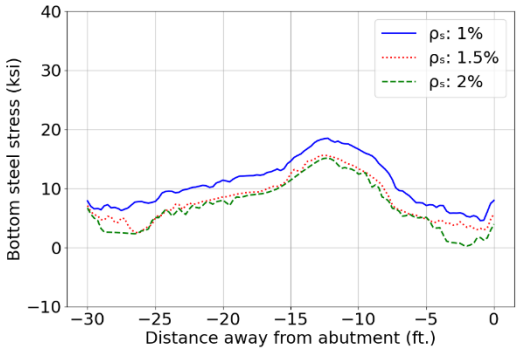

(c)

Figure 6.22: Combined axial and out-of-plane response of the approach slab for different reinforcement ratios at the top layer: (a) Vertical displacement; (b) Top steel stress; (c) Bottom steel stress.

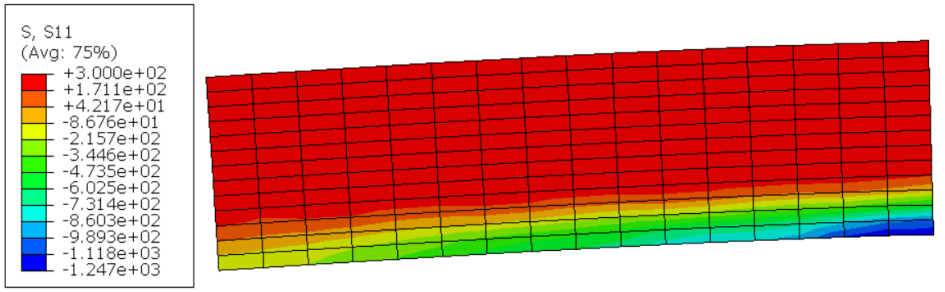

(a)

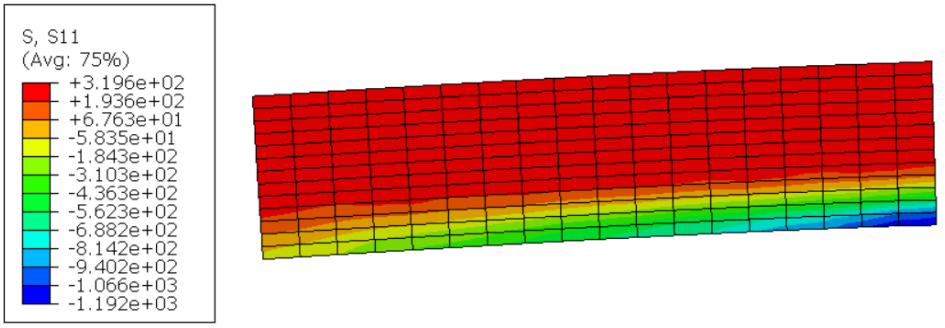

(b)

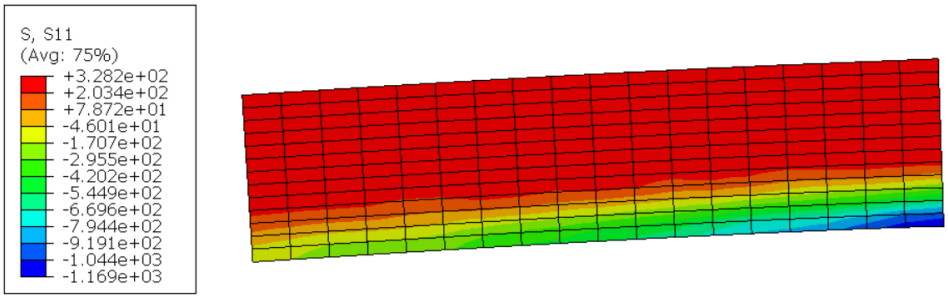

(c)

Figure 6.23: Longitudinal concrete stress contour plot of a local region of the approach slab (approximately 4 ft. long from the bridge abutment) with a top layer reinforcement ratio of: (a) 1%; (b) 1.5%; (c) 2%.

With a higher reinforcement ratio at the top layer, the neutral axis moves up slightly. The increase of reinforcement ratio at the top layer mostly affects the tensile stresses of the top steel. When the reinforcement ratio of the top layer is 1%, 1.5% and 2%, the largest average tensile steel stress is approximately 30 ksi, 22 ksi and 19.5 ksi, respectively. Table 6.1 summarizes the approximate location of the neutral axis (x), average concrete tensile stress in the tension region, average tensile stress at the top layer, and the corresponding calculated maximum tensile stress at the bridge end of the approach slab for each reinforcement ratio condition. The maximum tensile steel stress reduces from 36.4 ksi to 26 ksi when the top layer reinforcement ratio increases from 1% to 1.5%. When the reinforcement ratio reaches 2%, the maximum steel stress further decreases to 22.6 ksi.

In summary, an increase of the reinforcement amount in the top layer decreases the maximum steel stress at cracks and improves the cracking control within the local region of the approach slab near

the bridge abutment. This decrease is not proportional to the amount of reinforcement due to the shift of neutral axis and the variations in sectional forces with the reinforcement ratio.

Table 6.1: Comparison of response for different reinforcement ratios at the top layer.

$\rho_{s,top}$ (%)	x (in.)	$A_{c,ef}$ (in^2)	A_s (in^2)	$f_{c,ave}$ (ksi)	$f_{s,ave}$ (ksi)	$f_{s,max}$ (ksi)
1	3	3.33	0.13	0.25	30	36.4
1.5	4	3	0.195	0.26	22	26.0
2	4	3	0.26	0.265	19.5	22.6

Note: The symbols used in this table are defined in Eq. 6.1 and 6.2.

6.5.3 Thickness of Approach Slab

As discussed in Section 5.5.3, an increase in the thickness of the transition zone leads to an increase in the stiffness of the pavement, which impacts the system response due to the bridge-pavement interaction. The thickness of the approach slab will affect its flexural stiffness in resisting the out-of-plane effects as well.

The effects of the thickness of the approach slab on the out-of-plane response were evaluated using four section configurations. Three of the section configurations had constant thickness values over the entire length of the approach slab and the values of the thickness considered were 13 in., 15 in. and 16 in., respectively. The other section was tapered along the approach slab, with the thickness gradually increasing from 13 in. at the pavement end to 16 in. at the bridge end. The tapered approach slab had an inclined angle of 0.48° with respect to the base layer at the interface. The thickness of CRCP typically varies in a range between 7 in. to 15 in. A transition zone with an equal thickness as the CRCP it connects simplifies the construction procedure. However, a thicker approach slab could potentially have better performance in the case of the out-of-plane effects with an increased flexural stiffness. In such a condition, a tapered approach slab might be a preferable option to accommodate the difference in thickness and provide the desired strength as well.

Figure 6.24 compares the out-of-plane response of the approach slab with the four above-mentioned configurations. Increasing the thickness of the approach slab increases the flexural stiffness of the section, leading to relatively smaller deflections. The largest average tensile steel stress at the top layer decreases from approximately 12.5 ksi to 9 ksi when the thickness increases from 13 in. to 16 in.

The varying thickness of the tapered approach slab accommodates the demands along the approach slab. The section flexural stiffness gradually increases as the demand increases toward the bridge end. It results in an average tensile steel stress of approximately 7.5 ksi.

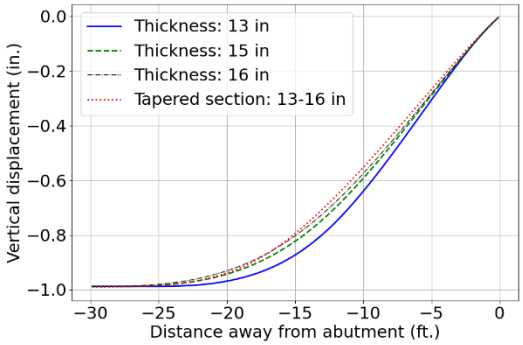

(a)

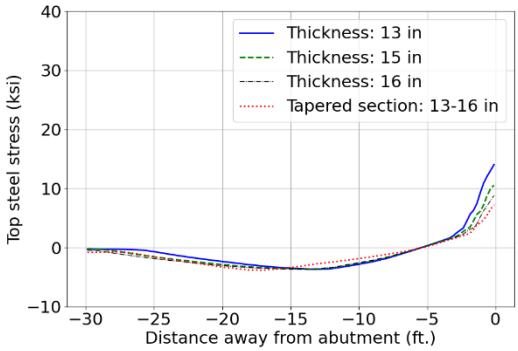

(b)

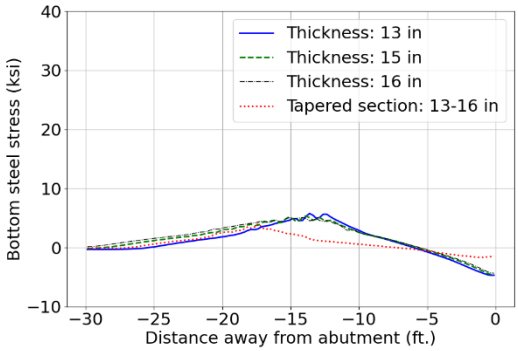

(c)

Figure 6.24: Out-of-plane response of the approach slab for different thicknesses: (a) Vertical displacement; (b) Top steel stress; (c) Bottom steel stress.

The response of the approach slab with a tapered section along the length with the combined axial and out-of-plane effects were further analyzed. Figure 6.25 compares its response with that of the benchmark model, which had a constant thickness of 13 in. along the length. The average tensile steel stress of the top layer at the bridge end reduces to approximately 21 ksi with a tapered approach slab. Figure 6.26 plots the longitudinal concrete stress contour of the local 4 ft. long of the approach slab near the bridge abutment. The average concrete stress near the bridge end of the approach slab in the tension region is approximately 270 psi. The reinforcement area in the top layer was 0.13 in^2. The neutral axis was located at approximately 4 in. to the compressive side. The effective concrete area in the tension region was determined as 4 in^2. It results in a maximum steel stress at cracks of approximately 29.4 ksi, which is lower compared to 36.4 ksi in the case of a constant thickness of 13 in.

In conclusion, for the seamless bridge-pavement system, a tapered approach slab is potentially a preferable option as varied sections accommodate the demands, leading to an optimal design. In addition, a tapered approach slab smoothly adjusts the thickness differences between the transition slab and approach slab without causing the disturbance of the underneath base under the longitudinal movement of the transition zone.

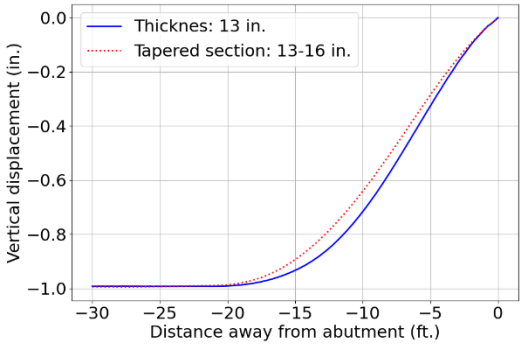

(a)

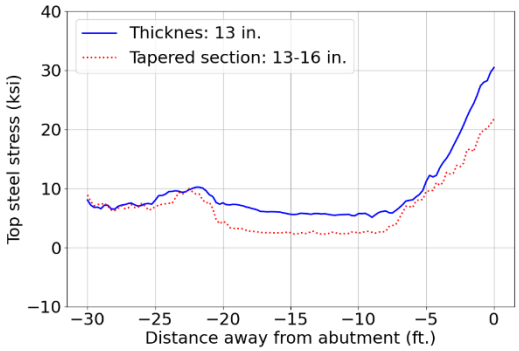

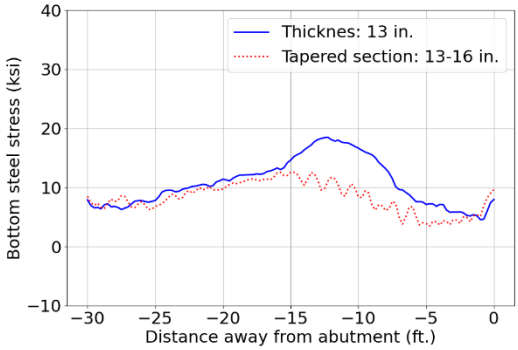

(b) (c)

Figure 6.25: Combined axial and out-of-plane response of the approach slab for different thicknesses: (a) Vertical displacement; (b) Top steel stress; (c) Bottom steel stress.

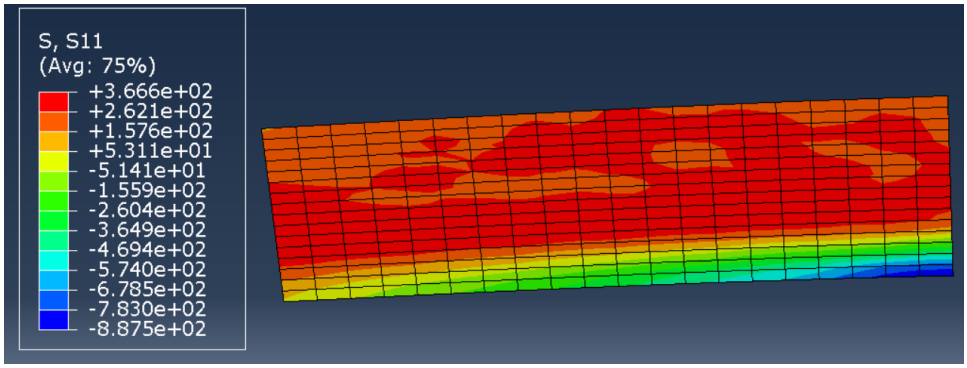

Figure 6.26: Longitudinal concrete stress contour plot of a local region of the approach slab (approximately 4 ft. long from the bridge abutment) for a tapered approach slab.

6.5.4 Differential Embankment Settlement

The magnitude of the differential embankment settlement between the bridge and pavement can vary as the embankment material properties and compaction conditions. Puppala et al. (2009) summarized the bump tolerances recommended in previous studies, above which the repair was needed. Some researchers suggested the use of an absolute value, such as 2.5 in. by Walkinshaw (1978). Some defined the allowable bumps as a function of the approach slab length, for example,

a settlement gradient of 1/200 by Wahls (1990) and Stark et al. (1995). In the Australia seamless bridge, a 1.6 in. settlement was used for the design of a 32-ft.-long approach slab, which was twice the predicted long-term settlement. Others used the International Roughness Index (IRI) to evaluate the bump issues, as adopted by TxDOT (Jayawickrama et al., 2005; James et al., 1991).

For the present study, a 1 in. settlement was deemed a reasonable amount. In this parametric study, the response of combined axial and out-of-plane effects of the approach slab were investigated when a larger embankment settlement, such as 2 in. and 3 in., occurred. Figure 6.27 presents the vertical displacement, steel stresses at the top and bottom layer of the approach slab in three cases of embankment settlement. A larger embankment settlement causes higher negative bending moment near the bridge abutment and results in a higher tensile stress at the top longitudinal reinforcement near the bridge abutment. The largest average tensile stress is approximately 40 ksi and 46 ksi when the embankment settles 2 in. and 3 in., respectively. Therefore, in order to satisfy the design criterion, the cross-section and reinforcement configuration of the approach slab must be modified if a larger embankment settlement is anticipated.

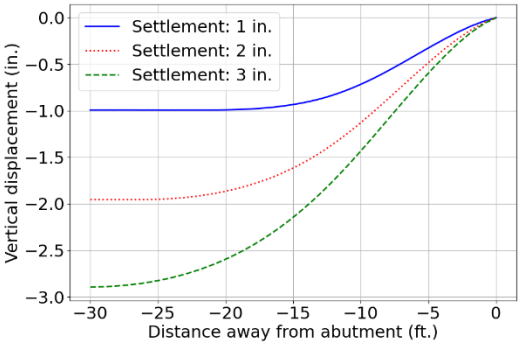

(a)

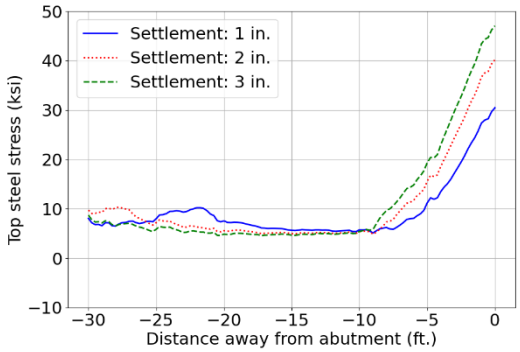

(b)

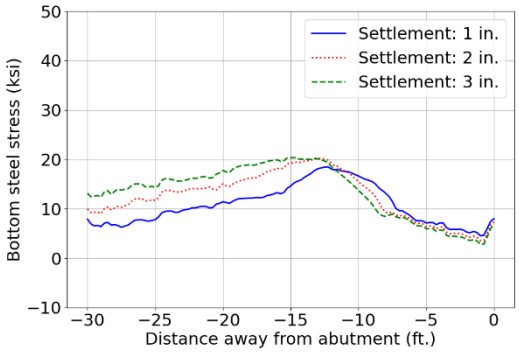

(c)

Figure 6.27: Response of combined axial and out-of-plane effects of the approach slab for different settlements: (a) Vertical displacement; (b) Top steel stress; (c) Bottom steel stress.

It should be noted that the unsupported length of the approach slab increases with larger embankment settlements. In the case of a 3 in. embankment settlement, the entire approach slab is separated from the base layer. This may lead to unsupported region of the transition slab due to

the out-of-effects. In this case, the approach slab should be designed longer than 30 ft. to limit the out-of-effects only in the approach slab.

6.5.5 Summary

In this chapter, a two-dimensional continuum FE model capable of simulating the cracking response was developed for the out-of-plane analysis of the approach slab when subjected to embankment settlement and vehicular loads. A contact condition at the concrete slab-base interaction was used to capture the shear stress-displacement relationship in the tangential direction and the separation of two surfaces in the normal direction considering the vertical loads. The proposed modeling scheme was also used to conduct the combined axial and out-of-plane analysis of the transition zone with a prescribed longitudinal displacement at the bridge end of the approach slab to represent the bridge movement due to thermal changes and concrete shrinkage. The effects of the reinforcement ratio and slab thickness of the approach slab, and level of embankment settlement on the combined axial and out-of-plane response of the approach slab were investigated through numerical parametric studies. The main conclusions and findings are summarized as follows:

- When subjected to embankment settlement and vehicular loads, the critical section in terms of maximum steel stress is at the bridge end of the approach slab, which is subjected to negative bending moment that results in tension at the top side. An idealized fixed-end boundary conditions at the bridge end of the approach slab overestimates the tensile stress of the top longitudinal reinforcement.
- The axial (temperature decrease) and out-of-plane effects add up and lead to higher tensile stresses in the top longitudinal reinforcement of the approach slab near the bridge end. The design criterion of limiting the maximum tensile steel stress is used to examine the serviceability limit state of the approach slab due to the combined effects.
- Based on the numerical parametric studies, the increase of the reinforcement ratio of the top layer significantly decreases the maximum tensile steel stress developed within the approach slab due to the combined effects, and therefore improves the cracking control in this critical region. The tensile stress decrease is less than linearly proportional to the amount of reinforcement. An increase of the thickness of the approach slab also decreases the maximum tensile stress. A tapered approach slab with gradually increasing thickness from the pavement end to the bridge end might be a more preferable option due to two reasons: 1) the varying thickness accommodates to the demand variations along the approach slab, which optimizes the use of the materials; 2) the tapered section gradually adjusts the difference of thicknesses between transition slab and approach slab to avoid disturbing the base layers when the transition zone moves longitudinally with temperature changes.

7. Instrumentation and Field Monitoring (Task 6)

7.1 Overview

Although the work plan for the research study included a task related to field instrumentation and monitoring, a suitable candidate bridge was not found with a construction schedule that satisfied the timeline of the study. Implementation of the design recommendations and monitoring of the performance are important steps to the success of this research. Therefore, the research team developed draft plans for the instrumentation scheme for a potential candidate bridge. Although the actual geometry of the candidate bridge may require modification of the instrumentation plan, the provisions in this chapter provide a good starting point for the field instrumentation and monitoring. For the future candidate seamless bridges, it is desired to gather and analyze data obtained from the instrumentation of the bridge and transition slab (and possibly the parallel conventional structure) in a timely fashion. To this end, the field monitoring system, sensors to obtain the measurements of interest are introduced in this chapter. A draft instrumentation plan is developed for future potential implementation projects when a suitable bridge is identified.

7.2 Instrumentation Techniques

7.2.1 Field Monitoring System

Both wireless and wired systems can be used for field monitoring. The determination of the system depends on the number of sensors that are to be placed on the bridge. One potential data acquisition system would be a wireless system such as the National Instruments (NI) Wireless Sensor Network (WSN). The system consists of wireless nodes that can be configured as either end nodes or router nodes that transmit data back to the wireless Gateway where data is stored. The system incorporates a modem that allows the system to be configured or data to be downloaded remotely. The NI WSN system that the researchers have used in the past is limited to approximately 70 instrumentation channels for collecting data from various types of sensors. An advantage of the WSN is that wires do not have to be placed along the full length of the bridge. However, placing and protecting the sensor nodes can be difficult. For an instrumentation of the transition slab, approach slab, and portions of the bridge, it might be difficult to locate the sensors properly. An alternative to the wireless sensor network is a hard-wired system. One of the common wired systems is Campbell Scientific (CS) Data Loggers. Although the data loggers are limited to 28 single ended or 14 differential inputs, multiplexors can be used to expand the number of input channels to well over 100 sensors. The multiplexors can be placed in a variety of locations on the site to accommodate sensor locations. The multiplexor is then wired back to the datalogger. The Gateway for the NI system as well as the CS data loggers are powered using 12-V Auto/Marine batteries. Depending on how long the system is to be monitored, solar panels can be used to recharge the batteries.

7.2.2 Field Monitoring Sensors

A variety of sensors can be used to monitor the bridge and the pavement. Foil strain gages will generally be used to monitor the strain in the reinforcing steel of the slabs and bridge deck. To measure the strains in the concrete, vibrating wire gages (VWG) such as those shown in Figure 7.1 can be used. A nice feature of the vibrating wire gages is that each gage also includes a thermistor that indicates the temperature at the location of the vibrating wire gage. The number of vibrating wire gages as well as the density of the layout depend on the desired instrumentation scheme. In some cases, strain in the cracked and uncracked concrete is desired, in which case a

dense mesh is necessary as shown in Figure 7.1. In addition to the vibrating wire gages, foil strain gages with moisture and mechanical protection can be seen on the reinforcing bars. Although the vibrating wire gages provide a measure of the temperature at the gage, thermocouples could be used as needed to obtain the required temperatures. Instead of depending on a dense mesh of sensors, a crack former might be utilized that provides a localized reduction in area might be prudent. The reduction in area would not be pronounced, but such a strategy would allow the researcher to "select" the region where a crack will form and make better use of the instrumentation to monitor the cracking behavior and resulting steel stresses at the crack location.

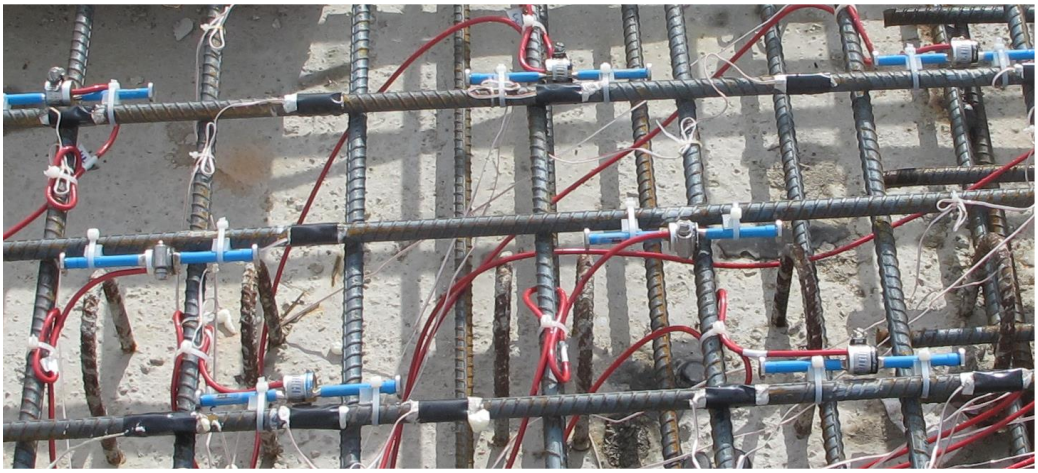

Figure 7.1: Vibrating wire strain gages for monitoring concrete strains and temperatures.

There are a variety of methods of measuring displacements. A common method in the laboratory is to use linear potentiometers. For field applications, obtaining sensors that are sufficiently robust to withstand the harsh environment is important. Figure 7.2 shows a string potentiometer that has been used on past field instrumentations. The wire transducer is connected to the point of interest and provides a measure of unidirectional deformation. Such a device could provide good insight into the movements of the ends of the bridge as well as locations along the transition slab.

Figure 7.2: Linear potentiometer (string potentiometer) for measuring displacements.

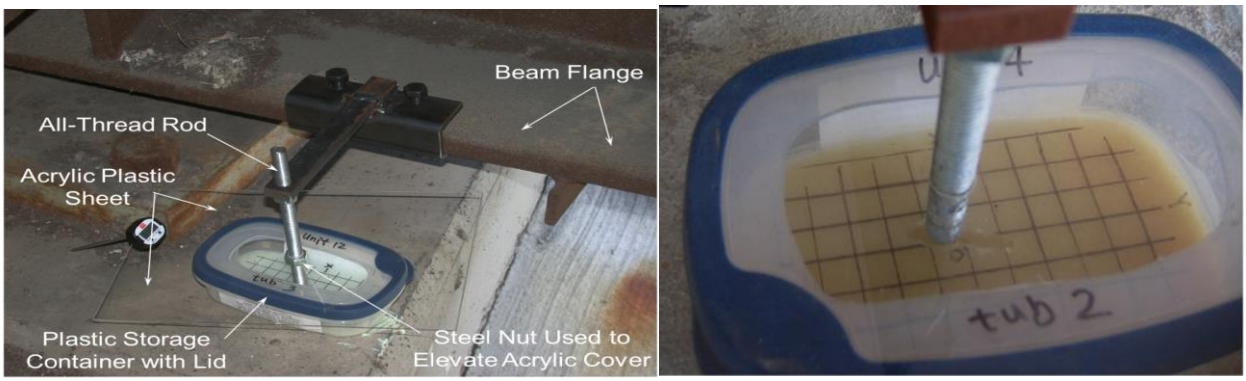

Figure 7.3: Wax trace box for simple deformational measurement (Chen et al., 2009).

Simple devices that can be used to provide a visual measure of the deformation in the form of the wax trace boxes have been developed (Chen et al., 2009) as shown in Figure 7.3. An indelible marker can be used to make a grid on the surface of the wax so that deformation can be recorded. In this case, a relatively coarse mesh was used; however, a finer grid is possible. A digital caliper can also be used to obtain more precise deformation readings. The devices shown in Figure 7.3 were developed for previous studies related to thermal movements in steel bridge systems. The magnitude and direction of the bridge movements at the bearings were desired in those studies. In this device, a "stylus" consisting of a threaded rod clamped to the beam flange is positioned in a container of microcrystalline wax which is mounted to the pier cap. As the bridge expands and contracts with the temperature, the stylus leaves a trace in the wax. The initial position of the stylus and temperature at installation is recorded. By tracking the temperature over the measuring time, multiple deformations can be obtained. The two extremes of the trace represent the deformations that have occurred at the maximum and minimum temperature. Instantaneous reading represents the deformation at the time of final reading. Depending on the range of expected deformations, a form of the wax trace box may be used if the resolution of the devices matches the expected deformations. Alternatively, string potentiometers will be used. To provide redundancy in the measurements, a combination of the two methods may also be utilized.

7.3 Instrumentation of Bridge and Transition Zone

Figure 7.4(a) and (b) show a scheme of the seamless bridge-CRCP system in the top view and elevation view. Only half of the structural system is displayed for simplicity. In this section, the regions of interest and preliminary selected locations of sensors are demonstrated on the half structure. If possible, instrumentation of transition and approach regions at both ends of the bridge will be instrumented and monitored. The major components include the bridge deck, link slab, approach slab and transition slab. The closure pour, which is a critical region once the bridge and the pavement are seamlessly connected, is also highlighted in the figure. The purpose of the closure pour is to allow the concrete in the bridge deck, link slab, transition slab, and approach to achieve suitable maturity prior to connecting the systems. This avoids problems with excessive cracking when the concrete is first placed. The location of the closure pour will be considered by the research team to provide the best behavior in the bridge.

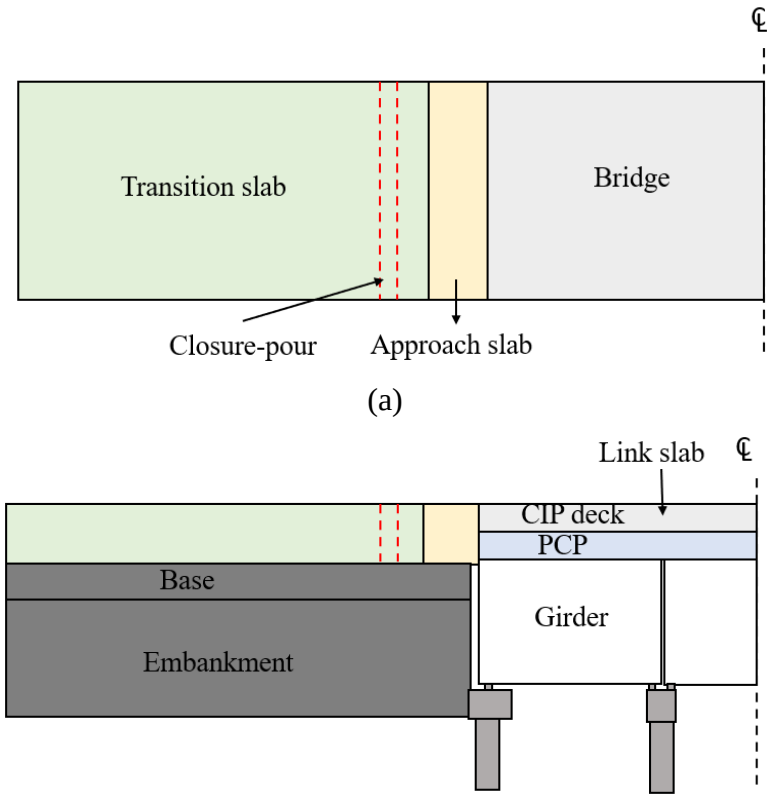

Figure 7.4: A scheme of seamless bridge-CRCP system: (a) top view; (b) elevation view.

Crack Response

In the case of temperature decrease, concrete is expected to crack in multiple regions, i.e., the transition zone, bridge deck composite with girder, link slab. The amounts of concrete strain and steel strain in the reinforced concrete member are important indicators of the level of cracking. The vibrating wire gages and foil strain gages should be placed in these components. The approach slab, link slab, and bridge deck that is adjacent to the bridge abutment, are the most critical members with the largest strain demand due to the seamless connection. These regions can be monitored with relatively dense-placed sensors. For the transition slab, a relatively large spacing between sensors can be used. As noted earlier, the research team will also consider introducing a short reduced region that is sure to experience cracking and allow the researchers to place gages at the location where cracking occurs and ensure useful data.

In the case that two layers of longitudinal reinforcement are used, the strains of concrete and steel at both layers are informative, particularly for the approach slab, which is subjected to out-of-plane effects due to the traffic loads and embankment settlement.

Longitudinal Displacement

It is of interest to monitor the longitudinal displacement at a few locations along the seamless system to evaluate the real response and validate the numerical models developed in Chapter 5.

The selected regions include: the approach slab at the bridge abutment end, the transition zone at the CRCP end, and multiple locations along the transition zone.

Embankment Settlement

The out-of-plane response of the approach slab is affected by the magnitude of the embankment settlement. The embankment settlement depends on multiple factors, including the properties of the embankment, construction control. The monitoring of the embankment settlement is beneficial to validate the detailed numerical models developed in Chapter 6 and guide on future approach slab of the similar geometry.

Closure Pour

The pavement and the bridge are connected seamlessly by using a closure pour of a small gap, which could be located near the bridge abutment. In Australia, the closure pour was made 60 ft. from the abutment. Prior to making the closure-pour, the pavement and the bridge expand/contract due to temperature fluctuations without interacting with each other. Once poured, the pavement and bridge deck are seamlessly connected as the concrete strength gains. It is significant important to monitor the behavior in this region before and after the concrete pour is made. Prior to casting concrete, the longitudinal movements at both ends of the gap should be measured. During and after the concrete is made, the strain of both concrete and steel within the closure-pour region should be monitored.

8. Design Recommendations (Task 7)

8.1 Overview

The design methodology for seamless bridge-CRCP systems in the U.S. should be consistent with the AASHTO LRFD Bridge Design Specifications (2020) and the AASHTO Pavement ME Design Procedure (VDOT, 2017) for the bridge and pavement components, respectively. Nevertheless, particular design and detailing aspects of seamless bridge-pavement systems differ from those of conventional bridges and pavements. Hence, a number of additional or modified design considerations are required for the following components:

- Transition zone. The particular behavioral demands of a given bridge must be accommodated with the proper length of the pavement transition zone between the bridge and conventional pavement, to dissipate movements of the bridge and transfer the longitudinal forces. The length and reinforcement of the transition zone should be properly designed to accommodate thermally-induced deformations and forces. Larger reinforcement ratios as compared to conventional pavement are generally needed in this zone to control cracking.
- Approach slab. Although approach slabs in conventional bridges are often isolated pavements, in a seamless bridge these slabs experience a combination of axial and flexural stresses with some rotational restraint from the composite bridge girders. The approach slab must accommodate the combination of axial stresses as well as stresses that result from flexure induced from the combination of traffic loads and settlement of the embankment.
- Bridge decks. The seamless connection also modifies the distribution of longitudinal forces within the bridge structure. The reinforcement ratios in the bridge decks directly over girders may need to slightly increase compared to conventional bridges for crack control. The link slabs over interior supports are critical regions where the axial demands are significantly higher since the bridge girders are not continuous at these locations. The reinforcement ratios in these regions should be adjusted to accommodate additional axial forces that are induced from frictional forces between the transition and approach slabs with the seamless bridge geometry.

General design guidelines are developed in this chapter for seamless bridge-CRCP systems on the basis of data obtained and insights gained through experimental testing and numerical modeling, as presented in previous chapters. These guidelines include: 1) the selection of proper bond breakers for the transition zone and recommended design values for the effective coefficient of friction at the pavement-base interface; 2) design and detailing recommendations for the transition zone and bridge decks; and 3) design loadings and design criteria. Simplified analytical models are developed to determine the stresses and deformations induced in the system considering axial and out-of-plane effects. Finally, a design example of a seamless bridge-CRCP system following the proposed design procedure is presented with preliminarily proposed detailing recommendations for the transition zone and critical bridge deck regions.

The design recommendations presented in this chapter correspond to seamless bridge-CRCP systems. Based on the numerical modeling in Section 5.7, the seamless connection technology can be adapted for circumstances where a jointed concrete pavement or flexible pavement is used on the pavement side. This is achieved by introducing a certain length of the conventional CRCP at

the end of the transition zone. Numerical parametric studies in Section 5.7.3 indicated that the minimum required length of the conventional CRCP is approximately 500 ft. The proposed simplified analytical method is also applicable for design of seamless connections for those pavements other than the CRCP, given that a sufficient length of the conventional CRCP is provided at the end of the transition zone. In addition to the developing simplified procedures for the design requirements considering the axial and flexural response of the transition, approach, and link slab regions, the chapter also includes a design example demonstrating the use of the simplified procedures.

8.2 General Design Recommendations

8.2.1 Bond Breakers for the Transition Zone

Table 8.1 provides a summary of the steady coefficients of friction obtained for different types of bond breakers investigated in the experimental study, as presented in Chapter 4. The bond breakers are listed in ascending order of the corresponding coefficients of friction.

The coefficient of friction of the concrete slab-base interface in the transition zone of a seamless bridge system should be low enough to prevent large tensile stress demands and severe cracking in the concrete slab, but not excessively low to avoid an overly-long transition zone. Based on the numerical parametric studies on the effects of friction coefficients at the concrete slab-base interface on the axial responses of the seamless system (see Section 5.5), target coefficients of friction in the range of 0.4-0.8 work well, however, values up to approximately 1.0 are also acceptable. Accordingly, felt paper and double-sided textured LLDPE sheets are recommended as bond breakers. Specifically, in this study, the felt paper that was tested was Type II following the ASTM standard (ASTM D4869, 2016), and the double-sided textured LLDPE sheets were 60-mil-thick with 16-mil asperities (Solmax). When common bases are used, such as CSB, HMA or CSB topped with a thin layer of HMA, the design coefficient of friction can be taken as 0.4 for double-sided textured LLDPE sheets and 0.7 for felt paper.

The selection of the specific bond breaker in the transition zone for a seamless bridge-pavement system depends on the project needs and requirements. As a reference, the felt paper and textured LLDPE sheet are evaluated and compared in the following four aspects:

- Structural effects: Between two bond breakers, felt paper will result in a shorter transition zone due to the larger coefficient of friction. Conversely, the demands of reinforcing steel in the transition zone and bridge decks will generally be lower with the use of a textured LLDPE sheet. For both materials, the variation in the steady shear strengths with the increased cyclic movements is insignificant as observed in the experimental testing.
- Construction: Asphalt-saturated felt paper is a low-cost product, which is easily accessible and commonly used as a sublayer in roofing applications to protect from rain, snow and other external factors. LLDPE sheets are widely used for landfill applications. Both materials are flexible and easy to install.
- Durability: The research team is confident in both double-sided LLDPE sheet and felt paper to serve as an effective bond breaker and that these materials provide a reliable coefficient of friction from the test conditions that were evaluated. The researchers have no data on the long-term performance of either material as a bond breaker. Textured LLDPE sheets have relatively high tearing resistance and may offer better long-term performance, which

was evidenced by significantly less visible damage observed in the LLDPE sheets via the post-test visual inspection of interface conditions in Phase II testing, as outlined in Section 4.3.6. Although repeatable cyclic behavior was observed at the concrete slab-base interface in the experimental testing, the researchers have no data on the long-term performance. Therefore, it is possible that the physical properties of felt paper may change in a field environment considering that it contains volatile compounds, leading to potential variation of coefficient of friction. Further investigation might be prudent to provide a better evaluation on the long-term performance of both bond breakers.

- Environmental impacts: From an environmental standpoint, both materials present similar limitations and opportunities. Asphalt-saturated felt paper can be made of recycled polyester and asphalt. However, similar to other asphalt-based materials, felt paper can be associated with potential environmental issues, such as the obstacles in recycling due to the rare presence of asbestos (not a problem with modern materials that do not contain asbestos), or potential risks for recycling workers due to the polycyclic aromatic hydrocarbons (PAHs) in asphalt (Townsend, 2007). LLDPE sheets can be made of renewable resources, but there can be issues regarding their disposal, recycling and waste management as they are not easily biodegradable. Nevertheless, increasing efforts are made to provide environmentally friendly solutions by reusing and recycling LLDPE sheets.

Table 8.1: Summary of coefficients of friction for different bond breakers.

Base type	Bond breaker	Coefficient of friction (steady)
CSB	Two smooth PE sheets	0.22
	One smooth PE sheet	0.28
	Single-sided spike HDPE sheet	0.3
CSB	Double-sided textured LLDPE sheet	0.4 (0.38-0.43)
CSB with thin HMA HMA	Felt paper	0.7 (0.68-0.73)

8.2.2 Design and Detailing Recommendations

Transition Zone

The detailing of the transition zone in design involves the specification of the slab thickness, as well as the length and detailing of the reinforcement steel. The thickness of the transition slab affects the axial response of the seamless system. However, it is practical to have a transition slab of an equal thickness as the conventional CRCP it connects to, which simplifies the construction procedure.

The minimum required length and reinforcement of the transition zone depend on factors such as the relative stiffness of the bridge and pavement elements, concrete slab-base interaction and imposed strains. The numerical parametric studies on typical TxDOT bridges in Chapter 5 provide some insight on the transition length. Common precast prestressed concrete girder bridges can consist of single span as well as multi-span applications. Therefore, in Texas these bridges most

often have a total bridge length in the range of 120 ft. to 500 ft., for which the use of a felt paper at the concrete slab-base interaction (friction coefficient of 0.7) results in the minimum required length of the transition zone in the range of 250 ft. to 320 ft. For these same systems, the use of a textured LLDPE sheet (friction coefficient of 0.4), the transition length will generally fall in the range of 300 ft. to 400 ft.

Based on the numerical studies in Chapter 5, some general rules are applicable for designing the longitudinal reinforcement in the transition zone. The reinforcement ratios in the transition zone are higher than applications with conventional CRCP to accommodate additional effects due to the bridge-pavement interaction under thermal changes. The magnitude of the increase in the reinforcement is determined based on the axial demand. In addition, it is efficient to gradually increase the reinforcement within the transition zone closer to the bridge abutment, which optimally adapts to the varying demands along the transition zone.

The numerical parametric studies in Section 5.5 indicate that a single design of a 400-ft.-long transition zone with reinforcement ratios varying between 0.75% and 1.45%, and a 30-ft.-long approach slab with 2% reinforcement ratio would be appropriate for the axial demands for most of the common precast prestressed concrete bridge configurations in Texas. While in some cases the design could be further optimized by reducing the amount of reinforcing steel, this indicates that some level of standardization can be achieved for design guidelines of seamless systems by providing an acceptable level of conservatism.

Table 8.2 provides a list of examples of the details in the transition zone and bridge decks of the seamless system used for these parametric numerical studies, including the thickness, reinforcement configuration and corresponding reinforcement ratio. For reference, the details of a conventional approach slab and bridge decks are also presented in parentheses in the table. Figure 8.1 presents a scheme of the transition zone and CRCP with corresponding labels for each component. The respective lengths for each segment of the transition slab and approach slab are also indicated. For a conventional CRCP, one layer of #6 reinforcing steel (with a diameter of 0.75 in.) is commonly placed at a spacing of 6.5 in. for an application with 11-in.-thick CRCP, corresponding to a reinforcement ratio of 0.62%. The reinforcement ratios of the transition zone are higher than that in the conventional CRCP. The increase in reinforcing can be achieved by either decreasing the bar spacing or using two layers of reinforcement.

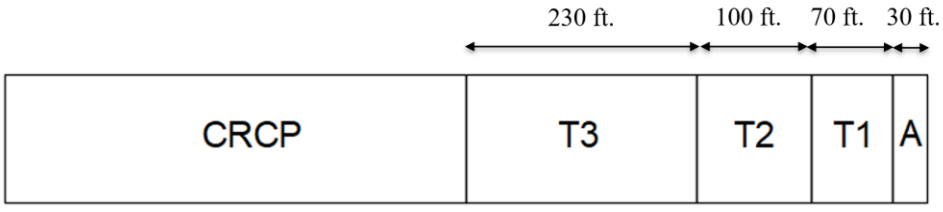

Figure 8.1: A scheme of transition zone in a seamless bridge-CRCP system.

Table 8.2: Reinforcing details for primary components in a seamless bridge-CRCP system used for numerical parametric studies.

Region	Reinforcement configuration[1]	Reinforcement ratio (%) [1]
Bridge deck (4.5-in.-thick)	#4 @ 6 in. (#4 @ 9 in.)	0.75 (0.5)
Link slab (8.5-in.-thick)	(T. Layer) #6 @ 5 in. (#4 @ 9 in.) [2] (B. Layer) #6 @ 5 in. (#4 @ 9 in.)	2.1 (0.52)
Approach slab (A) (13-in.-thick)	(T. Layer) #8 @ 6 in. (#5 @ 12 in.) (B. Layer) #8 @ 6 in. (#8 @ 6 in.)	2 (1.2)
Transition slab (T1)	(T. Layer) #6 @ 5.5 in. (B. Layer) #6 @ 5.5 in.	1.45
Transition slab (T2)	(T. Layer) #5 @ 5 in. (B. Layer) #5 @ 5 in.	1.1
Transition slab (T3)	#6 @ 5.5 in.	0.75
CRCP (11-in.-thick)	#6 @ 6.5 in.	0.62

Note:

1) The reinforcing details for the conventional bridge decks, link slabs and approach slab are included in parentheses for comparison.
2) "T. Layer" and "B. Layer" refer to the top and bottom layer of the reinforcement, respectively.

Approach Slab

A length of approach slab of 30 ft. long is likely appropriate for common embankment settlement situations without causing ride quality issues (bump at beginning of bridge). A longer approach slab is required when considering an embankment settlement (relative to the abutment) larger than 2 in., which is relatively rare.

The thickness of the approach slab also affects the flexural stiffness of the section. Although it simplifies the construction procedure by having an approach slab of the same thickness as the transition slab and CRCP, it is likely desired to increase the thickness of the approach slab in a seamless system. This is due to the higher demands as a result of the combined axial and out-of-plane effects as it reaches the bridge abutment. In such cases, a tapered approach slab with gradually increased thickness from the pavement end to the bridge abutment end might be a preferred option. On one hand, such a detail optimizes the use of materials as per the demands. On the other hand, this detail allows a gradual accommodation for the thickness differences between the transition zone and the approach slab.

The approach slab is subjected to axial stresses as the bridge expands and contracts, and significant flexural stresses as well due to embankment settlement and axle loads of the design truck or tandem. Due to thermal effects on the bridge, the axial stress component will lead to axial compression for temperature increase and axial tension for temperature decrease. The approach slab has

reinforcement at both top and bottom layer to resist the flexural moment due to vertical loads and settlement, where flexural effects result in the top layer subjected to flexural tension near the bridge abutment and the bottom layer subjected to flexural tension near the middle span. The reinforcement amount is likely to increase particularly at the top layer because increased axial force demands are expected due to the interaction between the bridge and transition zone. For example, the standard approach slab has a reinforcement ratio of 0.2% at the top layer and 1% at the bottom layer, corresponding to a total ratio of 1.2%. As listed in

Table 8.2, the total reinforcement ratio of the approach slab for the seamless systems analyzed increases to 2% uniformly distributed between two layers.

Bridge Decks

A seamless bridge-pavement connection also introduces additional axial forces in the bridge superstructure due to thermal changes. The effect of extra force is relatively minor for the portion of bridge deck that is composite with bridge girder (i.e., directly over bridge girder) since most of the axial force is taken by the girder. However, link slab regions are significantly affected with increased strain demands since girders are not continuous in these regions. For example, as listed in

Table 8.2, for a conventional bridge in Texas, the reinforcement ratio for link slabs significantly increases from 0.52% for a conventional bridge to 2.1% for a seamless bridge.

8.2.3 Design Loading and Criteria

Table 8.3 summarizes the design loads to be considered for the axial and out-of-plane effects. For the design of seamless bridge systems, concrete shrinkage and creep effects are not included because they are either not critical or negligible, for the reasons elaborated in Chapter 5. Therefore, it is reasonable to consider temperature changes only. For bridges throughout Texas, a temperature increase of 80°F and a temperature decrease of 55°F are considered. If the temperature effects are deemed different from this value recommended for Texas, the design thermal loading should be adjusted as per specific projects based on the concrete placement temperature and ambient temperature.

Table 8.3: Summary of design loads.

Loads	Proposed magnitudes
Temperature change	• Temperature decrease: -55°F • Temperature increase: 80°F
Self-weight	• 150 pcf for normal weight reinforced concrete
Embankment settlement	• 1 in.
Vehicle loads on approach slab	Designated HL-93 (AASHTO, 2020): • Design lane load • Design tandem

In this study, a 1 in. differential embankment settlement was considered, which is assumed as a reasonable estimate for controlling ride quality (bump at the end of bridge). However, this parameter depends on the soil type and compaction conditions, which should refer to field investigation reports if available for a more representative estimate. The traffic loads are determined as per AASHTO LRFD Bridge Design Specifications (2020). The axle locations of moving vehicle loads are considered to reflect the maximum response of interest due to the maximum effects for a specific approach slab.

Table 8.4 summarizes the proposed design criteria for seamless bridge-pavement systems for the serviceability and strength limit with different load combinations. For the serviceability limit state, the design criteria are specified in terms of the maximum tensile steel stress at cracks ($f_{s,max}$) and concrete compressive stress (f_c). The value of $f_{s,max}$ is calculated by dividing the total tensile force for the cracked reinforced concrete section by the reinforcing steel area (considering that at crack locations the tensile force is carried entirely by the reinforcing steel). In the case of temperature decrease, the proposed design criteria are consistent with current structural design standards, which limit the maximum steel stress at cracks to control the crack opening for serviceability limit state. As per the AASHTO LRFD Bridge Design Specifications (2020), the maximum steel stress should not exceed 60% of the yield strength f_y for reinforced concrete bridge structures. For reinforced concrete pavement, it is common to limit the maximum steel stress below two-thirds of the yield strength (Roesler et al., 2016).

Table 8.4: Proposed design criteria.

Effects	Limit state	Regions	Design limit
Axial effects (Temperature decrease)	Serviceability	Bridge decks	$f_{s,max} \leq 0.6\, f_y$
		Transition zone	$f_{s,max} \leq 2/3\, f_y$
Axial effects (Temperature increase)		Bridge decks & approach slab	$f_c \leq 0.6\, f_c'$
Combined out-of-plane & axial effects	Strength	Approach slab	$V_u \leq \varphi V_n$ [1] $M_u \leq \varphi M_n$
Combined out-of-plane & axial effects (Temperature decrease)	Serviceability	Approach slab	$f_{s,max} \leq 2/3\, f_y$

Note:

1) The terminologies *V* and *M* represent the shear and force, respectively. The subscripts *u* and *n* represent the demand and capacity, respectively. φ is the reduction factor. More details are included in Section 8.4.

In the case of temperature increase, the proposed design criterion is consistent with current structural design standards (AASHTO LFRD, 2020; CEB-FIP Model Code 90, 1993), which limit the concrete compressive stress to 60% of the 28-day concrete compressive strength f_c' to avoid microcracking for the serviceability limit state.

For the approach slab which is likely subjected to out-of-plane effects and axial effects simultaneously, both the strength limit state and the serviceability state should be examined. For the strength limit state, the shear and flexural moment demand due to the factored loads should be lower than the capacity of the section. Both out-of-plane effects and thermal effects (temperature decrease) cause tensile stress in the top layer of reinforcing steel of the approach slab at the bridge abutment, therefore, the maximum steel stress at this location due to the combined effects should be checked with the design limit for serviceability.

8.3 Simplified Method for Axial Response Analysis

8.3.1 Development of Simplified Method

A simplified analytical method is proposed in this section to determine the axial force demands in the seamless bridge-pavement systems, as an alternative to the more complex numerical models presented in Chapter 5. Before presenting the hypotheses of the analytical method, the axial response of the seamless system is reviewed based on the results of the numerical models. Figure 8.2(a) and (b) show an example of the seamless system analyzed in Section 5.4.3 to qualitatively illustrate the longitudinal movement and axial force expected in the seamless bridge-CRCP system subjected to temperature increase and decrease, respectively. Only half of the system is shown, and the bridge portion is marked in shadow for display. Some observations on the axial force and longitudinal displacement are summarized below (more details are discussed in Chapter 5):

- In the case of temperature increase, both the transition pavement and the bridge move away from the bridge center, whereas in the case of temperature decrease, both the transition pavement and the bridge move toward the bridge center.
- At the seamless connection, the longitudinal displacement and axial force are continuous between the transition pavement and the bridge.
- Due to temperature increase, both the transition pavement and the bridge are in compression, whereas due to temperature decrease, both the transition pavement and the bridge are in tension.
- The axial force within the transition zone gradually changes due to the accumulation of frictional forces generated at the pavement-base interface. The axial force within the bridge region is essentially constant.
- After the minimum required length of the transition zone, the longitudinal displacement is reduced to zero and the axial force becomes constant. Beyond this region, the pavement behaves as normal CRCP and has the same axial force as that in the end of the transition zone.

The simplified analytical method was developed based upon the above observations. Assumptions for the simplified method are listed as follows:

- A constant coefficient of friction is assumed at the interface between the concrete pavement and the slab with the bond breaker within the transition zone.
- In the case of temperature increase, elastic gross section properties are assumed. In the case of temperature decrease with concrete cracking, effective axial cross-sectional stiffness values of cracked reinforced concrete are assumed.

- The lateral stiffness of the abutment, piers, and elastoplastic bearings are neglected, assuming no restraint of the superstructure to bridge movement.

The development of the method is explained for the general system as shown in Figure 8.3, which could have multiple segments within the transition zone and bridge with varying sectional properties (such as material stiffness, reinforcement ratio, thickness, etc.). The structural model consists of transition zone with the minimum required length L_{p_req} and half of the bridge (full length of bridge is L_b) assuming the system is symmetric about the bridge center. The method uses the following coordinate system: a) the origin of the transition pavement is set at the end of the transition zone that is connected to the conventional CRCP, the horizontal axis is toward the bridge; and b) the origin of the bridge is set at the center of the bridge, and the horizontal axis is toward the pavement. The axial force (F_p, F_b) and longitudinal displacement (u_p, u_b) at any location of the transition pavement x_p ($0 \le x_p \le L_{p\_req}$) and the bridge x_b ($0 \le x_b \le L_{bridge}/2$) can be determined following the steps below.

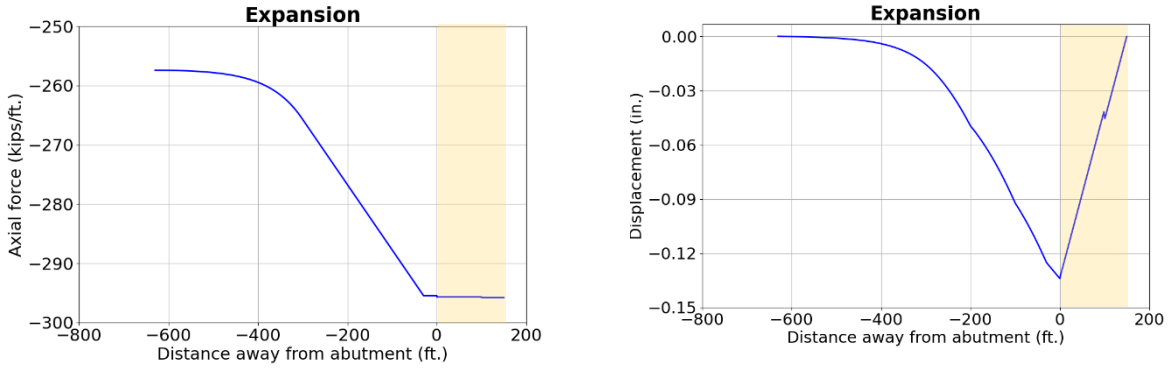

(a)

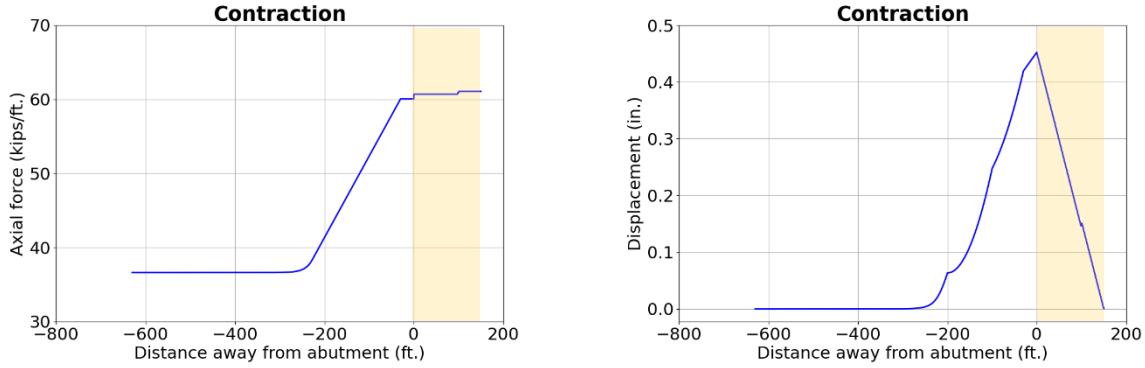

(b)

Figure 8.2: Axial force and longitudinal displacement of seamless bridge-CRCP system: (a) temperature increase; (b) temperature decrease.

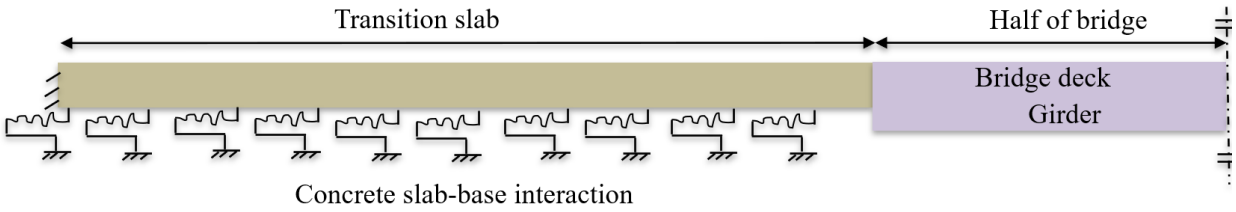

Figure 8.3: A scheme of the simplified structural model for the seamless system with axial loading.

- Step 1: Determine the axial force F_p at any distance x_p away from the conventional CRCP.

$$F_p(x_p) = F_0 - f_0 x_p \text{ (Temperature increase),} \quad \text{Eq. 8.1(a)}$$

$$F_p(x_p) = F_0 + f_0 x_p \text{ (Temperature decrease),} \quad \text{Eq. 8.1(b)}$$

where F_0 is the axial force within the CRCP due to temperature change. F_0 can be calculated for the corresponding thermal strain level in the CRCP with the pre-defined concrete and steel stress-strain relationships, as shown previously in Eq. 5.6.

And f_0 is the magnitude of the frictional force per unit length, and is given by the equation below:

$$f_0 = \mu \rho A_g, \quad \text{Eq. 8.2}$$

where:

μ = coefficient of friction at the concrete slab-base interface within the transition zone,

ρ = material density of the member,

A_g = gross cross-sectional area of the member.

- Step 2: Determine the axial force F_b at any distance x_b away from the bridge center.

$$F_b(x_b) = F_p(L_{p\_req}). \quad \text{Eq. 8.3}$$

- Step 3: Determine the displacement u_p at any distance x_p away from the conventional CRCP.

The longitudinal displacement u_p due to the axial effects has two components: the displacement due to temperature change $u_{p,T}$, and the displacement due to the axial force $u_{p,F}$, as shown in the equations below:

$$u_p(x_p) = u_{p,T}(x_p) + u_{p,F}(x_p), \quad \text{Eq. 8.4(a)}$$

$$u_T(x_p) = \alpha \Delta T x_p, \quad \text{Eq. 8.4(b)}$$

$$u_F(x_p) = \int_0^{x_p} \frac{F_p(x)}{(EA)_p(x)} dx, \quad \text{Eq. 8.4(c)}$$

where:

α = thermal coefficient of material,

ΔT = temperature change,

EA = axial cross-sectional stiffness at any location.

- Step 4: Determine the displacement u_b at any distance x_b away from the bridge center.

Similarly, the longitudinal displacement u_b is given by the equation below:

$$u_b(x_b) = \alpha \Delta T x_b + \int_0^{x_b} \frac{F_b(x)}{(EA)_b(x)} dx. \quad \text{Eq. 8.5}$$

- Step 5: Determine the minimum required length of the transition zone L_{p_req}.

The displacement at the transition pavement – bridge interface can be determined correspondingly following Eqs. 8.4 and 8.5:

$$u_p(x_p = L_{p\_req}) = \alpha \Delta T L_{p\_req} + \int_0^{L_{p\_req}} \frac{F_p(x)}{(EA)_p(x)} dx, \quad \text{Eq. 8.6}$$

$$u_b(x_b = L_b/2) = \frac{\alpha \Delta T L_b}{2} + \int_0^{\frac{L_b}{2}} \frac{F_b(x)}{(EA)_b(x)} dx. \quad \text{Eq. 8.7}$$

By equating the longitudinal displacements at the seamless connection by the two calculations above, the minimum required length of the transition zone L_{p_req} can be determined by solving the Eq. 8.8:

$$\alpha \Delta T L_{p\_req} + \int_0^{L_{p\_req}} \frac{F_p(x)}{(EA)_p(x)} dx = -\alpha \Delta T L_b/2 + \int_0^{L_b/2} \frac{F_b(x)}{(EA)_b(x)} dx. \quad \text{Eq. 8.8}$$

- Step 6: Determine the axial response of the seamless system (such as axial force, displacement, strain, stress, etc.) and check with design criteria.

Once the minimum required length of the transition zone is determined, the axial force within the transition zone and the bridge can be determined following Eqs. 8.1 and 8.3, respectively. The longitudinal displacement of the transition zone and bridge can be determined following the Eqs. 8.4 and 8.5.

8.3.2 Axial Stiffness of Reinforced Concrete Section

Temperature Increase: Elastic Axial Stiffness of Gross Section

In the case of temperature increases, both concrete pavement and bridge components are in compression and expected to remain elastic. Therefore, elastic gross cross-sectional properties are used. The elastic axial stiffness of the gross section (EA) is given by the Eq. 8.9:

$$(EA) = E_c A_g (1 + (n-1)\rho), \qquad \text{Eq. 8.9}$$

in which:

$$\rho = \frac{A_s}{A_g},$$

$$n = \frac{E_s}{E_c},$$

where:

E_c = Modulus of elasticity of concrete,

E_s = Modulus of elasticity of steel,

A_g = gross cross-sectional area,

A_s = cross-sectional area of steel,

ρ = reinforcement ratio.

Temperature Decrease: Effective Axial Stiffness of Cracked Section

In the case of temperature decreases, both concrete pavement and bridge decks are in tension and cracks occur when the concrete tensile strength is reached. Due to cracking, the axial stiffness is progressively reduced. The American Concrete Institute (ACI) committee 224 investigated the effects of cracking on axial stiffness of reinforced concrete members subjected to direct tension and proposed to use the effective cross-sectional axial stiffness $(EA)_e$ to develop the relationship between the axial force F and the average strain ε_m in the cracked reinforced concrete member, as shown in Eq. 8.10 (Darwin *et al*., 1986, ACI Report 224.2R):

$$F = (EA)_e \varepsilon_m, \qquad \text{Eq. 8.10}$$

Different methods have been proposed to estimate the effective axial stiffness $(EA)_e$, either in terms of the actual area of steel (A_s) and the effective (reduced) modulus of elasticity of steel ($E_{s,e}$), or the effective (reduced) area of concrete ($A_{c,e}$) and the modulus of elasticity of concrete (E_c), as shown in the Eqs 8.11(a) and (b), respectively:

$$(EA)_e = E_{s,e} A_s, \qquad \text{Eq. 8.11(a)}$$

$$(EA)_e = E_c A_{c,e}. \qquad \text{Eq. 8.11(b)}$$

In the present study, the effective axial stiffness written in terms of the reinforcing steel as suggested by the ACI Report 224.2R (Darwin *et al*., 1986) is adopted, as shown in Eq. 8.11(a):

$$E_{s,e} = \frac{E_s}{1-k(\frac{f_{scr}}{f_s})^2}, \qquad \text{Eq. 8.12}$$

in which:

$$f_{scr} = f_t'(\frac{1}{\rho} - 1 + n),$$

where:

f_{scr} = steel stress at cracks,

f_s = steel stress in the member, and $f_s = \frac{F}{A_s}$,

f_t' = concrete tensile strength,

k = 1.0 for first loading, and k = 0.5 for repeated or sustained loading.

8.3.3 Validation of Simplified Method

The developed simplified method was applied to determine the minimum required length of the transition zone and corresponding response of the seamless bridge-pavement system due to axial effects (thermal changes only). The prototype structure had the same details as that for numerical modeling in Section 5.4. The bridge had three spans with each span 100 ft. long. The details of the geometry of each structural segment are briefly summarized in Table 8.5.

Table 8.5: Details for bridge decks and transition zone for axial effects.

Region	Length (ft.)	Thickness (in.)	Reinforcement ratio (%)
Bridge deck	100	4.5	0.7
Bridge girder	100	8.5 [1]	-
Link slab	2	8.5	2.5
Approach slab (A)	30	11	2.0
Transition slab (T1)	70	11	1.45
Transition slab (T2)	100		1.1
Transition slab (T3)	To be determined [2]		0.75

Note:

1) Equivalent girder depth for a 1-in.-wide bridge assuming a uniform distribution of axial stiffnesses over the entire bridge width.
2) The minimum required length of the transition slab segment that is connected to the conventional CRCP is to be determined based on the simplified method.

The system had a unit-width of 1 in. The concrete compressive strength for the bridge girders was taken as 8 ksi and the modulus of elasticity was taken as 4578 ksi. The concrete compressive strength for the bridge deck and pavement was taken as 4 ksi and the modulus of elasticity was taken as 3530 ksi. The coefficient of friction was assumed to be 0.7 considering the use of felt paper within the transition zone, and the approach slab was assumed to be frictionless. The same magnitudes of temperature change were considered (80°F for temperature increase and 55°F for temperature decrease).

The model employed in the simplified analytical method consisted of half of the structure, including the transition zone, the first span of the bridge (100 ft. long), the link slab (2 ft. long) and a half of the middle span of the bridge (50 ft. long).

Axial Response with Temperature Increase

The calculation of the minimum required length of the transition zone and the corresponding axial analysis due to temperature increase are presented below.

- Determine the elastic axial stiffness for each structural component.

CRCP:

$$(EA)_{CRCP} = E_c A_g(1 + (n-1)\rho) = 3530\times11\times(1+(8.2\text{-}1)\times0.0075) = 40929 \text{ kips},$$

Transition slab segment 3:

$$(EA)_{T3} = 3530\times11\times(1+(8.2\text{-}1)\times0.0075) = 40929 \text{ kips},$$

Transition slab segment 2:

$$(EA)_{T2} = 3530\times11\times(1+(8.2\text{-}1)\times0.011) = 41910 \text{ kips},$$

Transition slab segment 1:

$$(EA)_{T1} = 3530\times11\times(1+(8.2\text{-}1)\times0.0145) = 42891 \text{ kips},$$

Approach slab:

$$(EA)_{A} = 3530\times11\times(1+(8.2\text{-}1)\times0.02) = 44431 \text{ kips},$$

Bridge deck composite with girder:

$$(EA)_{d\_g} = (EA)_{deck} + (EA)_{girder} = 3530\times4.5\times(1+(8.2\text{-}1)\times0.007) + 4578\times8.5 = 55597 \text{ kips},$$

Bridge link slab:

$$(EA)_{link} = 3530\times8.5\times(1+(8.2\text{-}1)\times0.025) = 35416 \text{ kips}.$$

- Determine the axial force within the CRCP F_0 due to temperature increase.

$$\varepsilon = 0 - \varepsilon_{th} = -\alpha\Delta T = -6.5\times10^{-6}\times80 = -0.52\times10^{-3},$$

$$F_0 = (EA)_{CRCP}\varepsilon = 40929\times(-0.52\times10^{-3}) = -21.28 \text{ kips},$$

- Determine the frictional force per unit in. f_0.

For transition slab segments:

$$f_0 = \mu\rho A_g = 0.7\times150/(12^3)\times11 = 0.000668 \text{ kips/in.}$$

- Calculate the minimum required length of transition slab segment 3.

The minimum required length of transition slab can be determined by solving Eq. 8.8. The minimum required length of transition slab segment 3 L_{T3_req} was determined as 213 ft. The axial force and longitudinal displacement along the transition zone and bridge were correspondingly determined and plotted in Figure 8.4. For comparison, the axial response of the system by using the numerical model developed in Chapter 5 is also plotted.

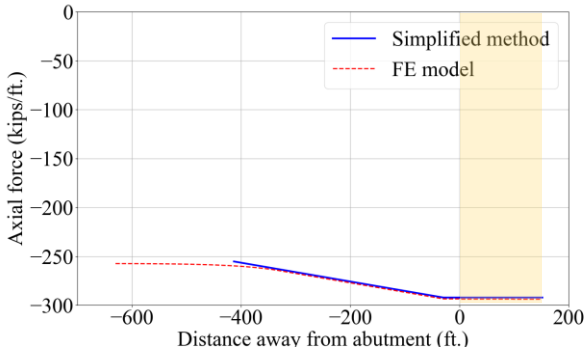

(a)

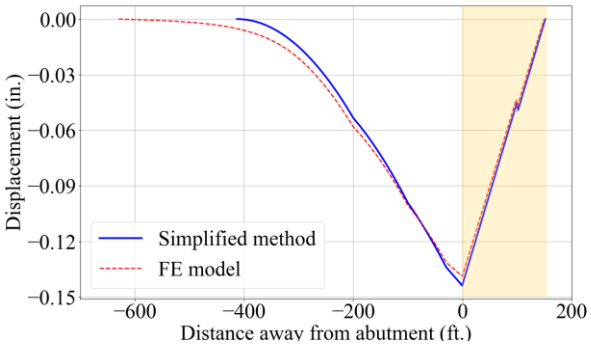

(b)

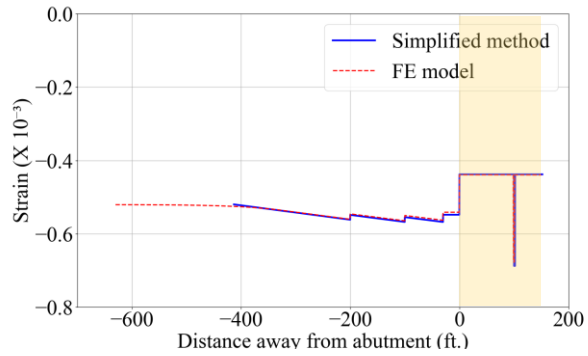

(c)

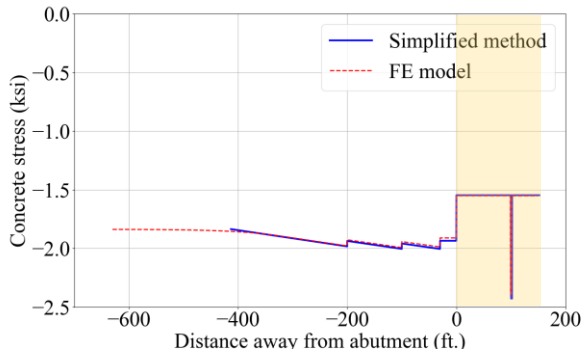

(d)

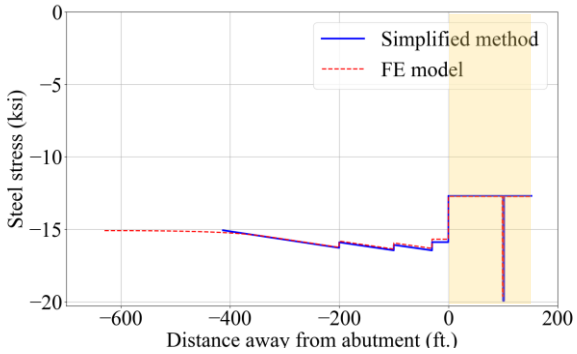

(e)

Figure 8.4: Comparison of results by simplified method and FE model (temperature increase): (a) Axial force; (b) Longitudinal displacement; (c) Strain; (d) Concrete stress; (e) Steel stress.

The axial response, including axial force, longitudinal displacement, strain, concrete stress and steel stress obtained using the proposed simplified method generally agrees well with the result obtained by the detailed FE model. The simplified method estimates the axial force at the bridge-pavement interface as -292.3 kips/ft., which is 99.4% of the value estimated by the FE model. The slight mismatch at the beginning of the transition slab segment 3 that is connected to the normal CRCP is observed, which is due to the slight difference of frictional models used in two methods. The FE frictional model assumes a linear increase (up to a relatively small displacement of 0.015 in.) before reaching the steady coefficient of friction, whereas the simplified method assumes a constant coefficient of friction for any movement. However, the effects of the initial slope on the global axial response of the system are negligible.

Axial Response with Temperature Decrease

The calculation of the minimum required length of the transition zone and the corresponding axial analysis due to temperature decrease are presented below.

- Determine the steel stress at cracks for each structural component.

CRCP:

$$f_{scr,CRCP} = f_t'(\frac{1}{\rho} - 1 + n) = 0.253\times(\frac{1}{0.0075} - 1 + 8.2) = 35.6 \text{ ksi},$$

Transition slab segment 3:

$$f_{scr,T3} = 0.253\times(\frac{1}{0.0075} - 1 + 8.2) = 35.6 \text{ ksi},$$

Transition slab segment 2:

$$f_{scr,T2} = 0.253\times(\frac{1}{0.011} - 1 + 8.2) = 24.8 \text{ ksi},$$

Transition slab segment 1:

$$f_{scr,T1} = 0.253\times(\frac{1}{0.0145} - 1 + 8.2) = 19.3 \text{ ksi},$$

Approach slab:

$$f_{scr,A} = 0.253\times(\frac{1}{0.02} - 1 + 8.2) = 14.5 \text{ ksi},$$

Bridge link slab:

$$f_{scr,link} = 0.253\times(\frac{1}{0.025} - 1 + 8.2) = 11.9 \text{ ksi}.$$

- Determine the axial force within the CRCP F_0 due to temperature decrease.

Based on Eq. 8.12, determine the effective stiffness of steel:

$$E_{s,e,CRCP} = \frac{E_S}{1-k(\frac{f_{scr,CRCP}}{f_S})^2} = \frac{E_S}{1-k(\frac{f_{scr,CRCP}}{F_0/A_S})^2}.$$

For validation purposes, k was taken as 1.0. Determine the average strain:

$$\varepsilon_{CRCP} = \frac{F_0}{E_{s,e,CRCP}A_S} = \frac{F_0}{E_S A_S}\left(1 - k\left(\frac{f_{scr}}{F_0/A_S}\right)^2\right).$$

Average strain of the CRCP due to temperature decrease is known:

$$\varepsilon = 0 - \varepsilon_{th} = -\alpha\Delta T = -6.5\times10^{-6}\times(-55) = 0.34\times10^{-3}.$$

By equating the estimated average strain ε_{CRCP} to 0.34×10^{-3}, the axial force F_0 can be determined:

$$F_0 = 3.39 \text{ kips}.$$

- Similarly, determine the effective axial stiffness of the steel for each structural component following Eq. 8.12.
- Calculate the minimum required length of transition slab segment 3.

A python script was developed to solve Eq. 8.8. The minimum required length of transition slab segment 3 L_{T3_req} is determined as 34 ft. The axial force and longitudinal displacement along the transition zone and bridge are correspondingly determined and plotted in Figure 8.5. The axial response of the system by using the numerical model developed in Chapter 5 is also plotted in Figure 8.5 for comparison.

It should be noted that the concrete tensile stress-strain relationship used to define material properties of each structural component in this FE model differs from the concrete constitutive laws (Vecchio and Collins, 1986) as presented in Chapter 5. The uniaxial concrete stress-strain curve for the FE model of the present chapter was derived based on the effective axial stiffness of the cracked reinforced concrete as used in the simplified method (Darwin *et al*., 1986, ACI Report 224.2R) to ensure a validation with consistent material models.

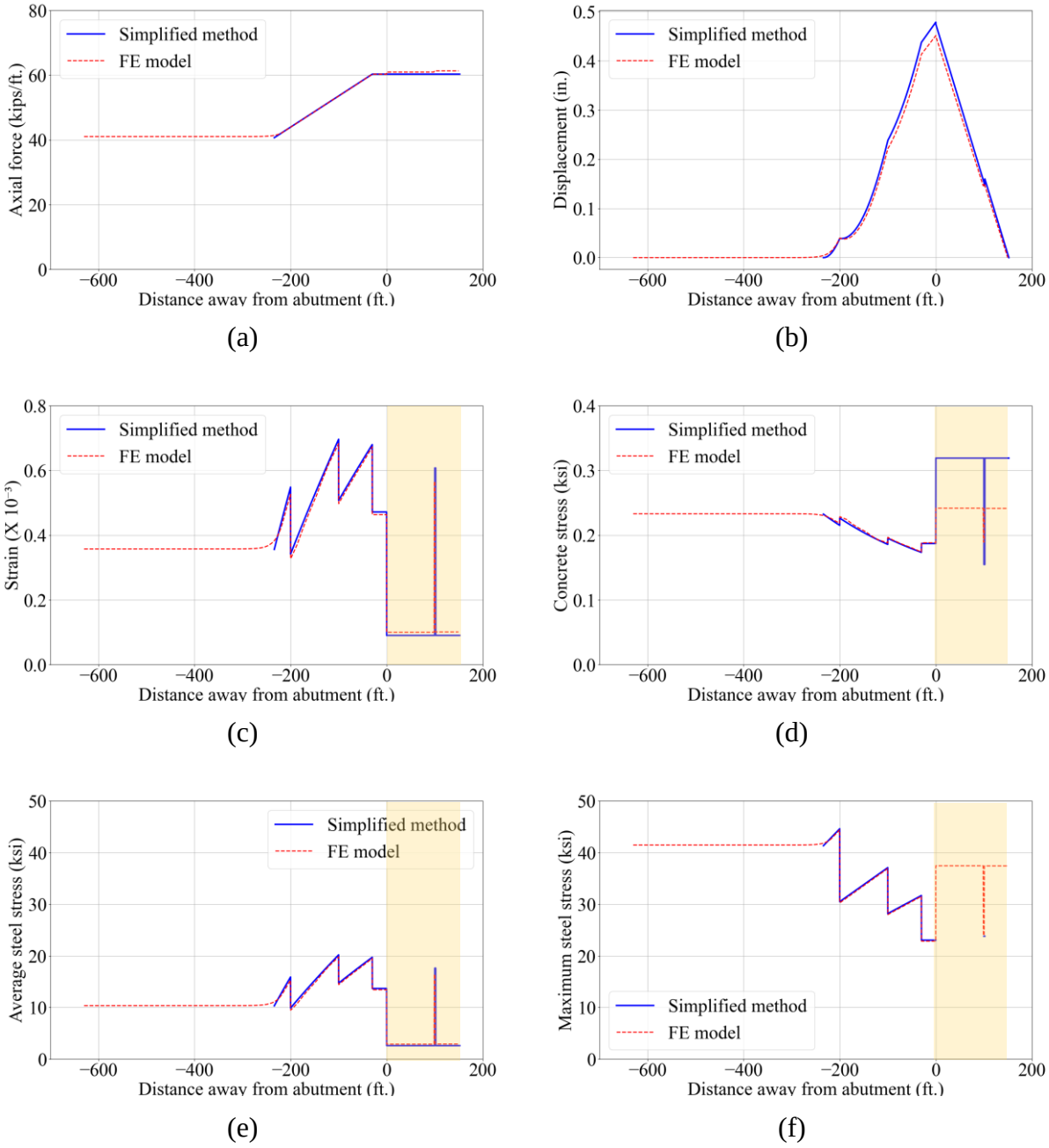

Figure 8.5: Comparison of results by simplified method and FE model (temperature decrease): (a) Axial force; (b) Longitudinal displacement; (c) Strain; (d) Concrete stress; (e) Average steel stress; (f) Maximum steel stress.

It should be mentioned that for simplicity, for the results using the simplified method shown in the Figure 8.5, elastic property was assumed for bridge deck after cracking instead of effective axial stiffness for simplicity. For the bridge deck composite with girder, the axial stiffness of the section consists of the contribution from the elastic girder and that from the cracked deck. Considering the axial stiffness of the elastic girder is significantly larger than that of the cracked deck, the elastic deck properties were used. However, the relative stiffness of the bridge to the pavement was not

affected by neglecting the reduction of axial stiffness of cracked deck. Both the simplified method and the FE numerical modeling method predict similar axial force and strain demands in the seamless system, as shown in Figure 8.5(a) and (c). The minimum required length of the transition zone is essentially the same using the two methods. The only difference is the concrete stress in the bridge deck composite with girder. The concrete stress of the deck is higher using the simplified method due to assumption of elastic properties. However, the simplified method is able to provide reasonable estimate of the maximum steel stress in critical components, i.e., transition zone and link slab, which is important to evaluate the crack width for the serviceability limit state.

If considering the elastic deck properties, the axial stiffness of the section is given by:

$(EA)_{d\_g} = (EA)_{deck} + (EA)_{girder}$ = 3530×4.5×(1+(8.2-1) ×0.007) + 4578×8.5 = 55597 kips.

To investigate the effects of the axial stiffness of the bridge deck on the global behavior of the seamless system, another extreme condition was considered by neglecting the cracked deck, and the axial stiffness of the section is given by:

$$(EA)_{d\_g} = (EA)_{girder} = 4578\times8.5 = 38910 \text{ kips.}$$

The value of the actual axial stiffness of the bridge deck composite with the girder falls in the range of two extreme conditions above. The axial response using two assumptions of deck axial stiffnesses is compared and plotted in Figure 8.6. The result in the simplified case of considering the elastic deck properties, indicating no reduction in axial stiffness after concrete cracks, matches closely with the FE model, which simulates the crack properties of the deck. Therefore, elastic deck properties are adopted in following investigations and recommended for the design of seamless bridge-bridge systems.

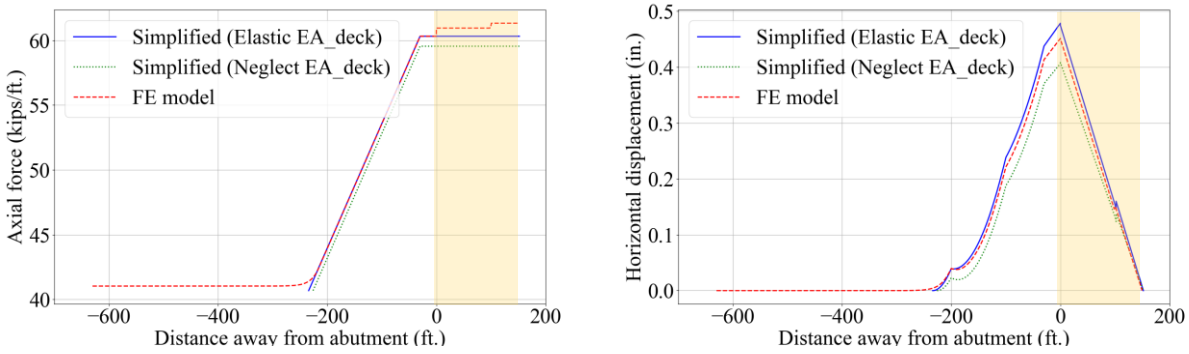

(a) (b)

Figure 8.6: Results for different axial stiffness of bridge deck: (a) Axial force; (b) Longitudinal displacement.

8.4 Simplified Method for Out-of-Plane Response Analysis

8.4.1 Development of Simplified Method

A simplified model to analyze the out-of-plane response of the approach slab is also proposed, as an alternative to the more complex numerical models of Section 6.4. It consists of a two-

dimensional (2D) elastic model that considers the approach slab as a frame element with cracked section properties. The unsupported length of the approach slab may vary depending on the magnitude of relative settlement between the two ends (Figure 8.7), however, for the developed simplified method, it is assumed that the entire length of approach slab is unsupported. Also, the support conditions at each end are idealized as a fixed support, to simplify the boundary conditions. The design is conservative with idealized fixed-fixed boundary conditions based on the investigation presented in Section 6.3.

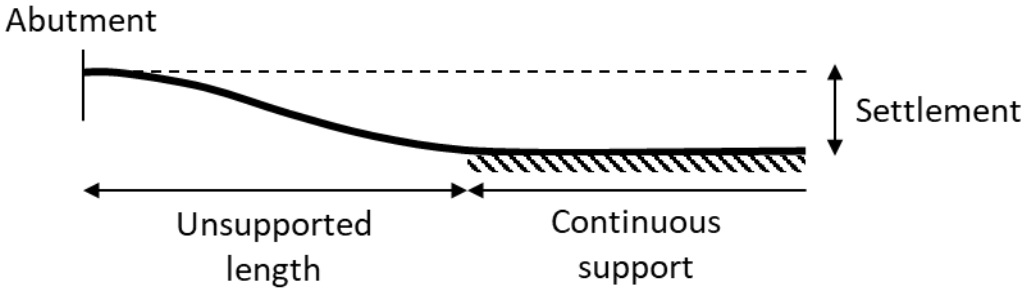

Figure 8.7: A scheme of approach slab subjected to embankment settlement.

The approach slab is treated as a 2-noded frame section of varying depth, and solved using matrix stiffness analysis and Hermitian shape vectors. A summary of formulas used is provided below in Eqs. 8.13 to 8.16. Notation given in bold type-face represents column vectors, such as $\boldsymbol{H}$. A bold type-face with an underscore represents a matrix, such as $\underline{\boldsymbol{k}}$. The Hermitian shape vector for a 2-noded frame element is given by Eq. 8.13, where x represents a point along the element of length L, and the corresponding degrees of freedom are as labelled in Figure 8.8. The vertical movement of a point along the element is given by Eq. 8.14. The stiffness matrix for a 2-noded frame element can be formulated as shown in Eq. 8.15, with modulus of elasticity, E and moment of inertia, I. For a tapered member, the moment of inertia will be a function of position x. Using the stiffness matrix, the end reactions due to end displacement, uniform loading, and point loads can be calculated using Eq. 8.16. A MATLAB script was developed to perform the computations based on these equations.

$$\boldsymbol{H} = \begin{bmatrix} H_1 \\ H_2 \\ H_3 \\ H_4 \end{bmatrix}, \qquad \text{Eq. 8.13}$$

where:

$$H_1 = 1 - 3\left(\frac{x}{L}\right)^2 + 2\left(\frac{x}{L}\right)^3,$$

$$H_2 = x - \frac{x^2}{L} + \frac{x^3}{L^2},$$

$$H_3 = 3\left(\frac{x}{L}\right)^2 - 2\left(\frac{x}{L}\right)^3,$$

$H_4 = -\frac{x^2}{L} + \frac{x^3}{L^2}$.

$$v(x) = \boldsymbol{H} * \boldsymbol{v}, \qquad \text{Eq. 8.14}$$

where:

$\boldsymbol{v} = [v_1 \quad \theta_1 \quad v_2 \quad \theta_2]^T$.

$$\underline{\boldsymbol{k}} = \int_0^L [\boldsymbol{H}"]^T \, EI \, [\boldsymbol{H}"] \, dx = [\boldsymbol{k_1} \quad \boldsymbol{k_2} \quad \boldsymbol{k_3} \quad \boldsymbol{k_4}], \qquad \text{Eq. 8.15}$$

$$\boldsymbol{F_{END}} = -\boldsymbol{F_{EQ}} = v_1 * \boldsymbol{k_1} - \int_s \boldsymbol{H}^T w(x) ds - \sum_{i=1}^{n} \boldsymbol{H}^T{}_{@\, x=x_i} P_i \qquad \text{Eq. 8.16}$$

where:

v_1 = vertical movement at left end relative to right end,

$\boldsymbol{k_1}$ = first column of stiffness matrix $\underline{\boldsymbol{k}}$,

$w(x)$ = factored distributed load as a function of position x,

ds = incremental distance along the length of approach slab,

$\boldsymbol{H}^T{}_{@\, x=x_i}$ = transpose of Hermitian shape vector evaluated at x_i,

P_i = point load at x_i.

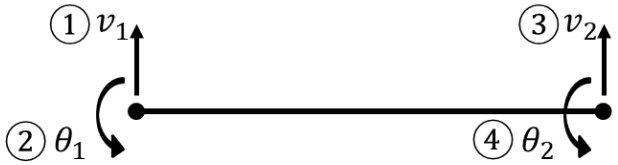

Figure 8.8: Degrees of freedom for a 2-noded frame element.

8.4.2 Load Considerations

The loads in the vertical direction considered for the approach slab include dead load, i.e., the self-weight of the approach slab, and the vehicular live load (HL-93) as specified in AASHTO LRFD Bridge Design Specifications (2020), which is a combination of the design truck or design tandem, and the design lane load. More details are included in Section 6.2.4. In addition, an anticipated end displacement due to embankment settlement is considered. In addition, the approach slab is also subjected to axial forces due to the thermal effects.

For the Eq. 8.16, embankment settlement is applied as end displacement, the self-weight of the slight and design lane load are considered as uniform loading, and axle loads from design truck and design tandem are considered as point loads. The calculations following the simplified method

are repeated for all possible positions of the vehicle loads for design truck and design tandem. Both directions of movement of traffic are considered for the design truck as the axle loads are unsymmetric.

8.4.3 Strength Limit State

For the strength limit state, the demands from the factored loads are compared against the capacity to evaluate the design. Based on the AASHTO LRFD Bridge Design Specifications (2020), the following load factors are considered: dead load factor of 1.25, live load factor of 1.75, and a dynamic allowance factor of 1.33 for design truck or design tandem.

For the strength limit state, a cracked (reduced) moment of inertia of $0.25I_g$ (I_g is the gross cross-sectional moment of inertia) is used for the analysis, based on ACI 318-19.

For the evaluation of demands, envelopes of maximum and minimum values of shear and flexural demand can be determined. The design capacity of the reinforced concrete section in shear and flexure is determined based on the equations provided in ACI 318-19. The flexural capacity is also affected by the axial force in the approach slab due to thermal changes. The strength reduction factor for shear and flexural capacity is taken as 0.75, 0.9, respectively, as per ACI 318-19. The axial force in the approach slab is estimated using the simplified method of Section 8.3. The flexural capacity is evaluated separately for positive and negative bending. By comparing the capacity against the demand envelope, the strength limit state can be examined.

8.4.4 Serviceability Limit State

For the serviceability limit state, the demands from unfactored loads are determined. A cracked (reduced) moment of inertia of $0.35I_g$ (I_g is the gross cross-sectional moment of inertia) is used for the analysis, which is 1.4 times of the value used for the strength limit state, based on ACI 318-19.

The maximum steel stresses at cracks in the most critical regions that have the largest positive or negative bending moment, are evaluated and compared against the design limit, which is 2/3 of the yield strength of steel.

It should be mentioned that the simplified analytical method to determine the strength demand is relatively conservative as idealized fixed-fixed boundary conditions are assumed for the approach slab. However, the approach slab is not fully fixed from rotation, but instead has some flexibility based upon the rotational stiffness of the bridge at the support location. A detailed investigation on the effects of boundary conditions on the response of the approach slab is presented in Section 6.3. The average steel stress with the idealized fixed-end boundary condition is approximately twice that value with an actual restrain from the bridge. Considering this conservatism, a reduction factor of 1.5 is recommended in the evaluation of flexural moment capacity under to account for the flexibility at the bridge end.

8.5 Design Procedure

Figure 8.9 presents the design flow for seamless bridge-pavement systems, which is an iterative procedure by adjusting design details in each component based on demands to satisfy the above-mentioned design criteria.

The first step is to establish the basic bridge and pavement information (geometry, material properties, etc.), and determine the specific design loads and design criteria. The second step is to assign a preliminary design of the transition slab, approach slab and bridge decks based on the basic bridge properties. The third step is to perform axial analyses on the entire seamless system using the simplified analytical method in Section 8.3, through which the minimum required length of the transition zone and the maximum steel stress in each component are determined. If the design criteria for the serviceability limit state are satisfied, the process proceeds to the fourth step for further analysis of the approach slab; otherwise, an adjustment is required in the design details for the transition zone and bridge decks and repeat the axial analysis until satisfied. In the fourth step, the shear and flexural moment demand of the approach slab due to the combined axial and out-of-plane effects are determined using the simplified analytical method in Section 8.4. If the design criteria are satisfied, the design procedure is complete; otherwise, adjust the design details in the approach slab and repeat the third and fourth steps until the response of the entire system satisfies the design criteria.

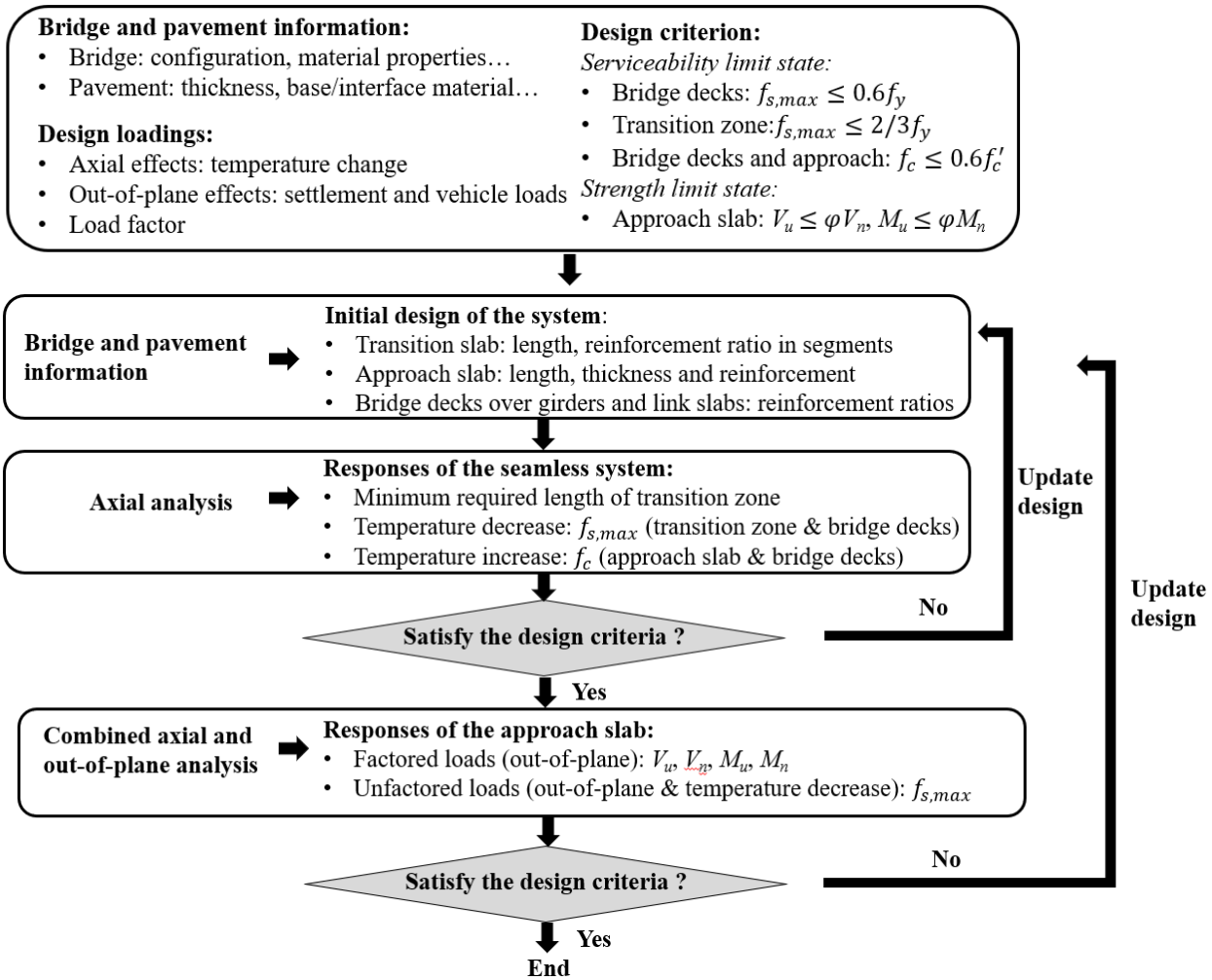

Figure 8.9: Design flow for a seamless bridge-pavement system.

8.6 Design Example

For demonstration purposes, a conventional prestressed concrete girder bridge to be constructed in Austin, Texas, is used to illustrate how a seamless connection with CRCP can be implemented. This section provides design details of the actual bridge following the proposed design process to adapt details for a seamless bridge system.

8.6.1 Bridge and Pavement Information

Bridge Information

The prototype bridge was based upon design details of a conventional bridge with basic properties provided by the research sponsor. The bridge has a non-skewed geometry with three spans of lengths 104 ft., 121 ft. and 75 ft. The total width of the bridge is 40 ft. The bridge decks are designed to act compositely with the five precast prestressed concrete I-girders (Tx54). Figure 8.10 shows the dimensions and section properties of the I-girder (Tx54). The gross area of the girder section is 817 in^2, and the area moment of inertia of the girder section about the x-axis is 299740 in^4, where the x-axis is along the transverse direction.

The original design of the composite bridge deck and girders made use of standard details used in Texas, which were 8.5 in. thick comprised of partial-depth PCPs of 4 in. thick and a continuous 4.5 in. thick CIP concrete layer, as shown in Figure 8.10(a). In the longitudinal direction, the CIP portion is reinforced with one layer of #4 rebars (with a diameter of 0.5 in.) at a maximum spacing of 9 in., corresponding to a reinforcement ratio of 0.5%. The link slab regions where the bridge decks are continuous between two adjacent simply supported spans use the common poor-boy continuous construction details commonly employed in Texas. Figure 8.10(b) shows the reinforcement details in the link slab regions, where a construction joint or controlled joint is indicated over the interior bents. In this bridge, the link slabs use a full depth of CIP concrete with two layers of longitudinal reinforcement with #4 at a maximum spacing of 9 in. at each layer. Correspondingly, the reinforcement ratio is approximately 1.3%.

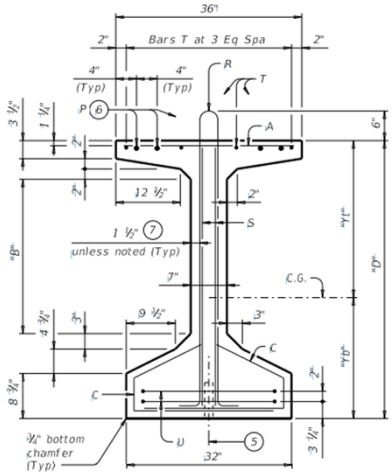

(a)

GIRDER DIMENSIONS AND SECTION PROPERTIES

Girder Type	"D" (in.)	"B" (in.)	"Yt" (in.)	"Yb" (in.)	Area (in^2)	"Ix" (in^4)	"Iy" (in^4)	Weight (9) (plf)
Tx54	54	30	30.49	23.51	817	299,740	46,707	880

(b)

Figure 8.10: I-girder (Tx54) details: (a) Girder shape and dimensions; (b) Girder dimensions and section properties.

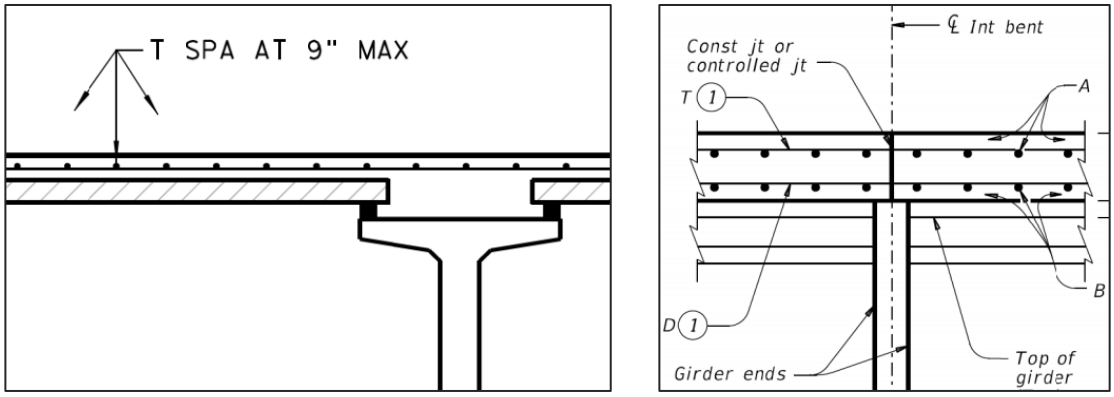

(a) (b)

Figure 8.11: Reinforcement details of bridge decks: (a) Decks over girders; (b) Link slabs.

The pier columns have a height of 16 ft. with a nearly square cross-section (36 in. × 39 in.). The design concrete compressive strength for concrete decks, girders and piers are 4 ksi, 8 ksi, and 3.6 ksi, respectively.

Pavement Information

The roadway pavement is 11-in.-thick CRCP. The supporting layers underneath the CRCP consist of a 24-in.-thick embankment and a 6-in.-thick CSB, as shown in Figure 8.12. A 1-in.-thick Type D HMA layer is applied between the CRCP and CSB. One layer of longitudinal reinforcement of #6 rebar (with a diameter of 0.75 in.) at a spacing of 6.5 in. are detailed, corresponding to a reinforcement ratio of 0.62%. The design concrete compressive strength for the pavement is 4 ksi.

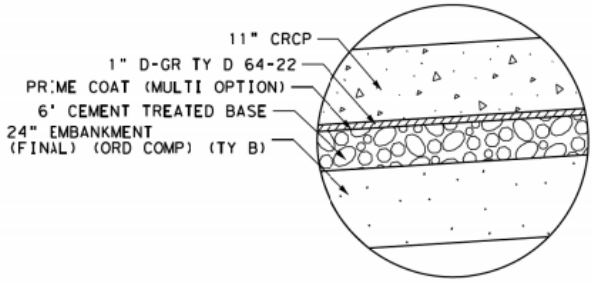

Figure 8.12: Details of CRCP, interface material and supporting layers.

Design Loading

The design loads established in Section 8.2.3 are used for this example.

Design Criteria for Serviceability Limit State

For Grade 60 steel, the acceptable limit of the maximum steel stresses at cracks for the transition zone and bridge decks are determined as 40 ksi and 36 ksi, respectively. Recall that these come from the respective limits of $\frac{2}{3}f_y$ and $0.6f_y$ for steel in pavements and bridge decks. For the approach slab and bridge decks with a concrete compressive strength of 4 ksi, the acceptable limit of the concrete compressive stress is determined as 2.4 ksi.

8.6.2 Analysis for Axial Effects

A coefficient of friction of 0.7 is used for the analysis and design, assuming a felt paper is utilized between the concrete slab and Type D HMA surface.

The bridge has three spans that are not perfectly symmetrical. Previous numerical investigation indicated that the slight asymmetry of the bridge does not result in a significant difference in the responses of the transition zone located on two sides of the bridge. Therefore, for simplicity, the bridge is modeled as symmetric with both first and last span of 104 ft. long. Making use of the simplified geometry, the expected results should be a relatively conservative design as the axial demands associated with larger thermal expansion/contraction of the longer-span bridges will increase. For simplicity, the transition zones on both sides are designed to have the same configuration and reinforcement details. These details are similar to those of the seamless systems analyzed in Chapter 5.

Table 8.6: Initial design details for bridge decks and transition zone for axial effects.

Region	Length (ft.)	Thickness (in.)	Longitudinal reinforcement	Reinforcement ratio (%)
Bridge deck (S1)	104	4.5	#4 @ 6 in.	0.74
Bridge deck (S2)	121			
Bridge deck (S3)	104			
Bridge girder	-	8.5	-	-
Link slab	2	8.5	#7 @ 5 in. #6 @ 5 in.	2.4
Approach slab	30	Tapered: 11-14	#7 @ 5 in. #7 @ 5 in.	1.92 (T. Layer: 0.96, B. Layer: 0.96)
Transition slab (T1)	70	11	#6 @ 6 in. #6 @ 6 in.	1.33
Transition slab (T2)	100		#5 @ 5.5 in. #5 @ 5.5 in.	1.0
Transition slab (T3)	To be determined		#4 @ 5 in. #4 @ 5 in	0.73

The transition zone is designed as a three-segment transition slab and an approach slab. Table 8.6 lists the length and thickness for each component, including bridge decks over girders, link slabs, approach slab and transition slabs. The transition slab has a constant thickness of 11 in. and the approach slab is designed as tapered section with thickness gradually increasing from 11 in. to 14 in. As noted in the last section, preliminary values were first selected based upon the basic geometry and material properties. The preliminary selection for the longitudinal reinforcement and corresponding reinforcement ratio are therefore presented. As indicated in Table 8.6, the reinforcement ratio in the last transition segment near the pavement slightly increased to 0.84% compared to a value of 0.62% for a conventional CRCP. The reinforcement ratios of the transition zone gradually increased (0.84%, 1.13% and 1.33%) toward the approach slab, which has a total

reinforcement ratio of 1.92% equally distributed in the top and bottom layers. Additional reinforcement details used for the calculations were – top cover of 2 in., bottom cover of 3 in.

The analysis of the axial response of the seamless system is conducted per unit width of pavement and bridge (1 in.), as recommended in Section 5.3.1. Accordingly, the equivalent depth of the bridge girder can be taken as 8.5 in. (per in. of width). The reinforcement ratio for the bridge decks over girders increases from 0.5% for the original bridge design to 0.74% for a seamless bridge design. The reinforcement ratio for the link slabs increases significantly from 0.52% to 2.4%.

The simplified analytical method presented in Section 8.3 can be used to determine the minimum required length of transition slab segment 3 and to verify stress limits for both cases of expansion (temperature increase of 80°F) and contraction (temperature decrease of 55°F). Following the steps as presented in Section 8.3.1, the minimum required length of the transition slab segment 3 that is connected to the conventional CRCP is 208 ft in the case of temperature increase, and this length is 27 ft. Therefore, the minimum required length of the entire transition zone can be determined as 408 ft., which is controlled by the case of temperature increase. Correspondingly, the axial responses of the seamless system due to temperature increase and temperature decrease can be determined as shown in Figure 8.13 and Figure 8.14, respectively.

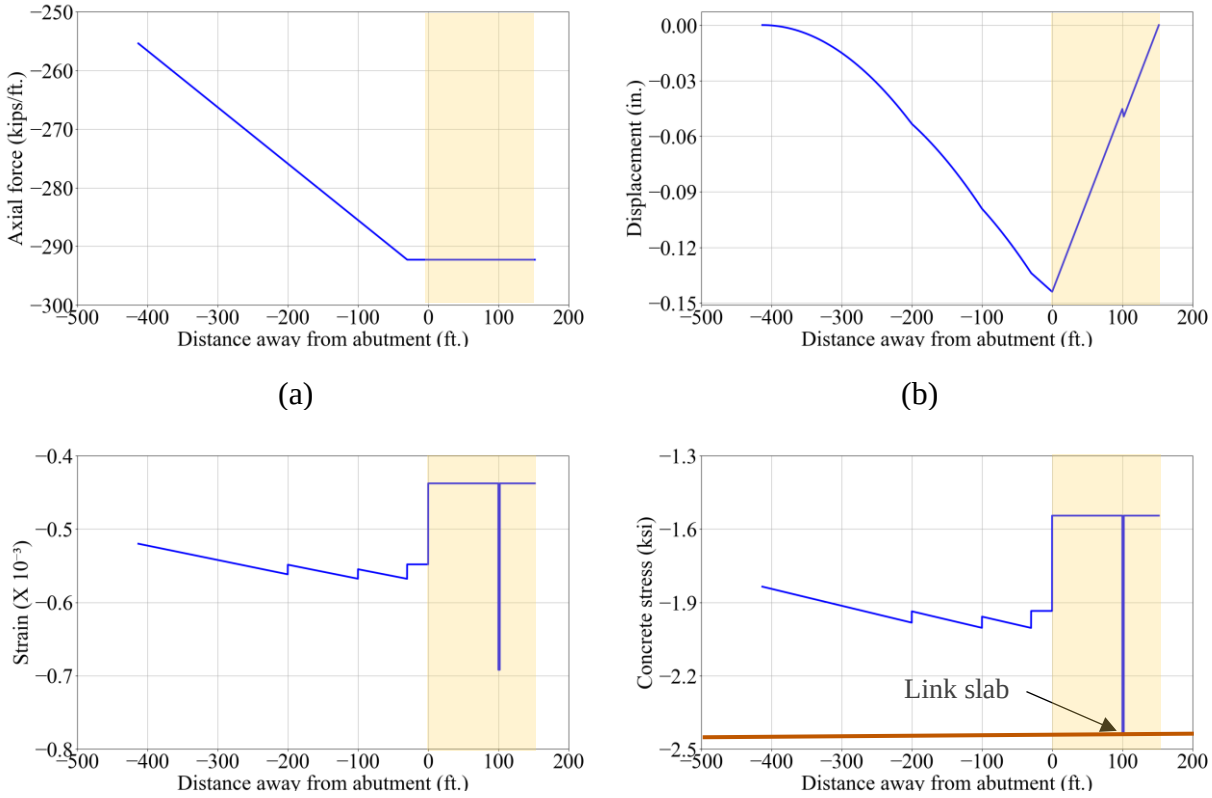

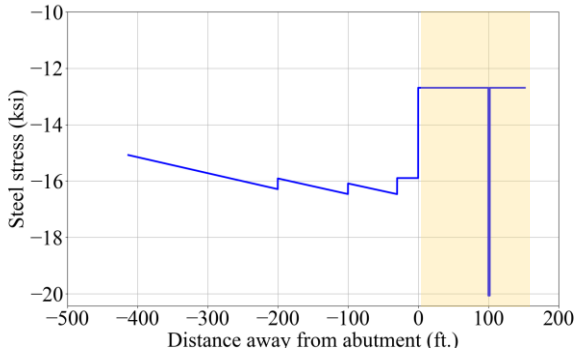

(e)

Figure 8.13: Axial response of the seamless system (temperature increase): (a) Axial force; (b) Longitudinal displacement; (c) Strain; (d) Concrete stress; (e) Steel stress.

In the case of temperature increase, the maximum concrete compressive stress occurs within the link slab is approximately 2.4 ksi, which is at the limit of design criteria (marked in the figure).

In the case of temperature decrease, the strain demands within the transition zone gradually increase toward the bridge abutment, as presented in Figure 8.14(c). Overall, the performance satisfies the design limit of 40 ksi for the transition pavement and 36 ksi for the link slab. The maximum steel stress at cracks for the approach slab is approximately 19 ksi, and the value for the link slab is approximately 20 ksi. The maximum steel stress at cracks for the bridge deck over girder is not shown as elastic properties were assumed.

In summary, due to the axial effects, the proposed design details satisfy the design criteria and the design proceeds to the next step, where the response of the approach slab due to the combined out-of-plane effects are analyzed and checked against the design criteria.

It should be noted that in this case study, the preliminary details are satisfactory and do not require iteration to satisfy the design for the axial effects. The accurate preliminary sizing is mostly attributed to the knowledge gained in the parametric studies of typical TxDOT bridges and pavements in Chapter 5, which share similarities with this actual bridge. For other geometry, an iterative design process will most likely be required for a seamless bridge-pavement system.

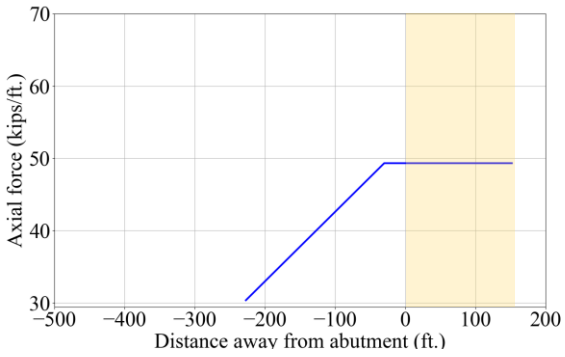

(a)

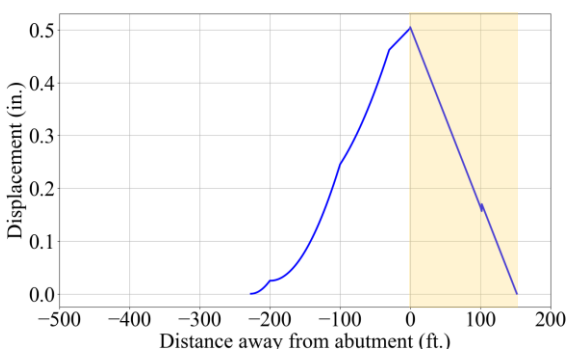

(b)

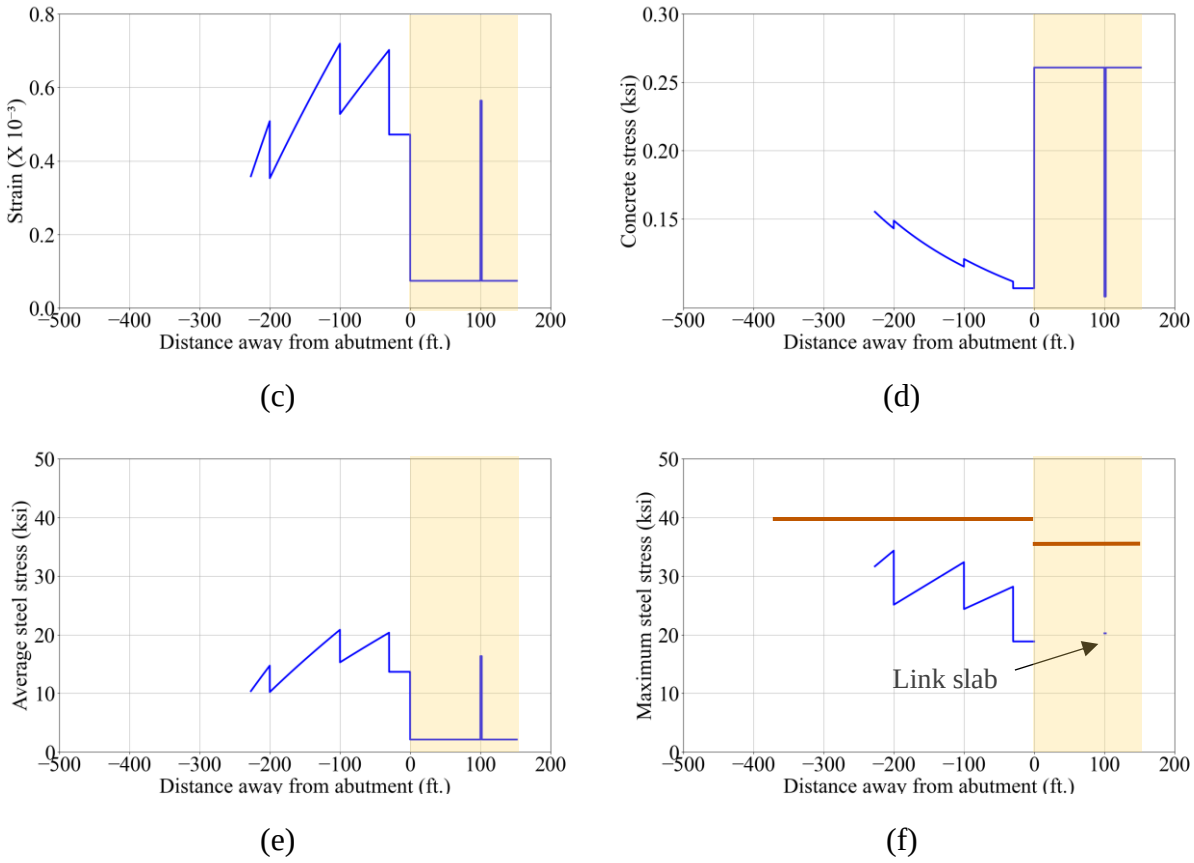

Figure 8.14: Axial response of the seamless system (temperature decrease): (a) Axial force; (b) Longitudinal displacement; (c) Strain; (d) Concrete stress; (e) Average steel stress; (f) Maximum steel stress.

8.6.3 Analysis for Combined Out-of-Plane and Axial Effects

The simplified method developed in Section 8.4 can be applied to determine the shear and flexural moment demand of the approach slab (1-ft.-wide) due to the out-of-plane (vehicular load and embankment settlement) effects. The calculations of the capacity with the presence of compressive axial force (in the case of temperature increase of 80°F) and tensile axial force (in the case of temperature decrease of 55°F) are conducted. For a 1-ft.-wide approach slab, the axial force is -291 kips in the case of temperature increase and 49 kips in the case of temperature decrease, as determined in Section 8.6.2.

Strength Limit State

The strength limit state is examined for the approach slab due to the factored out-of-plane effects. The comparison between shear demand and capacity, between flexural moment demand and capacity are presented in Figure 8.15 and Figure 8.16, for the cases of temperature increase and temperature decrease, respectively. From the perspective of capacities, both shear and flexural capacity decrease with distance moving away from the bridge, due to a reduction in the cross-sectional thickness. The shear capacity is barely affected by the axial force. In general, shear

capacity satisfies the demand for most of the approach slab, except at both ends of the approach slab where the shear capacity is slightly insufficient for the demand. However, the shear capacity in the local region at the supports is generally not a concern (ACI 318-19, 2019).

From the perspective of flexural moment, the maximum negative moment occurs at the bridge end and the maximum positive moment occurs at approximately the mid-span of the approach slab. The flexural capacity with the presence of compressive axial force is significantly larger than that with the tensile force. In general, the flexural moment capacity is sufficient for the demand at any location of the approach slab, which satisfies the strength limit state.

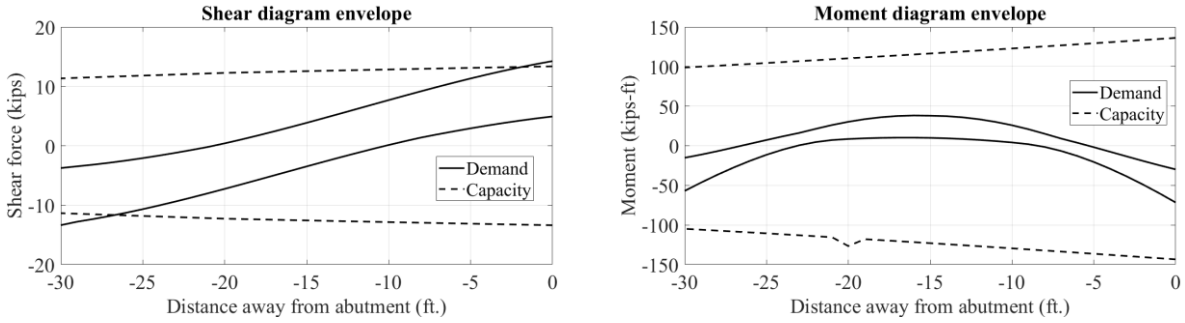

(a) (b)

Figure 8.15: Envelopes of demand and capacity (out-of-plane and temperature increase) for strength limit state: (a) shear; (b) flexural moment.

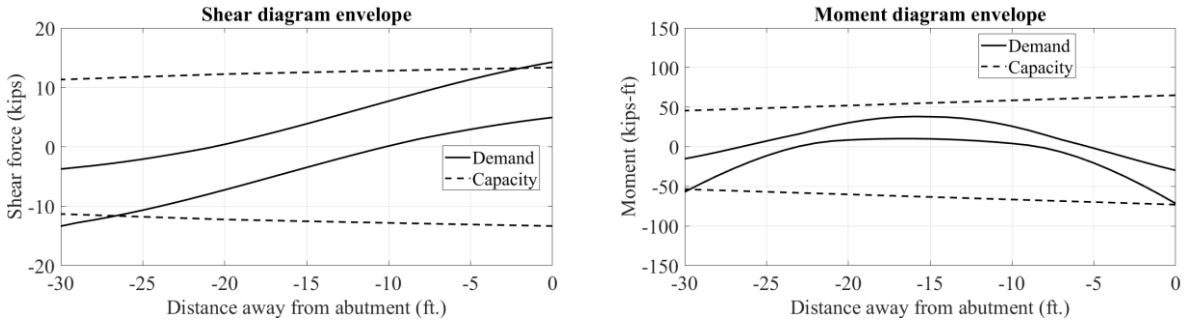

(a) (b)

Figure 8.16: Envelopes of demand and capacity (out-of-plane and temperature decrease) for strength limit state: (a) shear; (b) flexural moment.

Serviceability Limit State

The serviceability limit state is examined for the approach slab due to the combined unfactored out-of-plane and longitudinal thermal effects. The maximum steel tensile stress at cracks, and maximum concrete compressive stress at critical locations are investigated and compared with the design limit. Envelopes of maximum and minimum values of moment demand due to the unfactored out-of-plane effects only is presented Figure 8.17. The maximum negative bending moment occurs at the bridge abutment, with a value of -44.9 kips-ft, whereas the maximum positive bending moment occurs at approximately 16.5 ft away from the bridge abutment, with a

value of 19.3 kips-ft. Since an equal amount of reinforcement is used for the bottom and top layers for the approach slab, the response at the bridge abutment can be evaluated, which in this case is more critical for serviceability.

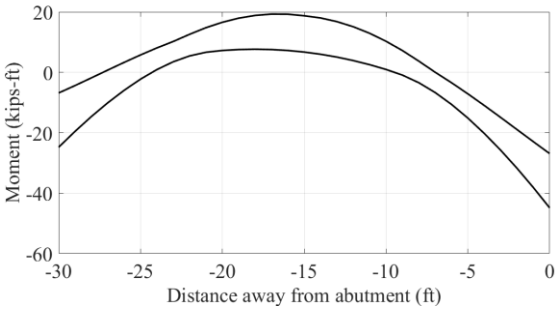

Figure 8.17: Envelopes of flexural moment demand (out-of-plane effects) for serviceability limit state.

As discussed in Section, a reduction factor of 1.5 is applied on the moment demand considering the overly conservatism with the assumption of fixed-end boundary condition at the bridge end. Therefore, the maximum bending moment is determined as:

$$M = 44.9/1.5 = 29.9 \text{ kips-ft.}$$

The maximum steel stress at cracks is determined based on the Eq. 6.2 ($f_{s,max} = (f_{c,ave}A_{c,ef} + f_{s,ave}A_s)/A_s$) following the steps below:

The effective moment of inertia for serviceability limit state is calculated as:

$$I_e = 0.35I_g = 0.35bd^3 = 0.35\times12\times14^3 = 960 \text{ in}^4.$$

The concrete tensile stress at the outmost fiber is determined as:

$$f_{c,max} = Md/2/I_e = 2.62 \text{ ksi.}$$

The average concrete tensile stress was therefore determined as 1.31 ksi.

The average tensile stress of steel is determined as:

$$f_s = f_{c,max}/E_c\ (d/2 - c)/(d/2)\ E_s = 15 \text{ ksi,}$$

where c is the concrete cover of steel on the tensile side, and is taken as 2 in.

The effective concrete area is determined following the Eq. 6.1 ($A_{c,ef} = \min\ (2.5 \times \left(c + \frac{\varphi}{2}\right), \frac{(h-x)}{3})$):

$$A_{c,ef} = min\ (2.5\times(c + d/2/2), (d - d/2)/2) = 2.33 \text{ in}^2.$$

As a result, the maximum steel stress at cracks is determined as:

$f_{s,max}$ = 16.9 ksi.

The response of the approach slab at the bridge end due to the axial effects corresponding to a temperature decrease and out-of-plane effects can be superimposed, causing even larger tensile steel stresses in the top approach slab at the bridge abutment. The maximum steel stress at cracks due to the axial effects and out-of-plane effects are 19 ksi, 16.9 ksi, respectively. The maximum steel stress due to the combined out-of-plane and axial effects is determined as 35.9 ksi using a simple linear superposition, which is below the design limit of 40 ksi for pavement. Therefore, the serviceability limit state is satisfied with the current design details.

In summary, for the strength limit state, the moment capacity is sufficient for the demand due to the factored loads. The strength capacity falls slightly short in meeting the shear demands at the two ends of the approach slab. The design details of the approach slab can be iterated to improve the shear capacity at critical locations, for example, slightly increasing the thickness of the approach slab at ends or slightly increasing the reinforcement amount at ends.

8.7 Summary

In this chapter, general design recommendations for seamless bridge-pavement systems are proposed, including the interface materials (bond breakers) for the transition zone and design detailing. A simplified analytical method for the axial response of the seamless system, and a simplified analytical method to conduct the linear analysis of the approach slab due to combined out-of-plane and axial effects with cracked sectional properties are developed. A design procedure is developed, and demonstrated with a design example of an actual bridge with CRCP. The key points are highlighted as follows:

- The seamless bridge-pavement system mainly involves the following additional or modified design considerations with respect to conventional bridge-pavement systems: determination of configuration and reinforcement for the transition slab, approach slab, bridge decks over girders, link slabs, and locally-strengthened bridge deck region near the abutment.
- Felt paper and double-sided textured LLDPE sheet are recommended as bond breakers in the concrete slab-base interface for the transition zone, which have steady friction coefficients of 0.7 and 0.4, respectively.
- An iterative design process of the seamless system includes the development of an initial design details based on the bridge and pavement information, the sequential evaluation of the axial response of the entire system and combined axial and out-of-plane response of the approach slab using the proposed simplified method. The design details need to satisfy the design criteria established in terms of allowable steel tensile stresses and concrete compressive stresses for serviceability limit state, and demand against capacity for strength limit state.

9. Summary, Conclusions and Future Work

9.1 Summary

The complete elimination of bridge expansion joints provides many benefits, such as a significant reduction of the maintenance costs, improvement of the long-term durability of the primary load-carrying components, and improvement of the vehicular performance. The primary goal of the research study documented in this technical memorandum is to study the behavior of seamless (jointless) bridge-pavement systems and propose general design recommendations for practical applications in the U.S. To achieve this objective, a comprehensive study including experimental testing and numerical modeling was conducted.

A two-phase experimental program consisting of unit-cell direct shear tests (Phase I) and large-scale push-off tests (Phase II) was performed to obtain the shear stress versus displacement relationships and determine the shear strength properties of different interfaces between concrete pavement and common base materials, and to identify candidate bond breakers for the transition zone of the pavement in a seamless bridge system. The bases investigated included granular bases (AASHTO Gravel No.8 and TxDOT Grade 3 Aggregate), and stabilized bases (CSB, HMA, and CSB topped with a thin layer of HMA). Eight interface materials were examined with an intent to break the bond and control the level of interface restraint, including 1-in.-thick HMA layer, woven-geotextile, non-woven geotextile, felt paper, and various types of polyethylene (PE) sheets (one or two layers of smooth PE sheets, spike HDPE sheet, and textured LLDPE sheet). In addition, the effects of scale and cyclic displacement demands on the interface shear resistance were discussed. The sliding (failure) planes and post-test interface conditions were also investigated.

To understand the behavior of the seamless bridge-pavement system, two types of numerical models were developed using commercial finite element analysis software. First, a structural model of the entire seamless bridge-pavement system was used to investigate the axial response of the system when subjected to thermal contraction and expansion effects as well as shrinkage. Second, a more detailed continuum finite element model of the transition zone was used to analyze the response of this zone of the pavement due to combined axial and out-of-plane (vertical) effects, when subjected to differential embankment settlement, vehicular loads in addition to temperature effects. Numerical parametric studies of the response under axial effects were conducted to identify the key design characteristics affecting the performance of the seamless system. The parameters investigated included the friction coefficient at the concrete slab-base interface, slab thickness and reinforcement ratio of the transition zone, span length, number of spans and girders, girder size of the bridge, and temperature changes for the bridge and pavement components. Numerical parametric studies were also conducted for the parameters that affect the combined axial and out-of-plane response of the approach slab, including the reinforcement ratio and slab thickness of the approach slab, and level of embankment.

Based on the results and findings of the experimental testing and numerical modeling, general design recommendations were developed, including the selection of bond breakers in the transition zone, design verification criteria and design details. Simplified analytical models were developed to determine the stresses and deformations induced in the system considering axial and out-of-plane effects. A design example of an actual bridge in Texas modified to include a seamless connection with CRCP was presented using the proposed design procedure.

While the study was primarily focused on seamless bridges with CRCP, the results obtained can also be useful in applications of the seamless concept for other roadway pavements (e.g., flexible and jointed concrete pavements) in which a certain length of conventional CRCP can be introduced at the end of the transition zone. The response of this modified system was also analyzed numerically and the required length of the additional CRCP on the axial response was investigated.

9.2 Conclusions

The main conclusions and findings of the experimental and numerical studies are summarized as follows:

- Polyethylene sheets and felt paper eliminate the adhesion at the concrete slab-base interface, whereas 1-in.-thick HMA layer, woven geotextile and non-woven geotextile are not suitable to be used as bond breakers in the transition zone of seamless bridge-pavement systems. The steady coefficient of friction provided by the bond breakers is listed in descending order as follows: felt paper (approximately 0.7); double-sided textured LLDPE sheets (approximately 0.4); single-sided spike HDPE sheets (approximately 0.3); and smooth PE sheets (approximately 0.25). Felt paper and double-sided textured LLDPE sheets are recommended as bond breakers for the transition zone, which provide a friction coefficient within the range of the target coefficient of friction (as discussed below) based on the numerical parametric studies. The performance of felt paper and double-sided textured LLDPE sheets are compared in four aspects: 1) both materials are expected to provide stable steady coefficient of friction over cyclic movements due to annual temperature changes; 2) both materials involve simple construction; 3) LLDPE sheet has better durability based on the fewer post-test damages as observed in the testing; 4) both materials present similar limitations and opportunities regarding their environmental impact.
- The axial response of the seamless bridge-pavement system is mainly controlled by the magnitude of the temperature changes. The performance of the seamless system in the case of contraction (temperature decrease), which causes tensile forces in the system, is more critical as the concrete in the transition zone and bridge decks are expected to crack. Neglecting the shrinkage effects tends to lead to a conservative design. Two design criteria are established to satisfy standard serviceability limit state requirements: 1) limit the maximum steel stress at cracks below 60% and two-thirds of the yield strength for the bridge decks and pavement, respectively, to control the crack width within the acceptable limit; 2) limit the concrete compressive stress below 60% of the concrete compressive strength to avoid microcracking. The critical regions are identified as the approach slab near the bridge abutment and link slabs, where a relatively large increase in axial demands is expected due to the seamless connection.
- The numerical parametric studies indicate that the axial response of the seamless system is significantly affected by the coefficient of friction at the transition pavement-base interface, with a larger value leading to higher force demands in the transition zone and bridge decks and shorter length of the transition zone. To balance the length of the transition zone with the magnitude of the forces, a target range of coefficients of friction were approximately established to be 0.5-0.8; however, values up to 1.0 are also acceptable. The axial response also depends on the relative stiffness of the bridge and pavement elements. The changes in parameters, such as the slab thickness, reinforcement ratio of the transition slab, number of

girders, and girder size, will modify the relative stiffness between the pavement and the bridge, thus affecting the demand in the system.

- In addition to the axial effects, the response of the approach slab is also affected by the out-of-plane behavior as the approach slab likely loses base support due to the differential embankment settlement, while it needs to carry vehicular loads. The critical regions of the approach slab include: 1) in the case of combined axial (temperature decrease) and out-of-plane effects, the top side near the bridge abutment, where relatively large maximum tensile steel stresses at cracks occur; and 2) in the case of combined axial (temperature increase) and out-of-plane effects, the bottom of the slab near the bridge abutment and top of the slab at approximately mid-span of the slab, where the largest concrete compressive stresses occur. Numerical parametric studies indicate that increasing the reinforcement ratio and slab thickness of the approach slab can result in lower maximum steel stresses at cracks with the combined axial and out-of-plane effects. A tapered approach slab with gradually increasing thickness from the pavement end to the bridge end can provide a practical and efficient option to meet design and constructability needs.
- Based on the results of the analysis with the axial and out-of-plane effects and parametric studies, general design recommendations regarding the longitudinal reinforcement amount are provided for the seamless bridge-pavement system, as follows: 1) increase the reinforcement ratio of the transition zone compared to that in a conventional CRCP, and a gradual increase toward the bridge provides an efficient solution; 2) increase the total reinforcement ratio of the approach slab as compared to a conventional design, providing a higher amount of steel in the top layer compared to the bottom layer; 3) increase the reinforcement ratio in the bridge link slabs over interior supports (poor-boy continuous) and possibly slightly increase the reinforcement ratio for the remaining decks that act composite with the girders; and 4) extend the top layer reinforcement of the approach slab into the beginning of the bridge deck near the abutment. A design procedure of the seamless system is proposed, which involves the definition of transition slab thickness and reinforcing details for the transition zone and bridge deck supported by the sequential evaluation of the axial response of the entire system and combined axial and out-of-plane response of the approach slab using the numerical models proposed in this study. The procedure is applied iteratively until the design criteria are satisfied.

9.3 Future Work

The construction, instrumentation and field monitoring of a pilot bridge project with a seamless connection using common practices in the U.S. and Texas is deemed essential. The collection of the field data on the actual response of a seamless bridge-CRCP system can be used for the validation of the numerical models developed in this study, and to validate construction details. While seamless bridges were already constructed and instrumented in Australia, this technology needs to be further investigated in the field and demonstrated for U.S. bridge and pavement construction practices. The field monitoring studies will also provide insight on the long-term field performance of the bond breakers.

In addition, future work is also recommended to develop construction details, such as, strategies to close the gap between the bridge and pavement, the construction of base with a desired slope for a tapered approach slab, and changes of reinforcement configuration within the transition zone. It can be complemented with the findings from the future field monitoring.

References

AASHTO (American Association of State Highway and Transportation Officials). (2020). LRFD Bridge Design Specifications, 9th Edition.

Abaqus version 2017 (2016) [Computer software]. Dassault Systèmes, Providence, RI, USA.

Abaqus Analysis User's Manual (2017). Version 2017, *Dassault Systèmes Simulia Corp*.

ACI (American Concrete Institute). (2019). Building Code Requirements for Structural Concrete and Commentary ACI 318-19.

Ala, N. (2011). Seamless bridge and roadway system for the US practice (Doctoral dissertation). *The University of Nebraska-Lincoln*.

Ala, N., and Azizinamini, A. (2016a). Proposed design provisions for a seamless bridge system: Cases of flexible and jointed pavements. *Journal of Bridge Engineering*, 21(2): 04015045.

Ala, N., and Azizinamini, A. (2016b). Experimental study of seamless bridge transition system for U.S. practice. *Journal of Bridge Engineering*, 21(2): 04015046.

ASTM (American Society for Testing and Materials). (2021). C39-21 Standard test method for compressive strength of cylindrical concrete specimens.

ASTM (2017). D1633-17 Standard test methods for compressive strength of molded soil-cement cylinders.

ASTM (2016). D4869-16 Standard specification for asphalt-saturated organic felt underlayment used in steep slope roofing.

ASTM (2019). D588-19 Standard test methods for moisture-density (unit weight) relations of soil-cement mixtures.

ASTM (2017). E1745-17 Standard specification for plastic water vapor retarders used in contact with soil or granular fill under concrete slabs.

Au, A., Lam, C., Au, J., & Tharmabala, B. (2013). Eliminating deck joints using debonded link slabs: Research and field tests in Ontario. *Journal of Bridge Engineering*, *18*(8), 768-778.

Beer, D. (2021). No bump – at pavement to bridge transitions. *TxDOT/CCT Concrete Conference, 11/18/2021*.

Bridge, R., Griffiths, S., and Bowmaker, G. (2005). The concept of a seamless concrete pavement and bridge deck. *Australian Structural Engineering Conference 2005: Structural Engineering: Preserving and Building into the Future*.

Birtel, V. A. M. P., & Mark, P. (2006). Parameterised finite element modelling of RC beam shear failure. In The 19th Annual International ABAQUS Users' Conference, 14, 95-108.

Burke Jr, M. P. (2009). Integral and semi-integral bridges. *John Wiley & Sons.*

Cackler, T., Burnham, T., & Harrington, D. (2018). Performance assessment of nonwoven geotextile materials used as the separation layer for unbonded concrete overlays of existing concrete pavements in the US.

Caner, A., & Zia, P. (1998). Behavior and design of link slabs for jointless bridge decks. *PCI Journal*, 43(3).

CEB (Euro-International Committee for Concrete). (1993). CEB-FIP Model Code 90.

Chan Suh, Y., Woo Lee, S., & Soo Kang, M. (2002). Evaluation of subbase friction for typical Korean concrete pavement. *Transportation Research Record*, *1809*(1), 66-73.

Chen, Q., T. Helwig, R. Herman, G. Grisham, and Y. Arikan. (2009). Effects of Thermal Loads on Texas Steel Bridges. TxDOT Research Report 5040-1. *The University of Texas at Austin*.

Chia, W. S., McCullough, B. F., & Burns, N. H. (1986). Field evaluation of subbase friction characteristics. *Texas Department of Transportation.*

Civjan S. A., Bonczar C. H., Breña S. F., DeJong J. T., and Crovo D. S. (2007). Integral Abutment Bridge Behavior: Parametric Analysis of a Massachusetts Bridge. *Journal of Bridge Engineering*, 12(1), 64-71.

Civjan, S. A., Kalayci, E., Quinn, B. H., Breña, S. F. and Allen, C. A. (2013). Observed Integral Abutment Bridge Substructure Response. Engineering Structures, 56(3), 1177-1191.

Darwin, D., Scanlon, A., Gergely, P., Bishara, A. G., Boggs, H. L., Brander, M. E., ... & Poston, R. W. (1997). Cracking of concrete members in direct tension. ACI committee, 224(224.222), R221-224.

Friberg, B. F. (1954). Frictional resistance under concrete pavements and restraint stresses in long reinforced slabs. *Highway Research Board Proceedings*, 33.

fib (International Federation for Structural Concrete). (2013). Fib Model Code for Concrete Structures 2010, 1st Edition.

Frosch, R. J. (1999). Another look at cracking and crack control in reinforced concrete. *Structural Journal*, *96*(3), 437-442.

Ge, X., Munsterman, K., Deng, X., Reichenbach, M., Park, S., Helwig, T., ... & Bayrak, O. (2021). Designing for Deck Stress Over Precast Panels in Negative Moment Regions (No. FHWA/TX-21/0-6909-1/5-6909-01-1). *The University of Texas at Austin*.

Goldbeck, A. T. (1917). Friction Tests of Concrete on Various Sub-bases. *Journal Proceedings*, 13(2), 239-245.

Griffiths, S., Bowmaker, G., Bryce, C., & Bridge, R. (2005). Design and construction of seamless pavement on Westlink M7, Sydney, Australia. In *Proc., 8th Int. Conf. on Concrete Pavements* (pp. 21-38). *International Society for Concrete Pavements*.

Griffiths, S., Bowmaker, G. (2012). Actual performance of seamless pavements in Australia. *25th ARRB Conference-Shaping the future: linking policy, research and outcomes*, Perth, Australia.

Griffiths, S., Bowmaker, G., Wheeler, K. (2013). No seam stress. *Roads & Bridges*.

Griffiths, S. (2018). The elimination of deck joints-Seamless pavements. *TxDOT/CCT Concrete Conference*.

Ha, S., Yeon, J., Won, M. C., Jung, Y. S., & Zollinger, D. G. (2012). User's Guide for TxCRCP-ME Design Software: Volume I-User's Guide and Volume II-Software Architecture (No. Report 0-5832-P3). *Texas Department of Transportation.*

Hein, D.K., Rao, S., Tayabji, S. and Lee, H. (2017). Base and subbase for concrete pavement. (No. FHWA-HIF-16-005). *Federal Highway Administration*.

Hyzak, M. (2018). Seamless Bridges. *TxDOT BRG Webinar 9/13/18*, available at http://ftp.dot.state.tx.us/pub/txdot-info/brg/webinars/2018-0913/05.pdf.

Hyzak, M. (2021). Concrete durability and corrosion guidance. *TxDOT/CCT Concrete Conference.*

Jin, X., Shao, X., Peng, W., & Yan, B. (2005). A new category of semi-integral abutment in China. *Structural engineering international*, *15*(3), 186-188.

Jeong, J. H., Park, J. Y., Lim, J. S., & Kim, S. H. (2014). Testing and modelling of friction characteristics between concrete slab and subbase layers. *Road Materials and Pavement Design*, *15*(1), 114-130.

Lepech, M. D., & Li, V. C. (2009). Application of ECC for bridge deck link slabs. *Materials and Structures*, *42*(9), 1185-1195.

Lee, S. W. (2000). Characteristics of friction between concrete slab and base. *KSCE Journal of Civil Engineering*, 4(4), 265-275.

Li, S., Tian, B., Niu, K., Sun, Z., & Zhou, W. (2013). Characteristics of Base Friction for Concrete Pavement Structure in China: Experimental Study. *Transportation research record*, *2367*(1), 107-112.

Lin, Y. (2010). Tension stiffening model for reinforced concrete based on bond stress slip relation (Master thesis). *The Pennsylvania State University*.

Lock, R. J. (2002). Integral bridge abutments. *University of Cambridge, Department of Engineering*.

Malviya, J. (2021). Structural analysis of seamless bridge system (Master thesis). *The University of Texas at Austin*.

Maitra, S. R., Reddy, K. S., & Ramachandra, L. S. (2009). Experimental evaluation of interface friction and study of its influence on concrete pavement response. *Journal of transportation engineering*, *135*(8), 563-571.

midas Bridge, <https://www.midasbridge.com/en/solutions/integral-bridges>

Mohamed, A. M. M. (2017). Evaluation of soil-reinforcement composite interaction in geosynthetic-reinforced soil structures (Doctoral dissertation). *The University of Texas at Austin.*

NYSDOT (New York State Department of Transportation). (2005). Bridge Manual – 3rd Edition.

Otto Rasmussen, R., & Rozycki, D. K. (2001). Characterization and modeling of axial slab-support restraint. *Transportation Research Record*, *1778*(1), 26-32.

Roesler, J. R., Hiller, J. E., & Brand, A. S. (2016). Continuously Reinforced Concrete Pavement Manual, Guidelines for Design, Construction, Maintenance, and Rehabilitation (No. FHWA-HIF-16-026). *Federal Highway Administration*.

Saraf, S., Choi, P., Ryu, S., Ha, S., Ghebrab, T., & Won, M. C. (2013). Minimize premature distresses in continuously reinforced concrete pavements (No. FHWA/TX-14-0-6687-1). *Texas Department of Transportation*.

Standards Australia (2004). Australian Standard, Bridge design Part 1: Scope and general principles. AS 5100.

Stott, J. P. (1961). Tests on materials for use in sliding layers under concrete road slabs. *Civil Engineering*, *56*(663), 1297.

Sümer, Y., & Aktaş, M. (2015). Defining parameters for concrete damage plasticity model. *Challenge Journal of Structural Mechanics*, *1*(3), 149-155.

Thorenfeldt, E. (1987). Mechanical properties of high-strength concrete and applications in design. *Symposium Proceedings, Utilization of High-Strength Concrete.*

Thorkildsen, E. T. (2020). Case Study: Eliminating Bridge Joints with Link Slabs-An Overview of State Practices (No. FHWA-HIF-20-062). *Federal Highway Administration*.

Thippeswamy, H. K., GangaRao, H. V., & Franco, J. M. (2002). Performance evaluation of jointless bridges. *Journal of Bridge Engineering*, *7*(5), 276-289.

Timms, A. G. (1964). Evaluating subgrade friction-reducing mediums for rigid pavements. *Highway Research Record*, 60, 28-38.

Townsend, T., Powell, J., & Xu, C. (2007). Environmental issues associated with asphalt shingle recycling. *Construction Materials Recycling Association, US EPA Innovations Workgroup*.

TxDOT (Texas Department of Transportation). (2019). Pavement Manual: Rigid pavement design.

TxDOT (2014). Standard specifications for construction and maintenance of highways, streets and bridges.

TxDOT Item 247 (2014). Flexible base.

TxDOT Item 276 (2014). Cement treatment (Plant-mixed).

TxDOT Item 300 (2014). Asphalts, Oils, and Emulsions.

TxDOT Item 341 (2014). Dense-graded hot-mixed asphalt.

TxDOT Item 360 (2014). Concrete pavement.

TxDOT. CRCP-ME Design software.

TxDOT (a). I-girder dimensions.

https://ftp.dot.state.tx.us/pub/txdotinfo/brg/design/pdf/a-21.pdf.

TxDOT. (2015). Bridge approach slab - Concrete pavement (BAS-C).

https://ftp.dot.state.tx.us/pub/txdot-info/cmd/cserve/standard/bridge/bascste1.pdf.

VDOT (Virginia Department of Transportation). (2017). AASHTOWare Pavement ME User Manual.

Vecchio, F. J., & Collins, M. P. (1993). Compression response of cracked reinforced concrete. *Journal of structural engineering*, *119*(12), 3590-3610.

Wesevich, J. W., McCullough, B. F., & Burns, N. H. (1987). Stabilized subbase friction study for concrete pavements. *Texas Department of Transportation.*

White, H. (2007). Integral abutment bridges: Comparison of current practice between European countries and the United States of America. *New York State Department of Transportation*.

Wimsatt, A. J., McCullough, B. F., & Burns, N. H. (1987). Methods of analyzing and factors influencing frictional effects of subbases. *Texas Department of Transportation.*

Wing, K. M., & Kowalsky, M. J. (2005). Behavior, analysis, and design of an instrumented link slab bridge. *Journal of Bridge Engineering*, *10*(3), 331-344.

Wolde-Tinsae, A. M., Klinger, J. E., & White, E. J. (1988). Performance of jointless bridges. *Journal of performance of constructed facilities*, *2*(2), 111-125.

Won, M. (2021). CRCP in Texas. *TxDOT/CCT Concrete Conference.*

Yousefpoursadatmahalleh, H. (2015). Short-term and time-dependent stresses in precast network arches (Doctoral dissertation). *The University of Texas at Austin*.

Zhan, X., Liu, K., Zhao, Y. B., & Yan, H. (2021). Tensile Performance of SHCC Road-Bridge Link Slabs in Fully Jointless Bridges. *Advances in Civil Engineering*.

Zhan, X., Shao, X, & Liu, G. (2014). Ductility performance analyses of the semi-integral jointless bridge. In *Proceedings of the 2014 Technical Congress on Resources Environment and Engineering*.

Zheng, S., Liu, Y., Yoda, T., & Lin, W. (2016). Parametric study on shear capacity of circular-hole and long-hole perfobond shear connector. *Journal of Constructional Steel Research*, 117, 64-80.

Zheng, Y., Zhang, L. F., & Xia, L. P. (2018). Investigation of the behavior of flexible and ductile ECC link slab reinforced with FRP. *Construction and Building Materials, 166*, 694-711.

Zollinger, D., Moon, W., Ley, T., Riding, K., Wimsatt, A., Zhou, W., ... & Choi, P. (2014). Implementation of curing, texturing, subbase, and compaction measurement alternatives for continuously reinforced concrete pavement (No. FHWA/TX-13/5-6037-01-1). *Texas Department of Transportation.*

Zornberg, J., Helwig, T., Walter, J., and Morsy, A. (2017). Task 2-Assess the state of the practice through existing literature (Research project 0-6936 report). *Texas Department of Transportation.*

Solmax. Technical data sheet for textured LLDPE sheet.

https://www.solmax.com/uploads/tech-paper-document-en-files/lldpe-series-60-mil-black-textured-americas-imperial-units-technical-data-sheet.pdf.